Aix*Marseille université
Socialement engagée

NNT : 2024AIXM0324

THÈSE DE DOCTORAT

Soutenue à Aix-Marseille Université
le 29 octobre 2024

Gaya BENANE

Lepton Flavor Universality test using $B^0 \to D^{*-}\tau^+\nu_\tau$ with $\tau^+ \to 3\pi^\pm(\pi^0)\nu_\tau$ decays at LHCb

Discipline
Physique et Sciences de la Matière

Spécialité
Physiques des Particules et Astroparticules

École doctorale 352
Physique et Sciences de la Matière

Laboratoire/Partenaires de recherche
Centre de Physique des Particules de Marseille

Composition du jury

Emi KOU Directrice de recherche, IJClab	Rapporteure
Jean-François MARCHAND Chargé de recherche, LAPP	Rapporteur
Patrick ROBBE Directeur de recherche, IJClab	Examinateur
Cristinel DIACONU Directeur de recherche, CPPM	Président du jury
Olivier LEROY Directeur de recherche, CPPM	Directeur de thèse

LHCb

CENTRE DE PHYSIQUE DES PARTICULES DE MARSEILLE
CPPM

Affidavit

Je soussigné, Gaya Benane, déclare par la présente que le travail présenté dans ce manuscrit est mon propre travail, réalisé sous la direction scientifique d'Olivier Leroy, dans le respect des principes d'honnêteté, d'intégrité et de responsabilité inhérents à la mission de recherche. Les travaux de recherche et la rédaction de ce manuscrit ont été réalisés dans le respect à la fois de la charte nationale de déontologie des métiers de la recherche et de la charte d'Aix-Marseille Université relative à la lutte contre le plagiat.

Ce travail n'a pas été précédemment soumis en France ou à l'étranger dans une version identique ou similaire à un organisme examinateur.

Fait à Marseille, le 11 décembre 2024.

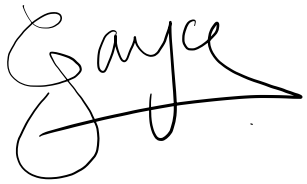

Cette œuvre est mise à disposition selon les termes de la Licence Creative Commons Attribution - Pas d'Utilisation Commerciale - Pas de Modification 4.0 International.

Liste de publications et participation aux conférences

Liste des publications réalisées dans le cadre du projet de thèse:

1. Test of lepton flavour universality using $B^0 \to D^{*-}\tau^-\overline{\nu}_\tau$ decays with hadronic τ channels, Physical Review D, 12 june 2024.

2. Proceedings du Journées de Rencontres de Jeunes Chercheurs (hal-04118967) Oct 23–29, 2022, Gaya Benane, La Rivière in Saint-Jean-de-Monts, France.

Participation aux conférences et écoles d'été au cours de la période de thèse:

1. Hadron 2023, June 5–9, 2023, Genova, Italy. Presentation (conférence internationale, on behalf of the LHCb collaboration)

2. GDR – Intensity Frontier Workshop, Nov 2–4, 2022, Domaine Lyon Saint-Joseph, France. Presentation (conférence nationale)

3. Journées de Rencontres de Jeunes Chercheurs, 2022, Oct 23–29, 2022, La Rivière in Saint-Jean-de-Monts, France. Presentation (conférence nationale)

4. The 2023 European School of High-Energy Physics, Sept 6–19, 2023, Grenaa, Denmark, (école d'été)

5. School of Statistics, May 16–20, 2022 (école d'été)

"*Somewhere, something incredible is waiting to be known.*"

— Carl Sagan

Abstract

The Standard Model of Particle Physics predicts that the three charged leptons e, μ, and τ, should have identical electroweak couplings. The only distinction between them arises from their masses, due to their interactions with the Higgs field. However, experiments such as BaBar, Belle, Belle II and LHCb, have observed deviations from these predictions, particularly in the $b \to c\ell\nu_\ell$ transitions, known as *charged-current flavor anomalies*. This thesis investigates the $B^0 \to D^*\tau\nu$ decays, with the τ lepton being reconstructed from its hadronic decays $\tau \to 3\pi\nu(\pi^0)$. The study aims to measure $\mathbf{R}(D^*)$, which is a ratio of the former's decay branching fraction to the $B^0 \to D^*\mu\nu$ branching fraction. This observable is used for Lepton Flavor Universality test in $b \to c\ell\nu_\ell$ transitions. By utilizing techniques such as ReDecay for fast simulation, and Multivariate Analyses for signal selection, this analysis builds upon and improves the methods used in previous LHCb measurements: the first analysis [1, 2] was performed on data collected during the Run 1 (2011–2012), the second one [3] on initial stages of data collection during Run 2 (2015–2016). This thesis present for the first time a measurement using the full Run 2 dataset (2015–2018). The precision of the $\mathbf{R}(D^*)$ measurement is refined, currently achieving approximately 3.8% statistical uncertainty. Although the final value is currently *blinded*, pending the estimation of systematical uncertainties and an internal LHCb collaboration review, this thesis presents a comprehensive documentation of the analysis.

Résumé

Selon le Modèle Standard de la Physique des Particules, les leptons chargés e, μ et τ devraient présenter des couplages électrofaibles identiques, se distinguant uniquement par leurs masses en raison de leurs differents couplages au champ de Higgs. Toutefois, des écarts par rapport à ces prédictions ont été observés dans les transitions $b \to c\ell\nu_\ell$ lors d'expériences menées par BaBar, Belle, Belle II, et LHCb. Ce phénomène est connu sous le nom d'*anomalies de changement de saveur dans les courants chargés*. L'objectif principal de cette étude est de mesurer le rapport $\mathbf{R}(D^*)$, défini comme le ratio des taux de désintégration $B^0 \to D^*\tau\nu$ et $B^0 \to D^*\mu\nu$. Cette observable est utilisée comme test de l'Universalité de la Saveur Leptonique dans les transitions $b \to c\ell\nu_\ell$. Cette thèse se focalise sur les désintégrations $B^0 \to D^*\tau\nu$, où le lepton τ est reconstruit à partir de ses désintégrations hadroniques $\tau \to 3\pi\nu(\pi^0)$. En utilisant des techniques telles que ReDecay pour la simulation rapide et des Analyses Multivariées pour la sélection du signal, cette analyse s'appuie sur et améliore les méthodes utilisées dans les mesures précédentes de LHCb : la première analyse [1, 2] a été réalisée sur les données collectées pendant le Run 1 (2011–2012), et la seconde [3] sur une partie des données collectées pendant le Run 2 (2015–2016). Cette thèse présente pour la première fois une mesure utilisant l'ensemble des données du Run 2 (2015–2018). La précision de la mesure de $\mathbf{R}(D^*)$ est affinée, atteignant actuellement une incertitude statistique d'environ 3.8%. Bien que la valeur finale soit actuellement *masquée*, en attendant une estimation des incertitudes systématiques et une revue interne dans la collaboration LHCb, cette thèse présente une documentation complète de l'analyse.

Résumé Étendu

Introduction

Le Modèle Standard (SM) décrit trois des quatre forces fondamentales de la nature et classe les particules subatomiques en fermions (quarks et leptons) et bosons (de jauge et de Higgs). Les fermions se répartissent en trois générations aux propriétés identiques, sauf pour la masse. Le SM postule que les interactions entre leptons chargés et bosons de jauge sont universelles (LFU), une fois les différences de masse prises en compte.

Cependant, des anomalies récentes dans les désintégrations semi-leptoniques des mésons B suggèrent des violations potentielles de la LFU. Ces anomalies apparaissent dans les processus $B \to D^{(*)}\ell\nu$, où le ratio des fractions d'embranchement :

$$\mathbf{R}\left(D^{(*)}\right) = \frac{\mathrm{Br}(B \to D^{(*)}\tau\nu)}{\mathrm{Br}(B \to D^{(*)}\ell\nu_\ell)} \,,$$

dépasse les prédictions du SM, indiquant une nouvelle physique possible.

Des théories au-delà du SM, comme celles avec des bosons de Higgs chargés, des bosons vecteurs, ou des leptoquarks, pourraient expliquer ces anomalies. Ces théories prévoient des particules se couplant de manière privilégiée à la troisième génération de leptons, avec des masses autour du TeV.

Le LHC au CERN, et plus particulièrement l'expérience LHCb permet de tester ces théories. Initialement dédié à l'étude de l'asymétrie CP et des désintégrations rares des particules à quark b, LHCb explore maintenant la LFU et réalise des mesures précises des hadrons b et c.

Cette recherche vise à tester la LFU dans les désintégrations semi-leptoniques des mésons B via le ratio $\mathbf{R}(D^*)$, utilisant les désintégrations $B^0 \to D^{*-}\tau^+\nu_\tau$. Le lepton τ^+ est reconstruit en modes hadroniques. Avec les données du Run 2 de LHCb (2015–2018), l'analyse améliore la précision et la fiabilité par rapport aux études antérieures [1-3].

Méthodologie

L'étude actuelle vise à mesurer $\mathbf{R}(D^*)$, le rapport des fractions d'embranchement des désintégrations semi-leptoniques du méson B^0, défini comme :

$$\mathbf{R}(D^*) \equiv \frac{\mathrm{Br}(B^0 \to D^{*-}\tau^+\nu_\tau)}{\mathrm{Br}(B^0 \to D^{*-}\mu^+\nu_\mu)} \, .$$

Cette observable permet de tester l'hypothèse d'universalité de saveur des leptons dans cette désintégration.

Dans le mode signal, $B^0 \to D^{*-}\tau^+\nu_\tau$, le D^{*-} se désintègre principalement en $\overline{D}^0$ et π^-, avec une fraction d'embranchement de :

$$\mathrm{Br}(D^{*-} \to \overline{D}^0\pi^-) = 67.7 \pm 0.5\% \, ,$$

et un mode de désintégration $\overline{D}^0$ en K^+ et π^-, avec une fraction d'embranchement de :

$$\mathrm{Br}(\overline{D}^0 \to K^+\pi^-) = 3.950 \pm 0.031\% \, .$$

Les mesures de $\mathbf{R}(D^*)$ effectuées par LHCb utilisent les deux modes de désintégration du τ^+ :

- Les désintégrations *muoniques* $\tau^+ \to \mu^+\nu_\mu\overline{\nu}_\tau$, avec une fraction d'embranchement de :

$$\mathrm{Br}(\tau^+ \to \mu^+\nu_\mu\overline{\nu}_\tau) = 17.4\% \, ,$$

- Le mode de désintégration *hadronique* $\tau^+ \to 3\pi^\pm(\pi^0)\overline{\nu}_\tau$, avec une fraction d'embranchement de :

$$\mathrm{Br}(\tau^+ \to 3\pi^\pm(\pi^0)\overline{\nu}_\tau) = 13.5\% \, .$$

La désintégration hadronique du τ^+ est choisie pour l'étude présentée ici. Le mode de normalisation $B^0 \to D^{*-}3\pi$ (qui sert d'étape intermédiaire) est introduit. En prenant le rapport du signal au mode de normalisation, la plupart des effets systématiques (détecteur et reconstruction) sont efficacement compensés.

Le mode de normalisation partage les mêmes états finaux visibles que le signal, mais sans neutrinos, permettant ainsi une reconstruction complète du pic de masse du B^0.
Le rapport $\mathbf{R}(D^*)$ peut être exprimer ainsi :

$$\mathbf{R}(D^*) = \frac{\mathrm{Br}(B^0 \to D^{*-}\tau^+\nu_\tau)}{\mathrm{Br}(B^0 \to D^{*-}\mu^+\nu_\mu)} = \frac{\mathrm{Br}(B^0 \to D^{*-}\tau^+\nu_\tau)}{\mathrm{Br}(B^0 \to D^{*-}3\pi^\pm)} \cdot \frac{\mathrm{Br}(B^0 \to D^{*-}3\pi^\pm)}{\mathrm{Br}(B^0 \to D^{*-}\mu^+\nu_\mu)}$$

Le rapport mesuré est donné par :

$$\mathcal{K}(D^{*-}) \equiv \frac{\mathrm{Br}\left(B^0 \to D^{*-}\tau^+\nu_\tau\right)}{\mathrm{Br}\left(B^0 \to D^{*-}3\pi^\pm\right)} ,$$

et peut être exprimé en termes de rendements de signal et de normalisation, d'efficacités et de fractions d'embranchement de désintégration du τ^+, comme suit :

$$\mathcal{K}(D^{*-}) = \frac{N_{\mathrm{sig}}}{N_{\mathrm{norm}}} \cdot \frac{\varepsilon_{\mathrm{norm}}}{\varepsilon_{\mathrm{sig}}} \cdot \frac{1}{\mathrm{Br}\left(\tau^+ \to 3\pi^\pm\overline{\nu}_\tau\right) + \mathrm{Br}\left(\tau^+ \to 3\pi^\pm\pi^0\overline{\nu}_\tau\right)} .$$

Les rendements sont obtenus à partir de l'ajustement aux données :

- Le rendement du signal, noté N_{sig}, est dérivé en utilisant un ajustement par vraisemblance maximale étendu en histogramme sur trois dimensions :
  - Le carré de quantité de mouvement transférée aux leptons, avec 8 bins :

$$q^2 \equiv (p_B - p_{D^*})^2 ,$$

  - La durée de vie du τ^+, t_τ, avec 8 bins ;
  - L'Anti-D_s^+ BDT, avec 6 bins.
- Le rendement de normalisation, $N_{\mathtt{norm}}$, est estimé à partir d'un ajustement de vraisemblance maximale non binné, à la distribution de masse du système $D^*3\pi^\pm$.
- Les efficacités $\varepsilon_{\mathtt{sig}}$ et $\varepsilon_{\mathtt{norm}}$ sont obtenues à partir de la simulation. Plus précisément, l'efficacité du signal est obtenue à partir de la moyenne pondérée des deux modes de désintégration du τ^+– $\tau^+ \to 3\pi^\pm\overline{\nu}_\tau$ et $\tau^+ \to 3\pi^\pm\pi^0\overline{\nu}_\tau$–selon leurs fractions d'embranchement.

Enfin, $\mathbf{R}(D^*)$ est obtenu en utilisant la fraction d'embranchement connue du mode de normalisation, mesurée par LHCb [4], BaBar [5], et Belle [6]. La valeur moyenne [7] est donnée par :

$$\mathrm{Br}(B^0 \to D^{*-}3\pi^\pm) = (7.21 \pm 0.28) \times 10^{-3} ,$$

et la fraction d'embranchement du dénominateur de $\mathbf{R}(D^*)$, telle que mesurée dans [8] :

$$\mathrm{Br}(B^0 \to D^{*-}\mu^+\nu_\mu) = (5.06 \pm 0.02 \pm 0.12)\% .$$

Les principales sources de bruit de fond pour le mode signal $B^0 \to D^{*-}\tau^+\nu_\tau$ et $\tau^+ \to 3\pi\overline{\nu}_\tau$ sont :

- **Bruits de fond prompts** : $B^0 \to D^*3\pi X$, où le système 3π provient directement de la désintégration du B^0 ;
- **Bruits de fond double charme** : $B^0 \to D^{*-}DX$, où $D \to 3\pi^{\pm}X$;
- **Effet de cascade** provenant des mésons D^{*-} excités, dénotés par D^{**} ;
- **Combinatoires** impliquant des combinaisons aléatoires de particules reconstruites dans un événement de collision pp faussement assemblées en un candidat signal unique.

En revanche, le bruit de fond associé au mode de normalisation est principalement combinatoire et nettement plus faible.

Sélection Des Événements

La reconstruction de la cinématique des désintégrations suit les méthodes décrites dans les Références [1-3]. Les candidats de type *signal* sont formés en combinant un méson D^{*-} qui se désintègre selon $D^{*-} \to \pi^-\overline{D}^0(\to K^+\pi^-)$ et un système de $3\pi^{\pm}$ détaché du vertex de désintégration du B^0, en raison de la durée de vie non négligeable du lepton τ^+.
Le principal bruit de fond provient des désintégrations de B^0 où le système $3\pi^{\pm}$ provient directement du vertex du B^0, appelées ici les bruits de fond *prompts*. Pour réduire ce bruit de fond, la distance entre les vertex de B^0 et $3\pi^{\pm}$ le long de la direction du faisceau, normalisée par son incertitude, notée Δz, doit être supérieure à 2.
Les désintégrations double-charm[1] $B \to D^{*-}D(X)$ constituent le deuxième bruit de fond dominant, avec une topologie de vertex détaché similaire à celle des désintégrations signal. Les autres bruits de fond sont éliminés en exigeant que le système $3\pi^{\pm}$ provienne d'un vertex commun.

Trois catégories de données et de simulations sont utilisées : signal, normalisation et contrôle. Les échantillons de contrôle sont utilisés pour étudier le bruit de fond double-charm et sont enrichis en désintégrations de D_s^+. La sélection des échantillons se déroule en deux étapes. D'abord, des critères de sélection communs éliminent les candidats issus de combinaisons

[1] X représente les particules non reconstruites présentes dans la chaîne de désintégration, et (X) celles qui peuvent ou non être présentes.

aléatoires de par ticules de l'état final. Ensuite, des critères spécifiques sont appliqués à chaque ensemble.

Critères de Sélection Communs

Les critères de sélection communs visent à éliminer les bruits de fond prompts et combinatoires. Les traces compatibles avec l'hypothèse de kaon ou de pion et ayant $p > 2\,\mathrm{GeV/c}$ et $p_T > 250\,\mathrm{MeV/c}$ sont sélectionnées pour former les candidats $\overline{D}^0$, avec une masse entre $[1840, 1890]\,\mathrm{MeV/c^2}$ et un p_T supérieur à $1.2\,\mathrm{GeV/c}$. Les candidats $\overline{D}^0$ sont combinés avec des traces de pion ayant $p_T > 110\,\mathrm{MeV/c}$ pour former les candidats D^{*-}, avec une différence de masse (Δm) entre 143 et $148\,\mathrm{MeV/c^2}$. Les régions latérales de $m(\overline{D}^0)$ dans les intervalles $[1825, 1840]\,\mathrm{MeV/c^2}$ et $[1890, 1905]\,\mathrm{MeV/c^2}$ et Δm entre $[150, 160]\,\mathrm{MeV/c^2}$ sont utilisées pour étudier le bruit de fond combinatoire.

Les candidats τ^+ sont formés de trois traces, chacune avec $p_T > 250\,\mathrm{MeV/c}$ et compatible avec l'hypothèse de pion. De plus, le vertex $3\pi^\pm$ doit être séparé du vertex primaire (PV) associé à la désintégration signal d'au moins 10 fois l'incertitude sur la distance de séparation. La distance radiale entre le vertex $3\pi^\pm$ et le centre du faisceau dans le plan transverse doit être entre $[0.2, 5.0]\,\mathrm{mm}$ pour éviter des erreurs dues aux interactions secondaires ou à un PV. le bruit de fond combinatoire est réduit en associant les candidats $\overline{D}^0$ et τ^+ au même PV. Pour les événements avec une masse de B^0 supérieure à $5150\,\mathrm{MeV/c^2}$, la signification de l'IP des candidats $\overline{D}^0$ et $3\pi^\pm$ par rapport au PV associé doit être supérieure à 4.

Sélection du Signal

Les candidats de type signal $B^0 \to D^{*-}\tau^+\nu_\tau$ sont identifiés grâce à un critère de vertex détaché et à la suppression de bruits de fond, où les désintégrations de D_s^+ imitent les désintégrations hadroniques de τ^+.

Dans les désintégrations $B^0 \to D^{*-}\tau^+\nu_\tau$, le vertex $3\pi^\pm$ est détaché du vertex B^0. Le vertex B^0 est associé au point d'approche le plus proche entre les trajectoires de D^{*-} et $3\pi^\pm$. Un classificateur (BDT) est utilisé pour identifier cette topologie. Ce BDT utilise les positions des vertexs $\overline{D}^0$, B^0 et $3\pi^\pm$, leurs incertitudes, la masse du $3\pi^\pm$, et les moments des traces du candidat B^0. Ce classificateur est entraîné avec des désintégrations simulées $B^0 \to D^{*-}\tau^+\nu_\tau$ comme signal et des productions simulées promptes $b\overline{b} \to D^{*-}3\pi^\pm X$ comme bruit de fond. Ce BDT a une meilleure performance que les méthodes précédentes, avec un taux de rejet de fond 20% plus élevé pour la même efficacité de signal.

Les désintégrations D_s^+, qui constituent un bruit de fond majeur, sont traitées en utilisant la

cinématique des désintégrations, comme les limites de masse $\pi^+\pi^-$ et la présence de particules neutres. Un autre classificateur (anti-D_s^+ BDT) est entraîné sur des désintégrations simulées de $B^0 \to D^{*-}\tau^+\nu_\tau$ et de D_s^+. Il améliore la suppression des bruits de fond. La distribution de cette BDT est également utilisée comme variable d'ajustement pour estimer le rendement des désintégrations $B^0 \to D^{*-}\tau^+\nu_\tau$.

La masse invariante du système $3\pi^\pm$ doit être inférieure à $1600\,\mathrm{MeV}/c^2$ pour éliminer les bruits de fond double-charm. La masse $D^*3\pi^\pm$ est limitée à $5100\,\mathrm{MeV}/c^2$, en cohérence avec la présence de neutrinos dans l'état final des désintégrations de signal.

Sélection du Mode de Normalisation

La sélection des candidats $B^0 \to D^{*-}3\pi$ repose sur la reconstruction complète des désintégrations $B^0 \to D^{*-}3\pi^\pm$ et sur le fait que le système $3\pi^\pm$ provient directement du méson B^0. Les candidats B^0 sont choisis dans l'intervalle de masse $[5150, 5400]\,\mathrm{MeV}/c^2$. La sélection reste similaire à celle du mode $B^0 \to D^{*-}\tau^+\nu_\tau$ pour minimiser les biais systématiques dans la mesure du ratio $\mathcal{K}(D^{*-})$. Pour garantir cela, le vertex de désintégration $\overline{D}^0$ doit être plus en aval que le vertex $3\pi^\pm$, similaire au critère de détachement du système $3\pi^\pm$ dans les désintégrations $B^0 \to D^{*-}\tau^+\nu_\tau$. L'anti-$D_s^+$ BDT et les critères de sélection de $m(3\pi)$ ne sont pas appliqués. Toutefois, cela ne biaise pas $\mathcal{K}(D^{*-})$, car l'efficacité reste élevée pour les désintégrations $B^0 \to D^{*-}\tau^+\nu_\tau$.

Échantillons de Contrôle

Le principal bruit de fond après l'application des critères de sélection est constitué des désintégrations double-charm $B \to D^{*-}D(X)$, où D représente un méson D_s^+, D^+, ou D^0. Des échantillons de contrôle sont utilisés pour étudier ces bruits de fond et ajuster les corrections pour les échantillons simulés, ce qui est essentiel pour construire les PDFs de bruit de fond dans l'ajustement du signal.
L'analyse des désintégrations impliquant des mésons D_s^+ se fait en deux étapes : d'abord, des corrections sont appliquées aux fractions de désintégration simulées, et ensuite, la composition des différentes désintégrations $B \to D^{*-}D(X)$ est déterminée pour contraindre les composants de bruit de fond dans l'ajustement.

Modèle de Désintégration $D_s^+ \to 3\pi X$

Les désintégrations hadroniques du lepton τ, le canal signal, sont dominées par l'état $a_1(1260)^+$, qui se désintègre en $\rho^0\pi^+$. La situation devient complexe car le D_s^+ peut aussi se désintégrer en $a_1(1260)^+$, imitant ainsi la désintégration du signal. De plus, la fraction d'embranchement

de cette désintégration n'est pas bien connue.

Il y a également un risque de mauvaise identification dans la chaîne de désintégration :

$$D_s^+ \to \eta' X \quad \text{avec} \quad \eta' \to \rho^0 \gamma \,.$$

Le ρ^0, provenant de la désintégration du D_s^+, peut être attribué par erreur à une désintégration de τ^+.

Pour que la simulation reflète correctement les données réelles, les contributions de différentes résonances sont normalisées avec précision. Cela inclut les résonances provenant de fractions d'embranchement inconnues, en particulier la résonance η'.
Un examen détaillé des fractions de désintégration de $D_s^+ \to 3\pi X$ est mené en utilisant un échantillon enrichi de données, sélectionné sur la base des critères de l'anti-D_s^+ BDT. Un ajustement simultané de maximum de vraisemblance en histogramme est réalisé aux distributions de quatre variables de masse. Ces variables sont specifiquement choisies afin de distinguer efficacement les modes de désintégration de D_s^+, en tenant compte des particules neutres supplémentaires, potentielles dans le processus de désintégration.

Les composantes de désintégration de D_s^+ correspondant à des voies de désintégration spécifiques. Les résonances impliquées sont η, η', ω, ϕ, et des contributions non résonantes. Les paramètres d'ajustement sont affinés en utilisant des échantillons de simulation adjusté, en plus des contraintes supplémentaires pour améliorer la stabilité de l'ajustement.

Échantillon de Contrôle pour les Désintégrations $B \to D^{*-} D_s^+(X)$

L'échantillon de contrôle pour les désintégrations $B \to D^{*-} D_s^+(X)$ est crucial pour fournir des contraintes sur l'ajustement du signal. Cet échantillon, enrichi en désintégrations $B \to D^{*-} D_s^+(X)$ où $D_s^+ \to 3\pi$, diffère de la sélection standard : en s'assurant que la masse du 3π est proche de la masse du D_s^+. Le critère sur l'anti-D_s^+ BDT est également omis, ainsi que les contraintes de masse sur B^0 et τ^+.

Cette sélection capture à la fois les désintégrations exclusives $B^0 \to D^{*-} D_s^{(*,**)+}$ et inclusives $B \to \overline{D}^{**} D_s^+(X)$ et $B_s^0 \to D^{*-} D_s^+(X)$, où $\overline{D}^{**}$ et D_s^{**+} désignent des mésons charmés ou charmés-étranges de masse plus élevée.

L'analyse utilise un ajustement de maximum de vraisemblance étendu et en histogramme pour la distribution de la différence de masse $\Delta M \equiv m(D^{*-}3\pi) - m(\overline{D}^0) - m(3\pi)$. Elle prend en compte la distribution de q^2, qui varie en fonction de la présence de particules supplémentaires dans les modes inclusifs. La fonction de densité de probabilité (PDF) totale pour l'ajustement

est :

$$\mathcal{P} = f_{comb}\mathcal{P}_{comb} + \frac{(1 - f_{comb})}{k} \sum_i f_i \mathcal{P}_i,$$

où f_{comb} représente la fraction de fond combinatoire et f_i sont les fractions relatives des différentes composantes $B \longrightarrow D^{*-}D_s^+(X)$. Le modèle de chaque composante est dérivé de simulations, assurant une modélisation précise des caractéristiques de la désintégration.

L'ajustement évalue les distributions de ΔM, de q^2, du temps de désintégration du candidat τ^+ (t_τ), et de l' anti-D_s^+ BDT. Les fractions dérivées de l'ajustement sont utilisées comme contraintes gaussiennes dans l'ajustement d'extraction du signal, après avoir tenu compte des différences d'efficacité entre les échantillons de contrôle et de signal.

Fit du Signal et du mode de Normalisation

Les méthodes pour extraire les rendements de signal et de normalisation et calculer le rapport final $\mathbf{R}(D^*)$ sont décrites. La stratégie suit les techniques des mesures précédentes (*cf.* Refs. [1-3]). Le rendement du signal reste masqué et les resultats sont préliminaires.

Fit du Signal

Le rendement du signal (N_{sig}) est déterminé à l'aide d'un ajustement de maximum de vraisemblance étendu appliqué aux distributions de q^2, t_τ, et de l'anti-D_s^+ BDT. Le processus d'ajustement utilise huit bins pour q^2 et t_τ, et six bins pour le BDT, couvrant les intervalles de $[0, 11]\,\mathrm{GeV}^2/c^4$ $[0, 2]\,\mathrm{ps}$ et $[-0.2, 0.5]$, respectivement. Le modèle d'ajustement est un modèle tridimensionnel, avec les composants clés suivants :

- Les modes de signal avec les désintégrations $\tau^+ \longrightarrow 3\pi\overline{\nu}_\tau$ et $\tau^+ \longrightarrow 3\pi\pi^0\overline{\nu}_\tau$.
- Les fonds provenant des désintégrations en cascade et divers fonds combinatoires.

Les paramètres d'ajustement comprennent :

- N_{sig} : Nombre d'événements signal.
- $f_{\tau^+\to 3\pi\overline{\nu}_\tau}$: Fraction des désintégrations $\tau^+ \longrightarrow 3\pi\overline{\nu}_\tau$.
- $f_{\overline{D}^{**}\tau\nu}$: Fraction des désintégrations en cascade.
- $N_{D^0}^{same}$: Nombre de candidats $B \longrightarrow D^{*-}D^0(X)$ avec le même vertex.

- Diverses fractions et rendements associés à différents modes de désintégration et composants de bruit fond.

L'ajustement est réalisé en deux étapes : d'abord avec une variation libre de la fractions D^0 et une contrainte Gaussienne sur celle de D_s^+. L'ajustement est ensuite réitéré, avec des valeurs fixes pour ces paramètres, obtenues à partir du précédent ajustement. Cette procédure aboutit à un rendement de signal de $N_{sig} = 7909 \pm 280$.
L'incertitude statistique sur le rendement s'améliore de 4.1% à 3.5% entre les itérations.
L'ajustement est validé comme étant non biaisé grâce à des études de pseudo-expérience.

Fit du Mode de Normalisation

Dans la publication précédente [3], le rendement du mode de normalisation a été déterminé en utilisant la méthode sPlot, qui a désormais été remplacée par une méthode d'extrapolation. Le rendement est extrait d'un ajustement de vraisemblance maximale non biné à la masse du système $D^{*-}3\pi^{\pm}$.
L'ajustement utilise une fonction Crystal Ball et deux fonctions Gaussiennes pour le signal, tandis que les contributions de bruit de fond sont modélisées par une fonction exponentielle. L'ajustement prend également en compte les contributions d'autres désintégrations pouvant imiter le pic B^0.

Le rendement de normalisation est obtenu comme suit :

1. Ajuster la masse B^0 dans les fenêtres spécifiées de $m(D^0)$ et Δm pour obtenir le rendement total de B^0.

2. Ajuster la masse B^0 dans les régions de bande latérale pour estimer le rendement du faux D^{*-}.

3. Soustraire le rendement du faux D^{*-} du rendement total de B^0 pour obtenir le véritable rendement de B^0.

4. Déterminer le rendement total de D_s^+ et l'utiliser pour trouver le véritable rendement de D_s^+.

5. Soustraire le véritable rendement de D_s^+ du véritable rendement de B^0 pour obtenir le rendement de normalisation.

Les paramètres de résolution sont contraints en utilisant des échantillons MC, avec une préférence pour les données MC de B^0 en raison de leur simplicité. Les résultats finaux montrent

un rendement total de B^0 de 103590 ± 353, le véritable rendement de B^0 de 94533 ± 473, et un rendement de normalisation de :

$$N_{\mathtt{norm}} = 93173 \pm 441 \ . \tag{0.1}$$

L'incertitude provenant de la méthode d'extrapolation est quantifiée en utilisant le bootstrap, résultant en une incertitude statistique de ±441 événements.

Calcul Préliminaire du Rapport $R(D^*)$

Tous les éléments nécessaires sont maintenant en place pour mesurer $\mathbf{R}(D^*)$.
En utilisant les rendements de signal et de normalisation calculés, $\mathcal{K}(D^{*-})$ est donné par :

$$\mathcal{K}(D^{*-}) = 1.829 \pm 0.067. \tag{0.2}$$

Ce chiffre inclut les incertitudes provenant des rendements, des efficacités et des fractions d'embranchement. Le rapport $\mathbf{R}(D^*)$ est alors déterminé :

$$\mathbf{R}(D^*) = 0.265 \pm 0.010\,(\mathtt{stat.}) \pm X\,(\mathtt{syst.}) \pm 0.012\,(\mathtt{ext.}), \tag{0.3}$$

avec une valeur centrale masquée. Les incertitudes sont classées comme statistique, systématique (en cours d'estimation) et externe, dérivée des fractions d'embranchement. L'incertitude statistique relative sur $\mathbf{R}(D^*)$ est de 3,8%.

Une valeur de $\mathbf{R}(D^*)$ à partir des données de 2015–2016 est [3] :

$$\mathbf{R}(D^*) = 0.260 \pm 0.015\,(\mathtt{stat.}) \pm 0.016\,(\mathtt{syst.}) \pm 0.012\,(\mathtt{ext.}). \tag{0.4}$$

L'incertitude statistique relative était de 5,8% avec l'ensemble de données partiel, mais elle a diminué à 3,8% avec l'ensemble complet de données. Des améliorations supplémentaires de la précision sont attendues avec les raffinements dans les ajustements de contrôle et de signal.

Conclusion

Cette étude mesure le rapport $\mathbf{R}(D^*)$ avec les données de collisions proton-proton collectées par LHCb de 2015 à 2018, pour une luminosité intégrée de 6 fb^{-1}. Le lepton τ^+ est reconstruit via ses désintégrations hadroniques $\tau^+ \to 3\pi^\pm(\pi^0)\nu_\tau$.
L'analyse partielle de Run 2 sur les données de 2015–2016 a donné [3] :

$$\mathbf{R}(D^*)|_{2015\text{–}2016} = 0.260 \pm 0.015\,(\mathtt{stat.}) \pm 0.016\,(\mathtt{syst.}) \pm 0.012\,(\mathtt{ext.}) \ .$$

Plusieurs améliorations ont été apportées : optimisation de la sélection en ligne, corrections d'efficacité, et une nouvelle méthode d'ajustement de normalisation. Des échantillons de MC pour le D_s^+ ont également été ajoutés.
Un ajustement préliminaire du signal a été réalisé. Le résultat final est masqué en attendant l'amélioration des ajustements et l'estimation des incertitudes systématiques :

$$\mathbf{R}(D^*)|_{\text{Run 2}} = 0.265 \pm 0.010\,(\texttt{stat.}) \pm X\,(\texttt{syst.}) \pm 0.012\,(\texttt{ext.})\,.$$

L'incertitude systématique est principalement statistique ; l'augmentation de la taille de l'échantillon permettra de la réduire.

Il est prévu que le nombre de paramètres libres dans l'ajustement sera réduit grâce aux nouveaux modes de désintégration mesurés par BESIII [9, 10], améliorant ainsi les contraintes sur le rendement D_s^+ et la fraction D^+.
Cette analyse est dans un état avancé. Les efforts actuels se concentrent sur le raffinement de l'ajustement et l'estimation des incertitudes systématiques. Une réanalyse des données du Run 1 est en cours pour les combiner avec ceux du Run 2.

Aknowledgements

I would like to thank my supervisor, Olivier, whose enthusiasm for meticulous detail and too frequent check-ins ensured that I never had to experience the solitude or depression often associated with PhD research. I am grateful to Chen, whose vast knowledge and willingness to assist at any time were invaluable throughout my PhD journey. To my LHCb colleagues–Dorothea, Anton, Julien, Andy, Bogdan and Ching-Hua–I am deeply grateful. Working alongside such knowledgeable and dedicated individuals has been both an honor and a profound learning experience. Special thanks also to the proponents of the $\mathbf{R}(D^*)$ measurement–Guy, Bo, and Resmi.

I owe a huge thank you to the CPPM team, the best comrades-in-arms a PhD student could hope for. Whether it was for sharing resources, or just being there for coffee breaks, your collective wisdom and friendship made what seemed an impossible journey remarkably enjoyable. Together, we survived the perils of PhD life! Big thanks to Brigitte for helping me navigate through the deep madness of paperwork necessary to obtain my resident permit, year after year! I extend my gratitude for Elisabeth, my lab mentor, and Aoife, my former supervisor. Special thanks to the lunchtime running crew, the "Furious Foxes", for the energy boosts and the much-needed breaks. Your camaraderie on those runs was revigorating.

I am deeply grateful to my parents, my family, my friends and my girlfriend Isoline, for thier committed support and endless patience. Your love, encouragement, and occasional distractions kept me grounded and reminded me there's a world outside physics.

Table of Contents

Affidavit i

Liste de publications et participation aux conférences ii

Abstract v

Résumé vi

Résumé Étendu vii

Aknowledgements xviii

Table of Contents xix

Introduction 1

1. Standard Model 3
- 1.1. Quantum Field Theory . . . 3
- 1.2. Symmetries . . . 6
  - 1.2.1. Discret Symmetries . . . 6
  - 1.2.2. Continuous Symmetry . . . 8
  - 1.2.3. Fermions and Gauge Bosons . . . 9
- 1.3. Quantum Chromodynamics . . . 10
- 1.4. Electroweak Interaction . . . 11
- 1.5. Flavors . . . 12
- 1.6. Quark Mixing . . . 13
- 1.7. Bound States . . . 15
- 1.8. Summary of the Standard Model . . . 20

2. Phenomenology 23
- 2.1. Lepton Flavor Universality Tests . . . 23
  - 2.1.1. Universality of weak interactions . . . 24

2.1.2. Flavor Changing Neutral Currents . . . 25
2.1.3. Flavor Changing Charged Currents . . . 27
2.2. Effective Field Theories . . . 30
2.2.1. Standard Model Extensions . . . 30
2.2.2. Heavy Quark Effective Theory . . . 31
2.3. Theory of $B \to D^* \ell^+ \nu_\ell$ Decays . . . 33
2.4. Beyond Standard Model . . . 41
2.4.1. Two Higgs Doublet Model . . . 42
2.4.2. Vector Bosons . . . 42
2.4.3. Leptoquarks . . . 42
2.4.4. Experimental Constraints . . . 43

3. The LHCb Experiment **47**
3.1. Flavor Physics Experiments . . . 47
3.2. The Large Hadron Collider . . . 48
3.3. LHCb Detector . . . 52
3.3.1. The Traking System . . . 56
3.3.2. Particle Identification . . . 62
3.3.3. The Trigger System . . . 68
3.3.4. LHCb Softwares . . . 71
3.4. The LHCb Upgrades . . . 72

4. Methodology **76**
4.1. Strategy . . . 76
4.2. Reconstruction of Decay Kinematics . . . 79
4.2.1. Signal Hypothesis . . . 79
4.2.2. Double-Charm Assumption . . . 81
4.3. Analysis Workflow . . . 83
4.4. Datasets . . . 83
4.4.1. Collision Data . . . 83
4.4.2. Monte-Carlo Simulation . . . 85
4.4.3. Monte-Carlo Reweighting . . . 85
4.5. Role Highlights . . . 94

5. Selection and Efficiency **97**
5.1. Geometrical Acceptance . . . 98
5.2. The Trigger . . . 98
5.3. Preselection Criteria . . . 104
5.4. Initial Offline Selection Cuts . . . 109
5.5. Multivariate Analysis . . . 110
5.5.1. Anti-Combinatorial BDT . . . 112

5.5.2. Charged Isolation BDT . . . 118
5.5.3. Detachment BDT . . . 121
5.5.4. Anti-D_s^+ BDT . . . 126
5.6. Mode-Specific Cuts . . . 135
5.6.1. Signal-Like Events Selection . . . 135
5.6.2. Normalization Mode Criteria . . . 136
5.7. Efficiency Calculation . . . 137

6. Control Samples **141**
6.1. D_s^+ Decay Model . . . 141
6.2. $B \to D^* D_s^+(X)$ Control Mode . . . 148
6.3. $B \to D^{*-} D^0(X)$ and $B \to D^{*-} D^+(X)$ Control Modes . . . 152

7. Fit Results **155**
7.1. Signal Fit Results . . . 155
7.1.1. Fit Model and Templates . . . 156
7.1.2. Fit Validation . . . 164
7.1.3. Blinding Scheme . . . 165
7.1.4. Blinded Fit to Data . . . 166
7.1.5. Fit Results for Different Datasets . . . 172
7.1.6. Qualitative Uncertainty Estimation . . . 174
7.1.7. Fixing D^0 and D_s^+ Fractions . . . 174
7.2. Normalization Fit . . . 176
7.2.1. Extrapolation Method . . . 177
7.2.2. MC Constraints on the Resolution Parameters . . . 177
7.2.3. Fit Results . . . 178
7.3. Preliminary Results . . . 181

8. Systematic Uncertainties **183**
8.1. Signal Model . . . 183
8.2. Selection . . . 184
8.3. Template Size . . . 185
8.4. Empty Bins . . . 186
8.5. Background Models . . . 186
8.5.1. Impact of D_s^+ Decay Correction Weights . . . 186
8.5.2. $B \to D^{*-}(D^0, D_s^+)X$ Background Model . . . 187
8.5.3. $B \to D^{*-}(D^+, D^0, D_s^+)X$ Background Template Shapes . . . 187
8.5.4. $B \to D^{*-} 3\pi^{\pm} X$ Background Template Shapes . . . 188
8.5.5. Combinatorial Templates . . . 188
8.5.6. $m(3\pi)$ Variation . . . 188
8.6. Normalization Model . . . 188

8.7. Summary . . . 188

Conclusion **189**

Bibliography **191**

Appendix **209**

A. Methodology **210**
A.1. Reconstruction of the Decay Kinematics . . . 210
A.2. Fast Simulation with ReDecay . . . 210
A.3. PDG Review . . . 212
A.4. Monte-Carlo Correction . . . 214
A.4.1. Polarization of D^* in Two-Body Decays . . . 214
A.4.2. Polarization of D_s^* in Two-Body Decays . . . 214
A.4.3. Vertex Error Correction . . . 216

B. Selection and Efficiency **218**
B.1. L0 Trigger Corrections . . . 218
B.1.1. TOS Efficiency . . . 218
B.1.2. TIS Efficiency . . . 218
B.2. Preselection . . . 220
B.3. Multivariate Analysis . . . 220
B.3.1. BDT Methods . . . 220
B.4. Efficiency Calculation . . . 224
B.4.1. Selection Step Efficiency . . . 224
B.5. Trigger Configuration Key Table . . . 230

C. Fit results **232**
C.1. Signal Fit . . . 232
C.1.1. Fit Validation . . . 232
C.2. Normalization Fit . . . 232

D. Systematic Uncertainties **236**

Acronyms **239**

Introduction

The Standard Model of Particle Physics (SM) describes three of the four known fundamental interactions and classifies all known subatomic particles. The elementary particles of the SM are divided into two categories: *fermions* and *bosons*. Fermions are further divided into *quarks* and *leptons*, which are the building blocks of matter. While, bosons are either *gauge bosons*, responsible for mediating the interactions between particles, or the *Higgs boson*, responsible for the mass of the elementary particles. The building blocks of matter, quarks, and leptons, comes in three generations, or *flavors*. They only differ in their masses, and other properties, such as *electric charge*, *weak isospin*, and *weak hypercharge*, are identical. The Lepton Flavor Universality (LFU) is a principle of the SM, which asserts that the interaction of charged leptons—electrons, muons, and taus—with gauge bosons are *identical*, provided that differences in their respective masses are accounted for.

Recent observations, however, suggest potential violations of LFU in semileptonic decays of B mesons. Anomalies in processes like $B \to D^{(*)}\ell\nu$, where ℓ is a lepton, indicate possible differences in interaction strengths among the three lepton generations, not accounted for by the SM. These discrepancies can be quantified by the ratio of branching fractions:

$$\mathbf{R}\left(D^{(*)}\right) = \frac{\mathrm{Br}(B \to D^{(*)}\tau\nu_\tau)}{\mathrm{Br}(B \to D^{(*)}\ell\nu_\ell)} \,,$$

which compares the branching fractions of B meson decays into final states that include a $D^{(*)}$ meson and different leptons.

Measurements of these ratios were performed by BaBar [11, 12], Belle [13–17], Belle II [18], and LHCb [1, 2, 19–21]. These studies utilized various decay modes of the τ lepton, including both the *hadronic* modes $\tau \to \pi\nu$, $\tau \to \rho\nu$, and $\tau \to 3\pi\nu(\pi^0)$, as well as the *muonic* channel $\tau^+ \to \mu^+\nu_\mu\nu_\tau$. The global average of the $\mathbf{R}(D)$–$\mathbf{R}(D^*)$ ratio is 3.3σ above the SM prediction [8].

To explain these deviations, several Beyond the Standard Model (BSM) theories have been proposed. Notably, models involving Charged Higgs bosons, Vector Bosons, or Leptoquarks pro-

vide plausible explanations for these anomalies. Specifically, in the context of LFU-violating processes in semileptonic B decays, particles exhibiting preferential couplings to the third generation of leptons, with masses around the TeV scale, are expected to be at the origin of these deviations. These theoretical predictions offer compelling reasons for further experimental investigations to either validate or refute these BSM propositions.

The Large Hadron Collider (LHC) at CERN is a particle accelerator, specifically designed to probe the fundamental properties of particles at unprecedented energy levels. Among its four main experiments is LHCb, which was initially focused on studying CP asymmetry and the rare decay processes of particles containing the b-quark. Today, the scope of LHCb has broadened significantly. Its research program now encompasses a wide range of physics areas, including LFU tests, exotic hadron studies, and precise measurements of b and c-hadrons.

This research aims to test LFU in semileptonic B decays, via measurements of the $\mathbf{R}(D^*)$ ratio. More precisely, this is done using $B^0 \to D^{*-}\tau^+\nu_\tau$ decays, where the τ^+ lepton is reconstructed through its hadronic decay modes $\tau^+ \to 3\pi\overline{\nu}_\tau$ and $\tau^+ \to 3\pi\pi^0\overline{\nu}_\tau$. This analysis is based on data collected by the LHCb experiment during the Run 2 data-taking period (2015–2018) of the LHC, using proton–proton collisions at a center-of-mass energy of 13 TeV.

The analysis presented in this document follows the methodology introduced in the previous LHCb analysis, which analyzed data collected during the Run 1 (2011–2012) [1, 2] and initial stages of Run 2 (2015–2016) [3] the latter of which the author contributed to. This research incorporates a larger dataset (2017–2018) and improvements to the analysis techniques, enhancing both the precision and reliability of the results.

The structure of this document is outlined as follows: in Chap. 1, the theoretical framework of the SM is provided. In Chap. 2, the phenomenology of semileptonic B to D^* decays is explored. In Chap. 3, the experimental setup of LHCb is described, including instrumentation and data collection techniques. In Chap. 4, the methodology used in this analysis is covered, with an overview of the strategy for $\mathbf{R}(D^*)$ measurement, the structure of the analysis, and the handling of simulation samples. This chapter also highlights the contributions of the author to the analysis (*cf.* Sec. 4.5). In Chap. 5, the selection criteria used to ensure data sample purity are discussed, along with detailed efficiency calculations. In Chap. 6, the results from the fits to control samples are presented. In Chap. 7, the determination of signal and normalization yields, as well as the preliminary measurement of the blinded $\mathbf{R}(D^*)$ central value, are given. In Chap. 8, the sources of systematic uncertainties, crucial for understanding the reliability of the results, are listed. This chapter is at a preliminary stage, with the methodology and list of systematic uncertainties expected to be finalized within the next few months. Finally, the document presents a brief summary of the results and offers an outlook for future studies.

Chapter 1

Standard Model of Particle Physics

In this chapter, the SM [22–26] is presented, The first two sections introduce the basic concepts of Quantum Field Theory (QFT) (Sec. 1.1), and notion of symmetries and gauge theories (Sec. 1.2). Afterwards, Secs. 1.3 and 1.4 discuss the strong and Electroweak (EW) interactions, followed by a brief mention of the flavors in Sec. 1.5, quark mixing Sec. 1.6, and bound states Sec. 1.7. Finally, a brief overview of the SM is presented in Sec. 1.8.

1.1. Quantum Field Theory

QFT is a framework that describes the interactions of subatomic particles [25, 27]. Built upon the principles of quantum mechanics and special relativity, it serves as the theoretical foundation of the SM, explaining the behavior of particles and their interactions.

In the canonical quantization approach, the quantization of the classical field theory is achieved by promoting *field variables* to *operators* that obey certain commutation relations. The Klein-Gordon equation for scalar fields and the Dirac equation for fermions are introduced in this context, providing a quantum description of particles with spin-0 and spin-1/2, respectively.

Moreover, QFT addresses the issue of infinities that arise in the calculation of physical quanti-

ties, like the *mass* and *charge* of particles, through the *renormalization* procedure. This method involves redefining the theory's parameters to absorb these infinities, ensuring that the theory's predictions match experimental results with remarkable precision.

Reconciling the Schrödinger equation with the requirements of special relativity leads to the Klein-Gordon equation,

$$\left(\partial^2 - m^2\right)\phi = 0\,, \tag{1.1}$$

its solutions describe scalar fields with mass m:

$$\phi(x) = \int \frac{d^3p}{(2\pi)^3}\frac{1}{\sqrt{2E_p}}\left(a_p e^{-ip^\mu x_\mu} + b_p^\dagger e^{ip^\mu x_\mu}\right), \tag{1.2}$$

where x^μ, p^μ are the space-time and four-momentum coordinates, E_p is the energy of the particle with momentum p, a_p represents the annihilation operator for particles and $b_p^\dagger$ the creation operator for anti-particles, which satisfy the commutation relations:

$$\left[a_p, a_{p'^\dagger}\right] = (2\pi)^3\delta^{(3)}\left(p - p'\right), \tag{1.3}$$

and $\delta^{(3)}$ is the three-dimensional Dirac distribution.

The Klein-Gordon equation is not suitable for describing spin-$1/2$ particles, it leads to: negative probabilities, inconsistency with the Pauli exclusion principle, and the absence of a fundamental state. The Dirac equation, on the other hand, provides a consistent description of fermions. For a fermion with field ψ, the Dirac equation is given by:

$$\left(i\not{\partial} - m\right)\psi = 0\,, \tag{1.4}$$

where $\not{\partial} = \gamma^\mu\partial_\mu$ and γ^μ are the Dirac or gamma matrices. They form a representation of the Clifford algebra $\mathrm{Cl}_{1,3}(\mathbb{R})$, satisfying the anti-commutation relations:

$$\{\gamma^\mu, \gamma^\nu\} = 2g^{\mu\nu}\,, \tag{1.5}$$

with $g^{\mu\nu} = \mathrm{diag}(1, -1, -1, -1)$, the Minkowski metric. These anti-commutation relations are crucial for the quantization of fermionic fields. They ensure consistent probabilities, the existence of a fundamental state, the *vacuum*, and the satisfaction of the Pauli exclusion principle.

The solutions to the Dirac equation are four-component spinors, denoted as $u(p, \pm)$ and $v(p, \pm)$ for the positive and negative energy solutions, corresponding to particles and anti-particles. The solutions are interpreted as *fermions* and *anti-fermions*, each with two degenerated states in energy, corresponding to spin *up* and spin *down*, with values $+1/2$ and $-1/2$ respectively

for the spin operator S. To distinguish between these states, one introduces the helicity operator h, the projection of the spin operator of a particle along the direction of its momentum, the helicity operator is given by:

$$h = S \cdot p/\|p\| \ , \tag{1.6}$$

The helicity operator commutes with the Dirac Hamiltonian, hence helicity is a conserved quantity. However, it is not a Lorentz invariant quantity. The helicity operator has two eigenvalues, $\pm 1/2$, which lift the degeneracy of the energy states. The states with helicity $+1/2$ are called *right-handed*, while those with helicity $-1/2$ are called *left-handed* states. The chiral projectors, left and right handed, are defined as:

$$P_{\mathcal{L}} = \left(\not{1} - \gamma^5\right)/2 \ , \qquad P_{\mathcal{R}} = \left(\not{1} + \gamma^5\right)/2 \ , \tag{1.7}$$

where $\gamma^5 = i\gamma^0\gamma^1\gamma^2\gamma^3$. These operators are projectors:

$$P_{\mathcal{L}}^2 = P_{\mathcal{L}} \ , \qquad P_{\mathcal{R}}^2 = P_{\mathcal{R}} \ , \qquad P_{\mathcal{L}} \cdot P_{\mathcal{R}} = 0 \ , \qquad P_{\mathcal{L}} + P_{\mathcal{R}} = \not{1}. \tag{1.8}$$

For massless particles, chiral operators coincide with helicity operators, thus chirality is a good quantum number for massless particles.

Hamiltonians of QFTs cannot be diagonalized, due to the field's infinite number of degrees of freedom. Instead, perturbation theory is used to calculate the scattering matrix, or S-matrix, which relates the theoretical calculation to the experimental measurement. It is expressed as a function of the interaction Hamiltonian H_{int}:

$$S = \not{1} + i \int d^4x \, H_{\text{int}}(x) + \frac{1}{2!} \int d^4x \, d^4y \, H_{\text{int}}(x) \, H_{\text{int}}(y) + \cdots \tag{1.9}$$

The S-matrix is expressed as a series of terms, each corresponding to a different number of interactions between the particles. The first term, corresponding to no interaction, is the identity operator, and the second term, corresponding to one interaction, is the sum of all possible interactions between the particles. The third term, corresponding to two interactions, is the sum of all possible interactions between the particles, and so on.

In QFT divergences arise in the calculation of processes like vacuum polarization, self-energy and vertex corrections. These divergences are removed through the process of renormalization, if the theory is renormalizable[1]. The SM is a renormalizable theory and quantum gravity is perturbatively non-renormalizable.

[1]The renormalizability of a theory is a property that guarantee its predictive power at high energies.

Renormalizability involves redefining the theory's parameters to absorb the infinities. These parameters include the mass and the coupling constants, this leads to the running of the coupling constants and the appearance of the Landau poles. Renormalizability can be derived using analysis based on permutations and Feynman diagrams or via the Renormalization Group Equation (RGE), or Callan-Symanzik equations, based on the path integral formulation of QFT. The RGE are a set of differential equations, which describe how the parameters of the theory evolve under a change of the energy scale μ, it predicts the behavior of the coupling constants α_r at high energies. The RGE are given by:

$$\left(\mu\partial_\mu + \beta\partial_{\alpha_r} + n\gamma\right) G_r^{(n)} = 0\,, \tag{1.10}$$

where the beta function:

$$\beta = \mu\frac{\partial\alpha_r}{\partial\mu}\,, \tag{1.11}$$

controls how the coupling constant changes with the energy scale μ. The anomalous dimension:

$$\gamma = -\mu\frac{\partial \ln Z}{\partial\mu}\,, \tag{1.12}$$

dictates how the field renormalization constant[2] Z changes with the energy scale. And $G_r^{(n)}$ is the n-point correlation function.

1.2. Symmetries

Symmetry refers to a transformation under which Lagrangian remains invariant, or in the Hamiltonian formalism, when an operator commutes with the Hamiltonian of the system. According to Noether's theorem, such symmetry leads to the emergence of a conserved quantity, which serves as the symmetry's generator. Symmetries are classified into either continuous or discrete categories. Group theory provides the framework for describing continuous symmetries. In the following, discrete (Sec. 1.2.1) and continuous symmetries (Sec. 1.2.2) and their role in classification of elementary particles (Sec. 1.2.3) are described.

1.2.1. Discret Symmetries

The discrete symmetries are the charge conjugation, the parity and the time reversal symmetries:

[2]The renormalization constant relates the bare field ϕ_b to the renormalized field ϕ_r by: $\phi_b = \sqrt{Z}\,\phi_r$.

- Parity (P) is the transformation that changes the sign of the spatial coordinates, as follows

$$P : (t, x) \longrightarrow (t, -x) \tag{1.13}$$

  In terms of γ matrices the parity operator is defined as

$$P = \gamma^0 \tag{1.14}$$

- Charge conjugation (C) is the transformation that changes a particle into its antiparticle, swapping the sign of all charges, including electric charge, baryon number, and lepton number. For a fermion, it goes as:

$$C : \psi(x) \longrightarrow C\psi(x)C^{-1} \tag{1.15}$$

  where $\psi(x)$ is the field operator and C is the charge conjugation operator. The charge conjugation operator is defined as

$$C = i\gamma^2\gamma^0 \tag{1.16}$$

- Time reversal (T) is the transformation that changes the sign of the time coordinate, as follows

$$T : (t, x) \longrightarrow (-t, x) \tag{1.17}$$

While each of these symmetries can be violated under certain conditions within the SM (e.g., the weak interaction violates P and CP symmetries), the combined CPT symmetry is preserved in all known physical processes. In fact, CPT is a consequence of Lorentz invariance and the unitarity principle of quantum field theory [28, 29].

The Lorentz and parity transformations are used to classify observables in following way:

- *Scalars* maintain their invariance under Lorentz transformations, $\Lambda : \phi(x^\mu) \mapsto \phi(x'^\mu)$, and under parity transformations, $P : \phi(t, x) \mapsto \phi(t, -x)$.

- *Pseudo-scalars* differentiate themselves by changing sign under a parity transformation, unlike scalars. $\Lambda : \tilde{\phi}(x^\mu) \mapsto \tilde{\phi}(x'^\mu)$ and $P : \tilde{\phi}(t, x) \mapsto -\tilde{\phi}(t, -x)$.

- *Vectors* transform by the Lorentz matrix $\Lambda_{\mu\nu}$, highlighting their directional nature, $\Lambda : V^\mu(x^\mu) \mapsto \Lambda_{\mu\nu}V^\nu(x'^\mu)$. Under parity, vectors invert, reflecting a change in the direction while preserving magnitude, $P : V^\mu(t, x) \mapsto -V^\mu(t, -x)$.

- *Axial-vectors* also transform according to the Lorentz matrix $\Lambda : A^{\mu}(x^{\mu}) \mapsto \Lambda_{\mu\nu}A^{\nu}(x'^{\mu})$ but uniquely remain unaffected by parity transformations $P : A^{\mu}(t, x) \mapsto A^{\mu}(t, -x)$.

- *Tensors* undergo a more complex transformation, they transform by applying the Lorentz matrix to each index, $\Lambda : T^{\mu\nu}(x^{\mu}) \mapsto \Lambda_{\mu\rho}\Lambda_{\nu\sigma}T^{\rho\sigma}(x'^{\mu})$, and remain invariant under parity, $P : T^{\mu\nu}(t, x) \mapsto T^{\mu\nu}(t, -x)$.

- *Spinors* transform through a specific spinor representation of the Lorentz group, $S(\Lambda)$, $\Lambda : \psi(x^{\mu}) \mapsto S(\Lambda)\psi(x^{\mu})$ and under parity, are manipulated by the γ^0 matrix, $P : \psi(t, x) \mapsto \gamma^0\psi(t, -x)$.

1.2.2. Continuous Symmetry

Continuous symmetries are described by *Lie groups*, they are set of smooth, unbroken transformations that can be parameterized by continuous variable(s). These variables are the group's parameters, which are also known as the symmetry's generators. According to Noether's theorem, for every continuous symmetry of the action (integral of the Lagrangian over time), there is a corresponding conserved quantity.

Continuous symmetries can be classified into two categories: global and local symmetries. *Global Symmetries* are characterized by transformations with spacetime-invariant parameters, these symmetries apply universally, impacting all spacetime coordinates uniformly. A familiar example is the global phase invariance in quantum mechanics, which leads to the conservation of electric charge.
Local (gauge) Symmetries extend global symmetries by allowing the symmetry generators to vary across different points in space-time. The principle of local gauge invariance is fundamental in constructing the SM. It requires the introduction of gauge fields that mediate forces; for example, electromagnetism is described by $U(1)$ gauge symmetry, leading to the photon as the gauge boson. The *unitary group* is defined as:

$$U(n) = \left\{ U \in GL_n(\mathbb{C}) \,\middle|\, U^{\dagger}U = \mathbb{1} \right\}, \tag{1.18}$$

where $GL_n(\mathbb{C})$ is the set of all invertible complex $n \times n$ matrices. In case of 1 dimension, the group is set of complex numbers with unit modulus:

$$U(1) = \{ \exp(i\theta) \mid \theta \in \mathbb{R} \}, \tag{1.19}$$

$U(1)$ is an abelian group, which represent the set of rotations in the complex plane. A subgroup of $U(n)$ is the *special unitary group*, defined as:

$$SU(n) = \{ U \in U(n) \mid \det(U) = 1 \}. \tag{1.20}$$

Each Lie group is associated with a Lie algebra, which is the tangent space at the identity element of the group. The Lie algebra is defined as:

$$\mathfrak{su}(n) = \left\{ X \in \mathrm{M}_n(\mathbb{C}) \,\middle|\, X^\dagger = -X \right\}, \tag{1.21}$$

where $\mathrm{M}_n(\mathbb{C})$ is the set of all complex $n \times n$ matrices. Each element of $\mathfrak{su}(n)$ correspond to an infinitesimal transformation of the Lie group. The Lie algebra is equipped with Lie brackets, which capture the commutation relations between the generators of the group.

1.2.3. Fermions and Gauge Bosons

A representation of a Lie group $\mathrm{SU}(n)$ is a way of implementing the abstract group elements as concrete matrices acting on vectors in a vector space. These vectors can represent the state of a particle, and the matrices describe how these states transform under the symmetries associated with the group. A group representation is a homomorphism from the group to the set of invertible linear operators on a vector space. The representation of the Lie group is a Lie group homomorphism.

Fermions are represented in *fundamental representation* of a Lie group $\mathrm{SU}(n)$, symbolized as n, and anti-fermions in the *conjugate representation* $\bar{\mathrm{n}}$ (or n^*). The dimension of the representation corresponds to the number of basic states that the fermions can occupy under the symmetry described by $\mathrm{SU}(n)$. In this case, the fermions are said to "live in" or to span the fundamental representation, their quantum states transform according to the matrices of this representation when the symmetry operations of $\mathrm{SU}(n)$ are applied. This transformation behavior directly influences how fermions interact with each other and with bosons.

The gauge bosons are the physical manifestations of the Lie algebra's generators. They span the adjoint representation[3] of the Lie group, which is the representation of the group's generators acting on themselves. This representation is of dimension $n^2 - 1$, for $n > 1$.
Each generator of the algebra corresponds to a specific gauge boson, and the interactions among particles (mediated by these bosons) can be understood in terms of the commutation relations of these generators. This association between bosons and the Lie algebra underlines the *gauge principle*, where local gauge invariance necessitates the introduction of gauge bosons to preserve this symmetry when fields are locally transformed.

[3] In case of U(1), the adjoint representation is the trivial one, this reflects the fact that the U(1) gauge boson does not carry the charge it mediates and does not self-interact.

1.3. Quantum Chromodynamics

The strong interaction described by Quantum Chromodynamics (QCD), is a gauge interaction between colored quarks, described by the $\mathrm{SU}(3)_C$ gauge group. The quarks (anti-quarks) Lie in the fundamental (complex conjugate) representation of $\mathrm{SU}(3)$, denoted as 3 ($\bar{3}$) and the corresponding massless eight gauge bosons, are the gluons.

The non-Abelian nature of the $\mathrm{SU}(3)_C$ gauge group has profound implications for the behavior of its gauge bosons–gluons. Initially, the gluons acquire a color charge, a direct consequence of their non-trivial transformation properties under the action of the group. The color charge leads to the gluon self-interaction, *color confinement*, and *asymptotic freedom*[4], which are distinctive features of the strong interactions.

Following the gauge principle, a gauge invariant term can be constructed with the gluon fields $G^a_{\mu\nu}$, where a is the color index, thanks to the completely antisymmetric tensor $\epsilon^{\mu\nu\rho\sigma}$:

$$\mathcal{L}_\theta = \theta \left(\frac{\alpha_s}{8\pi}\right)^2 \epsilon^{\mu\nu\rho\sigma} G^a_{\mu\nu} G^a_{\rho\sigma} \,. \tag{1.22}$$

This term does not respect discrete symmetries P, T and CP. However, the experimental evidences are compatible with $\theta = 0$. This unnatural fine-tuning is known as the *strong*–CP *problem*. A possible solution to this problem is the Peccei–Quinn mechanism, which introduces a new scalar field, the *axion*, which is a good candidate for the dark matter.

From RGE (Eq. (1.10)), the running of the strong coupling constant α_s is derived:

$$\frac{1}{\alpha_s(\mu)} = \frac{1}{\alpha_s(\mu_0)} + \frac{\beta_0}{2\pi} \ln\left(\frac{\mu}{\mu_0}\right), \tag{1.23}$$

where μ is the energy scale, μ_0 is the reference energy scale, β_0 is the first coefficient of the beta function Eq. (1.11):

$$\beta_0 = (33 - 2N_f)/3 \,, \tag{1.24}$$

and $N_f (= 6)$ is the number of flavors.

In the asymptotic regime, the coupling constant decreases with increasing energy scale, allowing for the perturbative expansion of the theory. For $\mu > \Lambda_{QCD}$, which is the energy scale

[4] David Gross, Frank Wilczek, and Hugh David Politzer were awarded the Nobel Prize in Physics in 2004 for discovery of asymptotic freedom in QCD.

at which the coupling constant becomes small $\Lambda_{QCD} \sim 200\,\mathrm{MeV}$

$$\alpha_s(\mu) = \frac{12\pi}{\beta_0 \ln\left(\frac{\mu}{\Lambda_{QCD}}\right)} \,. \tag{1.25}$$

A contrario, at low energy scales $\mu < \Lambda_{QCD}$, the coupling constant becomes large, and the perturbative expansion breaks down. QCD becomes non-perturbative. Frameworks, like lattice–QCD are exploited to study this regime. The idea behind is to discretize the space-time and solve the QCD equations on a lattice, numerically. Other techniques, like operator product expansion, are used to separate short-distance effects, which can be treated perturbatively, from long-distance effects, which require non-perturbative methods.

1.4. Electroweak Interaction

The EW theory developed through the work of Sheldon Glashow[1], Abdus Salam[1], and Steven Weinberg[1] and John Clive Ward [30–32]. They postulate that the EW theory is at the origin of the weak interaction arising after the spontaneous and the electromagnetism interaction is the remaining unbroken symmetry. It unifies the weak interaction and electromagnetism, and is based on the gauge group:

$$\mathrm{SU}(2)_L \times \mathrm{U}(1)_Y \tag{1.26}$$

where $\mathrm{SU}(2)_L$ corresponds to the weak isospin, it interacts with left-handed fermions, and right-handed anti-fermions, thus maximally violating parity, let's refer to the third component of the weak isospin as T_3. The $\mathrm{U}(1)_Y$ corresponds to the weak hypercharge, the hypercharge Y is a generator of the $\mathrm{U}(1)_Y$ gauge group. Combination of weak isospin and weak hypercharge leads to the Gell-Mann–Nishijima formula, which played a crucial role in understanding the EW theory:

$$Q = T_3 + \frac{Y}{2}, \tag{1.27}$$

Before spontaneous symmetry breaking (SSB), the EW theory predicts the existence of four gauge bosons corresponding to the four generators of gauge group Eq. (1.26): three W bosons (W_1, W_2, W_3) associated with $\mathrm{SU}(2)_L$, and one B^0 boson associated with $\mathrm{U}(1)_Y$. These gauge bosons are initially massless, reflecting the gauge symmetry of the EW interaction.

The linear combinations of these bosons result in the massive $W^\pm$ and Z^0 bosons, and the

[1] Nobel Prize in Physics in 1979.

massless photon (γ):

$$W^{\pm} = \frac{1}{\sqrt{2}}(W_1 \mp iW_2), \tag{1.28a}$$

$$Z^0 = \frac{1}{\sqrt{g^2 + g'^2}} \left(gW_3 - g'B^0\right), \tag{1.28b}$$

$$\gamma = \frac{1}{\sqrt{g^2 + g'^2}} \left(g'W_3 + gB^0\right), \tag{1.28c}$$

where g and g' are the gauge couplings of $\mathrm{SU}(2)_\mathrm{L}$ and $\mathrm{U}(1)_\mathrm{Y}$, respectively.

The EW symmetry is spontaneously broken to $\mathrm{U}(1)_\mathrm{em}$ (the electromagnetic gauge symmetry) by the *Higgs mechanism*[5]. The Higgs is an $\mathrm{SU}(2)_\mathrm{L}$ doublet of complex scalar fields scalar field with a non-zero vacuum expectation value.

The EW interaction is spontaneously broken to the electromagnetic interaction via the Higgs field, as shown subsequently:

$$\mathrm{SU}(2)_\mathrm{L} \times \mathrm{U}(1)_\mathrm{Y} \xrightarrow{\text{SSB}} \mathrm{U}(1)_\mathrm{em} \tag{1.29}$$

The Higgs mechanism leads to the mass generation of fermions through the Yukawa coupling to the Higgs field. The broken symmetry Eq. (1.29) results in the appearance of three massless *Goldstone bosons*, these degrees of freedom are then absorbed by the $W^{\pm}$ and Z^0 bosons, giving them mass. The photon remains massless and is associated with the unbroken $\mathrm{U}(1)_\mathrm{em}$ symmetry which mediates the electromagnetic interaction and couples to electric charge.

1.5. Flavors

In the SM, there are three generation (or flavors) of quarks and leptons:

$$\begin{pmatrix} u & c & t \\ d & s & b \end{pmatrix}, \quad \begin{pmatrix} \nu_e & \nu_\mu & \nu_\tau \\ e & \mu & \tau \end{pmatrix} \tag{1.30}$$

A priori, there is no fundamental reason to expect the same number of generations in the quark and lepton sectors. However, this symmetry is crucial for the cancellation of *chiral anomalies* [33, 34]. In fact, the anomalies arising in the quark sector are precisely cancelled by

[5] Introduced by Robert Brout, François Englert and Peter Higgs in 1964 which were awarded by Nobel Prize in Physics in 2013.

those arising in the lepton sector, guaranteeing the anomaly freedom of the SM.

These generations are identical in all respects except for their masses. If one ignores the Yukawa couplings, the SM becomes invariant under the exchange of the three generations.

The fermion sector of the SM consists of three generations, each with an up-type quark u_i and a down-type quark d_i, and a charged lepton e_i and a neutrino ν_i. One might consider a $U(3)$ symmetry acting on the vector space spanned by the three generations of up-type quarks and a separate $U(3)$ symmetry for the down-type quarks. These symmetries could describe how the weak interaction, specifically the charged current interactions mediated by $W^{\pm}$ bosons, can change one left-handed quark flavor into another within each type (up-type or down-type), as parameterized by the Cabibbo-Kobayashi-Maskawa (CKM) matrix.

$$U(3)^5 = \underbrace{U(3)_Q \times U(3)_L}_{\text{left-handed } (\mathcal{L})} \times \underbrace{U(3)_u \times U(3)_d \times U(3)_e}_{\text{right-handed } (\mathcal{R})} \tag{1.31}$$

which acts on the left-handed and right-handed fermions as follows:

$$\begin{aligned} &U(3)_Q \mapsto \begin{pmatrix} u_i \\ d_i \end{pmatrix}_{\mathcal{L}}, \quad U(3)_L \mapsto \begin{pmatrix} \nu_i \\ e_i \end{pmatrix}_{\mathcal{L}}, \\ &U(3)_d \mapsto d_{i,\mathcal{R}}, \quad U(3)_u \mapsto u_{i,\mathcal{R}}, \quad U(3)_e \mapsto e_{i,\mathcal{R}}, \end{aligned} \tag{1.32}$$

where L stands for lepton and $\mathcal{L}$ ($\mathcal{R}$) for left-handed (right-handed) particles. The Yukawa couplings are the exclusive source of flavor violation in the SM. After spontaneous symmetry breaking, none of the SM interactions violate the baryon number and the lepton number. Consequently, the conservation of these numbers emerges as an accidental feature of the SM. Extensions of the SM could potentially introduce mechanisms that violate these numbers.

The first and second generation have small Yukawa coupling, the $U(2)^5$ remains a good approximate symmetry of the SM. Some models beyond the SM assume that the only source of flavor violation is the Yukawa couplings. This is called the Minimal Flavor Violation (MFV) hypothesis [35]. The MFV is used in models like the two Higgs doublet model, the supersymmetric SM and the little Higgs model.

1.6. Quark Mixing

Mesons containing b-quarks, such as B mesons, have measurable lifetimes on the order of $1\,\mathrm{ps}$ due to the dynamics of the strong and weak interactions. The phenomenon of B^0–$\overline{B}^0$ mixing, where the mesons oscillate between their flavor states, highlights the distinction between

mass and flavor eigenstates. The mass eigenstates are the states that propagate in time and are observed in experiment, the flavor eigenstates are the states that participate in the weak interaction.

Each generation of quarks and leptons have different masses, but the same quantum numbers. Yukawa couplings generate fermion masses, these couplings play an important role in understanding the interactions among fermion generations. The Yukawa term in the lagrangian, before spontaneous symmetry breaking, is given by

$$L_Y = \bar{\Psi}\hat{Y}\Phi\Psi + h.c. \tag{1.33}$$

where Ψ is the fermion field, Φ is the Higgs field and $\hat{Y}$ is the Yukawa matrix. The Yukawa matrix is a 3×3 matrix in flavor space. After spontaneous symmetry breaking, the Yukawa term becomes

$$L_Y = -\sum_{i,j} \bar{Q}_i Y_{ij} \Phi Q_j + \bar{L}_i Y_{ij} \Phi L_j + h.c. \tag{1.34}$$

where $Q_i = \begin{pmatrix} u_i \\ d_i \end{pmatrix}$ and $L_i = \begin{pmatrix} \nu_i \\ e_i \end{pmatrix}$ are the quark and lepton doublets, Φ is the Higgs doublet and the elements Y_{ij} correspond to the Yukawa matrix. Since the Yukawa matrix is non-diagonal, the physical states referred to as *mass eigenstates* $\begin{pmatrix} u_i \\ d_i \end{pmatrix}$ differ from the *interaction eigenstates* $\begin{pmatrix} u'_i \\ d'_i \end{pmatrix}$. The Yukawa matrix can be diagonalized using a unitary matrix V and a diagonal matrix Y_D as follows:

$$Y_{ij} = V_{ik} Y_{D,kl} V^{\dagger}_{lj} \ , \tag{1.35}$$

and the mass eigenstates are given by: $Q_i = V_{ij} Q_j$, leading to the CKM matrix:

$$V_{CKM} = V^{\dagger}_{uL} V_{dL} = \begin{pmatrix} V_{ud} & V_{us} & V_{ub} \\ V_{cd} & V_{cs} & V_{cb} \\ V_{td} & V_{ts} & V_{tb} \end{pmatrix}, \tag{1.36}$$

it is parameterized[6] by three angles and one complex phase. By introducing the angles θ_{12}, θ_{13}, θ_{23} and the phase δ, and notations $\cos\theta_{ij} = c_{ij}$, $\sin\theta_{ij} = s_{ij}$, the CKM matrix can be

[6] Any 3×3 unitary matrix can be parameterized by three angles and one complex phase

written as

$$V_{CKM} = \begin{pmatrix} 1 & 0 & 0 \\ 0 & c_{23} & s_{23} \\ 0 & -s_{23} & c_{23} \end{pmatrix} \begin{pmatrix} c_{13} & 0 & s_{13}e^{-i\delta} \\ 0 & 1 & 0 \\ -s_{13}e^{i\delta} & 0 & c_{13} \end{pmatrix} \begin{pmatrix} c_{12} & s_{12} & 0 \\ -s_{12} & c_{12} & 0 \\ 0 & 0 & 1 \end{pmatrix}. \tag{1.37}$$

The complex phase is the *only source*[7] of CP violation in the SM. A conventional parametrization of the CKM matrix, known as Wolfenstein parametrization [36], is given by

$$V_{CKM} = \begin{pmatrix} 1 - \lambda^2/2 & \lambda & A\lambda^3(\rho - i\eta) \\ -\lambda & 1 - \lambda^2/2 & A\lambda^2 \\ A\lambda^3(1 - \rho - i\eta) & -A\lambda^2 & 1 \end{pmatrix} + O(\lambda^4)\,, \tag{1.38}$$

Quark transitions are suppressed by order of $O(\lambda)$ between the *first* and *second* generation, $O(\lambda^2)$ between the *second* and *third* generation, and by $O(\lambda^3)$ between the *first* and *third* generation. The unitarity of the CKM matrix can be translated into six relations, which are called *unitarity triangles*. Any deviation from these relations would be a sign of new physics. The measured values of the CKM matrix elements are given by [7]:

$$|V_{CKM}| = \begin{pmatrix} 0.97435 \pm 0.00016 & 0.22500 \pm 0.00067 & 0.00369 \pm 0.00011 \\ 0.22486 \pm 0.00067 & 0.97349 \pm 0.00016 & 0.04182^{+0.00085}_{-0.00074} \\ 0.00857^{+0.00020}_{-0.00018} & 0.04110^{+0.00083}_{-0.00072} & 0.999118^{+0.000031}_{-0.000036} \end{pmatrix}, \tag{1.39}$$

In similar way, the lepton mixing is described by the Pontecorvo-Maki-Nakagawa-Sakata (PMNS) matrix.

1.7. Bound States

Historically, Gell-mann successfully explained the organization of *mesons* and *baryons* into *octets* and *decuplets* [37], using the $SU(3)_{flavor}$ approximate symmetry[8], providing a strong hint of the underlying threefold symmetry among the lightest quarks.

The bound states of quarks are known as *hadrons*. The hadron wave function is a product of

[7] Another possible source is the Lepton mixing matrix, if the neutrinos are Dirac-fermions.
[8] Where light quarks are set massless $m_u = m_d = m_s = 0$.

space-time, spin, flavor and color wave functions:

$$\Psi_{\text{hadron}} = \Psi_{\text{space}} \otimes \Psi_{\text{spin}} \otimes \Psi_{\text{flavor}} \otimes \Psi_{\text{color}} \,. \tag{1.40}$$

with $\mathrm{SU}(2)_{\text{spin}}$, and $\mathrm{SU}(3)_{\text{color}}$ symmetries. The flavor symmetry can be $\mathrm{SU}(2)_{\text{flavor}}$ or $\mathrm{SU}(3)_{\text{flavor}}$ depending on the number of flavors. Due to color confinement the hadrons must be *colorless*, meaning that the color wave function must be a singlet under the $\mathrm{SU}(3)_{\text{color}}$ group.

Mesons

Mesons are bound states of a quark and an anti-quark, the wave-function reads:

$$\Psi(q, \bar{q}) = \Psi_{\text{space}}(x_q, x_{\bar{q}}) \otimes \Psi_{\text{spin}}(s_q, s_{\bar{q}}) \otimes \Psi_{\text{flavor}}(f_q, f_{\bar{q}}) \otimes \Psi_{\text{color}}(c_q, c_{\bar{q}}). \tag{1.41}$$

where x_q, s_q, f_q and c_q are the space-time, spin, flavor and color coordinates of the quark q, respectively. The $\bar{q}$ denotes the anti-quark. Their color representation is given by:

$$3 \otimes \bar{3} = 8 \oplus 1 \,, \tag{1.42}$$

where the 3 and $\bar{3}$ are the color representations of the quark and anti-quark, respectively. The 1 and 8 are the singlet and octet representations of the color group $\mathrm{SU}(3)_{\text{color}}$. The flavor representation of the mesons is given by:

$$2 \otimes 2 = 3 \oplus 1 \,, \tag{1.43}$$

where the 2 is the flavor representation of the quark and anti-quark. The 1 and 3 are the singlet and triplet representations of the $\mathrm{SU}(2)_{\text{flavor}}$ group. The mesons are divided into:

- *Scalar mesons*: a_0, K_0, K_0^* and K_0^{**}.
- *Pseudoscalar mesons*: π, η, η', K and B^0.
- *Vector mesons*: ρ, ω, ϕ, J/ψ and D^*.
- *Axial-vector mesons*: a_1, K_1, K_1' and K_1''.
- *Tensor mesons*: f_2, K_2, K_2^* and K_2^{**}.

A non-exhaustive list of mesons is given in Tab. 1.1.

Meson	Quarks	J^{PC}	T_3	Mass (MeV/c^2)
Light mesons				
π	$u\bar{d}$	0^{-+}	0	139.57039(35)
ρ	$u\bar{u}$	1^{--}	1	775.26(23)
ω	$u\bar{u} + d\bar{d}$	1^{--}	0	782.66(13)
K	$u\bar{s}$	0^{-+}	0	493.677(16)
η	$u\bar{u} + d\bar{d} - 2s\bar{s}$	0^{-+}	0	547.862(17)
η'	$u\bar{u} + d\bar{d} + s\bar{s}$	0^{-+}	0	957.78(6)
ϕ	$s\bar{s}$	1^{--}	0	1019.461(16)
Charm mesons				
D	$c\bar{d}$, $c\bar{u}$	0^{-+}	0	1869.66(5)
D^*		1^{--}	1	2010.26(5)
D_s	$c\bar{s}$	0^{-+}	0	1968.36(7)
J/ψ	$c\bar{c}$	1^{--}	0	3096.900(6)
Beauty mesons				
B	$b\bar{u}$, $b\bar{d}$	0^{-+}	0	5279.34(12)
B_s	$b\bar{s}$	0^{-+}	0	5366.92(10)
Υ	$b\bar{b}$	1^{--}	0	9460.40(10)

Table 1.1.: Meson classification and properties [38].

Baryons

Baryons are bound states of three quarks. Their wave function can be expressed as:

$$\Psi(q_1, q_2, q_3) = \Psi_{\mathtt{space}}(x_1, x_2, x_3) \otimes \Psi_{\mathtt{spin}}(s_1, s_2, s_3) \otimes \Psi_{\mathtt{flavor}}(f_1, f_2, f_3) \otimes \Psi_{\mathtt{color}}(c_1, c_2, c_3). \tag{1.44}$$

where x_i, s_i, f_i, and c_i are the space-time, spin, flavor, and color coordinates of quark $i = 1, 2, 3$, respectively.
The $\mathrm{SU}(3)$ representation (either for color or flavor) decomposes as:

$$3 \otimes 3 \otimes 3 = 10 \oplus 8 \oplus 1 \,, \tag{1.45}$$

where the 3 represents the color or flavor state of the quark. The 1, 8 and 10 are the singlet, octet and decuplet representations of the $\mathrm{SU}(3)$ group.

The spin representation of the baryons is given by:

$$2 \otimes 2 \otimes 2 = 4 \oplus 2 \oplus 2 \,, \tag{1.46}$$

where the 2 in the tensor product is the spin representation of the quark. The 2 and 4 in the right-hand side are the doublet and quartet representations of the $\mathrm{SU}(2)_{\mathtt{spin}}$ group.

On one hand, to satisfy the Pauli exclusion principle, the baryon wave function Eq. (1.44) must be antisymmetric under the exchange of any two quarks. On the other hand, the color wave function must be totally antisymmetric, as the color representation is a singlet under $\mathrm{SU}(3)_{\mathtt{color}}$. Therefore, only symmetric combinations of spin and flavor representations are allowed:

$$\rho^{S}_{\mathtt{spin}} \otimes \rho^{S}_{\mathtt{flavor}} \quad \text{or} \quad \rho^{A}_{\mathtt{spin}} \otimes \rho^{A}_{\mathtt{flavor}} \,, \tag{1.47}$$

where $\rho^{S,A}_{X}$ are the symmetric and antisymmetric representations of the $\mathrm{SU}(n)_X$ group, respectively.
This lead to the following classification of baryons:

- *Octet baryons* (spin-1/2): arising from the combinations:

$$2_{\mathtt{spin}} \otimes 8_{\mathtt{flavor}} \tag{1.48}$$

  These includes: proton, neutron, Λ, Σ, Ξ and Ω.

- *Decuplet baryons* (spin-3/2):

$$4_{\mathtt{spin}} \otimes 10_{\mathtt{flavor}} \tag{1.49}$$

Baryon	Quarks	J^P	T_3	Mass (MeV/c^2)
Light baryons				
p	uud	$\frac{1}{2}^+$	$\frac{1}{2}$	938.27208816(29)
n	udd	$\frac{1}{2}^+$	$\frac{1}{2}$	939.5654205(5)
Λ	uds	$\frac{1}{2}^+$	0	1115.683(6)
Charm and Beauty baryons				
Λ_c	udc	$\frac{1}{2}^+$	0	2286.46(14)
Λ_b	udb	$\frac{1}{2}^+$	0	5619.60(17)

Table 1.2.: Baryon classification and properties [38].

including: Δ, Σ^*, Ξ^* and Ω^*.

A non-exhaustive list of baryons is given in Sec. 1.7.

Other States

In addition to these conventional hadrons, there are also exotic hadrons [39, 40], which include tetraquarks, pentaquarks, and hybrids:

- *Tetraquarks*
  Composed of two quarks and two anti-quarks, like the $X(3872)$ and $Z_c(3900)$ [41]

- *Pentaquarks*
  Made up of five quarks—four quarks and one anti-quark, like the $P_c(4450)$ [42].

- *Hybrids*
  Composed of quarks and gluons, like the $Y(4260)$.

The study of these exotic hadrons is an active area of research in the field of hadron spectroscopy.

1.8. Summary of the Standard Model

The SM is a QFT that describes the fundamental particles and their interactions. It is a gauge theory based on the product of three gauge groups:

$$\mathrm{SU(3)_C} \times \mathrm{SU(2)_L} \times \mathrm{U(1)_Y} \xrightarrow{\text{SSB}} \mathrm{SU(3)_C} \times \mathrm{U(1)_{em}} \tag{1.50}$$

The particle content of the SM is divided into fermions and bosons. Fermions are quarks and leptons, which comes in three generations, and each have an associated antiparticle. The classification according to their masses and quantum numbers are given in Tab. 1.3. The bosons are gauge bosons and the Higgs boson, as shown in Tab. 1.4. Elementary particles are summarized in Tabs. 1.3 and 1.4. The Higgs is the only scalar particle.

In total, the SM is described by 26 or 28 parameters, depending on the nature of neutrinos: 2 parameters are related to the Higgs sector, the vacuum expectation value and the Higgs mass, 3 parameters are related to the gauge sector, the strong coupling constant, the weak mixing angle and the electromagnetic coupling constant, CKM matrix has 4 parameters, 6 parameters are related to the six different quark masses, and 3 parameters from charged lepton masses, 3 parameters are related to the neutrino masses, 4 parameters are related to the PMNS matrix, additional 2 Majorana phases and 1 parameter for θ_{CP} QCD parameter.

The SM has been tested and verified by many experiments with unprecedented precision. However, several key challenges and open questions remain facing the SM:

- Unsatisfactory Theoretical Aspects:
  - *Hierarchy problem*
    The difference between the electroweak scale (approximately 100 GeV) and the Planck scale (around 10^{19} GeV), where gravitational interactions become significant, is a major theoretical challenge. It raises questions about the naturalness and stability of the Higgs mass against quantum corrections [43].
  - *Strong* CP*–problem*
    The absence of CP violation in the strong force, despite that QCD does not explicitly forbid CP violation, leading to proposals like the Peccei-Quinn theory [44, 45] and the hypothetical axion particle [46, 47].
  - *Fermion Mass Hierarchy and CKM Matrix*: The wide range of masses among the quarks and leptons and the pattern of their mixing angles, especially as encoded in the CKM matrix for quarks, remain unexplained within the SM framework [48].

Gen.	Particle		Mass		Q	T_3	Y_{left}	Y_{right}	B	L
First	up	u	$2.16^{+0.49}_{-0.26}$	MeV/c^2	$+\frac{2}{3}$	$+\frac{1}{2}$	$+\frac{1}{3}$	$+\frac{4}{3}$	$\frac{1}{3}$	0
	down	d	$4.67^{+0.48}_{-0.14}$		$-\frac{1}{3}$	$-\frac{1}{2}$	$-\frac{1}{3}$	$-\frac{2}{3}$		
	e-neutrino	ν_e	$< 2 \times 10^{-9}$	MeV/c^2	0	$+\frac{1}{2}$	0	0	0	+1
	electron	e	0.51099895000(15)		−1	$-\frac{1}{2}$	−1	−2		−1
Second	charm	c	1.27(2)	GeV/c^2	$+\frac{2}{3}$	$+\frac{1}{2}$	$+\frac{1}{3}$	$+\frac{4}{3}$	$\frac{1}{3}$	0
	strange	s	$93.4^{+8.6}_{-3.4}$	MeV/c^2	$-\frac{1}{3}$	$-\frac{1}{2}$	$-\frac{1}{3}$	$-\frac{2}{3}$		
	μ-neutrino	ν_μ	< 0.19	MeV/c^2	0	$+\frac{1}{2}$	0	0	0	+1
	muon	μ	105.6583755(23)		−1	$-\frac{1}{2}$	−1	−2		−1
Third	top	t	172.69 ± 0.3	GeV/c^2	$+\frac{2}{3}$	$+\frac{1}{2}$	$+\frac{1}{3}$	$+\frac{4}{3}$	$\frac{1}{3}$	0
	beauty	b	$4.18^{+0.03}_{-0.02}$		$-\frac{1}{3}$	$-\frac{1}{2}$	$-\frac{1}{3}$	$-\frac{2}{3}$		
	τ-neutrino	ν_τ	< 18.2	MeV/c^2	0	$+\frac{1}{2}$	0	0	0	+1
	tau	τ	1776.86(12)		−1	$-\frac{1}{2}$	−1	−2		−1

Table 1.3.: Quarks and leptons masses and quantum numbers. Symbols stands from left to right for *charge*, *weak-isospin*, *left-handed hypercharge*, *right-handed hypercharge*, *baryon number* and *lepton number*. The values are taken from [38].

	Boson	Symbol	Mass (GeV/c^2)	Charge	Spin
Gauge bosons	Photon	γ	0	0	1
	W boson	$W^\pm$	80.4	±1	1
	Z boson	Z	91.2	0	1
	Gluon	g	0	0	1
	Higgs boson	H	125.1	0	0

Table 1.4.: The SM bosons and properties [38].

- Missing Pieces for a Complete Description:

  - *Baryon Asymmetry*
    The observed imbalance between matter and antimatter in the universe cannot be adequately explained by the CP violation present in the SM [49].

  - *Dark Matter and Dark Energy*
    The SM does not account for dark matter and dark energy, which together constitute about 95% of the universe's total energy density. Their nature and properties are among the most significant mysteries in cosmology [50–52].

  - *Gravity's Incompatibility*
    Gravity, as described by general relativity, does not fit within the quantum field theory framework of the SM. This highlights the need for a quantum theory of gravity and points to the SM's limitations at high energy scales or in strong gravitational fields.

  - *Neutrino Physics*
    The discovery of neutrino oscillations, which indicates that neutrinos have mass, poses a significant challenge to the SM that originally predicted massless neutrinos [53, 54]. Understanding the mechanism by which neutrinos acquire mass, the exact values of those masses, and the precise parameters of neutrino mixing are areas of ongoing research. Additionally, determining the fundamental nature of neutrinos, specifically whether they are *Majorana* or *Dirac* particles, remains an open question [38].

In addition, some experiments yield results that do not fit neatly within the SM predictions, such as anomalies in muon $g-2$ measurements [55], rare decay processes and Lepton Flavor Universality violations in B–meson decays. While not definitive, these discrepancies could hint at physics beyond the SM. The experimental aspects is highly important to give a reliable direction to the theoretical developments.

Chapter 2

Phenomenology of Lepton Flavor Universality tests

In this chapter, the phenomenology of LFU tests, with a particular focus on the charged current transition $b \to c\ell\nu_\ell$, will be discussed. First, an overview of LFU tests will be presented in Sec. 2.1. The current status of Flavor Changing Neutral Current (FCNC) and Flavor Changing Charged Current (FCCC) measurements is briefly mentioned. Then, the framework of effective field theories, supplemented with relevant examples, will be outlined in Sec. 2.2. Additionally, the theory calculation of $B^0 \to D^{*-}\tau^+\nu_\tau$, including two common Form Factor (FF) parametrizations, are detailed in Sec. 2.3. Finally, in Sec. 2.4 a brief overview of theories BSM that could account for LFU violations will be presented.

2.1. Lepton Flavor Universality Tests

Glashow, Iliopoulos and Maiani (GIM) [56] proposed a mechanism to suppress FCNC in the SM, this mechanism predicted the charm quark. The generalisation of the GIM mechanism to the third generations lead to the CKM matrix. The SM predicts that the weak interactions are universal, meaning that the couplings of the gauge bosons to the leptons are the same for all generations. This is known as the LFU hypothesis.

The LFU hypothesis can be tested in many ways:

- FCNC: involves rare decays or interactions where the *flavor* changes but the *charge* remains the same (*e.g.* rare B meson decays, certain kaon decays).
- FCCC: comprises decays or interactions where both the *flavor* and *charge* change (*e.g.* semileptonic and leptonic decays of kaons, pions, tau, B and D mesons).
- Neutral Current (NC): consists of interactions where neither *flavor* nor *charge* changes (*e.g*, Z boson decays, neutrino neutral-current interactions, and Higgs boson decays).
- Lepton Flavor Violation (LFV): constitutes interactions where the *lepton flavor number* is not conserved, signaling new physics BSM (*e.g.* muon to electron decays, tau to muon/electron decays, and specific B meson decays).

2.1.1. Universality of weak interactions

Let's assume that the weak coupling is distinct for the three generations of leptons, and consider the decay of the heavy leptons τ and μ, denoted as ℓ. The decay rate is given by:

$$\Gamma(\ell \to e\bar{\nu}_e\nu_\mu) = \frac{G_F^e G_F^\ell}{192\pi^3} m_\ell^5 \tag{2.1}$$

For the muon, the total decay rate is given by:

$$\Gamma_\mu^{tot} \approx \Gamma(\mu \to e\bar{\nu}_e\nu_\mu) \tag{2.2}$$

For the tau, one needs to take into account the branching fraction of the tau electronic decay due to larger phase space

$$\mathrm{Br}(\tau \to e\bar{\nu}_e\nu_\tau) = \Gamma(\tau \to e\bar{\nu}_e\nu_\tau)/\Gamma_\tau^{tot} \tag{2.3}$$

Therefore, combining τ and μ lifetimes, the relative difference for the weak coupling constants G_F^μ and G_F^τ can be measured. All the quantities are precisely measured [38], summarized in Tab. 2.1

	τ	μ	e
Mass ($\mathrm{MeV/c^2}$)	1776.86(12)	105.6583755(23)	0.51099895000(15)
Lifetime (s)	$2.903(5) \times 10^{-13}$	$2.1969811(22) \times 10^{-6}$	–

Table 2.1.: Leptons mass and lifetime.

and $\mathrm{Br}(\tau \to e\bar{\nu}_e\nu_\tau) = 17.82(4)\%$, so that:

$$\frac{G_F^\tau}{G_F^\mu} = 1.0026 \tag{2.4}$$

Similar combination of the lifetimes of the τ and the μ can be used to measure the relative difference for the weak coupling constants G_F^μ and G_F^e. Both measurements are in agreement with the universality of the weak interaction

$$G_F = G_F^e = G_F^\mu = G_F^\tau. \tag{2.5}$$

Recent measurements of lepton flavor universality tests in W boson decays, have reported the following ratios [57]:

$$\frac{\mathrm{Br}\,(W \to \mu\nu)}{\mathrm{Br}\,(W \to e\nu)} = 0.9995 \pm 0.0022\ (\mathrm{stat.}) \pm 0.0036\ (\mathrm{syst.}) \pm 0.0014\ (\mathrm{ext.})\ , \tag{2.6}$$

which is in agreement with the universality of the weak interaction at the level of 0.5%.

2.1.2. Flavor Changing Neutral Currents

FCNC processes involve interactions where the flavor of a quark or lepton changes but the electric charge remains the same. These processes are rare in the SM and often occur via higher-order loops. In this context, the transition involves $b \to q\ell\ell$, or $c \to u\ell\ell$, where ℓ represents a lepton, and q is d or s, such as $B \to K^{(*)}\ell\ell$.

These transitions are mediated by electroweak processes, specifically through *box* and *penguin* diagrams, as illustrated in Fig. 2.1. Such decays are inherently suppressed in the SM due to their loop-level occurrence, they happen at higher order in perturbation theory. This suppression makes them a sensitive probe for new particles that could enhance the decay rate. Thus any deviation from the SM prediction would be an indirect sign of new physics.

Measurements using ratios of branching fractions of B meson decays to K and K* mesons have been made by BaBar [58], Belle [59] and LHCb [3, 60–62]. The ratio of branching fractions of B meson decays to K and K* mesons is defined as:

$$\mathbf{R}\left(K^{(*)}\right) = \frac{\mathrm{Br}\left(B \to K^{(*)}\mu^+\mu^-\right)}{\mathrm{Br}\left(B \to K^{(*)}e^+e^-\right)} \tag{2.7}$$

The latest result is from the LHCb collaboration [21] and comparison with SM calculations is shown in Fig. 2.2. These four measurements are compatible with the SM predictions, with the

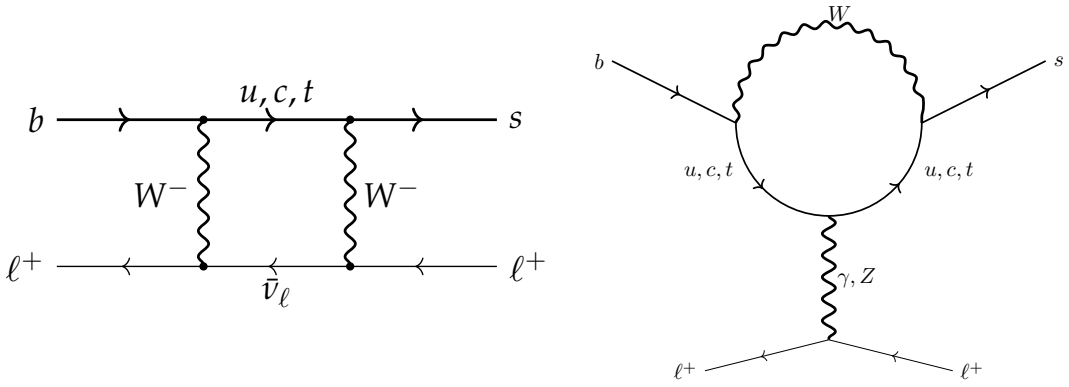

Figure 2.1.: Flavor changing neutral current represented by *box diagram* (left) and *penguin diagram* (right) Feynman diagrams.

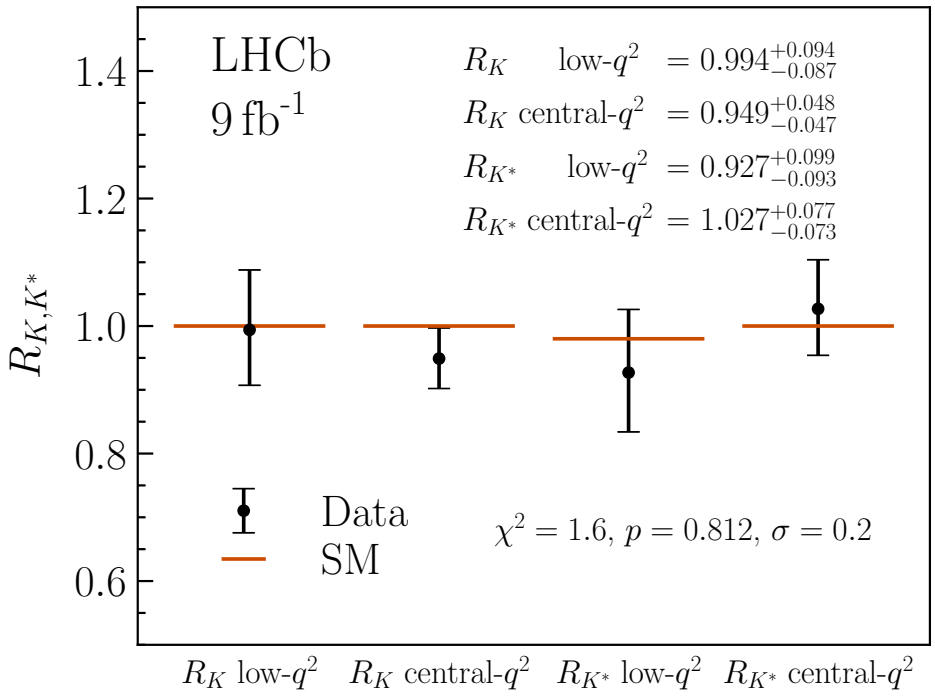

Figure 2.2.: The ratio of the branching fractions of $B \to K^{(*)}\ell\ell$ decays comparison between SM calculations and LHCb measurements [21].

overall agreement being within 0.2σ.

2.1.3. Flavor Changing Charged Currents

FCCC processes involve interactions where both the flavor and charge of a quark or lepton change. These interactions are mediated by the W boson in the SM. Unlike FCNC, FCCC transitions can occur at tree level. This may occur in:

- Leptonic decays of:
  - Heavy mesons, such as $B \to \ell\nu$ and $D \to \ell\nu$
  - Light mesons, such as $K \to \ell\nu$ and $\pi \to \ell\nu$
  - W boson decays to leptons.
  - Tau leptonic decays.
- Semileptonic decays of:
  - Heavy mesons, such as $B \to D^{(*)}\ell\nu$ and $D \to K\ell\nu$
  - Light mesons, such as $K \to \pi\ell\nu$
- Hadronic decays of:
  - Heavy mesons, such as $B \to D^{(*)}\pi$ and $D \to K\pi$
  - Light mesons, such as $\tau \to \pi\nu$, $\tau \to \rho\nu$

The transition between the third family and the first two families are a good probe for searching for New Physics (NP): these transitions involve processes that can reveal discrepancies from the SM's predictions, such as in mass hierarchy, flavor mixing, and CP violation. Particularly, the heavier masses of the third family make them more sensitive to potential new phenomena at higher energy scales, which might not significantly affect the lighter particles of the first two families.

The quark transition is governed by the CKM matrix. In $b \to c\ell\nu_\ell$ transitions, the matrix element V_{cb} comes into play. There is a long standing tension ($\sim 3\sigma$) between V_{cb} measurements from inclusive and exclusive decays [8]. According to some authors, this tension is believed to not be a sign of new physics [63], but rather an underestimation of the systematic or theoretical uncertainties is at the origin. Fortunately, taking ratios such as $\mathbf{R}\left(D^{(*)}\right)$ helps to cancel V_{cb} and reduce the hadronic form factors uncertainties. The general experssion for the ratio of branching fractions of semileptonic b–hadron X_b decay is given by:

$$R(X_c) = \frac{\mathrm{Br}\left(X_b \to X_c\tau\nu_\tau\right)}{\mathrm{Br}\left(X_b \to X_c\ell\nu_\ell\right)} \tag{2.8}$$

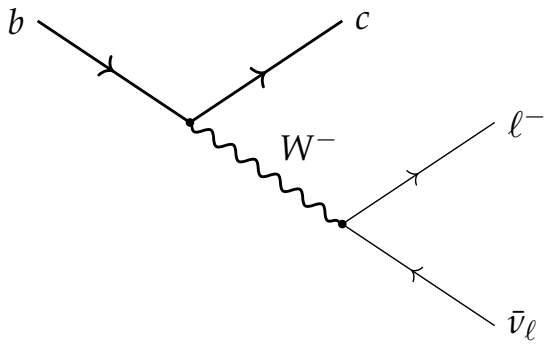

Figure 2.3.: Tree-level flavor changing charged current Feynman diagrams.

Where X_b represents mesons or baryons containing a b quark, and X_c represents mesons or baryons containing a c quark. More specifically, the emphasis is on the ratios of branching fractions of B meson decays to D and D^* mesons, defined as:

$$\mathbf{R}\left(D^{(*)}\right) = \frac{\mathrm{Br}\left(B \to D^{(*)}\tau\nu_\tau\right)}{\mathrm{Br}\left(B \to D^{(*)}\ell\nu_\ell\right)} \tag{2.9}$$

The BaBar collaboration measured both $\mathbf{R}(D)$ and $\mathbf{R}(D^*)$ using a purely leptonic τ-decay mode: $\tau^- \to \ell^-\bar{\nu}_\ell\nu_\tau$, where ℓ represents either μ or e [11]. Similarly, the Belle collaboration performed similar measurements, with hadronic τ-decay modes: $\tau^- \to \pi^-\nu_\tau$ and $\tau^- \to \rho^-\nu_\tau$ [13, 14]. The LHCb collaboration, measured $\mathbf{R}(D^*)$ ratio [1, 19] and both $\mathbf{R}(D)$ and $\mathbf{R}(D^*)$ through the muonic [64] τ-decay channel: $\tau^- \to \mu^-\bar{\nu}_\mu\nu_\tau$. Additionally, LHCb contributed to an exclusive analysis of the $\mathbf{R}(D^*)$ ratio through a hadronic τ-decay mode: $\tau^+ \to 3\pi^\pm(\pi^0)$ [2, 3, 65]. Then, the recent simultaneous measurements of $R(D^+)$ and $R(D^{*+})$ [66]. Finally, Belle II collaboration presented preliminary results [67]. The world-average, performed by HFLAV collaboration [8] is shown in Fig. 2.4. Interestingly, almost all the independent measurements of both $\mathbf{R}(D)$ and $\mathbf{R}(D^*)$ are systematically higher than the SM predictions. By exploiting the correlation between $\mathbf{R}(D)$ and $\mathbf{R}(D^*)$, as shown in Fig. 2.5, the combined measurement of $\mathbf{R}(D)$ and $\mathbf{R}(D^*)$ is in tension with the SM predictions at the level of 3.3σ, while $\mathbf{R}(D^*)$ alone is in tension with the SM predictions at the level of 2.5σ.

Besides, LHCb performed measurements of other ratios such as $R(J/\Psi)$ [62], $R(\Lambda_c)$ [68] as defined in Eq. (2.8), and measurements of D^* longitudinal polarization [69].

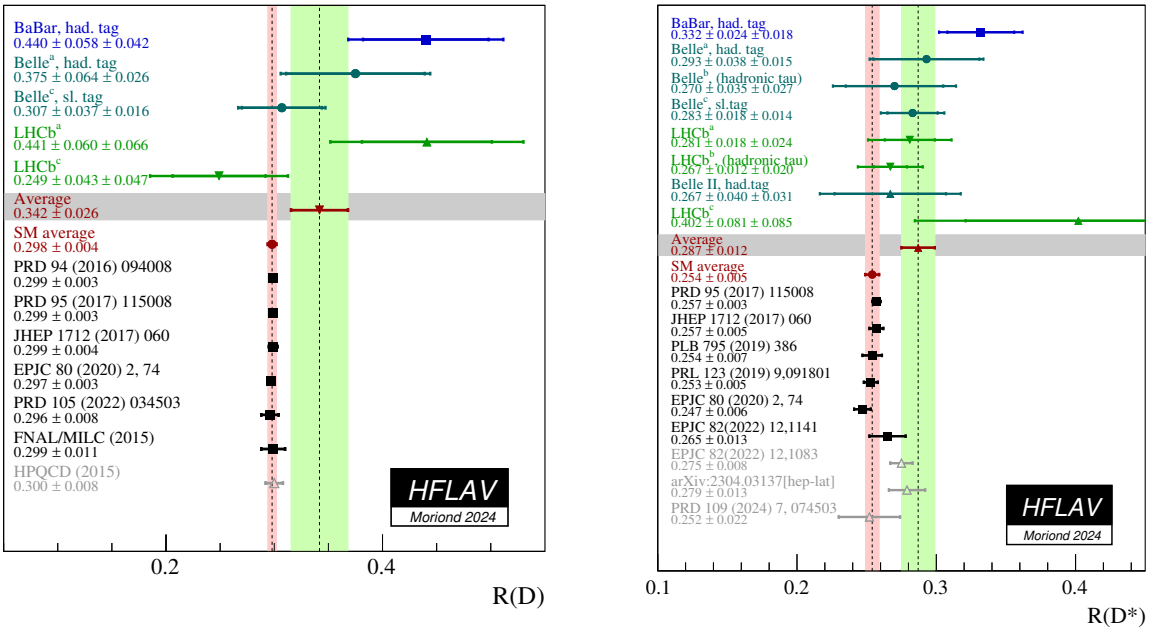

Figure 2.4.: Overview of the $\mathbf{R}(\mathrm{D})$ (left) and $\mathbf{R}(\mathrm{D}^*)$ (right) measurements. [8].

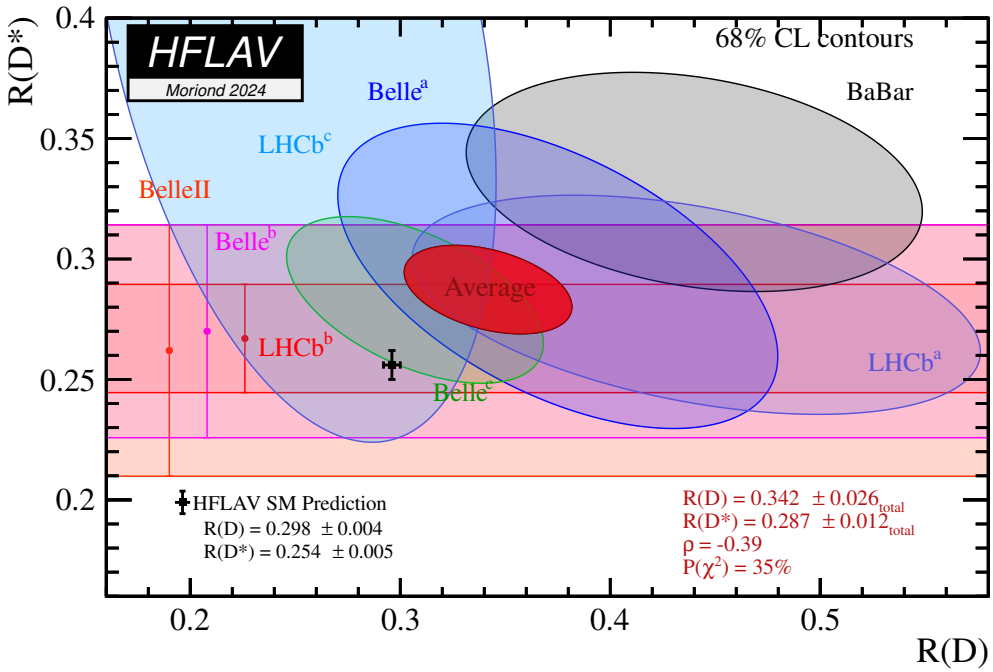

Figure 2.5.: Overview of $\mathbf{R}(\mathrm{D})$ and $\mathbf{R}(\mathrm{D}^*)$ measurements and their combined results. [8].

2.2. Effective Field Theories

Before delving into the theoretical calculation of $\mathbf{R}(D^*)$ ratio, it is worthwhile to introduce the concept of Effective Field Theory (EFT), which are extensively utilized in the study of the weak decays of hadrons containing heavy quarks.

Based on the premise that the detailed description of phenomena across all scales is not always necessary for understanding a given process, EFTs provide a systematic framework to disentangle the different scales. This tool yields an effective Lagrangian or Hamiltonian, which encodes the dynamics relevant to the phenomenon under consideration and retains only the interactions and particles that are relevant at the scale of interest. They can be categorized into various methodological approaches [27], as follows:

- *Top-down Approach*: is employed when the high-energy theory is well established, yet its complexity makes it impractical for describing phenomena occurring at lower energy scales. In such cases, EFT *integrates-out* heavy particles from the theory, thereby simplifying the description of the system at lower energy scales.
- *Bottom-up Approach*: is used when the theory becomes unclear beyond a certain energy scale. Here, the description provided by the EFT is presumed to be more fundamental than the existing theory at higher energy scales. The construction of such models typically involves the introduction of higher-dimensional operators, which are employed to describe new local interactions that emerge at these scales.
- *Symmetry-driven Approach*: analogous to the top-down methodology, nevertheless, it exploits symmetries of the system to simplify the theoretical framework instead of integrating-out the heavy particles.

2.2.1. Standard Model Extensions

The key idea is to separate the process under consideration into two distinct energy scales, the Infrared (IR) scale, which is the scale of interest, described by a local and analytical operator $\mathcal{O}_i$, and the Ultraviolet (UV) scale, which is encoded in the Wilson coefficient C_i:

$$L = L_{SM} + \frac{1}{\Lambda^2}\sum_i C_i \mathcal{O}_i + O\left(\frac{1}{\Lambda^3}\right), \tag{2.10}$$

Λ is the scale of new physics, and the sum runs over all possible operators of dimension 6. In dimension 5, there is only one operator, the *Weinberg operator*, which is not relevant for the present discussion.

Looking more closely at the $B^0 \to D^{*-}\tau^+\nu_\tau$ decay, a specific example of a $b \to c\ell\nu_\ell$ transition, the effective Hamiltonian for this transition, up to dimension-6 operators, is given by [70]:

$$H_{\text{eff}} = \frac{4G_F}{\sqrt{2}} V_{cb}\, O_{V_L} + \frac{1}{\Lambda^2} \sum_i C_i O_i \,, \tag{2.11}$$

where the operators are given by all four-fermion operators contributing to the $B^0 \to D^{*-}\tau^+\nu_\tau$ transition, and the corresponding Wilson coefficients C_i, assuming that the higher dimension operators respect the SM gauge symmetry, and not including the right-handed neutrino:

$$O_{S_R} = (\bar{c}P_R b)(\bar{\tau}P_L \nu) \,, \quad O'_{S_R} = (\bar{\tau}P_R b)(\bar{c}P_L \nu) \,,$$
$$O''_{S_R} = (\bar{\tau}P_R c^c)(\bar{b}^c P_L \nu) \,, \tag{2.12a}$$
$$O_{S_L} = (\bar{c}P_L b)(\bar{\tau}P_L \nu) \,, \quad O'_{S_L} = (\bar{\tau}P_L b)(\bar{c}P_L \nu) \,,$$
$$O''_{S_L} = (\bar{\tau}P_L c^c)(\bar{b}^c P_L \nu) \,, \tag{2.12b}$$
$$O_{V_L} = (\bar{c}\gamma_\mu P_L b)(\bar{\tau}\gamma^\mu P_L \nu) \,, \quad O'_{V_L} = (\bar{\tau}\gamma_\mu P_L b)(\bar{c}\gamma^\mu P_L \nu) \,,$$
$$O''_{V_L} = (\bar{\tau}\gamma_\mu P_L c^c)(\bar{b}^c \gamma^\mu P_L \nu) \,, \tag{2.12c}$$
$$O_{V_R} = (\bar{c}\gamma_\mu P_R b)(\bar{\tau}\gamma^\mu P_L \nu) \,, \quad O'_{V_R} = (\bar{\tau}\gamma_\mu P_R b)(\bar{c}\gamma^\mu P_L \nu) \,,$$
$$O''_{V_R} = (\bar{\tau}\gamma_\mu P_R c^c)(\bar{b}^c \gamma^\mu P_L \nu) \,, \tag{2.12d}$$
$$O_T = (\bar{c}\sigma^{\mu\nu} P_L b)(\bar{\tau}\sigma_{\mu\nu} P_L \nu) \,, \quad O'_T = (\bar{\tau}\sigma^{\mu\nu} P_L b)(\bar{c}\sigma_{\mu\nu} P_L \nu) \,,$$
$$O''_T = (\bar{\tau}\sigma^{\mu\nu} P_L c^c)(\bar{b}^c \sigma_{\mu\nu} P_L \nu). \tag{2.12e}$$

Some authors include right-handed neutrinos, for more general discussion (cf. [71]). These operators play role in models BSM, they are related to the potential new particles, and interactions as shown in Sec. 2.4.
The set of effective operators employed to address the anomalies in Lepton Flavor Universality might not entirely encompass the complexity of potential new physics. There could exist additional, significant interactions or dynamics not accounted for within the specified EFT model.

2.2.2. Heavy Quark Effective Theory

In the context of QCD, EFTs are indispensable for addressing the complexity introduced by multiple dimensionful scales, notably the Λ_{QCD} scale, which is the energy scale associated with strong interactions, and hadronization processes, and the various mass scales of quarks that span a broad momentum spectrum. Among these, the Heavy Quark Effective Theory (HQET) [72–74] plays an important role in the study of the weak decays of hadrons containing heavy quarks. It provides a systematic framework to analyze the properties and dynamics of these particles by exploiting the hierarchies of scales involved in their interactions.

The first observation relies on the fact that b and c quarks[1], denoted as Q are much heavier than the Λ_{QCD} scale, while the light quarks, u, d and s are referred to as q. Thus, the effects of the heavy quark mass can be separated from the dynamics of the strong interaction at the Λ_{QCD} scale. This allows for simplification of the QCD Lagrangian for processes involving heavy quarks.

A second key point, known as *heavy quark symmetry*, emerges in the limit where the heavy quark mass goes to infinity. In this limit, heavy quarks of different flavors (but the same velocity) behave similarly within hadrons, this symmetry leads to simplifications in the theoretical description of hadronic states. More specifically, hadrons containing a single heavy quark Q, such as $B^{(*)}$, $D^{(*)}$, Λ_b and Λ_c, are characterized by a typical size, $r_h \sim \Lambda_{QCD}^{-1}$ with a momentum transfer between Q and q of the order of Λ_{QCD} or lower. While the Compton wavelength $\lambda_Q \sim m_Q^{-1}$ of the heavy quark with mass m_Q, is much smaller than the hadron's size. This allows the heavy quark to be considered point-like within a much larger hadronic volume. The heavy quark's quantum numbers are localized within a volume approximately the size of λ_Q, while its color charge influences the surrounding cloud, which remains unconstrained by other degrees of freedom. Furthermore, the hadron's rest frame closely aligns with that of the heavy quark, allowing to use non-relativistic description. The hadron can be viewed as a heavy quark surrounded by a non-perturbative cloud of light quarks and gluons.

The HQET Lagrangian is derived from the QCD Lagrangian by systematically integrating out the heavy quark mass scale. It is expanded in terms of $1/m_Q$. The lagrangian involved in a semileptonic transition between a heavy quark Q, with velocity v to another heavy quark Q′ with velocity v', is [75]:

$$L_{HQET} = \overline{Q}(iv \cdot D)Q + \overline{Q'}(iv' \cdot D)Q' + \dots, \tag{2.13}$$

where D is the covariante derivative: $D = \partial + igA$, A is the gluon field, and the ellipsis represents higher-order terms in the expansion in powers of $1/m_Q$. The leading-order term Eq. (2.13) represents the heavy quark acting as a static color source, while higher-order terms (ellipses) account for corrections due to the finite mass of the heavy quark.

In the study of semileptonic decays of heavy mesons, the Isgur-Wise function [76, 77] corresponds to the leading-order behavior of the form factors. It encapsulates the effects of the strong interaction in such processes and is independent of the heavy quark mass in the heavy quark limit. Its universality allows for predictions of various transition rates between heavy mesons using a single function.

[1] In HQET, only b and c quarks are relevant, as t quarks decay before confinement.

The applicability of HQET is limited to processes where the heavy quark mass significantly exceeds the QCD scale. Corrections to HQET, necessary for precise predictions, can become computationally intensive, requiring techniques like lattice QCD to obtain non-perturbative parameters.

2.3. Theory of $B \to D^* \ell^+ \nu_\ell$ Decays

In the context of this thesis, the focus is directed towards the investigation of *semileptonic* B^0 decay processes leading to the production of a vector meson D^* in the final state.

Consider the decay process of a B^0 meson, characterized by momentum p_B and mass m_B, transitioning into a D^* meson—denoted by momentum p_{D^*}, mass m_{D^*}, and polarization ε—accompanied by a lepton pair, $B \to D^* \ell^+ \nu_\ell$. For analytical convenience, we introduce the subsequent variables [78]:

- The invariant mass squared of the lepton-neutrino system:

$$t = q^2 = (p_B - p_{D^*})^2 \tag{2.14}$$

  The range of q^2 is bounded between t_- and t_+

$$t_\pm = (m_B \pm m_{D^*})^2 \tag{2.15}$$

  t_+ correspond to the zero recoil limit, when the D^* meson is at rest in the B meson rest frame, and t_- correspond minimum q^2 when the kinematic limit is reached.

- Dimensionless parameters:

$$r = m_{D^*}/m_B \ , \tag{2.16a}$$

$$w = v_{D^*} \cdot v_B = \frac{m_B^2 + m_{D^*}^2 - t}{2 m_B m_{D^*}} \tag{2.16b}$$

  where v_B and v_{D^*} are the four-velocities of the B and D^* mesons, respectively. The limits on q^2 correspond to: $w_{\min} = 1$ and $w_{\max} = \frac{m_B^2 + m_{D^*}^2}{2 m_B m_{D^*}}$.

The evaluation of the decay amplitude for the $B^0 \to D^{*-} \tau^+ \nu_\tau$ necessitates an understanding of the hadronic matrix element associated with the weak current, which is parameterized by form factors. These form factors encapsulate the non-perturbative QCD dynamics.

Functionally dependent on the recoil parameter w, the form factors are delineated as the ma-

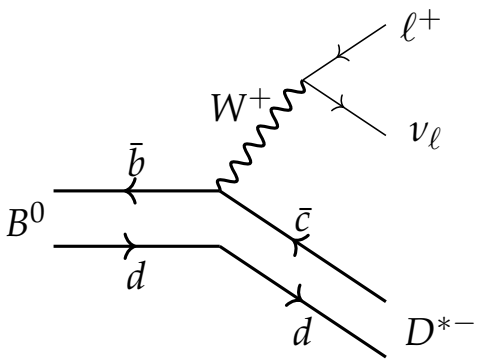

Figure 2.6.: Feynman diagram of the $B \to D^* \ell^+ \nu_\ell$ decay.

trix elements of the weak current transitioning between the initial and final hadronic states, as illustrated in Fig. 2.6. The parametrization of the axial and vector components of the hadronic matrix elements is expressed through the axial and vector form factors h_{A_1}, h_{A_3}, and h_V, as follows [78, 79]:

$$\langle D^*(p_{D^*}, \varepsilon)|\bar{c}\gamma_\mu\gamma_5 b|B(p_B)\rangle = i\varepsilon_\nu^* \sqrt{m_{D^*} m_B}\Big[g^{\mu\nu}(w+1)\, h_{A_1}(w) - v_B^\nu(v_B^\mu\, h_{A_2}(w) + v_{D^*}^\mu\, h_{A_3}(w))\Big], \tag{2.17a}$$

$$\langle D^*(p_{D^*}, \varepsilon)|\bar{c}\gamma_\mu b|B(p_B)\rangle = \epsilon^{\mu\nu}{}_{\rho\sigma}\varepsilon_\nu^* \sqrt{m_{D^*} m_B} v_B^\rho v_{D^*}^\sigma\, h_V(w)\,, \tag{2.17b}$$

where:

$$h_{A_1}(w) = C_{A_1}\xi(w) \tag{2.18a}$$

$$h_{A_2}(w) = C_{A_2}\xi(w) \tag{2.18b}$$

$$h_{A_3}(w) = (C_{A_1} + C_{A_3})\xi(w) \tag{2.18c}$$

$$h_V(w) = C_V\xi(w) \tag{2.18d}$$

ξ is the Isgur-Wise function, it encapsulates the non-perturbative QCD dynamics in the heavy quark limit. They correspond to the leading-order behavior of the form factors in $B \to D^*$ decays. The coefficients C_{A_1}, C_{A_2}, C_{A_3} and C_V are obtained from the HQET. The helicity amplitutdes are given by [78, 80]:

$$H_\pm(w) = (w+1)\left[h_{A_1}(w) \pm \frac{w-1}{\sqrt{w^2-1}} h_V(w)\right], \tag{2.19a}$$

$$H_0(w) = y(w+1)\left[(w-r)h_{A_1}(w) - (w-1)\left\{r h_{A_2}(w) + h_{A_3}(w)\right\}\right], \tag{2.19b}$$

$$H_S(w) = y\sqrt{w^2-1}\left[(w+1)h_{A_1}(w) - (1-wr)h_{A_2}(w) - (w-r)h_{A_3}(w)\right], \tag{2.19c}$$

where $y^2(1-2wr+r^2) = 1$. The differential decay rate using the *helicity amplitude formalism* is given by:

$$\frac{d\Gamma}{dw} = |V_{cb}|^2 |\eta_{EW}^2| \frac{G_F^2 m_B^5}{16\pi^3} \left(1 - \frac{m_\ell^2}{q^2}\right) r^3 \left(w^2-1\right)^{1/2} \left\{ \frac{1}{3y^2} \left(1 + \frac{m_\ell^2}{2q^2}\right) \left[|H_+|^2 + |H_-|^2 + |H_0|^2\right] + \frac{m_\ell^2}{2m_B^2} |H_S|^2 \right\}, \tag{2.20}$$

where V_{cb} is the CKM matrix element, η_{EW} is the electroweak correction factor, G_F is the Fermi constant, and m_ℓ is the lepton mass. The decay rate is integrated over the range of w to obtain the total decay rate Eq. (2.29). It is noteworthy that the scalar helicity amplitude, denoted as H_S, undergoes suppression by a factor of m_ℓ^2 / m_B^2, rendering it negligible for $\ell = \mu$ or e.

The form factors, as functions of the recoil parameter w, are derived primarily at minimal values of w. To broaden the applicability of these functions across the entire kinematic range, a standard, model-independent parametrization is requisite. The most widely acknowledged parametrizations in scholarly literature are the Caprini-Lellouch-Neubert (CLN) [81] and the Boyd-Grinstein-Lebed (BGL) [82, 83] parametrizations. The aforementioned parametrization are described subsequently. Derived from the form factors as indicated in Eq. (2.17), one can establish the subsequent ratios of form factors:

$$R_1(w) = \frac{h_V(w)}{h_{A_1}(w)}, \tag{2.21a}$$

$$R_2(w) = \frac{h_{A_3}(w) + r h_{A_2}(w)}{h_{A_1}(w)}, \tag{2.21b}$$

these ratios compose the CLN parametrization, which is articulated as follows:

$$h_{A_1}(w) = h_{A_1}(1) \left[1 - 8\rho^2 z + \left(53\rho^2 - 15\right) z^2 - \left(231\rho^2 - 91\right) z^3\right], \tag{2.22a}$$

$$R_1(w) = R_1(1) - 0.12(w-1) + 0.05(w-1)^2, \tag{2.22b}$$

$$R_2(w) = R_2(1) + 0.11(w-1) - 0.06(w-1)^2, \tag{2.22c}$$

where ρ and $h_{A_1}(1)$ are free parameters, exhibiting model dependency; these parameters are ascertained through experimental data or lattice QCD computations.
The values of $R_1(1)$ and $R_2(1)$ are defined at their respective quantities at $w = 1$. The value of

CLN parameters are [8]:

$$\begin{aligned} \rho^2 &= 1.121 \pm 0.024 \\ R_1(1) &= 1.269 \pm 0.026 \\ R_2(1) &= 0.853 \pm 0.017 \end{aligned} \tag{2.23}$$

This parametrization is based on dispersion relations, unitarity, and HQET. Despite its simplicity, it encounters limitations. Specifically, it does not encapsulate higher-order correction terms in the $1/m_c$ expansion [81].

The BGL parametrization [82–84] is based on dispersion relations, analyticity and crossing symmetry. This framework offers model independent approach for the parametrization of form factors, eschewing any presuppositions related to the heavy quark symmetry, which is compromised by higher order corrections in $1/m_c$ expansion.
The domain of q^2 is extended into the complex plane, facilitating the introduction of a conformal mapping that transitions from the q^2 plane to the unit disk within the z complex plane. This allows for the expansion of the form factors as power series in terms of z. The z expansion is carried out for the form factors f, g, $\mathcal{F}_1$, and $\mathcal{F}_2$, which are obtained from a combination of h_X form factors:

$$g(w) = \frac{h_V(w)}{m_B \sqrt{r}}, \tag{2.24a}$$

$$f(w) = m_B \sqrt{r}(1+w) h_{A_1}(w), \tag{2.24b}$$

$$\mathcal{F}_1(w) = m_B^2 \sqrt{r}(1+w)\Big[(w-r)h_{A_1}(w) - (w-1)\left(r h_{A_2}(w) + h_{A_3}(w)\right)\Big], \tag{2.24c}$$

$$\mathcal{F}_2(w) = \frac{1}{\sqrt{r}}\Big[(1+w)h_{A_1}(w) + (rw-1)h_{A_2}(w) + (r-w)h_{A_3}(w)\Big], \tag{2.24d}$$

where r and w are defined in Eq. (2.16). This redefinition aligns the form factors with the helicity amplitudes $H_- - H_+$, $H_+ + H_-$, H_0, and H_S, respectively [85]. Thus, the form factor $\mathcal{F}_2$ is important only with massive leptons, in particular in the determination of $\mathbf{R}(D^*)$. The form factor expansion leads to:

$$f(z) = \frac{1}{P_{1^+}(z)\phi_f(z)} \sum_{n=0}^{\infty} a_n z^n, \tag{2.25a}$$

$$g(z) = \frac{1}{P_{1^-}(z)\phi_g(z)} \sum_{n=0}^{\infty} b_n z^n, \tag{2.25b}$$

$$\mathcal{F}_1(z) = \frac{1}{P_{1^+}(z)\phi_{\mathcal{F}_1}(z)} \sum_{n=0}^{\infty} c_n z^n, \tag{2.25c}$$

$$\mathcal{F}_2(z) = \frac{1}{P_{1^-}(z)\phi_{\mathcal{F}_2}(z)} \sum_{n=0}^{\infty} d_n z^n, \tag{2.25d}$$

where the *Blashcke factors* $P_{1^\pm}$ accounts for sub-threshold poles due to B^* bound states $J^P = 1^\pm$ resonances :

$$P_{1^-}(z) = \prod_{i=1}^{4} \frac{z - z_{p_i}}{1 - z z_{p_i}}, \qquad P_{1^+}(z) = \prod_{i=1}^{4} \frac{z - z_{q_i}}{1 - z z_{q_i}}, \tag{2.26}$$

where $p_{1,2,3,4}$ are the vector B_c^* states, and $q_{1,2,3,4}$ are the axial-vector states.

$$z_X = \frac{\sqrt{t_+ - m_X} - \sqrt{t_+ - t_-}}{\sqrt{t_+ - m_X} + \sqrt{t_+ - t_-}} \tag{2.27}$$

with $t_\pm = (m_B \pm m_{D^*})^2$, and $X = \{p_i, q_i\}_{i\in\{1,\dots,4\}}$ and the *outer functions* $\phi_{f,g,\mathcal{F}_1,\mathcal{F}_2}$ (Eq. (2.28)) encodes the QCD dispersion relations and kinematic constraints, which are the only non-analytic functions in the z plane. The non-analyticity of the form factors is encoded in χ^T and $\tilde{\chi}^L$ functions.

$$\phi_g(z) = \sqrt{\frac{256 n_I}{3\pi\chi^T(+u)}} \frac{r^2(1+z)^2(1-z)^{-1/2}}{\left[(1+r)(1-z) + 2\sqrt{r}(1+z)\right]^4}, \tag{2.28a}$$

$$\phi_f(z) = \frac{1}{m_B^2}\sqrt{\frac{16 n_I}{3\pi\chi^T(-u)}} \frac{r(1+z)(1-z)^{3/2}}{\left[(1+r)(1-z) + 2\sqrt{r}(1+z)\right]^4}, \tag{2.28b}$$

$$\phi_{\mathcal{F}_1}(z) = \frac{1}{m_B^3}\sqrt{\frac{8 n_I}{3\pi\chi^T(-u)}} \frac{r(1+z)(1-z)^{5/2}}{\left[(1+r)(1-z) + 2\sqrt{r}(1+z)\right]^5}, \tag{2.28c}$$

$$\phi_{\mathcal{F}_2}(z) = \sqrt{\frac{128 n_I}{\pi\tilde{\chi}^L(-u)}} \frac{r^2(1+z)^2(1-z)^{-1/2}}{\left[(1+r)(1-z) + 2\sqrt{r}(1+z)\right]^4}, \tag{2.28d}$$

with $u = m_c/m_b$, t_+ (resp. t_-) is threshold for BD^* (resp. D^*) production, t_0 is a free parameter, chosen of convergence optimization of the series expansion of the form factors $t_0 = t_+ - \sqrt{t_+ - t_-}$. The coefficients of series a, b, c and d are determined from experimental data/theoretical calculations as shown in Tab. 2.2.

The main reason for calculating the ratio of branching fractions is to substantially minimize the theoretical uncertainties related to FFs. Moreover, this approach leads to the cancellation of many parameters in the ratio, including CKM matrix elements and the B meson lifetime. The ratio $\mathbf{R}\left(D^{(*)}\right)$ Eq. (2.9) is computed using HQET, QCD sum rules and experimental data,

	Lattice QCD	Lattice + BaBar	Lattice + Belle	Lattice + both	$h_{A_1}(1)$ + both
a_0	0.0330(12)	0.0331(12)	0.0325(11)	0.0321(10)	0.0262(42)
a_1	−0.156(55)	−0.091(41)	−0.160(45)	−0.147(31)	0.03(15)
a_2	−0.12(98)	−0.19(20)	−0.69(94)	−0.63(20)	−0.12(12)
b_0	0.01229(23)	0.01229(22)	0.01238(22)	0.01249(22)	0.01228(23)
b_1	−0.003(12)	0.0104(72)	0.015(10)	0.0021(43)	0.0046(48)
b_2	0.07(53)	0.44(17)	−0.30(24)	0.07(11)	−0.17(21)
c_0	0.002059(38)	0.002058(37)	0.002073(37)	0.002092(37)	0.002056(38)
c_1	−0.0058(25)	−0.0010(11)	0.0010(17)	0.00062(86)	0.00163(92)
c_2	−0.013(91)	0.022(50)	0.035(57)	0.060(26)	0.017(37)
c_3	–	0.24(77)	−0.34(76)	−0.94(48)	−0.66(62)
d_0	0.0509(15)	0.0517(15)	0.0522(15)	0.0531(14)	–
d_1	−0.328(67)	−0.220(55)	−0.180(49)	−0.201(42)	–
d_2	−0.02(96)	0.20(92)	−0.01(90)	0.0007(8980)	–
χ^2/dof	0.63/1	8.50/4	111/79	126/84	104/76
$\sum_i a_i^2$	0.47 ± 0.36	0.05 ± 0.12	0.7 ± 2.0	0.43 ± 0.30	0.04 ± 0.05
$\sum_i (b_i^2 + c_i^2)$	0.13 ± 0.14	0.56 ± 0.98	0.54 ± 1.43	0.90 ± 1.17	0.57 ± 0.55
$\sum_i d_i^2$	0.54 ± 0.40	0.46 ± 0.35	0.41 ± 0.23	0.41 ± 0.33	–
$V_{cb} \times 10^3$	39.1(1.0)	38.17(85)	38.40(78)	39.35(91)	–
$\mathbf{R}(D^*)$	0.265(13)	–	–	0.2484(13)	–

Table 2.2.: FFs expansion coefficients till the second order and the corresponding V_{cb} and $\mathbf{R}(D^*)$ values from the BGL parametrization [78].

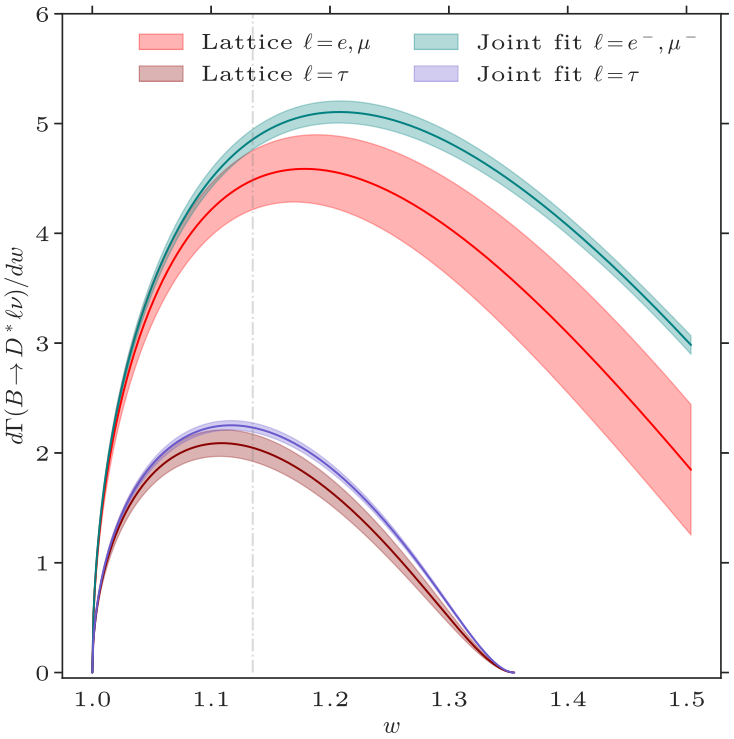

Figure 2.7.: Differential decay rate of the $B \to D^* \ell^+ \nu_\ell$ decay as function of the recoil parameter w, calculated from lattice-only QCD data (light leptons in red and τ in brown) and joint fit of lattice and experimental data (light leptons in green and τ in purple) [78].

it is also possible to calculate $\mathbf{R}\left(D^{(*)}\right)$ directly from lattice [78], with:

$$\mathrm{Br}\left(B \to D^{(*)} \ell \nu_\ell\right) = \tau_B \int_1^{w_{\mathrm{max},\ell}} dw \, \frac{d\Gamma}{dw} \,, \tag{2.29}$$

where τ_B the B meson lifetime, and $w_{\mathrm{max},\ell} = \left(1 + r^2 - m_\ell^2 / M_B^2\right)/2r$, and the differential decay rate is given by Eq. (2.20). The differential decay rate as function of the recoil parameter is shown in Fig. 2.7, comparing the extraction using lattice-only data with joint fit obtained from lattice and experimental data. The direct integration of the differential decay rate leads to the ratio value obtained in Tab. 2.2.

The recent $\mathbf{R}(D)$ and $\mathbf{R}(D^*)$ calculations are summarized in Tab. 2.3.

	$\mathbf{R}(D^*)$	$\mathbf{R}(D)$	Ref.
FNAL/MILC	0.265 ± 0.013	–	[78]
HPQCD	0.279 ± 0.013	–	[86]
JLQCD	0.252 ± 0.022	–	[87]
BaBar	0.252 ± 0.005	–	[88]
I. Ray *et al.*	0.258 ± 0.012	0.304 ± 0.003	[89]
P. Gambino *et al.*	$0.254\ ^{+0.007}_{-0.006}$	–	[85]
F. U. Bernlochner *et al.*	0.257 ± 0.003	0.299 ± 0.003	[90]
S. Jaiswal *et al.*	0.257 ± 0.005	–	[91]
M. Bordone *et al.*	0.250 ± 0.003	0.297 ± 0.003	[92]
	0.247 ± 0.006	0.298 ± 0.003	
D. Bigi *et al.*	0.260 ± 0.008	–	[93]
	–	0.299 ± 0.003	[94]
G. Martinelli *et al.*	0.275 ± 0.008	–	[95]
	0.261 ± 0.020	0.296 ± 0.008	[96]
HFLAV theory average	0.254 ± 0.005	0.298 ± 0.004	[8]

Table 2.3.: Summary of recent $\mathbf{R}(D^*)$ and $\mathbf{R}(D)$ calculations using lattice–QCD, QCD sum rules, experimental data and combined fit.

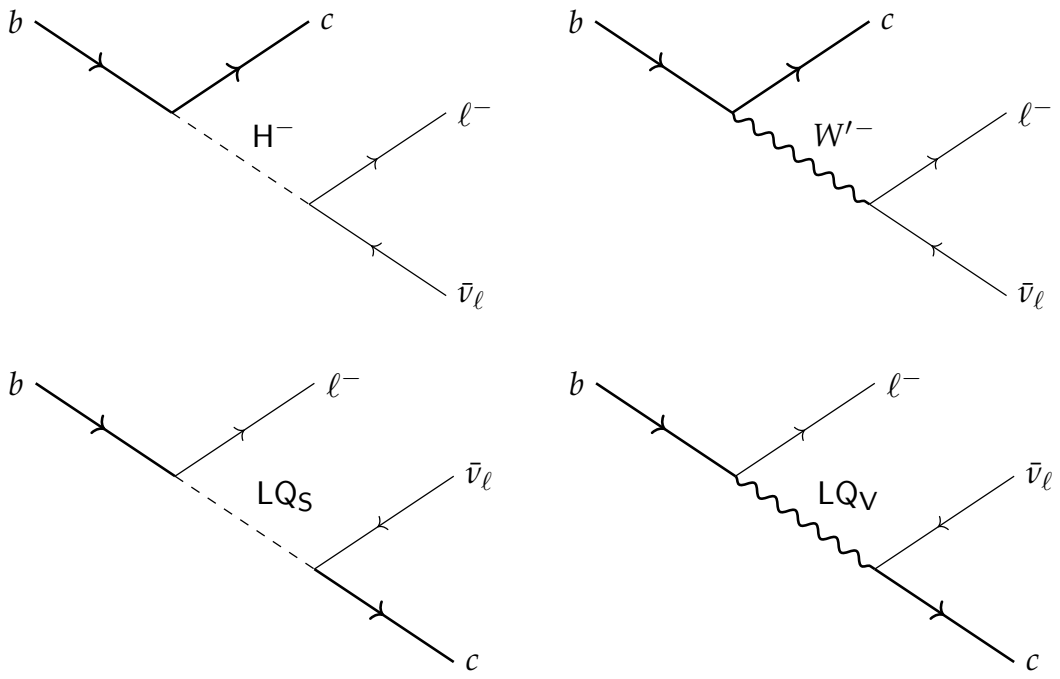

Figure 2.8.: Feynman diagrams of the processes contributing to the $b \to c\ell\nu_\ell$ transition beyond the SM. From left to right: charged Higgs, vector boson, scalar Leptoquark and vector Leptoquark.

2.4. Beyond Standard Model

Several BSM theories have been proposed to complete the SM, to cite a few: Supersymmetry (SUSY) [97], Grand Unified Theories (GUTs) [98], technicolor [99], extra dimensions, and composite models [100]. These models could contain new particles/interactions which would contribute to the $b \to c\ell\nu_\ell$ transition. For any BSM theory to be viable, it must align with existing experimental constraints, such as meson decays, meson–antimeson mixing, bounds on Lepton Flavor Violation, and Lepton Flavor non-universality in purely leptonic decays.

A comprehensive review of BSM models that may elucidate the anomalies observed in $b \to c\ell\nu_\ell$ transitions can be found in the referenced literature [101–107]. This non-exhaustive list underscores the rigorous criteria any new model must meet to be considered a plausible extension of the SM. The main particles that could contribute to the $b \to c\ell\nu_\ell$ transition are the charged Higgs, vector bosons, scalar leptoquarks, and vector leptoquarks, as shown in Fig. 2.8.

2.4.1. Two Higgs Doublet Model

The Two Higgs Doublet Model (2HDM) is the extension of the SM Higgs sector, was proposed as a solution to the flavor anomalies. It introduces two Higgs doublets, thus obtaining four physical Higgs bosons: two charged Higgs bosons $H^{\pm}$ and two neutral Higgs bosons, a CP-even H^0 and a CP-odd A^0.
In type II 2HDM [108], one Higgs doublet couples to down-type quarks and charged leptons and the other to up-type quarks. The Minimal Supersymmetric Standard Model (MSSM) is an example of a 2HDM.
The charged Higgs boson $H^{\pm}$ could contribute to the $b \to c\ell\nu_\ell$ transition. The charged scalar particle would couple proportionally to the mass of the fermion involved in the interaction, thus the muon is less massive than the tau, this would be at the origin of lepton flavor universality violation.

2.4.2. Vector Bosons

Vector Boson W' introduced in [106] is a heavy gauge boson that couples to the fermions. The W' boson is a generic prediction of many models BSM, such as the left-right symmetric model, the grand unified theories, and the little Higgs models.

$$O_{V_{\mathcal{L}}} = (\bar{c}\gamma^{\mu}P_{\mathcal{L}}b)(\bar{\tau}\gamma_{\mu}P_{\mathcal{L}}\nu_{\tau}) \tag{2.30}$$

An $SU(2)_L$ triplet of massive vector bosons [106], W' and Z', which couples predominantly to the third generation of quarks and leptons, could explain charged current anomalies in $b \to c\ell\nu_\ell$ transitions.

2.4.3. Leptoquarks

Leptoquarks emerge naturally in the framework of GUTs, such as Pati-Salam [32]. Specifically, the $SU(4)$ gauge group provides a unified description of quarks and leptons by assigning a fourth color charge to leptons. As consequence of the spontaneously breaking of the $SU(4)$ symmetry, massive leptoquarks are generated [109], and the $SU(3)$ group remains unbroken, preserving the gluons massless. Leptoquarks (LQ) of interest carry both B and L, baryon and lepton numbers. To maintain the quark–lepton–LQ interactions gauge invariant, group theory imposes the leptoquarks to be color triplet:

$$3 \otimes 1 \otimes \bar{3} = 8 \oplus 1 \tag{2.31}$$

As consequence, interactions involving lepton–Leptoquark–lepton are forbidden, whereas a quark–Leptoquark–quark interaction is possible. Due to distinct singlet or doublet nature

of quarks and leptons under $SU(2)_L$, the leptoquarks can exhibit singlet, doublet, or triplet properties. Finally, the LQ hypercharge is deduced from the nature of quarks and leptons under $U(1)_Y$, using hypercharge conservation. The relevant operators which describe scalar Leptoquark are:

$$O_{S_L} = (\bar{c}P_L b)(\bar{\tau}P_L \nu) \,, \quad O''_{S_L} = (\bar{\tau}P_L c^c)(\bar{b}^c P_L \nu) \,,$$
$$O''_{S_R} = (\bar{\tau}P_R c^c)(\bar{b}^c P_L \nu) \,, \tag{2.32}$$

and vector Leptoquark:

$$O_{V_L} = (\bar{c}\gamma_\mu P_L b)(\bar{\tau}\gamma^\mu P_L \nu) \,, \quad O'_{V_R} = (\bar{\tau}\gamma_\mu P_R b)(\bar{c}\gamma^\mu P_L \nu) \,,$$
$$O''_{V_R} = (\bar{\tau}\gamma_\mu P_R c^c)(\bar{b}^c\gamma^\mu P_L \nu) \,, \tag{2.33}$$

If one restricts to leptoquarks which couple to the third and the second generation [110], the interaction Lagrangian that contributes to the $b \to c\ell\bar{\nu}$, involving Leptoquark interactions with quarks and leptons is given by [111]:

$$L^{LQ} = L^{LQ}_{F=0} + L^{LQ}_{F=-2} \,, \tag{2.34}$$

where $F = 3B + L$, the Lagrangian $L^{LQ}_{F=0}$ describes the interactions of leptoquarks with $F = 0$, involves the following terms:

$$L^{LQ}_{F=0} = \left(h^{ij}_{1L}\, \bar{Q}_{iL}\gamma^\mu L_{jL} + h^{ij}_{1R}\, \bar{d}_{iR}\gamma^\mu \ell_{jR}\right) U_{1\mu} + h^{ij}_{3L}\, \bar{Q}_{iL}\sigma\gamma^\mu L_{jL} U_{3\mu}$$
$$+ \left(h^{ij}_{2L}\, \bar{u}_{iR} L_{jL} + h^{ij}_{2R}\, \bar{Q}_{iL} i\sigma_2 \ell_{jR}\right) R_2 \,, \tag{2.35a}$$

and the Lagrangian with leptoquarks with $F = -2$ is given by:

$$L^{LQ}_{F=-2} = \left(g^{ij}_{1L}\, \bar{Q}^c_{iL} i\sigma_2 L_{jL} + g^{ij}_{1R}\, \bar{u}^c_{iR}\ell_{jR}\right) S_1 + g^{ij}_{3L}\, \bar{Q}^c_{iL} i\sigma_2\sigma L_{jL} S_3$$
$$+ \left(g^{ij}_{2L}\, \bar{d}^c_{iR}\gamma^\mu L_{jL} + g^{ij}_{2R}\, \bar{Q}^c_{iL}\gamma^\mu \ell_{jR}\right) V_{2\mu} \,, \tag{2.35b}$$

$\psi^c = C\bar{\psi}^T = C\gamma^0\psi^*$ is a charge-conjugated fermion field. The quantum numbers and representations under SM gauge group of the leptoquarks involves in Eq. (2.35) are summarized in Tab. 2.4.

2.4.4. Experimental Constraints

The experimental constraints on the various hypothetical particles that could explain LFU violation in $b \to c\ell\nu_\ell$ transitions are disfavoring most of the models.

	$(SU(3)_C, SU(2)_L, U(1)_Y)$	spin	F
S_1	$(\bar{3}, 1, 1/3)$	0	-2
S_3	$(\bar{3}, 3, 1/3)$	0	-2
R_2	$(3, 2, 7/6)$	0	0
V_2	$(\bar{3}, 2, 5/6)$	1	-2
U_1	$(3, 1, 2/3)$	1	0
U_3	$(3, 3, 2/3)$	1	0

Table 2.4.: Leptoquark classification according to their representation in the SM gauge group, and their quantum numbers.

The type-II 2HDM generates the operator O_{S_R}

$$O_{S_R} = (\bar{c} P_R b)(\bar{\tau} P_L \nu_\tau) \tag{2.36}$$

with the Wilson coefficient:

$$\frac{C_{S_R}}{\Lambda^2} = -2\sqrt{2}\, G_F V_{cb} \frac{m_b m_\tau}{m_{H^\pm}^2} \tan^2 \beta. \tag{2.37}$$

The 2HDM type II is excluded by experiments [11, 12], while the type III could explain both $\mathbf{R}(D)$ and $\mathbf{R}(D^*)$ anomalies [112].

In 2HDM of type III [112], both Higgs doublets couple to up quarks and down quarks as well, with MSSM-like Higgs potential. Type III can either respect MFV [35, 113, 114] or involve flavor violation structure, specifically in the *up* sector are considered, to explain both $\mathbf{R}(D)$ and $\mathbf{R}(D^*)$ anomalies [112], with Higgs mass around $M_H = 500\,\mathrm{GeV}$.

Low-mass Leptoquarks (below $1.58\,\mathrm{TeV}$ for scalar Leptoquarks $S_{1,3}$ and $1.95\,\mathrm{TeV}$ for vector Leptoquarks V_2, U_3) are generally not favored due to exclusion by LHC data [115, 116].
The R_2 Leptoquark has similar constraints to $S_{1,3}$, with mass limits typically above $1\,\mathrm{TeV}$. It faces stringent experimental bounds especially when coupled to lighter generations of quarks and leptons [116–118].

The U_1 Leptoquark shows a 3σ level of support to explain the $\mathbf{R}(D)$ and $\mathbf{R}(D^*)$ anomalies, with both left and right-handed interactions [119]. Fig. 2.9 shows the constraints on the Wilson coefficients C_{LL} and C_{LR} for the U_1 Leptoquark. The ellipses denote the 1, 2, and 3σ contours fitting only $b \to c$ observables. The SM corresponds to the black dot at $C^c_{LR} = C^c_{LL} = 0$.

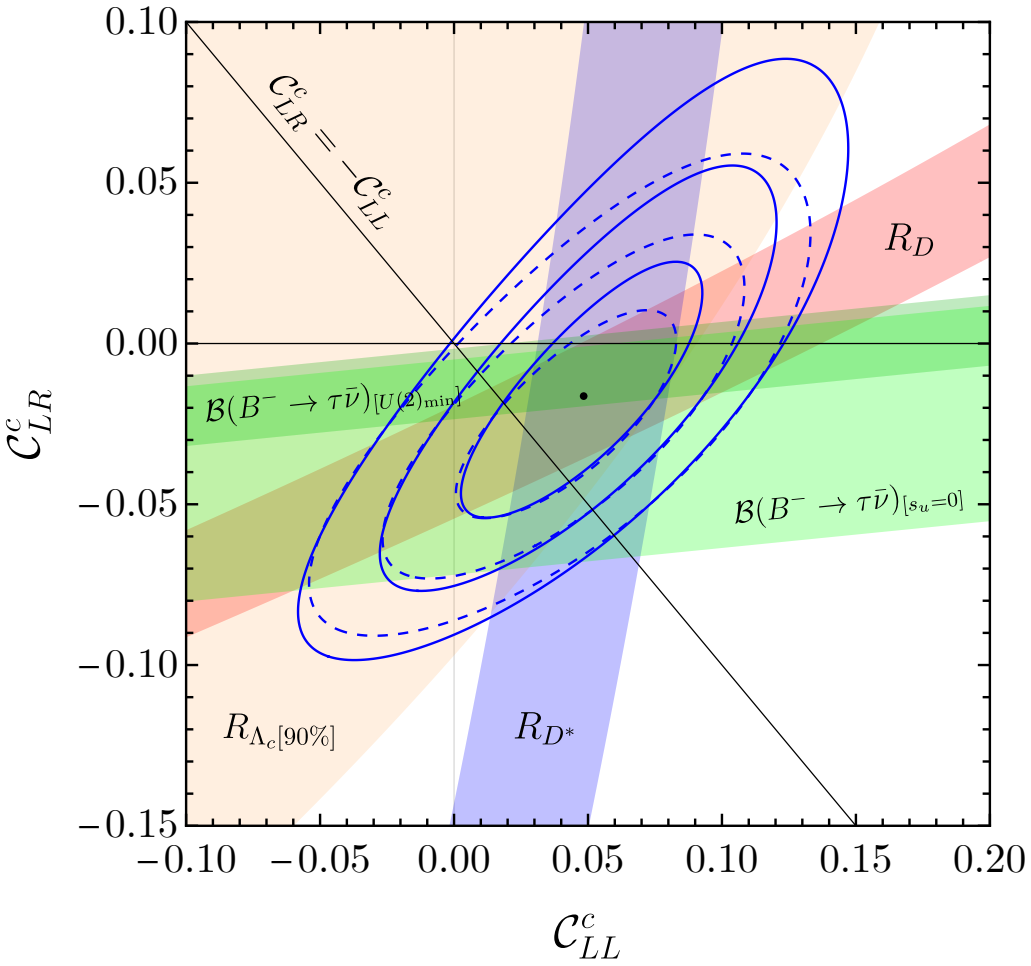

Figure 2.9.: Constraints on the Wilson coefficients C_{LL} and C_{LR} from χ^2–fit to low-energy observables [119].

Concluding Notes

It is noteworthy that LFU tests serve as effective probes for testing the SM; however, some new physics models may also comply with the LFU hypothesis. The challenge of distinguishing new physics from SM predictions necessitates model-independent measurements, employing angular observables and other variables sensitive to new physics. Moreover, it is essential to consider the correlations of several observables, such as the longitudinal τ polarizations, the D^* polarization, the distributions of q^2, as well as the forward-backward asymmetry to distinguish among the various BSM theories. Although, these considerations falls beyond the scope of this thesis, upcoming measurements and angular analyses will be able to differentiate the interactions that could potentially be responsible of non-lepton-flavor universality in $b \to c\ell\nu_\ell$ transitions.

Chapter 3

The LHCb Experiment

In this chapter, a comprehensive overview of the LHCb experiment and its role within the broader context of particle physics is provided. The discussion begins with Flavor Physics experiments (Sec. 3.1), which offer a complementary approach to the measurements performed by LHCb. Following this, the LHC is introduced in Sec. 3.2, with a brief description of the stages of the proton beam acceleration. An in-depth exploration of the LHCb detector is presented in Sec. 3.3, highlighting its design and characteristics. The specific components of the LHCb detector, including the tracking system (Sec. 3.3.1), the particle identification system (Sec. 3.3.2), the trigger system (Sec. 3.3.3), and the software and computing infrastructure (Sec. 3.3.4), are examined in detail. The chapter concludes with an overview of the ongoing and planned upgrades for the LHCb detector (Sec. 3.4).

3.1. Flavor Physics Experiments

Flavor physics is often explored through the study of B mesons at B-*factories* and *hadron colliders*. The high mass of B mesons allows for diverse decay channels, making them excellent candidates for investigating CP violation and matter-antimatter asymmetries. These complex decay processes offer insights into the SM and may reveal evidence of new physics.

The former B-factories BaBar and Belle, and the current Belle II, are designed with the features: accurate reconstruction of charged-particle trajectories; precise measurement of neutral particle energies; and good identification of photons, electrons, muons, charged kaons.

The BaBar experiment [120], located at the Stanford Linear Accelerator Center (SLAC) in the United States, operated from 1999 to 2008 at center-of-mass energies near the $\Upsilon(4S)$ resonance[1](at 10.58 GeV), and luminosity of 10^{33} $\mathrm{cm}^{-2}\mathrm{s}^{-1}$. It was designed around the PEP-II electron-positron collider[121], which produced asymmetric-energy beams (9 GeV electrons and 3.1 GeV positrons) to create B meson pairs. The primary aim of BaBar was to investigate CP violation.

The Belle experiment [122] was conducted at the High Energy Accelerator Research Organization (KEK) in Tsukuba, Japan, utilizing the KEKB electron-positron collider. Like BaBar, Belle collected data from 1999 to 2010, focusing on the study of CP violation[2] and B meson decays. It operated at beam energies of 8.0 GeV and 3.5 GeV for electrons and positrons, respectively, and a luminosity of 10^{34} $\mathrm{cm}^{-2}\mathrm{s}^{-1}$.

Furthermore, the legacy of BaBar and Belle continues through the current dedicated experiments, Belle II and the LHCb experiment (Sec. 3.3). Belle II [125] is an upgrade of the Belle experiment and operates at the SuperKEKB accelerator, a significantly upgraded version of KEKB. Launched in 2018, with its improved detector and the increased luminosity of SuperKEKB, expected to reach 8×10^{35} $\mathrm{cm}^{-2}\mathrm{s}^{-1}$, Belle II is expected to significantly surpass the capabilities of its predecessor, allowing for even more precise measurements and the potential discovery of new physics phenomena.

Hadron colliders have the advantage of high statistics due to the accessible high energy and luminosity. Diverse production and decay mechanisms (such as B-meson, charm meson, rare kaon, and baryon decays) and a wide range of decay channels to test LFU are available. On the other hand, B-factories, having access to the $\Upsilon(4S)$ resonance, enable the reconstruction of the full decay kinematics of the B mesons, including the neutrinos. It is important to note that at hadron colliders like LHCb, all species of B hadrons are produced, including B^0, B^+, B_s^0, and Λ_b. In contrast, at the $\Upsilon(4S)$ energy, accessible to Belle II, only B^0 and B^+ mesons are produced. Despite operating in different regions and using different accelerators, LHCb and Belle II share the common goal of probing the frontiers of the SM, with their studies being highly complementary.

3.2. The Large Hadron Collider

The LHC [126] is the world's largest particle accelerator, located at CERN, near Geneva, Switzerland. Encased within an underground tunnel approximately 27 km in circumference, and

[1]The $\Upsilon(4S)$ resonance is a particle state that decays into a pair of B mesons $e^+e^- \to \Upsilon(4S) \to B\bar{B}$.
[2]Both experiments provided significant evidence for the phase in the CKM matrix [123, 124].

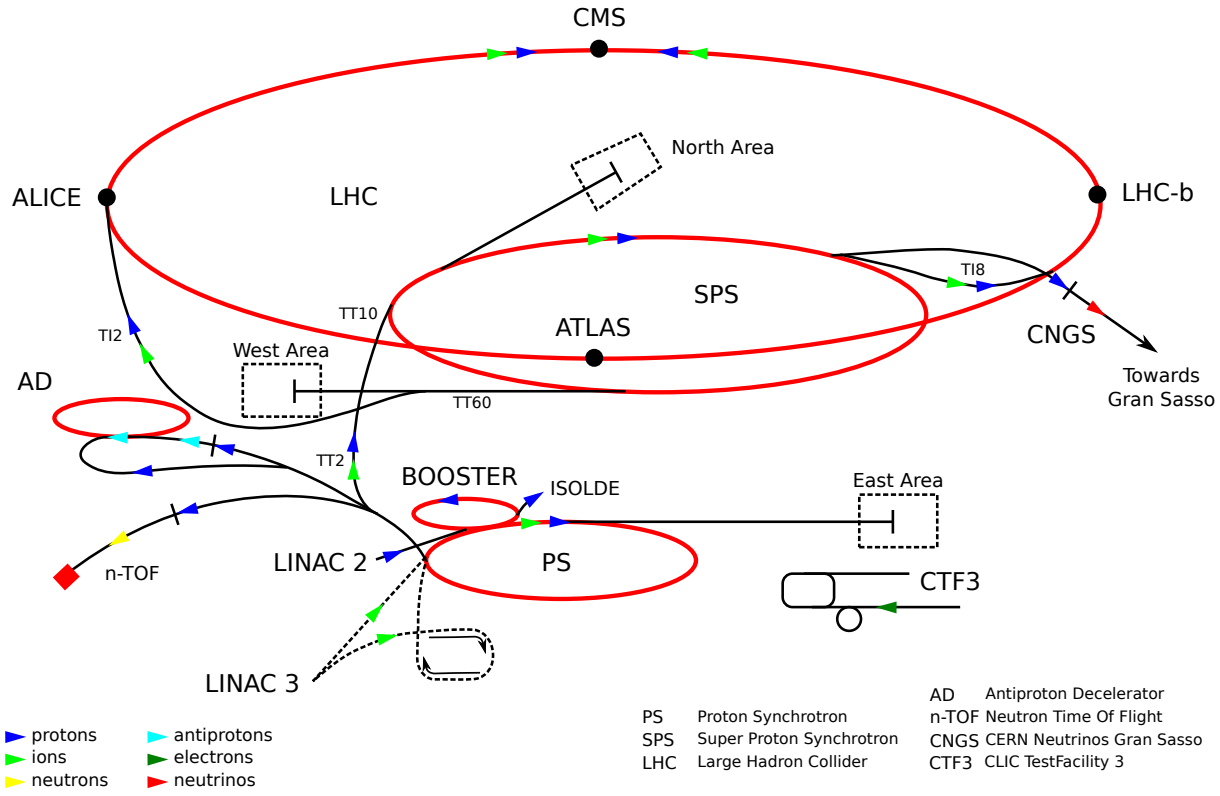

Figure 3.1.: Scheme of the CERN accelerator complex [126].

buried between 50 to 175 m below the surface.

It hosts four primary experiments: ATLAS [127], CMS [128], LHCb [129], and ALICE [130], each situated at distinct interaction points along the collider. It is the successor of the Large Electron-Positron Collider (LEP), an electron-positron collider that operated from 1989 to 2000. The LHC's primary objectives was to explore the Higgs boson, which was discovered in 2012, advancing our understanding of the SM, and investigating potential new physics BSM.

Engineered to accelerate protons, the LHC collides these protons at these interaction points. During Run 1, the LHC operated at a center-of-mass energy of 7 TeV and 8 TeV, and in Run 2, at 13 TeV. Additionally, it accelerates heavy ions, like lead, to 2.76 TeV per nucleon, for quark-gluon plasma studies.

The protons undergo a multistage acceleration process to incrementally increase their energy before entering the LHC ring. A schematic of the CERN accelerator complex is shown in Figure 3.1.

The acceleration process begins with hydrogen atoms, which are ionized to extract protons. A $100\,\mathrm{ms}$ pulse of protons is injected into the Linac 2 linear accelerator[3], where they are accelerated to $50\,\mathrm{MeV}$.

Subsequently, they are boosted to $1.4\,\mathrm{GeV}$ by the Proton Synchrotron Booster (PSB), which utilizes four synchrotron rings stacked vertically. The journey continues through the Proton Synchrotron (PS), enhancing their energy to $25\,\mathrm{GeV}$ within a $628\,\mathrm{m}$ circumference using 277 electromagnets, including 100 dipoles, for beam guidance. Finally, the protons are accelerated to $450\,\mathrm{GeV}$ in the Super Proton Synchrotron (SPS), which concludes the pre-acceleration stage.

The LHC ring comprises superconducting magnets and acceleration structures, maintained at $-271.3\,^{\circ}\mathrm{C}$ by superfluid helium to achieve the necessary conditions for superconductivity. Proton beams are injected into the LHC in opposite directions and are guided by 1,232 dipole magnets. The path of the protons is further refined by 392 quadrupole magnets, focusing the beams to increase collision probabilities.

Radiofrequency (RF) cavities, sixteen in total, are embedded within the LHC structure. These cavities generate oscillating electric fields, progressively accelerating the protons over approximately $20\,\mathrm{min}$–or 10^7 revolutions–until they reach the desired energy level, optimizing conditions for particle collisions and experiments.

The LHC successor, the High-Luminosity Large Hadron Collider (HL-LHC) is an upgrade to the existing LHC, aimed at significantly increasing the luminosity of the machine. Scheduled to begin operations in 2029, with the goal of collecting data at a rate ten times greater than the current LHC capabilities. The LHC/HL-LHC timeline is shown in Fig. 3.2.

Achieving such high luminosity involves several technical upgrades and innovations, including the development and installation of new, high-field superconducting magnets, more robust beam collimation systems, and advanced detector technologies to handle the increased data rates. The technical upgrades and innovations planned for the LHC will necessitate significant advancements in data processing and analysis techniques to effectively handle the increased volume of information collected by the experiments.

[3] After Long-Shutdown 2, Linac 4 is used from 2020, with an energy of $160\,\mathrm{MeV}$.

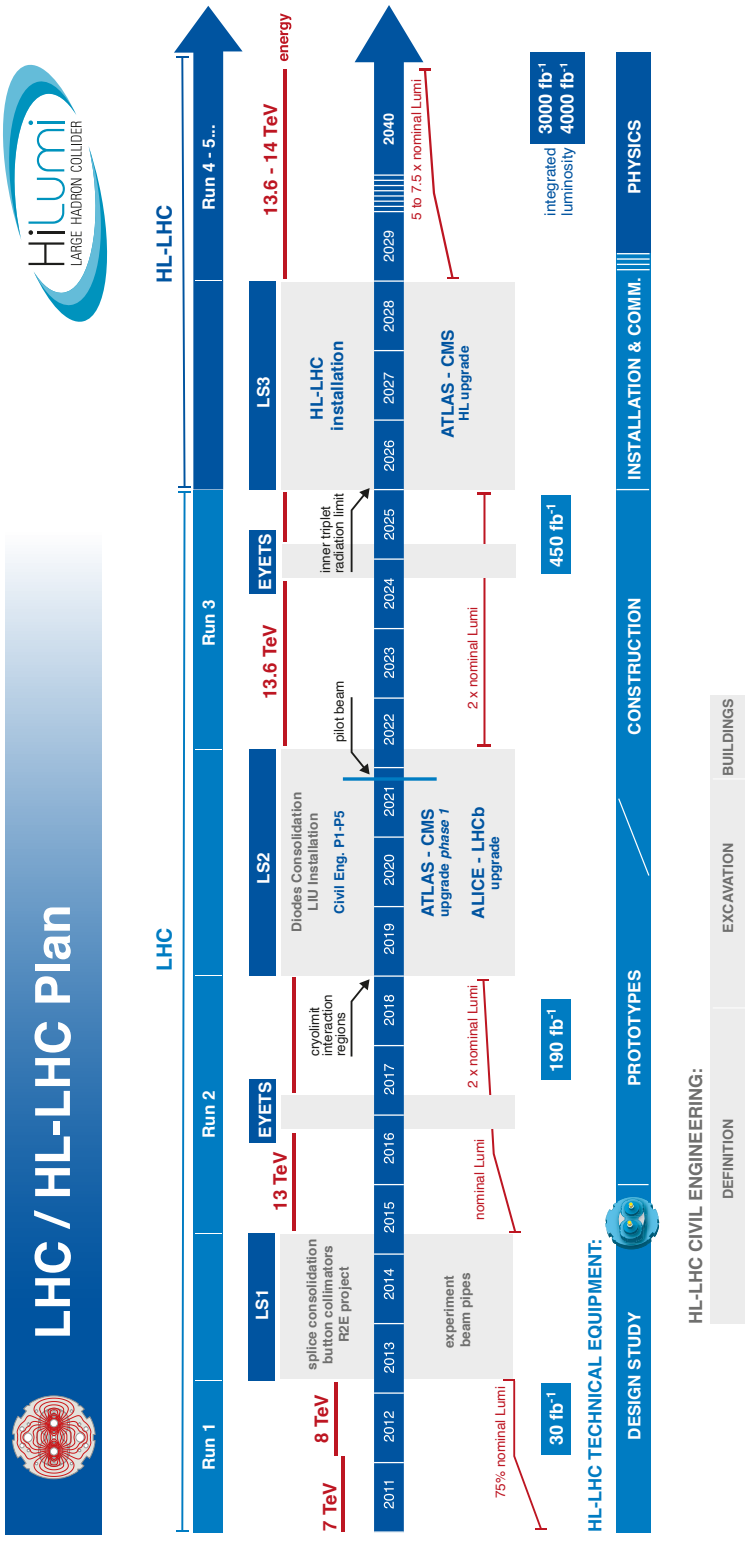

Figure 3.2.: LHC/HL-LHC timeline and plan, with corresponding nominal collision energy and luminosity [131].

3.3. LHCb Detector

The LHCb experiment[129] is a dedicated heavy-flavour physics experiment at the LHC, specifically designed for searches of CP violation and the rare decays of heavy–b and c-hadrons. The physics program has expanded over time, to include electroweak physics, soft-QCD and heavy-ion physics.

The LHCb detector, shown in Fig. 3.3, is designed as a forward single-arm spectrometer covering the pseudorapidity range $2 < \eta < 5$, where:

$$\eta = -\ln\left(\tan\left(\theta/2\right)\right) \ , \tag{3.1}$$

corresponding to the polar angle range $10 < \theta < 250$ mrad and the azimuthal angle range $10 < \phi < 300$ mrad. This configuration is specifically adapted to detect b-quark, which after hadronization, exhibit distinctive kinematic properties, such as significant transverse momentum and a tendency to be produced in forward or backward directions, indicative of a highly non-isotropic production process, as illustrated in Fig. 3.4.

Left panel of Fig. 3.4 shows the simulated polar angle (θ_1,θ_2) distribution of $b\overline{b}$ quark pairs, with the LHCb acceptance highlighted in red. The right side of Fig. 3.4, illustrates the pseudorapidity (η) distribution of $b\overline{b}$ quark pairs, highlighting how the LHCb's sensitivity region, marked in red, complements the broader coverage areas of general-purpose detectors such as ATLAS or CMS, drawn in yellow.

The production of b quarks are dominated by *gluon fusion* and *quark-antiquark* annihilation processes. Within the LHCb detector, the count of $b\overline{b}$ pairs $N_{b\overline{b}}$, is given by:

$$N_{b\overline{b}} = \sigma_{b\overline{b}} \int L\,dt \ , \tag{3.2}$$

where $\sigma_{b\overline{b}}$ is the production cross-section of b quarks and L is the instantaneous luminosity, expressed as:

$$L = \frac{n^2 N_b f}{4\pi\sigma_{xy}} F \ , \tag{3.3}$$

n is the number of particles per bunch, N_b is the number of bunches, f is the frequency of the bunches, σ_{xy} is the transverse beam size, which is also expressed as function of the emittance ϵ and the amplitude function β^* and a relativistic factor γ, $\sigma_{xy} = \epsilon\beta^*/\gamma$, and F is a geometric luminosity reduction factor due to the crossing angle of the beams.

Leveling mechanisms are employed to adjust the transverse beam separation, ensuring a con-

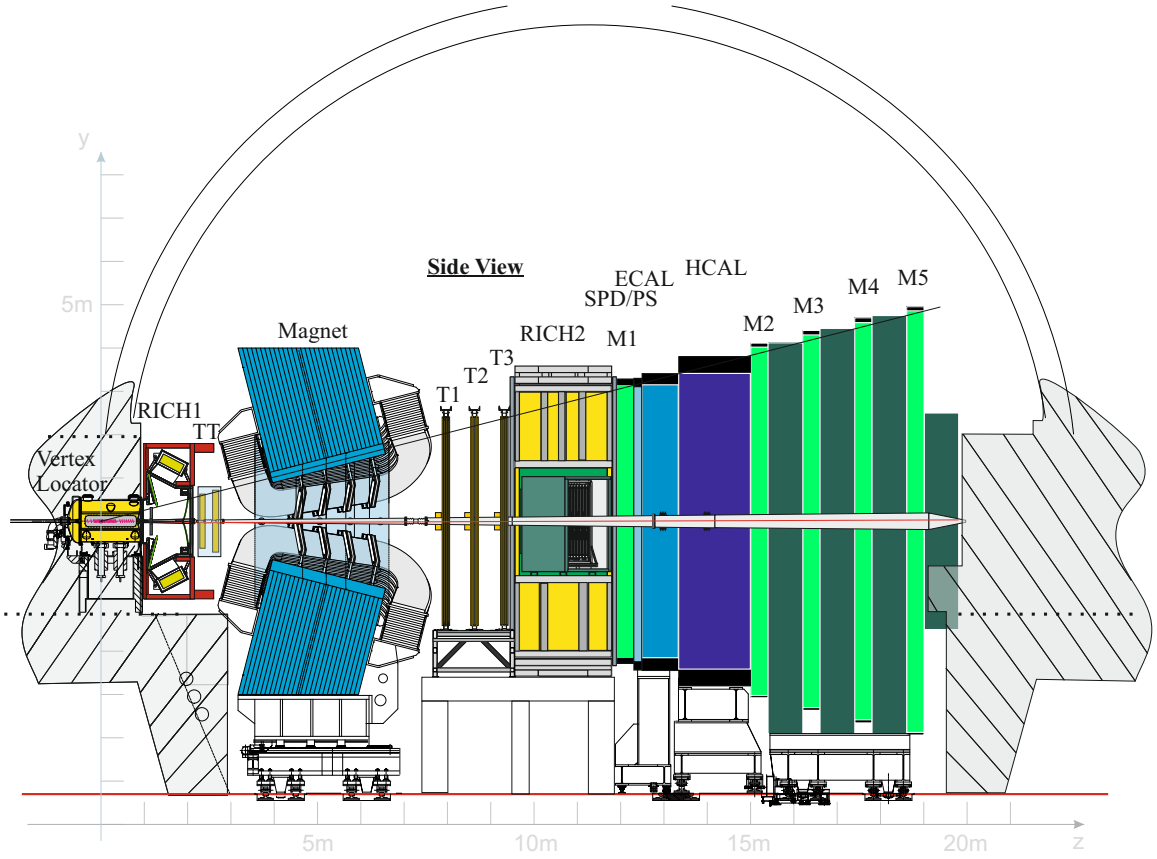

Figure 3.3.: Side view of the LHCb spectrometer [129].

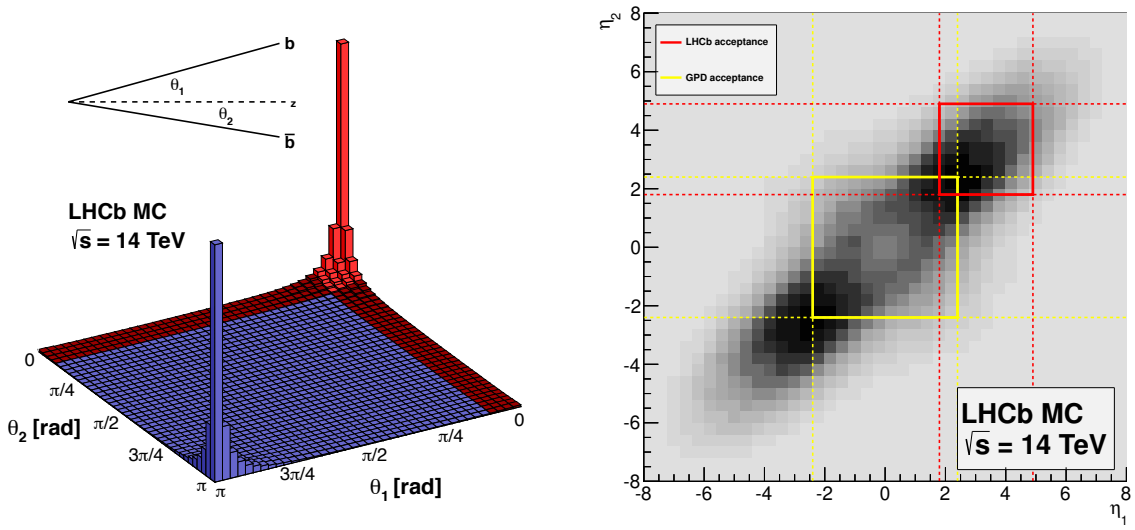

Figure 3.4.: Distribution of simulated $b\bar{b}$ quark pairs by polar angle (left) and pseudorapidity (right) [132].

stant luminosity during data taking. In the LHCb experiment, the luminosity[4] is deliberately reduced to maintain around 1–2 proton-proton collisions per bunch crossing. This reduction is crucial for minimizing pile-up, particularly important aspect for LHCb. By minimizing pile-up, detached vertices are reliably identified, which is essential for accurately reconstructing B meson decays and unambiguously associating them with the correct primary vertex–an aspect that is less critical for the general-purpose detectors at the LHC.

From its start-up in 2010 up until 2018, the LHCb detector, operating at a luminosity of approximately 4×10^{32} $\mathrm{cm}^{-2}\mathrm{s}^{-1}$ during Run 1 and Run 2, collected 9 fb^{-1} of pp collision data, along with specialized datasets from lead-lead and proton-lead collisions.In the context of this thesis, our analysis focuses on data collected during Run 2, covering the period from 2015 to 2018. The integrated luminosity collected by the LHCb detector between 2010–2023 is represented in Fig. 3.5.

In the subsequent sections, the components of the LHCb detector, as configured for the Run 2 data-taking period, are detailed. The tracking system is discussed in Sec. 3.3.1. This is followed by an overview of the particle identification system in Sec. 3.3.2, and then a description of the trigger system in Sec. 5.2. The software and computing system are outlined in Sec. 3.3.4. A

[4]The nominal luminosity in LHCb is lower that the LHC design luminosity, which is $\sim 10^{34}$ $\mathrm{cm}^{-2}\mathrm{s}^{-1}$.

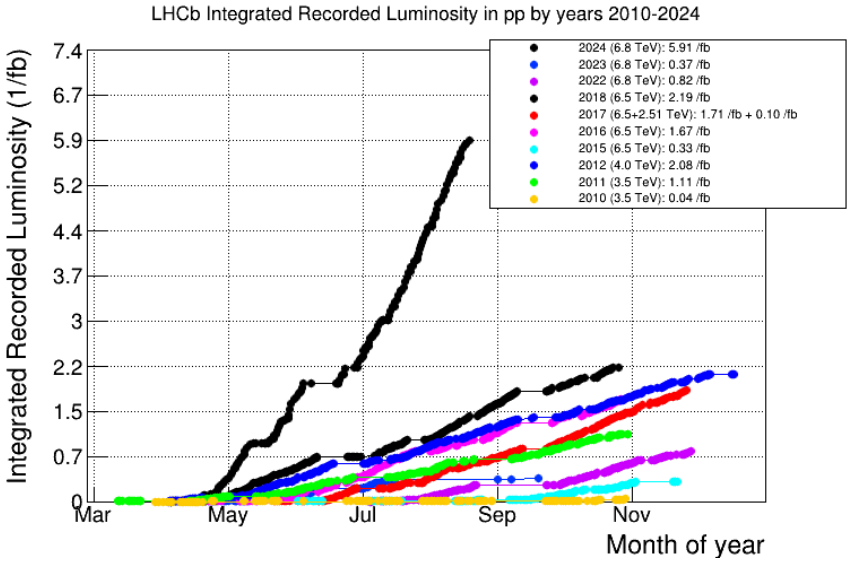

Figure 3.5.: Integrated Luminosity recorded by LHCb during Run 1–Run 3 [133].

Dataset	**Run 1**		**Run 2**			**Run 3**
	2011	2012	2015–2016	2017	2018	2022 – 2025
Integrated Luminosity (fb^{-1})	1.0	2.0	1.925	1.71	2.19	ongoing
Center-of-Mass Energy (TeV)	7	8	13			13.6

Table 3.1.: Integrated luminosity and center of mass energy for the LHCb Run 1, Run 2 and Run 3 data-taking periods.

brief update on the present state and forthcoming upgrade is provided in Sec. 3.4.

3.3.1. The Traking System

The tracking system of the LHCb detector is designed to measure the momentum, the trajectories, the vertices and the charge of charged particles produced in the proton-proton collisions. It is composed of the following sub-detectors: the Vertex Locator (VELO) and the Tracker Turicensis (TT), both situated upstream of the magnet. The T1–T3 stations, composed of the Inner Tracker (IT) and the Outer Tracker (OT), are situated downstream of the magnet.

3.3.1.1. The Vertex Locator

The VELO [134] is located around the interaction point. It is used to measure precisely the position of the Primary Vertex (PV) and the Secondary Vertex (SV). Reliable measurements of the SVs are important, as they are distinctive signature of hadrons containing b and c quarks. The VELO consists of two separable halves, retracted during beam injection and closed during the data taking periods. Each half is made of 21 modules aligned along the beam-line, as shown in Fig. 3.6. Within each module are two types of silicon sensors–R and ϕ. The R (ϕ) sensors measure the radial coordinate (azimuthal angle) of the track. The position of the stations along the beam-line gives a measurement of the z coordinate. In addition, four silicon sensors of type R are placed upstream, aiming to distinguish between single and multiple interactions.

VELO is designed to conform to the LHCb acceptance. By requiring that a particle crosses at least three VELO stations to be reconstructed, the VELO provides an azimuthal angle coverage of 390 mrad for particles originating from the interaction region.

3.3.1.2. The Tracker Turicensis

The TT is located downstream of the VELO. It is used, along with the mangnet and the other tracking stations to measure the momentum and the charge of charged particles. It is composed of 4 rectangular silicon microstrip sensors, arranged in a x-u-v-x configuration. In this arrangement the modules in the x–layers are aligned vertically, whereas those in the u and v layers are respectively inclined by $+5^\circ$ and -5° from the vertical direction as illustrated in Fig. 3.7. Track segments are reconstructed by matching the hits in two sets grouped in (x, u) and (v, x).

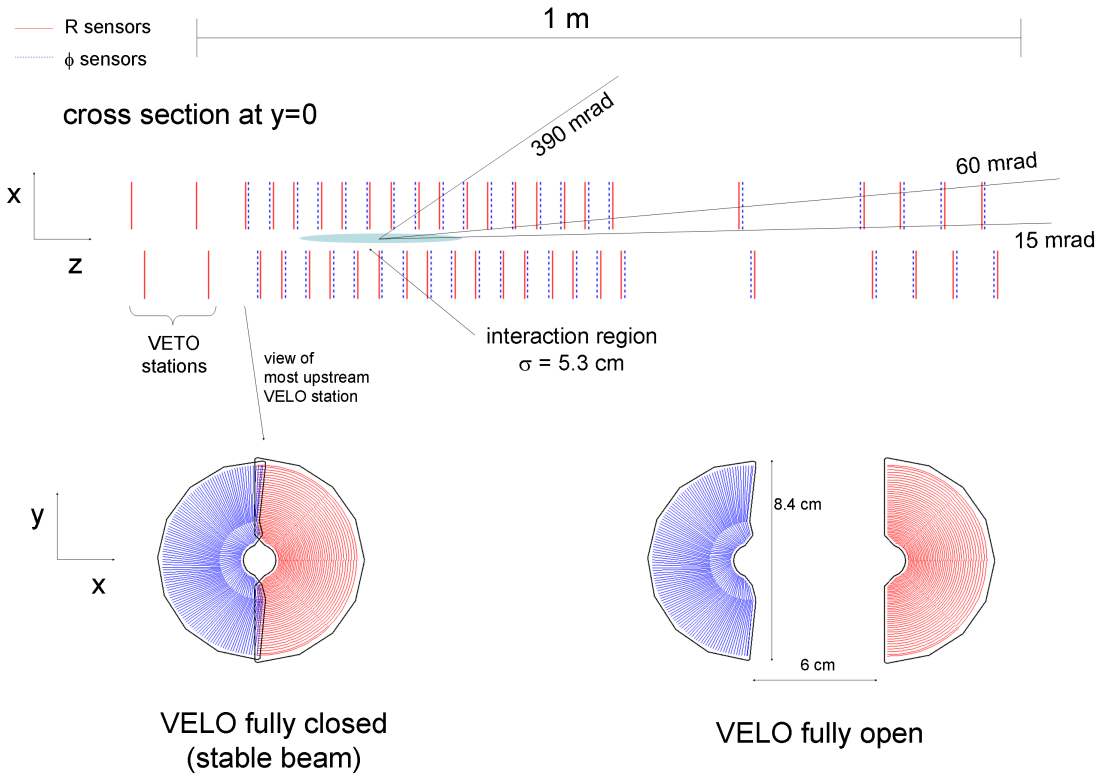

Figure 3.6.: Cross-section view of the VELO sensors in the xz plane (top) in the xy plane (bottom) in its closed and open positions. R (ϕ) sensors are shown with solid red (dashed blue) lines. Two pile-up veto stations are located upstream [129].

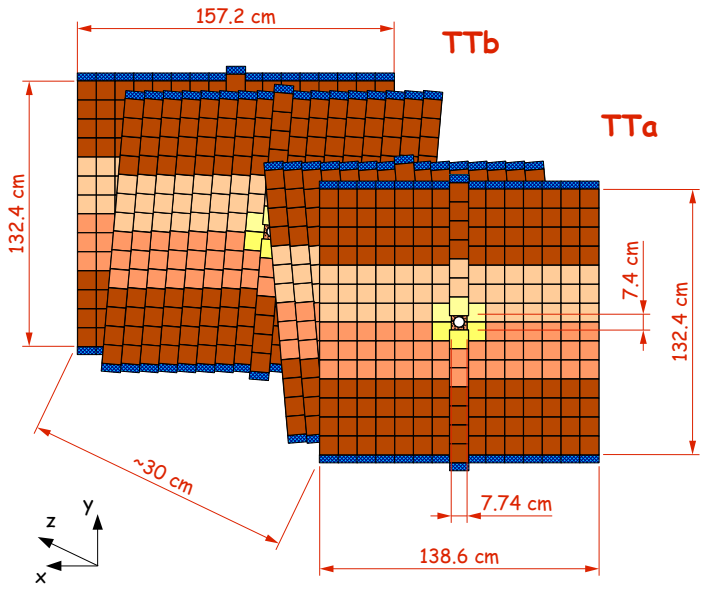

Figure 3.7.: Layout of the TT modules, colors highlight different readout sectors [135].

3.3.1.3. The Magnet

The LHCb magnet is a dipole magnet [136], composed of two saddle-shaped coils, with a bending power of 4 $\mathrm{T.m.}$ it is used to bend the trajectory of the charged particles to measure their momentum. The magnetic field profile is given in Fig. 3.9.

The magnetic field is vertical, its direction is reversed periodically during data taking period, to collect datasets of similar statistics for both polarities, *up* and *down*. It ensures that artifacts due to detector's design and orientation are minimized.

3.3.1.4. The Inner and Outer Tracker

Downstream the magnet, 3 tracking stations, T1-T3 each of which is made of 4 detection layers, arranged in the same x–u–v–x configuration, as the TT as shown in Fig. 3.8. Each layer has an inner and outer region. The IT [137] composed of silicon microstrip sensors, is centered around the beam-pipe, in a region with high particle density (in purple). The outer part of the tracker (OT) [138] is composed of straw tubes (in cyan), when a charged particle passes

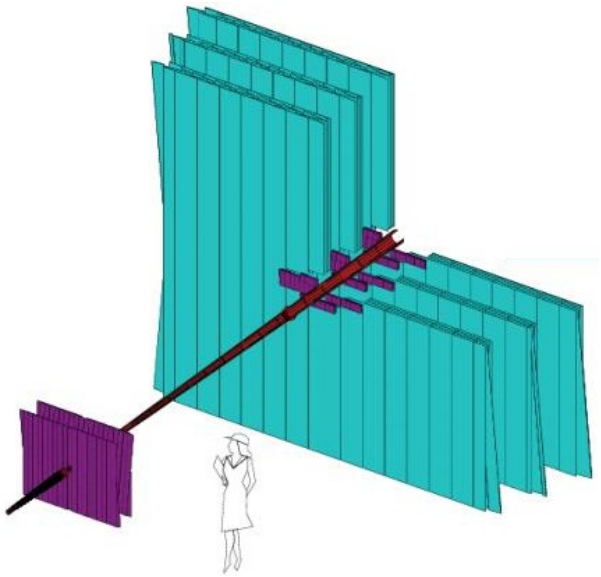

Figure 3.8.: OT straw-tube modules configuration in layers and stations (in cyan) [129].

through, it triggers the *drift-time detector*[5], which is made of a gas mixture of argon, oxygen, carbon dioxide to achieve a spatial resolution of 200 μm, and hit efficiency of 99%. It also provides trigger information.

3.3.1.5. Vertex and Track Reconstructions

The track reconstruction process within the LHCb detector begins in the VELO and the TT, where the influence of the magnetic field is negligible, facilitating the propagation of particles along essentially straight trajectories. The track reconstruction unfolds in two principal steps: pattern recognition and track fitting.

In the initial phase of pattern recognition, interaction points, or "hits", are identified within sub-detector components and assembled into segments to represent the particles' paths. This step enables the identification of potential trajectories from the recorded hits. For the reconstruction of long tracks (item 1), the *forward tracking* algorithm is employed. It starts with hits in the VELO and extrapolates these to the TT, seeking compatible hits. These segments are then extrapolated towards the OT region, where they are associated with compatible hits in these sub-detectors to form a coherent track.

[5]When a charged particle passes through, ionized particles are created in the medium and drift towards an electrode. The drift time is used to track back the position of the original particle's path through the detector.

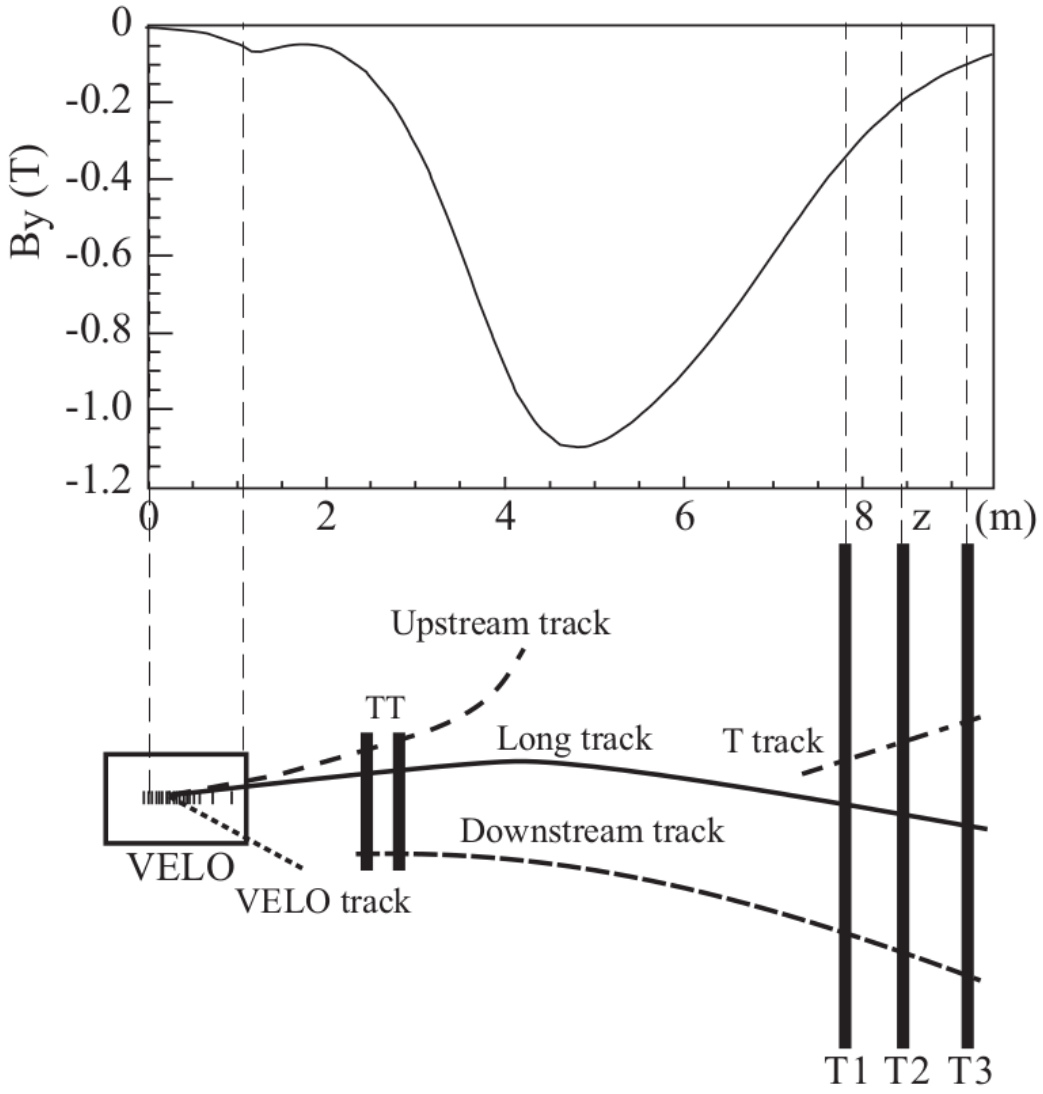

Figure 3.9.: Representation of the different types of tracks and their corresponding sub-detector hits, superposed with the magnetic field distribution [129].

The trajectories are classified as follows:

1. **Long Tracks**: Characterized by hits across all tracking stations, these tracks are indicative of particles with large momentum. They afford high-resolution measurements of momentum, PV, and Impact Parameter (IP) making them essential to physics analyses.
2. **Upstream Tracks**: These tracks, significantly deflected by the magnetic field due to their relative low momentum, register hits in the VELO and the T stations, aiding in the assessment of PID performance by the RICH1 detector.
3. **Downstream Tracks**: Recording hits in the TT and the OT, these tracks are associated with long-lived particles that decay outside the VELO, such as K^0_S and Λ.
4. **T Tracks**: Typically resulting from secondary interactions, these tracks validate the performance of the RICH2 detector.
5. **VELO Tracks**: Crucial for PV reconstruction, these tracks may arise from particles with large polar angles or those flying in backward direction.

The corresponding representation of these tracks is drawn in Fig. 3.9. The determination and refinement of track parameters, such as momentum, charge, PV, IP, polar (θ) and azimuthal (ϕ) angles, along with pseudo-rapidity (η), are achieved through the application of a *Kalman filter* algorithm [139, 140].

The efficiency of hit detection is notably high, with the TT achieving an order of 99%, coupled with a spatial resolution of approximately 50 μm. The VELO has an excellent tracking efficiency and a good resolution for PVs and IPs reconstruction. The tracking efficiency, defined as the fraction of the reconstructed tracks that are matched to a generated particle, is at the level of 98% for the VELO.

The PV resolution depends on the number of tracks `nTracks` used to reconstruct it. The resolution is better for higher `nTracks` as illustrated by Fig. 3.10. In Run 1, PVs were reconstructed using both VELO and long tracks, when in Run 2, the PVs were reconstructed using VELO tracks only. The PV resolution is similarly effective in both runs, in the x and y axis. Particularly, there is a 10% improvement in resolution along the z-axis. In addition, the pull distributions are more compatible with unit width Gaussian, in the three axis. These improvements are due to the absence of magnetic field in the VELO region, leading to simpler track fits.

The IP is defined as the distance of closest approach between a particle trajectory and a given PV which helps to distinguish prompt particles directly produced in the PV from secondary

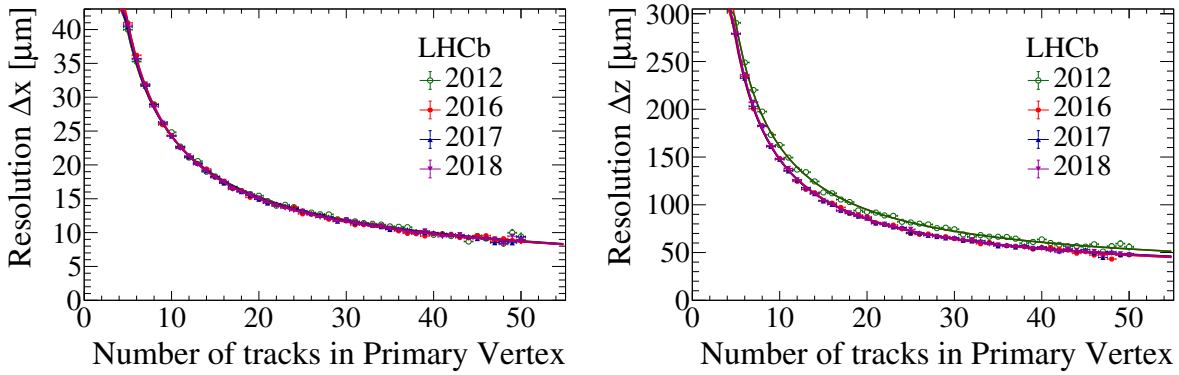

Figure 3.10.: PV resolution in the x–axis (left) and z–axis (right) as a function of the number of tracks used in the vertex fit, comparing offline Run 1 with online and offline Run 2 [141].

particles produced in the decay of long-lived particles. The resolution of IP in x and y-axes, determined using events with only one reconstructed PV, is shown in Fig. 3.11. The resolution of the IP shows linear dependence on the transverse momentum p_T, due to multiple scattering effetcs. For tracks with high p_T, the resolution is typically 12 μm.

3.3.2. Particle Identification

Scintillating Pad Detector (SPD) is an important feature of the LHCb experiment. It aims to distinguish between different particle species, such as pions, kaons, protons, electrons, and muons. The SPD is essential to reduce background sources, and to improve the signal purity, which are crucial for the measurements performed in LHCb. The SPD information is extracted using dedicated sub-detectors, including the Ring Imaging Cherenkov detectors, as detailed in Sec. 3.3.2.1, the calorimeter system described in Sec. 3.3.2.2, and the muon system, outlined in Sec. 3.3.2.3. This SPD information is combined with the tracking information to obtain SPD variables which are used in the physics analysis.

3.3.2.1. RICH Detectors

The Ring Imaging Cherenkov (RICH) detectors [142, 143] are based on the principle of the *Cherenkov effect*, which is the phenomena arising when a charged particle travels a dielectric medium with a speed v faster than the speed of light c in that medium. It results a Cherenkov radiation, which is a cone of light emitted in the direction of the particle. The opening angle of the cone is given by:

$$\theta_c = \arccos\left(\frac{1}{\beta n}\right) , \tag{3.4}$$

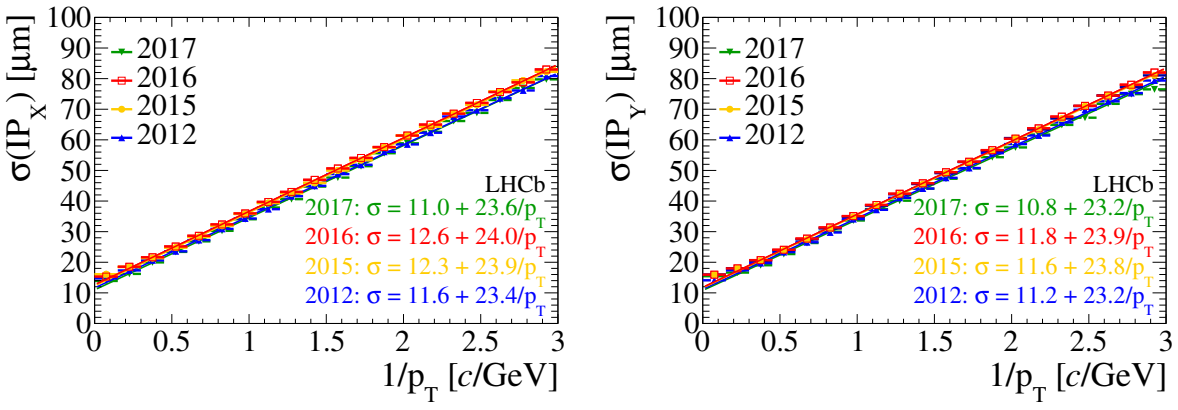

Figure 3.11.: IP resolution in the x–axis (left) and y–axis (right) projections as function of the inverse transverse momentum. Comparison between 2012 and 2015–2017 data [141].

with $\beta = v/c$, where c is the speed of light in vacuum, and n the medium's optical index. Measuring this angle allows the determination of the particle's velocity. After combining with the momentum measured by the tracking system, the mass of the particle –thus, its type– can be distinguished,.

Hybrid Photon Detectors (HPDs) are used to detect Cherenkov photons with wave-lengths in the range of 200–600 nm. The HPDs are located outside of the LHCb acceptance, at the focal plane of the RICH mirrors.

The primary role of the RICH detectors is the identification of charged hadrons ($\pi^{\pm}$, $K^{\pm}$). It also plays a role of charged lepton identification (e, μ) independently of the electromagnetic Calorimeter (Sec. 3.3.2.2) and the muon stations (Sec. 3.3.2.3). There are two RICH detectors (Fig. 3.12) with complementary momentum ranges. RICH1 covers the low momentum region, $1 < p < 60\,\mathrm{GeV/c}$, with an acceptance of ±25 to ±300 mrad in the horizontal plane, and ±25 to ±250 mrad in the vertical plane, suitable for soft particles which tend to have large polar angles. It is situated upstream of the magnet, between the VELO and the tracking system. It uses a aerogel and fluorobutane (C_4F_{10}) as medium.

Fig. 3.13 displays the Cherenkov angle (θ_c) as a function of track momentum for isolated tracks selected from data, specifically in the context of RICH1, which uses C_4F_{10} as the medium. It shows clear distinctions between the Cherenkov radiation bands of pions, kaons, and protons, with even the less sharply defined bands of muons being discernible.

In contrast, RICH2 is sensible to particles with higher momentum, 15 to above 150 GeV/c, which has a smaller polar angle, thus reduced acceptance, 15 to 120 mrad in the horizontal

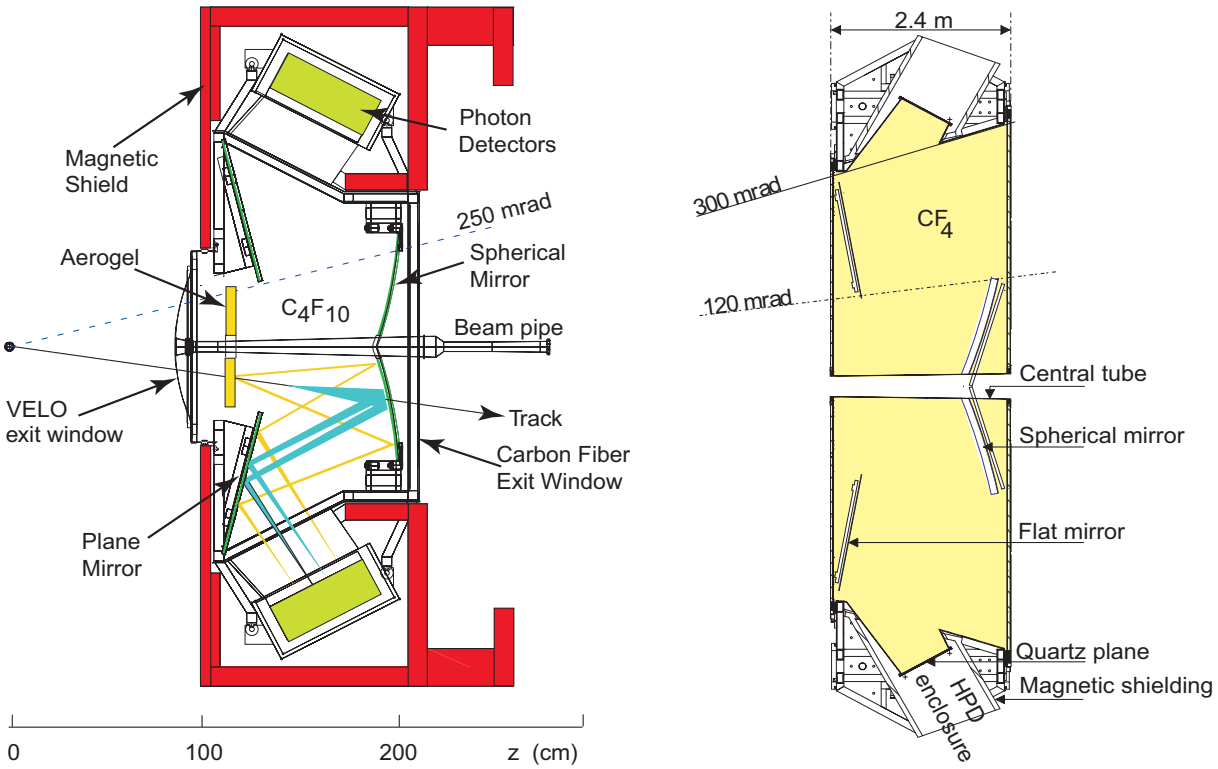

Figure 3.12.: Schematic layout of the RICH1 detector from a side view (left) and the RICH2 detector from a top view (right) [129].

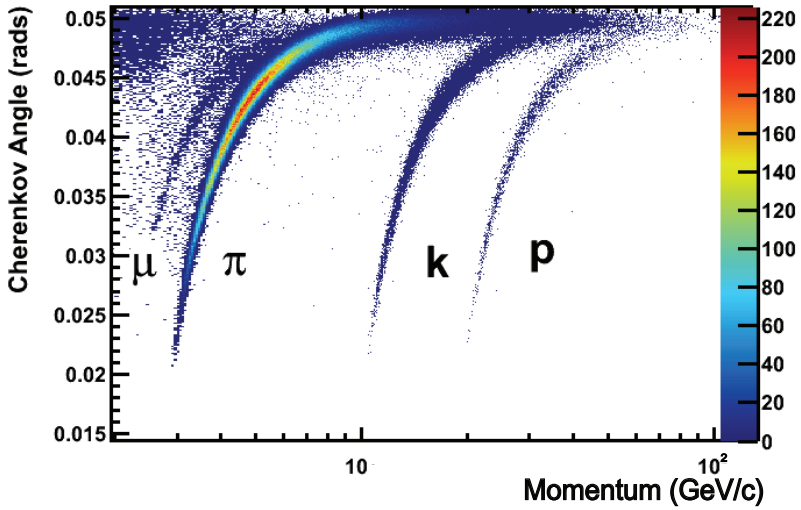

Figure 3.13.: Reconstructed Cherenkov angle as a function of track momentum in the C_4F_{10} medium [144].

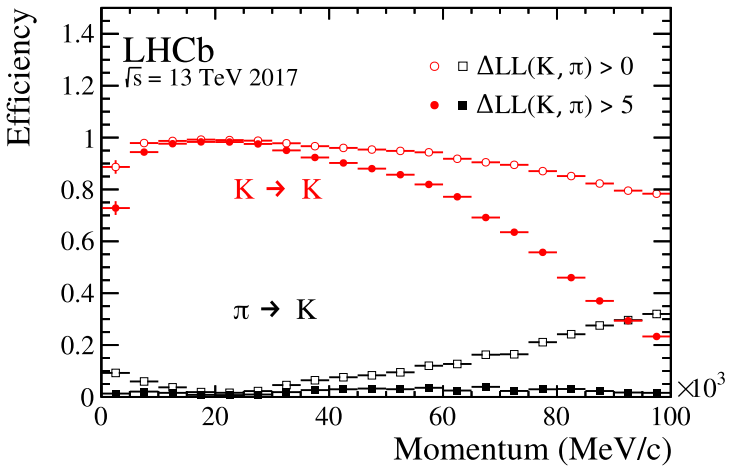

Figure 3.14.: The SPD efficiency (kaon) and the misidentification (pion) rate as function of the track momentum with loose (hollow shape) and tight (solid shape) selections on the DLL variables [136].

plane, and 15 to 80 mrad in the vertical plane. It uses CF_4 as gas radiator and it is located downstream of the magnet, between the tracking system and the first muon station (M1).

In Fig. 3.14, the SPD efficiency and the misidentification rate are shown as a function of track momenta, represented in red and black, respectively. The trade-off between maximizing the signal efficiency with a loose selection (in hollow shapes) and achieving high signal purity with a tight selection (in solid shapes) is illustrated.

3.3.2.2. The Calorimeter System

The calorimeter system [145, 146] is used to measure the energy of the EM particles, and to identify the electrons, and neutral hadrons, such as pions and photons. The calorimeter system consists of the SPD, the Preshower (PS), the Electromagnetic Calorimeter (ECAL) and the Hadronic Calorimeter (HCAL).

The lateral segmentation of the calorimeter is shown in Fig. 3.15. As the distance to the beam-line decreases, the number of channels on the calorimeter surface increases in response to the hit density, as highlighted by various colors in the figure. The SPD identifies charged particles, and allows electrons to be separated from photons. The PS detector identifies electromagnetic particles. Furthermore, the number of hits in the SPD (`nSPDHits`) provides an estimate of track multiplicity in collision, used at the very early trigger stage.

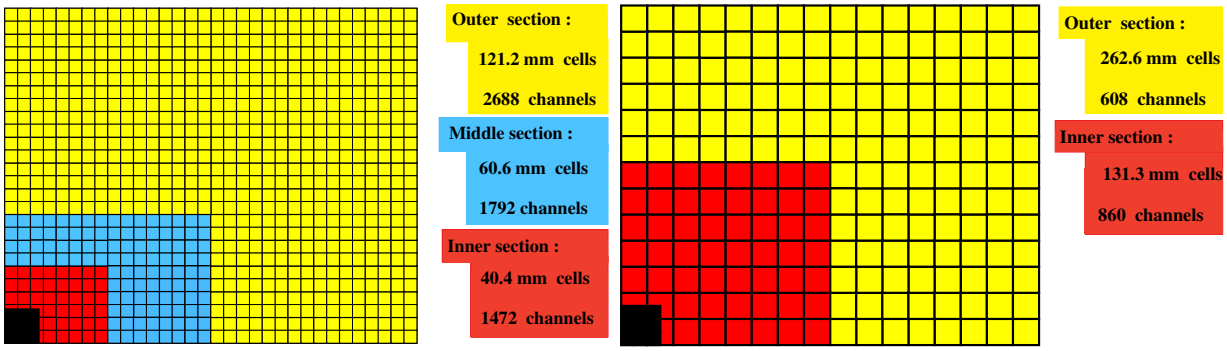

Figure 3.15.: Quarter lateral segmentation of the ECAL/PS/SPD (left) and HCAL (right) [129].

ECAL and HCAL are structured in an alternating pattern of lead (ECAL) and scintillator layers, with 25 radiation lengths, and iron (HCAL) and scintillator layers, with 5 interaction lengths, due to space limitation. ECAL measures the energy and postion of the electrons and photons, thus enabling the identification and reconstruction of neutral pions ($\pi^0 \longrightarrow \gamma\gamma$). While HCAL measures the energy of the neutral hadrons.

3.3.2.3. The Muon System

The muon system [147] is used to identify the muons, and to measure their momentum at the L0 trigger level. It consists of five stations, M1, which is located upstream of the calorimeter system, and M2 to M5 located downstream of the calorimeter system. The M2–M5 stations are interleaved with the 80 cm thick iron layers.

As the hits density decreases with the distance from the interaction point, the muon system is divided into four quadrants, in the x–y plane, with size ratio of $1 : 2 : 4 : 8$, as shown in Fig. 3.17, in such a way that the occupancy in each quadrant is approximately the same.

The M1 station inner region uses a triple–Gas Electron Multiplier detector, with a cathode pad plane, and anode wires. The M1 outer region and the M2–M5 stations are multiwire proportional chambers, with cathode strips, and anode wires.

Muon identification begins with trajectory reconstruction, which relies on the tracking system and the detection of hits in the muon stations. The count of these hits (stored on `isMuon` variable) leads to muons identification. An alternative for muon identification is by using the track discriminating variable $\mathrm{DLL}_{\mu\pi}$, obtained under the muon and non-muon track hypothesis. For high momentum, both identification variables are compatible with each other. In the low momentum region, `isMuon` has a better efficiency, while $\mathrm{DLL}_{\mu\pi}$ has a better purity.

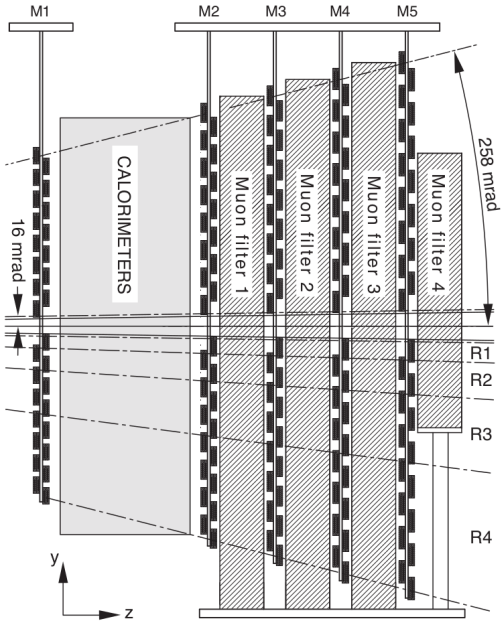

Figure 3.16.: Side view of the Muon system [129].

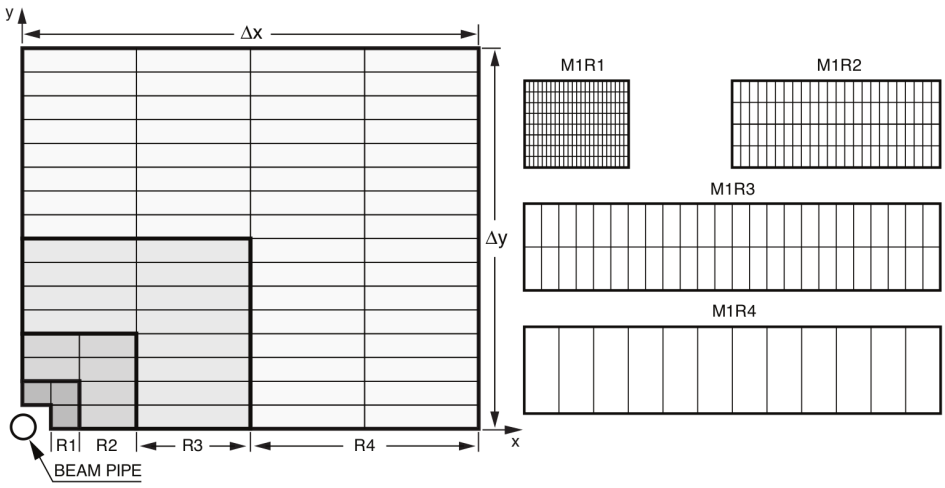

Figure 3.17.: Left: Muon quadrant. Right: Pads division in the four regions of the M1 station [129].

3.3.2.4. Combining Particle Identification Information

The SPD information from the RICH detectors, the calorimeter system and the muon system are combined to obtain SPD variables. These variable have better performance, and are the one used in physics analyses, to suppress the background, and to improve the signal purity. It is possible to sum over the DLL variables from each sub-detector,

$$\Delta \log L^{\text{comb.}} = \sum_i \Delta \log L^i \,, \tag{3.5}$$

or to use the multivariate analysis techniques, such as the Boosted Decision Trees (BDT), which takes into account the correlation between the SPD variables.

$$\text{ProbNN}(x) \qquad \text{with} \qquad x \in \{K, \pi, p, e, \mu\} \,. \tag{3.6}$$

The performances of such variables are measured using calibration samples from data.

The SPD efficiency is obtained using the `PIDCalib` package (LHCb software [148]), which summarizes the track SPD efficiency in control samples, based on parameters such as track transverse momentum, track pseudorapidity, or global event multiplicity (estimated, for example, by `nTracks`).

Electron identification is approximately 90% efficient with a 5% probability of misidentification as a hadron ($e \rightarrow h$). Kaon identification is slightly higher, with about a 95% efficiency and a similar 5% probability of being misidentified as a pion ($\pi \rightarrow K$). The highest efficiency is observed in muon identification, which stands at around 97%, though with a slightly variable misidentification probability ranging from 1% to 3% for pions being misidentified as muons ($\pi \rightarrow \mu$).

3.3.3. The Trigger System

The trigger system [141, 149] of the LHCb detector is designed to lower the event rate from the pp collisions, from an initial bunch crossing rate of approximately 40 MHz, as indicated in Fig. 3.18, to an offline manageable rate of 12.5 kHz, by selecting the events that are interesting for the physics analysis.

The trigger system is composed of two levels: a hardware-based trigger (L0) and the software-driven trigger (HLT). A schematic decision structure of the trigger system is shown in Fig. 3.18.

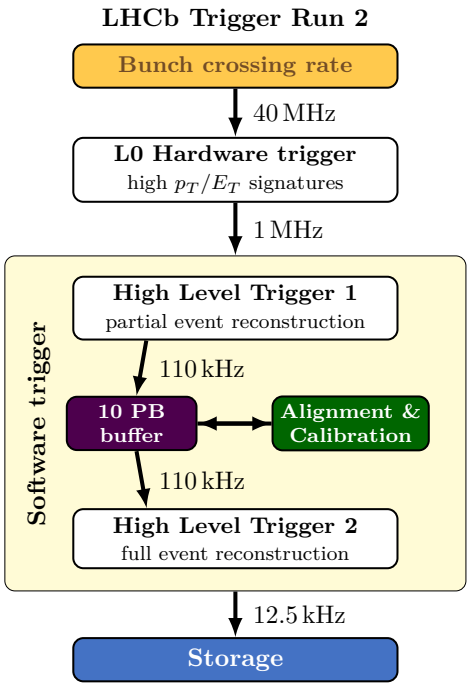

Figure 3.18.: Trigger configuration for Run 2 [141].

3.3.3.1. The Hardware Trigger

The hardware level trigger (L0) utilizes data from the calorimeters and muon systems to analyze the transverse energy (E_T) and transverse momentum (p_T) of final state particles, thereby reducing the event rate to 1 MHz, a level manageable for full detector readouts.

The L0–Calorimeter system uses data from four sub-detectors: SPD, PS, ECAL, and HCAL.These detectors differentiate between photon, electron, and hadron showers.

The system calculates the transverse energy (E_T) of clusters made of 2×2 cells within the same zone. The E_T for a cluster is:

$$E_T = \sum_{i=1}^{4} E_i \sin(\theta_i) \,, \tag{3.7}$$

where E_i is the energy in cell i, and θ_i is the angle between the z-axis and a neutral particle's path.

Three candidate types are identified:

- Hadron Candidate (`L0Hadron`): Highest E_T HCAL cluster. If there is a corresponding highest E_T ECAL cluster, the E_T of the hadron candidate is the sum of both clusters.
- Photon Candidate (`L0Photon`): Highest E_T ECAL cluster with 1 or 2 PS cells hit in front, and no SPD cell hit. In the inner ECAL zone, clusters with 3 or 4 PS cells hit are also accepted as photons. The E_T is from the ECAL alone.
- Electron Candidate (`L0Electron`): Same as the photon candidate, but with at least one SPD cell hit in front of the PS cells.

Each quadrant of the muon detector connects to a dedicated `L0` muon processor. There is no data exchange between quadrants, so muons crossing quadrant boundaries cannot be reconstructed by the trigger. Each processor identifies the two muon tracks with the highest and second-highest transverse momentum (p_T) within its quadrant.

Processors search for hits forming straight lines through the five muon stations, pointing towards the interaction point in the y–z plane. In the x–z plane, the search is limited to muons with $p_T \geqslant 0.5\,\mathrm{GeV/c}$. The track positions in the first two stations determine the p_T with about 25% resolution.

The muon trigger sets thresholds based on:

- `L0Muon` line: The highest p_T muons among the eight candidates.
- `L0DiMuon` line: The product of the highest and second-highest p_T muons.

The decision of retaining or rejecting an event is made by comparing these inputs to the fixed thresholds. Events with *at least* one candidate above the threshold are retained by the `L0` trigger. The `L0` cuts used for the analysis are listed in Tab. 5.1.

To ensure faster event reconstruction and manage high occupancy, SPD cuts on the maximum number of SPD hits (`nSPDHits`) are applied. These cuts maintain signal efficiency similar to when only E_T and p_T requirements are used. The `L0` output rate is 1 MHz.

3.3.3.2. The Software Trigger

The reduced bandwidth from the `L0` trigger is sent from Front-End Boards (FEBs) to the Event Filter Farm (EFF), consisting in thousands of multiprocessor PCs, which filter the data further. The High Level Trigger (HLT) is a program, which runs on the EFF [149]. It is divided in two disctinct parts, `HLT1` and `HLT2`.

In HLT1, long tracks are reconstructed using the forward tracking stations (IT and OT) and the VELO. Momentum is estimated from track fits, PVs are reconstructed using VELO tracks, and the IP of long tracks is computed. HLT1 decisions are based on track fit quality, IP, and p_T with predefined thresholds, reducing the rate to 43 kHz.

In HLT2, the full event reconstruction is performed, and the decision is made based on the reconstructed particles, such as pions, kaons, protons, electrons, and muons, and the reconstructed vertices PV, SV and IP. The decision–making process in HLT2 is based on thresholds and requirements on variables such as p_T, IP, DLL variables and χ^2 of vertex fits.

Both stages use *trigger lines*, which are sets of selection and reconstruction algorithms. An event is accepted at a given stage if it passes at least one of its trigger lines. In Run 2 there are around 20 HLT1 and 500 HLT2 trigger lines. The main ones covering the physics goal of the analysis are *topological trigger lines*, which base decisions on properties of combinations of 2, 3 or 4 tracks, called Topo–Tracks. Two Topo-Tracks are combined into a 2-body object if their Distance of Closest Approach (DOCA) is less than 0.2 mm. A 3-body (or 4-body) object is formed by adding another Topo-Track to the 2-body (or 3-body) object, ensuring the same DOCA requirement. This sequence improves the efficiency of topological trigger lines for inclusive $B \to DX$ decays, where X is a particle that is not reconstructed. The trigger allows some final state particles to be omitted when forming the trigger candidate.

Hlt1TrackMVA is developed to trigger on individual tracks. It operates by applying cuts across the two-dimensional plane that correlates PV displacement with transverse momentum. On the other hand, Hlt1TwoTrackMVA is designed to identify events based on pairs of tracks originating from a common displaced vertex. It utilizes reconstructed vertex and track data as inputs to a MultiVariate Analysis (MVA) classifier to select candidates.

In addition, exclusive lines requiring the reconstruction of the full decay chain are implemented to select specific final states.

The trigger requirements used for the study are listed in Tab. 5.2.

A combination of L0 configuration along with software trigger lines is stored in a unique identifier, known as the Trigger Configuration Key (TCK). The different TCK configurations and the corresponding cuts, are given in Fig. B.9.

3.3.4. LHCb Softwares

In the LHCb experiment, simulation is essential for physics analysis, serving as the baseline for comparing and interpreting real experimental data. They are performed within the Gauss soft-

ware framework [150]. This simulation framework aims to imitate particles' interactions from pp collisions (modeled using Pythia [151]) to the decay of particles (simulated via EvtGen) and the subsequent detector response (through Geant4 [152]). Following simulation, Boole transforms the hits generated by Gauss into digital signals. These signals are then processed to emulate the readout electronics of the detector, incorporating key parameters such as resolution and efficiency to mirror the real detector's performance accurately.

To enhance agreement between the simulated samples and observed data, several adjustments are systematically applied to the simulation, at further stages of the selection. These adjustments, detailed in Sec. 4.4.3, calibrate the distribution of parameters and variables to ensure an accurate alignment with the data collected by the LHCb detector.

From hereafter, simualtion and data processing are identical. The event reconstruction is accomplished by Brunel followed by the preselection with DaVinci, which is a software tool for offline data analysis, it performs track reconstruction, vertex fitting, particle identification, and event selection. It is underlying on Gaudi software framework, which is used to manage the data flow and the execution of the algorithms. Additional informations about the events are then computed with custom algorithms and some cuts are applied. Stripping lines are then used to further reduce the data size, and to select the events that are interesting for the given analysis, the data is saved in DST or mDST format. The preselection is the first step specific to each analysis. The preselection is the first step specific to each analysis. This results in 'ntuples' in the `root` format, ready for a specific analysis. Restripping compaign is used to update the stripping lines, and to reprocess the data with the updated stripping lines.

A schematic of the data flow in the LHCb software is shown in Fig. 3.19.

3.4. The LHCb Upgrades

Over Run 1 and Run 2 data taking periods, the LHCb detector was operating at luminosity below the nominal design luminosity of the LHC [141, 153]. The number of visible interactions per bunch crossing, known as pile-up, was up to 2.5, while the nominal design value was 0.4. At higher luminosity, large pile-up conditions would increase the combinatorial background and lower track reconstruction efficiency.

During Long Shut down 2, the LHCb detector went through many upgrades of its components, in order to improve the event rate, the data quality, and manage the pile-up conditions expected for the Run 3. Read out of the full detector is done at 40 MHz, and then events are filtered by the trigger system, which is fully software based.

The upgraded LHCb detector for Run 3 [154], as shown in Fig. 3.20, has been enhanced to

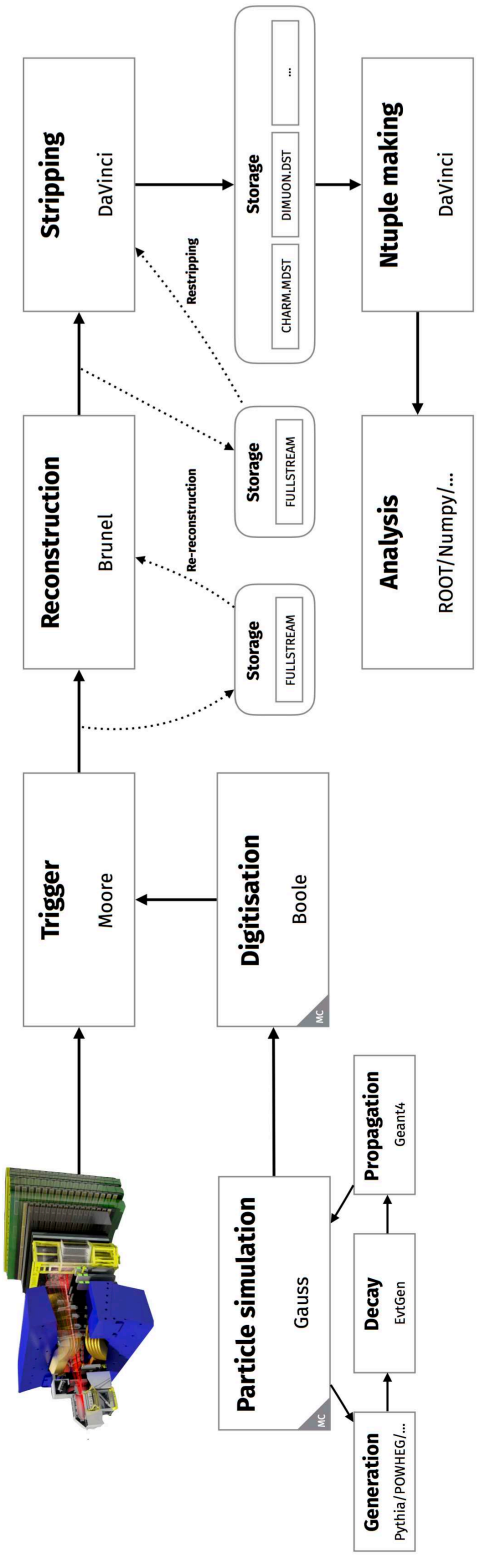

Figure 3.19.: Data flow in the LHCb software.

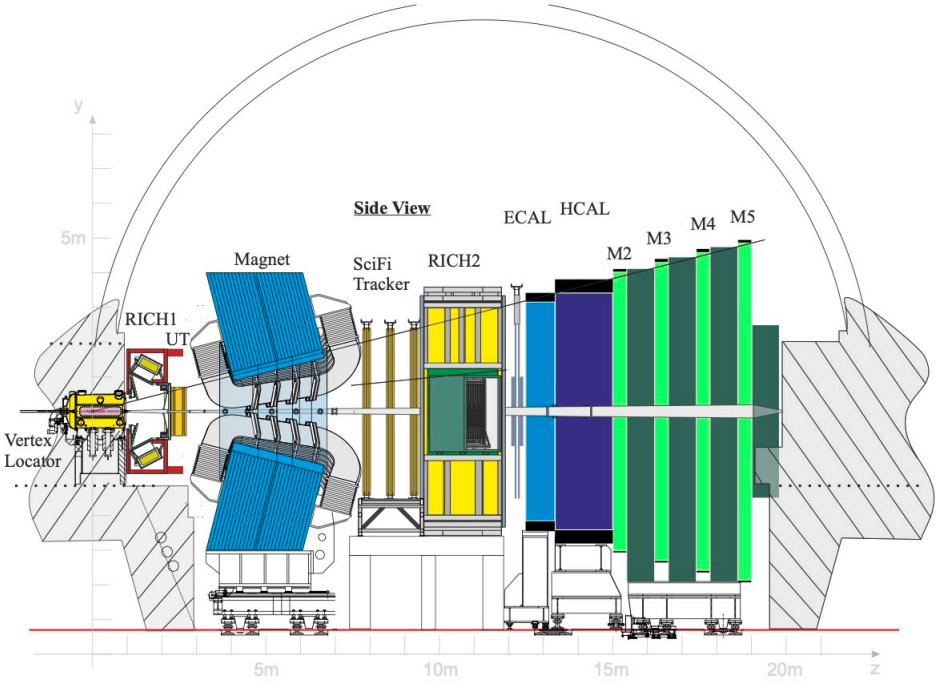

Figure 3.20.: Side view of the upgraded LHCb detector for Run 3 [154].

allow operation at higher instantaneous luminosities with more challenging pile-up conditions expected during Run 3. The instantaneous luminosity is anticipated to be five times greater than in previous running periods.

The real-time luminosity was measured using the L0 hardware trigger during Run 1 and Run 2. A dedicated photomultiplier detector, PLUME, which stands for Probe for Luminosity Measurement, has been installed.

The LHCb detector is expected to collect data corresponding to an integrated luminosity of $50\,\text{fb}^{-1}$ after the end of the Run 4 data taking period.

The data flow for the LHCb upgrade is shown in Fig. 3.21. The data collected by the detector is processed in real-time by the software-based Real-Time Analysis (RTA) system, which selects events of interest for further analysis. Designed to handle the high data rates expected during Run 3, the RTA system can process up to 40 MHz and perform complex event selection algorithms, such as events with multiple leptons or with high transverse momentum.

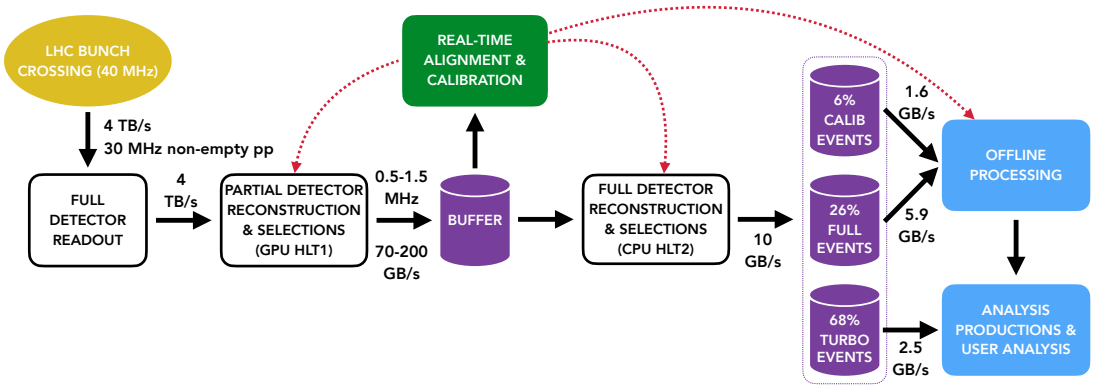

Figure 3.21.: LHCb upgrade dataflow, on the real-time analysis for Run 3 [155].

Chapter 4

Methodological Framework for Hadronic R(D*) Analysis

In this chapter, the methodology employed for the measurement of $\mathbf{R}(D^*)$, is outlined. The organization is as follows: Sec. 4.1 defines the strategy for measuring $\mathbf{R}(D^*)$ using three-prong tau decays. Sec. 4.2 describes the techniques for reconstructing signal and background decay kinematics, while Sec. 4.3 provides an overview of the analysis workflow. Sec. 4.4 discusses the datasets used and Sec. 4.4.3 the corrections applied to the Monte-Carlo (MC) samples. Unless specified otherwise, all presented plots use the 2018 dataset sample, whether data or MC. Finally, Sec. 4.5 highlights the contributions I made to the analysis.

4.1. Strategy for the Hadronic τ^+ Decay Analysis

The current study aims to measure $\mathbf{R}(D^*)$, the ratio of branching fractions of the semileptonic decays of the B^0 meson, defined as:

$$\mathbf{R}(D^*) \equiv \frac{\mathrm{Br}(B^0 \to D^{*-}\tau^+\nu_\tau)}{\mathrm{Br}(B^0 \to D^{*-}\mu^+\nu_\mu)} \,. \tag{4.1}$$

This observable provides a test of the LFU hypothesis in this decay, as discussed in Sec. 2.1.3.

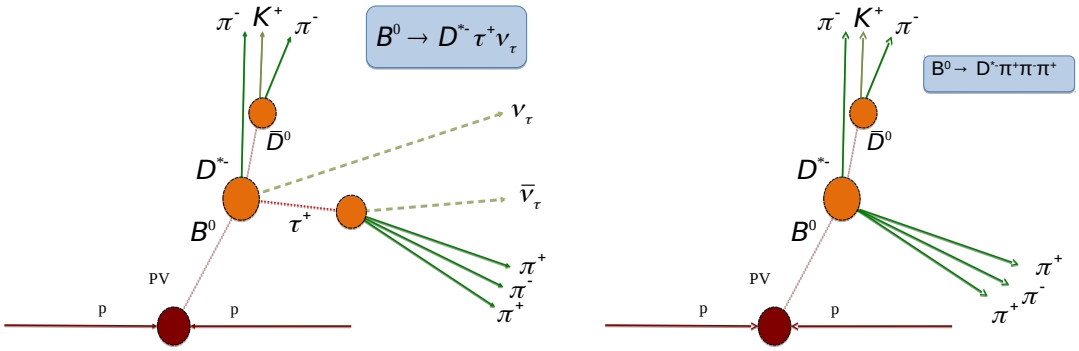

Figure 4.1.: Schematic view of the signal decay mode ($B^0 \to D^{*-}\tau^+\nu_\tau$) on the left, and the normalization mode ($B^0 \to D^{*-}3\pi$) on the right.

In the signal mode, $B^0 \to D^{*-}\tau^+\nu_\tau$, the D^{*-} is reconstructed into $\bar{D}^0$ and π^-. The branching fraction of which is[1]:

$$\mathrm{Br}(D^{*-} \to \bar{D}^0\pi^-) = 67.7 \pm 0.5\% \,, \tag{4.2}$$

and a $\bar{D}^0$, K^+ and π^- decay mode, with branching fraction:

$$\mathrm{Br}(\bar{D}^0 \to K^+\pi^-) = 3.950 \pm 0.031\% \,. \tag{4.3}$$

The $\mathbf{R}(D^*)$ measurements performed by the *hadronic* $\tau^+ \to 3\pi^\pm(\pi^0)\bar{\nu}_\tau$ decay, with branching fraction:

$$\mathrm{Br}(\tau^+ \to 3\pi^\pm(\pi^0)\bar{\nu}_\tau) = 13.5\% \,. \tag{4.4}$$

To measure the $\mathbf{R}(D^*)$ ratio, the normalization mode $B^0 \to D^{*-}3\pi$, which serves as an "intermediate step" is introduced. By taking the ratio of the signal to the normalization mode, most systematic effects (detector and reconstruction) are effectively canceled out. The normalization mode shares the same visible final states as the *signal mode*, but without invisible neutrinos, allowing for a full reconstruction of the B^0 mass peak. The topology of the signal and normalization modes are illustrated in Fig. 4.1.

The $\mathbf{R}(D^*)$ ratio reads as follows:

$$\mathbf{R}(D^*) = \frac{\mathrm{Br}(B^0 \to D^{*-}\tau^+\nu_\tau)}{\mathrm{Br}(B^0 \to D^{*-}\mu^+\nu_\mu)} = \frac{\mathrm{Br}(B^0 \to D^{*-}\tau^+\nu_\tau)}{\mathrm{Br}(B^0 \to D^{*-}3\pi^\pm)} \cdot \frac{\mathrm{Br}(B^0 \to D^{*-}3\pi^\pm)}{\mathrm{Br}(B^0 \to D^{*-}\mu^+\nu_\mu)} \tag{4.5}$$

[1]The common D^{*-} branching fractions are reported in Tab. A.1 (*cf.* [7]).

The observed ratio, referred to as $\mathcal{K}(D^{*-})$, is defined as:

$$\mathcal{K}(D^{*-}) \equiv \frac{\mathrm{Br}\left(B^0 \to D^{*-}\tau^+\nu_\tau\right)}{\mathrm{Br}\left(B^0 \to D^{*-}3\pi^\pm\right)} \,, \tag{4.6}$$

it can be expressed in terms of signal and normalization yields, efficiencies and τ^+ decay branching fractions, as:

$$\mathcal{K}(D^{*-}) = \frac{N_{\mathrm{sig}}}{N_{\mathrm{norm}}} \cdot \frac{\varepsilon_{\mathrm{norm}}}{\varepsilon_{\mathrm{sig}}} \cdot \frac{1}{\mathrm{Br}\left(\tau^+ \to 3\pi^\pm\overline{\nu}_\tau\right) + \mathrm{Br}\left(\tau^+ \to 3\pi^\pm\pi^0\overline{\nu}_\tau\right)} \,. \tag{4.7}$$

The yields are obtained from the fit to data, as follow:

- The signal yield, denoted by N_{sig}, is derived using an extended binned maximum-likelihood fit across three dimensions (*cf.* Sec. 7.1):
  - The squared momentum transfer to leptons with 8 bins:

$$q^2 \equiv (p_B - p_{D^*})^2 \,; \tag{4.8}$$

  - The τ^+ lifetime, t_τ, with 8 bins;
  - The Anti-D_s^+ Boosted Decision Tree (BDT) output (*cf.* Sec. 5.5.4), with 6 bins.
- The normalization yield, $N_{\mathtt{norm}}$, is estimated from an unbinned maximum-likelihood fit to the $D^*3\pi^\pm$ mass distribution (*cf.* Sec. 7.2).
- The efficiencies $\varepsilon_{\mathtt{sig}}$ and $\varepsilon_{\mathtt{norm}}$ are obtained from simulation (*cf.* Sec. 5.7). Specifically, the signal efficiency is obtained from the weighted average of the two τ^+ decay modes– $\tau^+ \to 3\pi^\pm\overline{\nu}_\tau$ and $\tau^+ \to 3\pi^\pm\pi^0\overline{\nu}_\tau$–according to their branching fractions.

Finally, $\mathbf{R}(D^*)$ is obtained using the known branching fraction of the normalization mode, measured by LHCb [4], BaBar [5], and Belle [6]. The average value [7] is given by:

$$\mathrm{Br}(B^0 \to D^{*-}3\pi^\pm) = (7.21 \pm 0.28) \times 10^{-3} \,, \tag{4.9}$$

and the branching fraction of the $\mathbf{R}(D^*)$ denominator, as measured in [8]:

$$\mathrm{Br}(B^0 \to D^{*-}\mu^+\nu_\mu) = (5.06 \pm 0.02 \pm 0.12)\% \,. \tag{4.10}$$

The primary background sources for the signal mode $B^0 \to D^{*-}\tau^+\nu_\tau$ and $\tau^+ \to 3\pi\overline{\nu}_\tau$ are:

- **Prompt backgrounds**: $B^0 \to D^*3\pi X$, where the 3π system comes directly from the B^0 decay;

- **Double-charm backgrounds**: $B^0 \to D^{*-}DX$, where $D \to 3\pi^{\pm}X$;
- **Feed-down** from excited D^{*-} mesons, denoted by D^{**};
- **Combinatorics** Involving particles from random combinations of reconstructed particles in a pp collision event mistakenly assembled into a single signal candidate.

In contrast, the background associated with the normalization mode is predominantly combinatorial and significantly smaller.

4.2. Reconstruction of Decay Kinematics

In the signal decay the two neutrinos are not reconstructed. However, thanks to precisely measured decay vertices of the $\overline{D}^0$, $3\pi^{\pm}$ system and B^0, and exploiting some vectorial algebra, it is possible to mitigate that shortcoming. Also, similar techniques are used in reconstructing backgrounds with missing neutral particles.

The following sections describe the reconstruction techniques in the signal and $B \to D^{*-}D_s^+(X)$, with $D_s^+ \to 3\pi N$ hypotheses (where N denotes a system of unreconstructed neutral particles). These methods were described in the $\mathbf{R}(D^*)$ analysis using Run 1 dataset [1, 19] and are summarized in this section.

The resulting momenta are exploited by the MVA described in Sec. 5.5.4, used to discriminate signal from $B \to D^*D_s^+X$ backgrounds. The variables are also used to derive the q^2 and decay time of the τ^+-candidate, which are used in the signal yield fit (*cf.* Sec. 7.1).

q^2 and τ^+ lifetime resolutions are shown in Fig. A.1.

4.2.1. Signal Hypothesis

Despite the two missing neutrinos, the measured τ^+ vertex and the approximate B^0 vertex allow for the reconstruction of their flight directions (where the B^0 vertex is a line from the PV to the B^0 decay vertex; the τ^+ one is a line between the B^0 and τ^+ decay vertices). Using their known masses allows to derive the magnitude of the momenta up to 2-fold ambiguities in the laboratory frame, in units where $c = 1$.

The decay of a mother particle, denoted as m, is characterized by its mass m_m, momentum $\vec{p}_m$, and energy E_m. The mother particle decays into a system of visible daughter particles, labeled d, and an invisible neutrino u_ν. The daughter system has a mass m_d, momentum $\vec{p}_d$, and energy E_d. In cases where multiple visible daughters are produced, the total momentum and

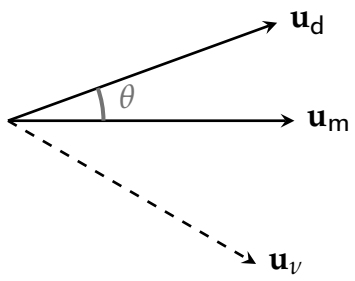

Figure 4.2.: Illustration of the angle between the mother particle m and the daughter system d.

energy of the system are calculated as the sums of the momenta and energies of the individual daughters d_i:

$$\vec{p}_d = \sum \vec{p}_{d_i}, \quad E_d = \sum E_{d_i} \tag{4.11}$$

For simplicity, the momentum magnitude is denoted as $p_x = \|\vec{p}_x\|$. Conservation of energy and momentum allows for the momentum of the invisible neutrino to be determined based on the properties of the mother and visible daughter particles, assuming that the neutrino is massless. It results the following expression for the magnitude of the mother particle's momentum, up to a two-fold ambiguity:

$$p_m = \frac{\left(m_m^2 + m_d^2\right) p_d \cos\theta \pm E_d \sqrt{\left(m_m^2 - m_d^2\right)^2 - 4 m_m^2 p_d^2 \sin^2\theta}}{2\left(E_d^2 - p_d^2 \cos^2\theta\right)}, \tag{4.12}$$

where θ is the angle between the momentum vectors of the mother and daughter particles:

$$\theta = \arccos\left(u_m \cdot u_d\right), \tag{4.13}$$

with $u_x = \vec{p}_x / p_x$ being the unit vectors of the x particle's momenta. If the decay did not include a neutrino, this angle would be zero. In practice, the maximum value of θ, determined by the kinematic phase space limit, is used:

$$\theta^{\max} = \arcsin\left(\frac{m_m^2 - m_d^2}{2 m_m p_d}\right), \tag{4.14}$$

which helps to lift the ambiguity in the calculation of the mother's momentum. This methodology is applied to the reconstruction of the momentum of a τ particle, where the visible

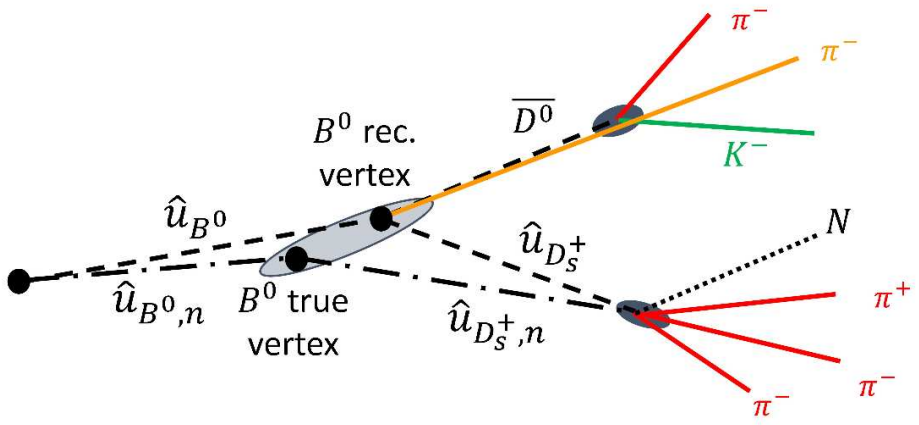

Figure 4.3.: Flight directions of the B^0 and D_s^+ in the $B^0 \to D^{*-}D_s^+$ and $D_s^+ \to 3\pi^\pm N$ decays.

daughters are a 3π system.

$$p_\tau \approx p_\tau(\theta^{\max}) = \frac{\left(m_\tau^2 + m_{3\pi}^2\right) p_{3\pi} \cos\theta^{\max}}{2\left(E_{3\pi}^2 - p_{3\pi}^2 \cos^2\theta^{\max}\right)} \,. \tag{4.15}$$

Similarly, the same calculation is extended to obtain the momentum of a B^0 particle, where the visible daughters comprise the $D^*\tau$ system:

$$p_{B^0} \approx p_{B^0}(\theta^{\max}) = \frac{\left(m_{B^0}^2 + m_{D^*\tau}\right) p_{D^*\tau} \cos\theta^{\max}}{2\left(E_{D^*\tau}^2 - p_{D^*\tau}^2 \cos^2\theta^{\max}\right)} \,. \tag{4.16}$$

This approach leads to an accurate determination of the momentum transfer squared q^2 (*cf.* Eq. (4.8)), and the decay time of the τ^+ candidate, t_{τ^+}. The precision achieved is sufficient to discriminate the signal from the D^{*-} D X backgrounds. These variables are used in the signal yield fit, detailed in Sec. 7.1.

4.2.2. Double-Charm Assumption

The dominant backgrounds after the selection process are primarily due to $B^0 \to D^{*-}DX$ decays, with $B^0 \to D^{*-}D_s^+$ and $D_s^+ \to 3\pi^\pm N$ being especially significant. Fig. 4.3 illustrates the flight directions of the B^0 and D_s^+ in this decays. The original B^0 flight direction u_{B^0} is compared to the improved direction, $u_{B^0,n}$, which accounts for the neutral particles in the D_s^+ decay. The anti-D_s^+ BDT, discussed in Sec. 5.5.4, requires the kinematic reconstruction of this decay mode, as detailed here.

From the known flight directions of the B^0, D_s^+, the D^{*-} vertex position, and the B^0 mass, the momentum conservation equation can be explicitly formulated based on these parameters:

$$\vec{p}_B = \vec{p}_{D_s^+} + \vec{p}_{D^{*-}} \tag{4.17}$$

The following expressions can be straightforwardly, denoting the scalar products as s and the vectorial products as ν, for the B^0 momentum:

$$p_{B,\nu} = p_{D^{*-}} \left\| \frac{u_{D^{*-}} \times u_{D_s^+}}{u_B \times u_{D_s^+}} \right\| , \tag{4.18a}$$

$$p_{B,s} = p_{D^{*-}} \frac{u_{D^{*-}} \cdot u_B - \left(u_{D^{*-}} \cdot u_{D_s^+}\right)\left(u_B \cdot u_{D_s^+}\right)}{1 - \left(u_B \cdot u_{D_s^+}\right)^2} , \tag{4.18b}$$

and for the D_s^+ momentum:

$$p_{D_s,\nu} = p_{D^{*-}} \left\| \frac{\vec{u}_{D^{*-}} \times u_B}{|u_{D_s^+} \times u_B|} \right\| , \tag{4.19a}$$

$$p_{D_s,s} = p_{D^{*-}} \frac{\left(u_{D^{*-}} \cdot u_B\right)\left(u_B \cdot u_{D_s^+}\right) - u_{D^{*-}} \cdot u_{D_s^+}}{1 - \left(u_B \cdot u_{D_s^+}\right)^2} . \tag{4.19b}$$

These methods, while equivalent when no additional particles are present, diverge when extra particles are present. Consequently, both results are employed in the anti-D_s^+ MVA. This partial reconstruction technique does not require assigning a specific mass to the $3\pi^{\pm}N$ system, allowing the reconstructed mass to serve as a discriminating variable. Furthermore, the reconstructed B^0 momenta, denoted as $p_{B,\nu}$ and $p_{B,s}$, are enhanced by accounting for the presence of neutral particles in the D_s^+ decay, indicated by $p_{B,\nu n}$ and $p_{B,sn}$.

One might be tempted to think that this technique could effectively discriminate between the $B^0 \to D^{*-}D_s^+$ backgrounds and the signal, which includes two missing neutrinos. Unfortunately, other backgrounds such as $B \to D^{*-}D^0(X)$ and $B \to D^{*-}D^+(X)$ also exhibit missing energy. This missing energy mainly arises from two unreconstructed kaons at the B^0 and $3\pi^{\pm}$ vertices, rendering these backgrounds similar in profile to the signal. Therefore, the reconstruction technique just described must be complemented by a precise multivariate analysis, which is detailed in the following chapter.

	2015–2016	2017	2018
Integrated Luminosity (fb^{-1})	1.92	1.71	2.19

Table 4.1.: Integrated luminosity for each dataset.

4.3. Analysis Workflow

The workflow of this analysis is complex. To provide an overview of the strategy and facilitate comprehension of the subsequent chapter, a schematic representation is presented in Fig. 4.4. This diagram can be summarized as follows:

i). **Dataset:** Customization of simulation software is carried out to produce all required samples. This includes making or adapting generator cuts and filtering scripts to minimize CPU usage and disk space for the MC samples. Filtering (Stripping) is implemented for pre-selection, alongside physics checks to ensure correct decay chains in the decay-describing simulation inputs (referred to as DEC files) and initial ReDecay validation.

ii). **Selection:** Reprocessing of "raw" simulation and collision data into analysis–ready ROOT-tuple format is performed using the DaVinci software [156]. An initial cut-based selection is applied here. Subsequently, simulated samples are reweighted to better align with expected collision data characteristics. The data and simulation then undergo further cut-based and multivariate analysis, according to specific modes.

iii). **Measuring $\mathcal{K}(D^{*-})$:** At this stage, normalization and signal yields are extracted, efficiencies are computed, and $\mathcal{K}(D^{*-})$ is determined from these values.

iv). **Final Result:** The $\mathcal{K}(D^{*-})$ value is combined with external branching fractions to derive $\mathbf{R}(D^{*})$. Systematics are evaluated to address uncertainties in the final result.

4.4. Datasets

4.4.1. Collision Data

The data was collected during Run 2, from 2015 to 2018, with a total integrated luminosity of $5.8\,fb^{-1}$, and at energy at the center of mass of 13 TeV.
The luminosity for each dataset is reported in Tab. 4.1 .
The trigger configuration varies during data taking periods. A summary of cuts employed at the level-0 trigger is given in App. B.1.

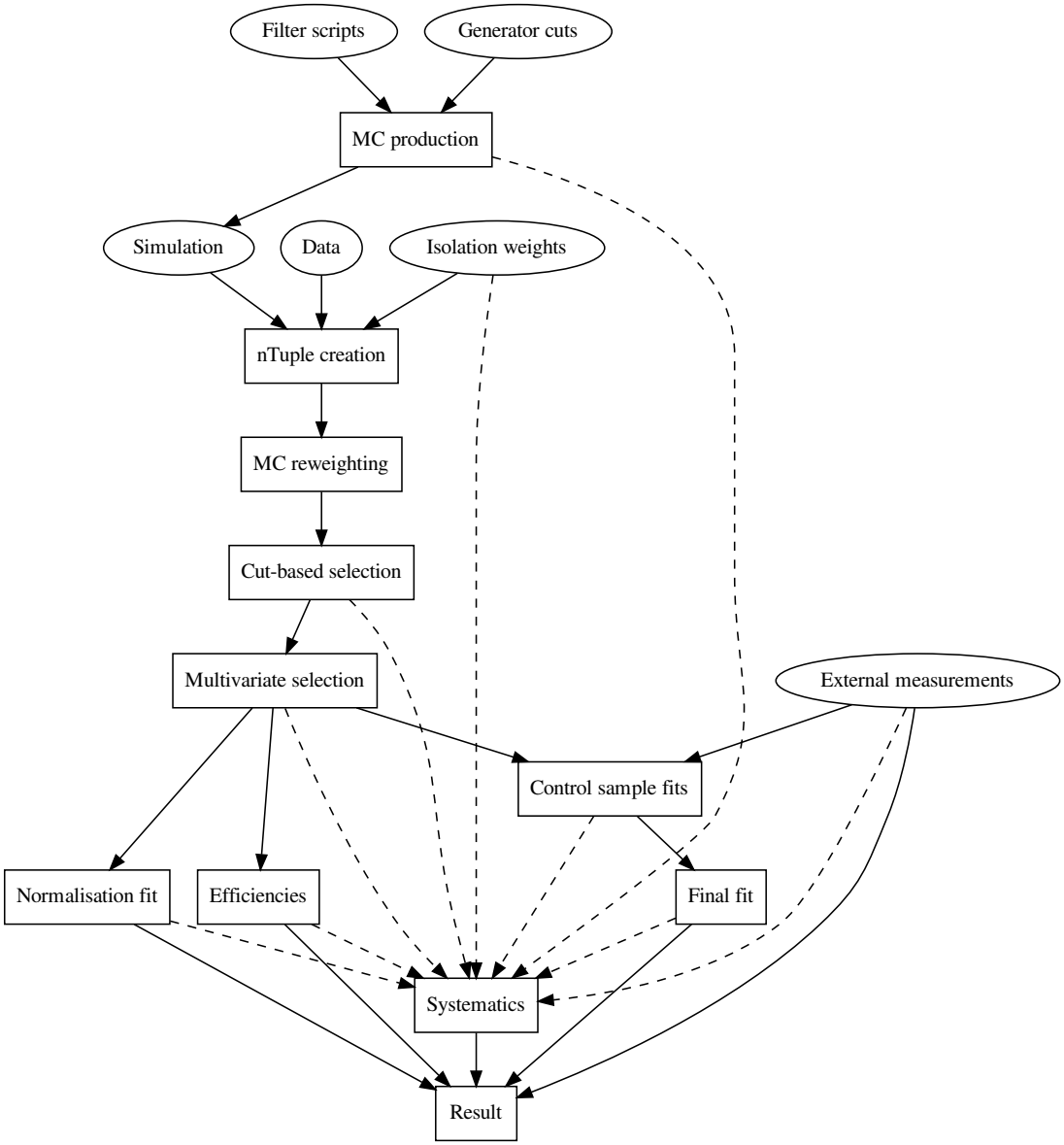

Figure 4.4.: Overview of the analysis workflow: starting with simulation setup, followed by event selection, signal and normalization fits, efficiency computations, systematic analysis, and concluding with the final $\mathbf{R}(D^*)$ result [157].

4.4.2. Monte-Carlo Simulation

A fast simulation method was employed to produce a large sample size, details of which are discussed in [157]. Part of the MC sample was generated using the ReDecay technique, a summary of which can be found in [158]. The data is used to model background shapes in signal fits, and also supports Machine Learning-based MVA training presented in Sec. 5.5, efficiency calculations in Sec. 5.7, and fit validation in Chap. 7.

The MC samples for the Run 2, with the corresponding number of generated and filtered[2] events, are listed in Tab. 4.2.
Throughout the document[3] $b\bar{b} \to D^{*-}3\pi X$ is referred to as the *inclusive MC sample*, $B^0 \to D^{*-}D_s^+X$ as the D_s^+ *cocktail MC sample*, and $b\bar{b} \to D^{*-}D^{(0,+)}X$ as the D^0 or D^+ *MC sample*.

In the $B^0 \to D^{**}\tau^+\nu_\tau$ where $\tau^+ \to 3\pi^\pm\overline{\nu}_\tau$ decays, D^{**} refers to any of these states: $D_1(2420)^-$, $D_0^*(2300)^-$, $D_1^{'}(2430)^-$, or $D_2(2460)^-$.

Similarly, for the decays $B^+ \to D^{**0}D_s^+X$ and $B^0 \to D^{**-}D_s^+X$, where D^{**} denotes the states $D_1(2420)^{(0,-)}$, $D_1^{'}(2430)^{(0,-)}$, or $D_2(2460)^{(0,-)}$. The branching fractions and the contributions from various D^{**} states are detailed in Tab. 4.3, based on simulations of the inclusive $b\bar{b} \to D^{*-}3\pi X$ sample. The observed values exceed the theoretical predictions referenced in [159]. This discrepancy will be taken into account in the systematic uncertainties (*cf.* Chap. 8).

4.4.3. Monte-Carlo Reweighting

The MC samples are reweighted and/or rescaled to account for discrepancies between the simulated and observed data. The corrections applied to the MC samples include FF reweighting, adjustments in kinematic variables, corrections for the D^* and D_s^* mesons polarizations in two-body decays, and 3π dynamics correction, specific to the normalization mode. Additionally, a vertex error correction is applied to align the vertex resolution in the MC samples with that observed in data.

4.4.3.1. Form Factor Reweighting

The MC signal samples are generated using the Isgur-Wise parametrization for the form factor at the EvtGen level, as referenced in [76]. These samples are subsequently reweighted

[2] Number of events after applying online cuts (*cf.* Sec. 5.3).
[3] X represents one or more additional final state particles that aren't reconstructed.

Decay Descriptor		EventType	Events [M] Generated	Filtered
$B^0 \to D^{*-}\tau^+\nu_\tau$	(with $\tau^+ \to 3\pi^\pm\overline{\nu}_\tau$)	11160001	257.0	30.0
	(with $\tau^+ \to 3\pi^\pm\pi^0\overline{\nu}_\tau$)	11563020	198.0	49.0
$B^0 \to D^{*-}3\pi^\pm$		11266018	651.0	12.0
$B^0 \to D^{**}\tau^+\nu_\tau$	(with $\tau^+ \to 3\pi^\pm\overline{\nu}_\tau$)	11566430	53.0	4.0
		11566431	245.0	16.0
$B_s^0 \to D^{*-}D_s^+X$	(with $D_s^+ \to 3\pi^\pm X$)	13996621	125.0	1.0
	(with $D_s^+ \to K\pi X$)	13996622	69.0	0.09
	(with $D_s^+ \to \ell\nu_\ell X$)	13996623	30.0	0.3
	(with $D_s^+ \to a_1(1260)^+X$ and $a_1(1260)^+ \to \pi^+2\pi^0$)	13996624	27.0	0.2
$B^+ \to D^{*-}D_s^+X$	(with $D_s^+ \to 3\pi^\pm X$)	12997623	148.0	2.0
	(with $D_s^+ \to K\pi X$)	12997624	78.0	0.2
	(with $D_s^+ \to \ell\nu_\ell X$)	12997625	45.0	0.5
	(with $D_s^+ \to a_1(1260)^+X$ and $a_1(1260)^+ \to \pi^+2\pi^0$)	12997626	31.0	0.3
$B^0 \to D^{*-}D_s^+X$	(with $D_s^+ \to 3\pi^\pm X$)	11896623	436.0	6.0
	(with $D_s^+ \to K\pi X$)	11896624	302.0	0.5
	(with $D_s^+ \to \ell\nu_\ell X$)	11896625	142.0	1.0
	(with $D_s^+ \to a_1^+X$ and $a_1(1260)^+ \to \pi^+2\pi^0$)	11896626	92.0	0.8
$b\overline{b} \to D^{*-}3\pi^\pm X$		27163970	18132.0	74.0
$b\overline{b} \to D^{*-}D^{\{0,+\}}X$		27163971	822.0	6.0
Total		–	21884.0	205.0

Table 4.2.: Sample sizes for Generated and Filtered simulation data across various decay descriptors. The Eventtype is an 8 digit number that categorizes specific particle decay processes for simulations, and is specific to LHCb.

D^{**} state	$B \to D^{**}\tau\nu_\tau$ Br_1	$D^{**} \to D^{*-}X$ Br_2	Product of Br [%] $Br_1 \times Br_2$	Ratio to $B^0 \to D^*\tau\nu$ $Br_1 \times Br_2/Br_{sig}$
$D_1'(2430)^0$	0.002	0.66	0.132	0.088
$D_1(2420)^0$	0.0013	0.67	0.09	0.06
$D_2^*(2460)^0$	0.002	0.21	0.042	0.028
$D_0(2400)^0$	0.002	0	0	0
		Total from B^+	0.264	0.1756
$D_1'(2430)^+$	0.002	0.33	0.066	0.044
$D_1(2420)^+$	0.0013	0.33	0.04	0.027
$D_2^*(2460)^+$	0.002	0.1	0.02	0.013
$D_0(2400)^+$	0.002	0	0	0
		Total from B^0	0.126	0.084

Table 4.3.: List of branching fractions involving the D^{**} used in the inclusive $b\bar{b} \to D^{*-}3\pi^{\pm}X$ MC.

to conform the BGL parametrizations (Sec. 2.3), utilizing the HAMMER package [160]. The parameterization is taken from Tab. 2.2 using the lattice and both BaBar and Belle data (5th column).

The distributions of three variables used in the signal fit, are illustrated in Fig. 4.5, both before and after the reweighting process.

4.4.3.2. Adjustments in Kinematic Variables

To align the kinematics of particles in the MC samples with those observed in data, a BDT-based reweighting technique, as described in [161], is employed. This method allows for the simultaneous reweighting of multiple variables while preserving their correlations. The variables considered for this adjustment include:

- Pseudorapidity of the B^0, $\eta(B^0)$
- Transverse momentum of the B^0, $p_T(B^0)$

The effect of reweighting on these variables' distributions is shown in Fig. 4.6.

Additionally, the distributions of `nTracks` and `nSPDHits` are individually rescaled to match the data more closely. The determination of Particle Identification (PID) efficiency using PIDCalib (*cf.* Sec. 5.7) is based on `nSPDHits`. It has been observed that MC simulations tend

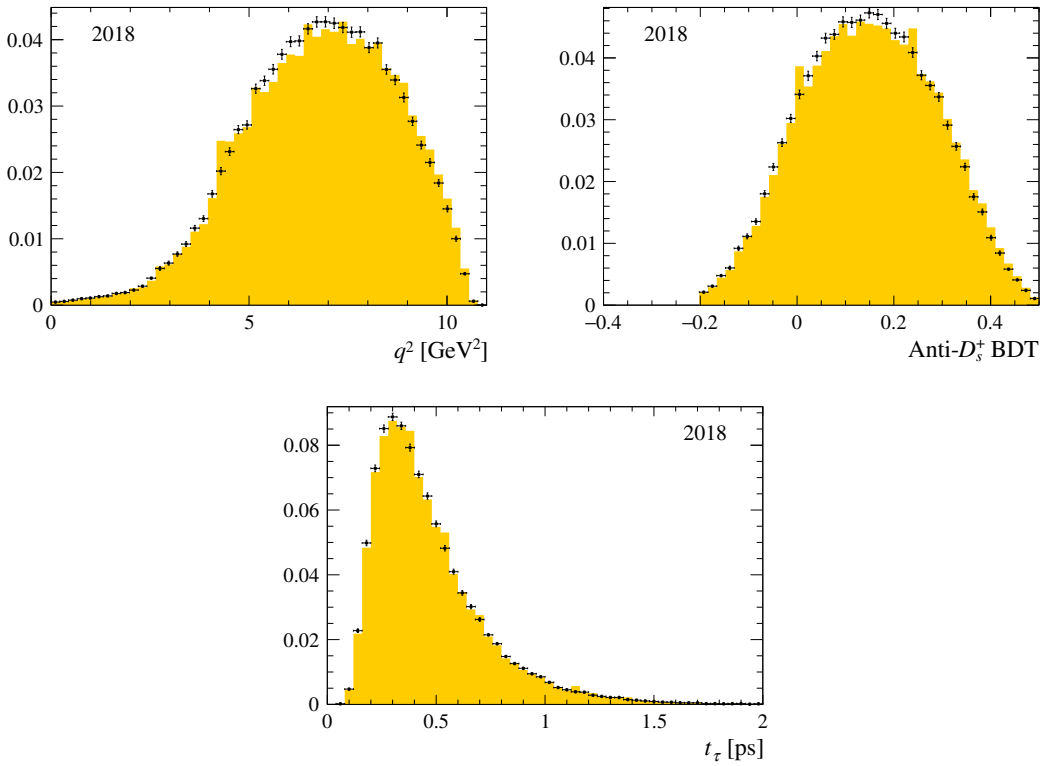

Figure 4.5.: Distribution of the q^2, anti-D_s^+ BDT and τ^+ decay time before (filled yellow) and after (black dots) the BGL Form Factor reweighting in the $B^0 \to D^{*-}\tau^+\nu_\tau$ and $\tau^+ \to 3\pi\overline{\nu}_\tau$ signal MC sample.

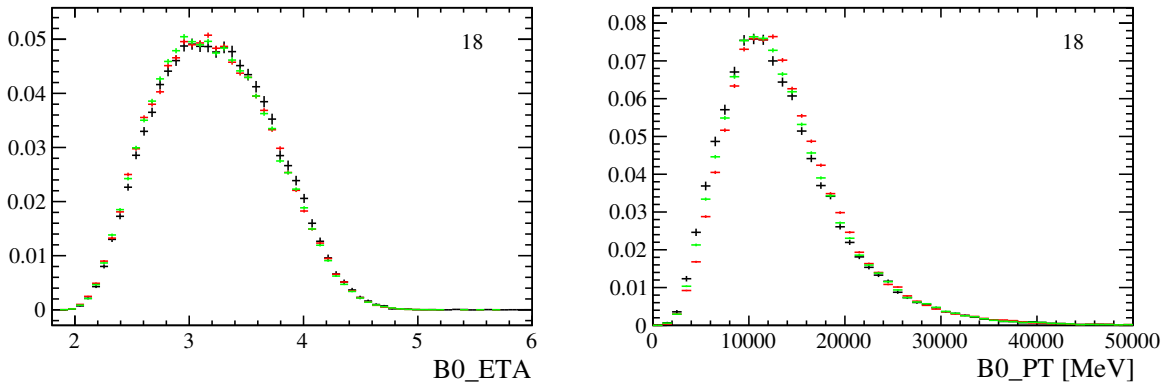

Figure 4.6.: Distributions of η (left) and p_T (right) for B^0 before and after kinematic reweighting in the $B^0 \to D^{*-}3\pi$ MC, and s-weighted $B^0 \to D^{*-}3\pi$ peak in data. The red and green curves represent events before and after reweighting, respectively, while the black data points show events in data.

Variable	2015–2016		2017–2018
	Sim09c	Sim09e	Sim09k
`nTracks`	1.1	1.2	1.1
`nSPDHits`	1.59	1.87	1.75

Table 4.4.: Scaling factors for the `nTracks` and `nSPDHits` distributions in the Sim09c, Sim09e and Sim09k MC samples.

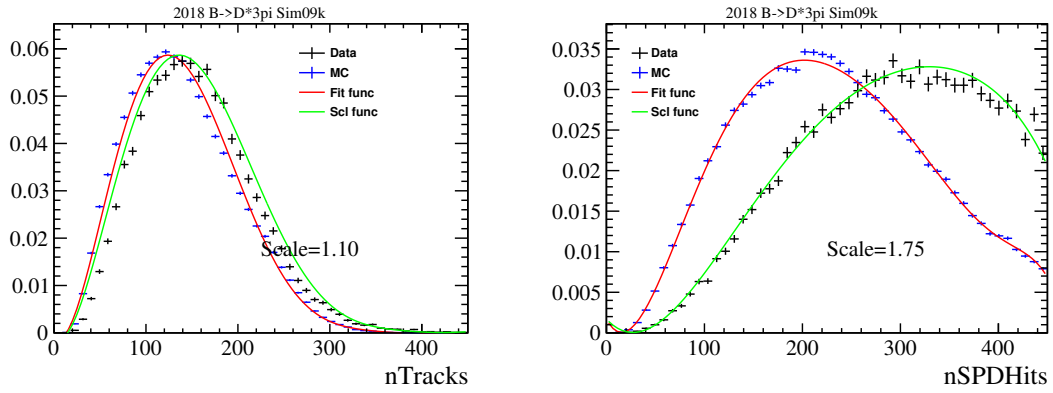

Figure 4.7.: Distributions of `nTracks` (left) and `nSPDHits` (right) for B^0 samples before and after rescaling in the $B^0 \to D^{*-}3\pi$ MC and s-weighted $B^0 \to D^{*-}3\pi$ peak in data. Red and green histograms represent events before and after rescaling, respectively; black data points represent events in data.

to underestimate `nSPDHits` compared to the data. Consequently, a correction is applied by scaling. This scaling factor is derived from a comparison of the `nSPDHits` distributions between s-weighted data and MC-matched simulations.

The rescaling is performed separately for the simulation versions[4]: Sim09c, Sim09e and Sim09k. Specifically, the scaling factors for `nTracks` and `nSPDHits` are summarized in Tab. 4.4. Distributions for the `nTracks` and `nSPDHits` variables before and after the rescaling are shown in Fig. 4.7.

[4] A simulation version refers to a specific release of simulation software used to model particle interactions and detector responses in the LHCb experiment.

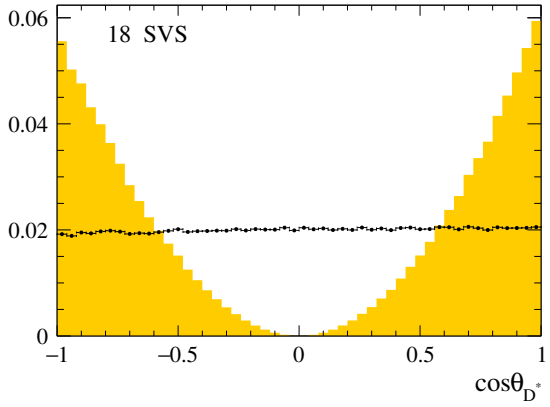

Figure 4.8.: Distribution of $\cos\theta_{D^*}$ for the inclusive $b\bar{b} \to D^{*-}3\pi X$ MC sample, before (black) and after (yellow) correcting for D^* polarization in SVS decays.

4.4.3.3. Polarization of D^* in Two-Body Decays

Inclusive MC samples for the $b\bar{b} \to D^{*-}3\pi X$ and $b\bar{b} \to D^*D^{(0,+)}X$ are generated under the assumption that the D^* mesons exhibit no initial polarization, thus setting the longitudinal polarization fraction, f_L, to 1/3. However, for two-body Scalar to Vector Scalar (SVS) decays, such as $B \to D^*D^0$, conservation of angular momentum necessitates that the D^* mesons be longitudinally polarized, implying an f_L of 1. To rectify this in the MC samples, a weight factor is introduced to adjust the longitudinal polarization in SVS decays.

The differential decay rate is described by the relation:

$$\Gamma(S \to VS) \propto 2f_L \cos^2\theta_{D^*} + (1 - f_L)\sin^2\theta_{D^*}\,, \tag{4.20}$$

where θ_{D^*} represents the helicity angle. A correction factor is computed as the ratio of decay rates for $f_L = 1$ over $f_L = 1/3$. SVS decays are identified within the inclusive MC samples using LoKi functors[5], and the appropriate weights are then applied. The $\cos\theta_{D^*}$ distribution, both before and after applying the correction for SVS decays, is depicted in Fig. 4.8. The fractions of SVS decays are approximately 10% and 5%, in the $b\bar{b} \to D^{*-}3\pi X$ and $b\bar{b} \to D^*D^{(0,+)}X$ simulated samples, respectively.

The impact of applying a correction factor on the analysis variables–q^2, anti-D_s^+ BDT output,

[5] LoKi is a toolkit for the LHCb software framework, DaVinci, that provides a set of functors for the manipulation of particle properties.

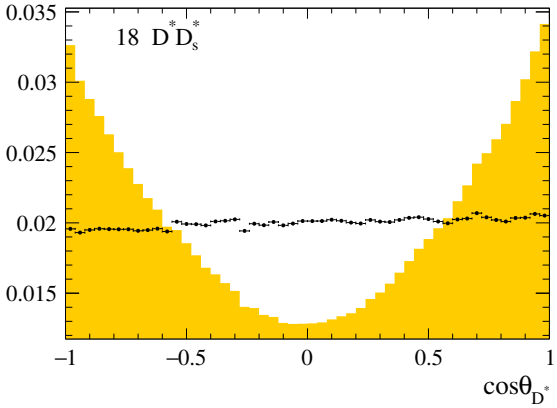

Figure 4.9.: Distribution of $\cos\theta_{D^*}$ for the inclusive $b\bar{b} \to D^{*-}3\pi X$ MC sample, before (black) and after (yellow) correcting for D_s^* polarization.

and τ^+ lifetime is negligible, as shown in Fig. A.3.

4.4.3.4. Polarization of D_s^* in Two-Body Decays

In the $B \to D^* D_s^*$ simulated sample, the D_s^* vector meson is initially generated with equal polarization fractions of 1/3 for each of the three states. The longitudinal polarization fraction is subsequently adjusted to $f_L = 0.578$ to align with recent measurements [162].

Fig. 4.9 shows the distribution of $\cos\theta_{D^*}$ for the inclusive $b\bar{b} \to D^{*-}3\pi X$ MC sample, before and after correcting for D_s^* polarization in SVS decays. The impact of applying a correction factor on the analysis variables—q^2, anti-D_s^+ BDT output, and τ^+ lifetime is also found to be negligible, as shown in Fig. A.4.

4.4.3.5. 3π Dynamics for the Normalization Mode

The dynamics of the 3π system in the $B^0 \to D^{*-}3\pi$, as simulated in MC, do not fully align with those observed in the data, as illustrated in Fig. 4.10. The peak corresponding to the D_s^+ meson observed in the data can be disregarded, as this contribution is subtracted from the normalization yield (*cf.* Sec. 7.2). However, an overall shift between the data and the MC simulation is evident. To correct for this discrepancy, the MC is reweighted using the ratio of the $m(3\pi)$ distributions in data and MC, as shown in Fig. 4.11.

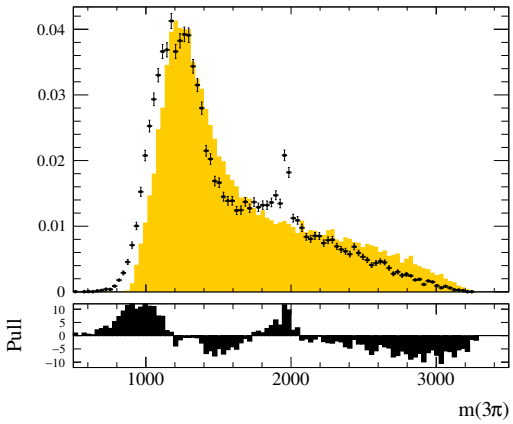

Figure 4.10.: Comparison of the $m(3\pi)$ distribution between sweighted data and MC. The MC is represented by the yellow histogram, and the sweighted data by black points.

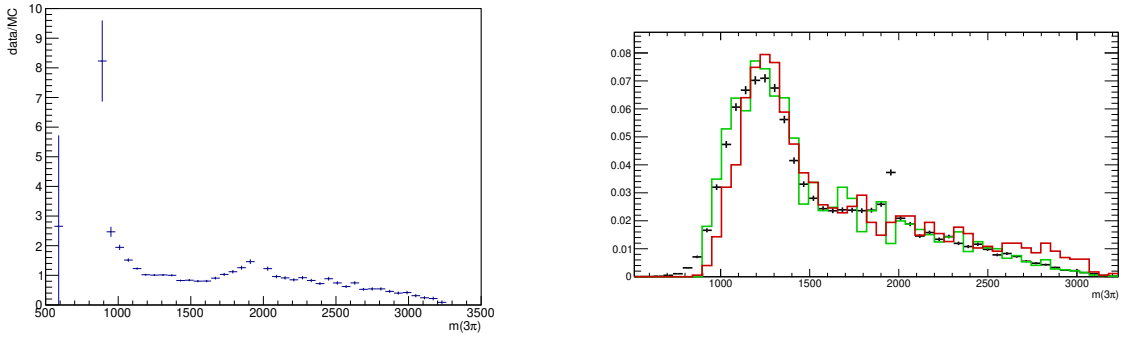

Figure 4.11.: Left: Ratio of the $m(3\pi)$ distribution between data and MC. Right: $m(3\pi)$ distribution after reweighting, with MC shown before reweighting (red) and after reweighting (green), alongside data (black points).

4.4.3.6. Vertex Error Correction

The vertex reconstruction algorithm has exhibited inconsistencies across different data-taking periods, resulting in discrepancies between real data and simulated samples in vertex-related variables, including χ^2_{IP}, vertex position, and its uncertainty. These inconsistencies were absent in Run 1, where data and simulation showed excellent agreement. However, the data quality from 2015 to 2016 deteriorated due to radiation damage to the detector, leading to acceptable, but imperfect, agreement after applying a scaling factor. The situation further declined in 2017-2018, as adjustments made to the vertex reconstruction algorithm were applied *exclusively* to real data, not to the simulated samples. Consequently, this introduced significant discrepancies, particularly in vertex position distributions and their uncertainties, which are critical for rejecting background from prompt $B \longrightarrow D^{*-}3\pi^{\pm}X$ decays, where the $3\pi^{\pm}$ originate directly from B decays.

To address these discrepancies and achieve good agreement between data and simulation, a correction method based on the transverse momentum (p_T) of final state tracks is applied to the distribution of $\Delta z(PV, \tau^+)$, where Δz represents the separation between vertices normalized by their vertex errors:

$$\Delta z(X_a, X_b) = \frac{z(X_a) - z(X_b)}{\sqrt{\sigma_z^2(X_a) + \sigma_z^2(X_b)}} \,, \tag{4.21}$$

Here, $z(X_i)$ denotes the vertex position of particle X_i, and $\sigma_z(X_i)$ is the associated vertex error. The correction is implemented in three steps using data and MC samples of $B^+ \longrightarrow J/\Psi K^+\pi^+\pi^-$ decays as control samples, where the J/Ψ vertex serves as a reliable proxy for the B^+ vertex:

1. The Δz distribution is fitted in continuous $\max(1/p_T)$ bins, where p_T is the transverse momentum of the three charged tracks (K^+ or $\pi^{\pm}$). The distribution is modeled with two Gaussian functions, with the width of the broader Gaussian fixed across all fits. The narrower Gaussian width, referred to as σ, is used as a proxy for Δz. The σ distributions in data are shown in Fig. 4.12 (*cf.* Fig. A.5 for MC samples).

2. The σ is treated as a function of $\max(1/p_T)$ and modeled with a polynomial of degree 2. The error variable in each event, both in data and simulation, is then scaled by a factor derived from this polynomial, ensuring that the Δz pulls exhibit a unit Gaussian width. The corresponding fits to data are shown in bottom-right of Fig. 4.12 (*cf.* Fig. A.5 for MC samples).

3. The modified error variable distribution in MC samples is reweighted using GBReweighter [161] to match the corresponding distribution in data.

This correction method ensures that the Δz resolution is consistent across different data-taking periods, thus improving the agreement between data and simulation and allowing for an accurate evaluation of selection efficiencies using simulated samples. Figures illustrating these steps are provided in Fig. 4.13 is given to illustrate the effect of the correction on the $z(\tau^+)$ distribution.

4.5. Highlights of My Role in the Project

My contributions to this analysis can be summarized as follows: initially, I performed a thorough cross-check on the analysis using 2015–2016 datasets, by cross-checking the results from ROOT-tuple productions to the final fits. I also contributed to systematic studies, including the effect of BDT cuts and of the efficiency calculation. Then, the dataset was extended[6] to the full Run 2, with several improvements: I explored the effects of changes in stripping and trigger configurations, developed a vertex correction scheme to reconcile differences between new data algorithms and existing MC simulations, and improved efficiency calculations by eliminating multiple event candidates. I participated in developing a new method for calculating the normalization yield and estimating bias via bootstrapping. Furthermore, I enhanced the analysis code to generate separate results per dataset for cross-checks, providing greater flexibility. The FFs are now parameterized using the BGL parameterization, instead of the CLN one, previously used. Additionally, I contributed to the production of D_s^+ MC samples. A scheme to constrain current free parameters in the signal fit was also developed thanks to BESIII branching fraction measurements [9, 10], but has not yet been implemented.

[6] Including 2017 and 2018 data.

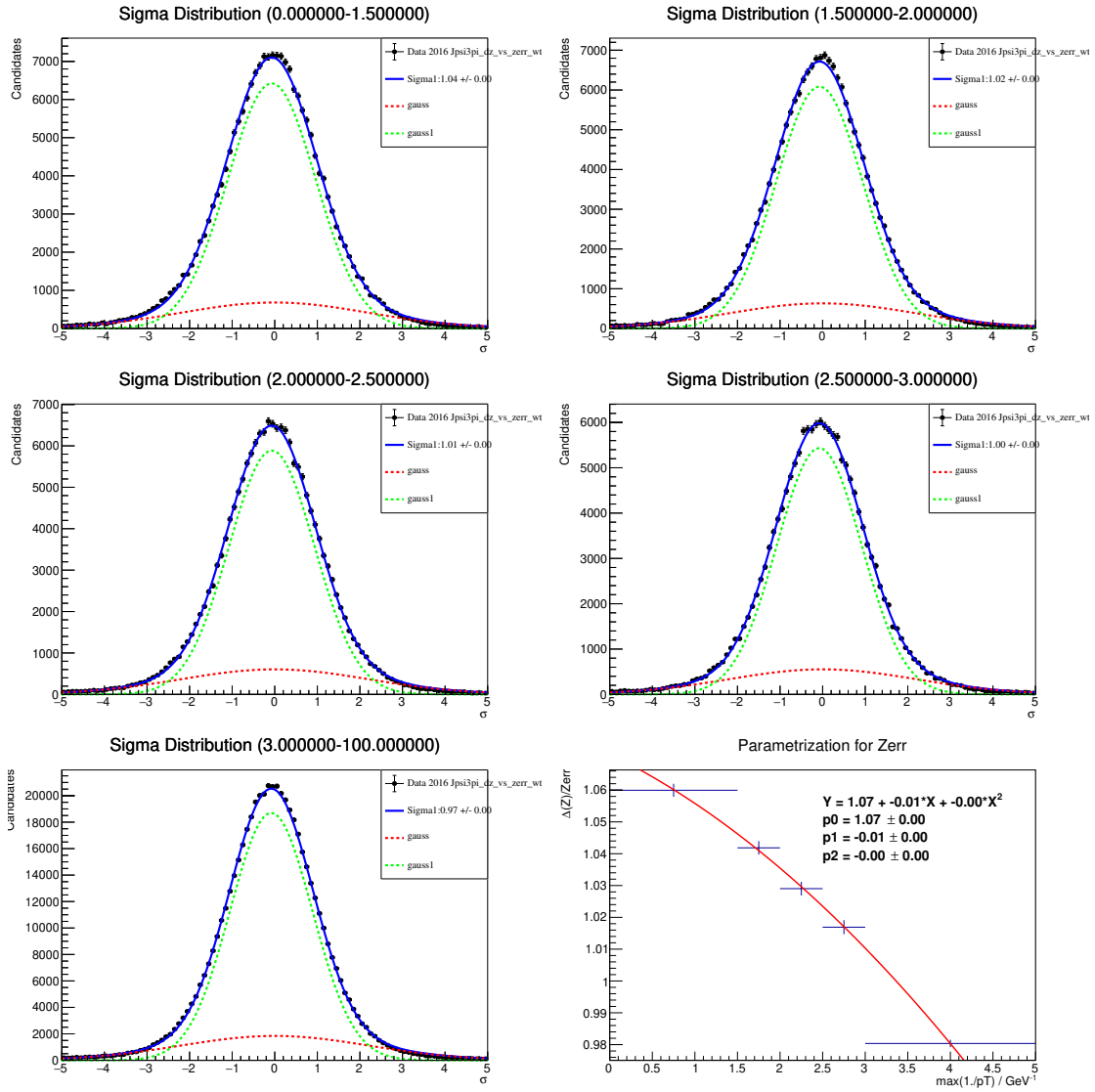

Figure 4.12.: σ distributions for different $\max(1/p_T)$ bins from data samples. The bottom-right panel shows σ as a function of $\max(1/p_T)$ along with the corresponding fitted function.

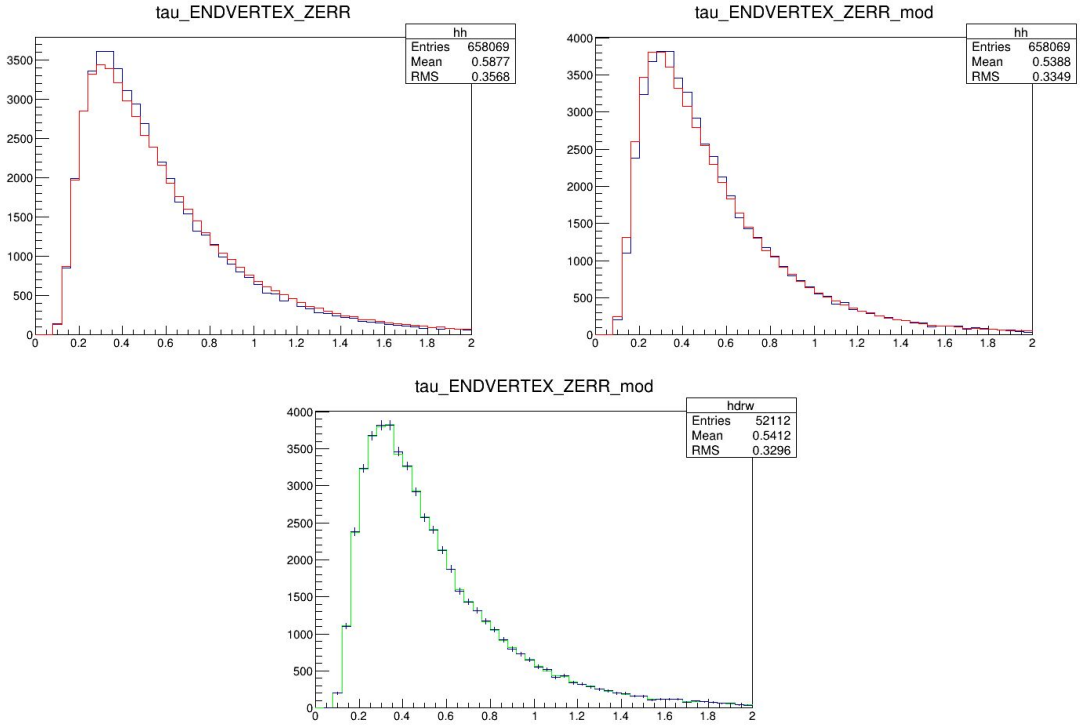

Figure 4.13.: Distributions of $z(\tau^+)$ for raw data/MC sample (top-left) after data/MC rescale (top-right) and after data/MC rescale and reweighting (bottom).

Chapter 5

Event Selection and Efficiency Calculation

In this chapter, the selection criteria for the *signal* and *normalization* modes are described. It is crucial that the requirements for these modes are as similar as possible to ensure that the systematic uncertainties from these modes are effectively canceled when calculating the $\mathbf{R}(D^*)$ ratio.

The selection process for data and simulation goes through several steps, that can be split in two categories:

- Online Selection: this phase involves preliminary, real-time data filtering before storage, aimed at reducing data volume by retaining only events of high physics interest.
- Offline Selection: in this post-storage stage, detailed analysis is performed on data saved in the ROOT ntuples format, ready to be used for analysis.

The chapter is structured as follows: the "online" selection is described first, it comprises the geometrical acceptance of the LHCb detector (Sec. 5.1), the trigger correction (Sec. 5.2), and finally, the preselection (Sec. 5.3) which includes stripping, filtering and the DaVinci reconstruction, used to build the ROOT ntuples.

The 'offline' selection begins with initial cuts common to all samples (Sec. 5.4). Next, the

MVA techniques are discussed in Sec. 5.5. The mode-specific cuts are described in Sec. 5.6, where distinction between the signal and normalization modes is made . Finally, the efficiency calculation is discussed in Sec. 5.7, where the normalization-to-signal mode efficiency ratio is computed. This ratio is the first intermediate result that contributes to the $\mathbf{R}(D^*)$ formula.

The strategy closely follows the one used in the previous analysis [3], with some modifications, which can be summarized as follows:

- The preselection criteria have become tighter in MC simulations for 2017 and 2018.
- New MC samples describing different D_s^+ decay modes have been added
- The MVA employs the same variables as the previous analysis. However, due to larger statistics, the training and testing samples for both signal and background use only a small fraction of the total sample[1].
- As discussed in Sec. 4.4.3.6, a methodology to adjust the vertex error in simulations has been developed. For now, the standard cut on Δz ($\Delta z < 2$), the flight distance in the z direction between τ^+ and B^0 vertices is applied. The effect of the vertex correction is planned to be studied further.

5.1. Geometrical Acceptance

Due to the geometrical coverage of the LHCb detector, only a part of the events of interests are recorded. This effect impacts efficencies of the signal and normalization modes and is studied for the simulated samples with EvtGen. The geometrical acceptance obtained is reported in Tab. 5.17.

5.2. The Trigger

The trigger lines used in this analysis are classified as:

- Trigger Independent of Signal (TIS): events are recorded based on trigger lines that operate independently of the signal part within the event.
- Trigger On Signal (TOS): refers to the requirement that the signal candidate itself must have caused the trigger decision. If the signal is removed, the event would not be recorded.

[1] 1 M events are shown to be sufficient.

	2015	2016	2017	2018	Run 2
Trigger	E_T (GeV) >				nSPDHits <
L0Hadron	3.6	3.7	3.46	3.79	450
L0Photon	2.7	2.78	2.47	2.95	450
L0Electron	2.7	2.4	2.11	2.38	450
p_T (GeV/c) >					
L0Muon	2.8	1.8	1.35	1.75	450
Muon High p_T	6.0				–
p_T^2 $(GeV/c)^2$ >					
L0DiMuon	1.69	2.25	1.69	3.24	900

Table 5.1.: Selection criteria applied for the L0 hardware trigger in Run 2 collision data, by data-taking year [141].

This classification helps to determine the trigger efficiency with data already filtered by the online trigger selection process. In a first approximation, TIS and TOS can be considered as independent samples, as they are defined by distinct trigger lines. TOS efficiency can be determined by the ratio of $N_{TIS\,\&TOS}$ the number of events that pass the TIS and TOS trigger lines to N_{TIS} the number of events that pass the TIS trigger lines:

$$\varepsilon_{TOS} = \frac{N_{TIS\,\&TOS}}{N_{TIS}} . \tag{5.1}$$

Similarly, TIS efficiency can be determined by the ratio of $N_{TIS\,\&TOS}$ the number of events that pass the TIS and TOS trigger lines to N_{TOS} the number of events that pass the TOS trigger lines:

$$\varepsilon_{TIS} = \frac{N_{TIS\,\&TOS}}{N_{TOS}} . \tag{5.2}$$

The decision of retaining or rejecting an event is made by comparing these inputs to the fixed thresholds. Events with *at least* one candidate above the threshold are retained by the L0 trigger. The L0 cuts used during the Run 2 data-taking period are listed in Tab. 5.1.

The trigger lines used in the analysis are listed in Tab. 5.2. They consist in a logical "OR" on the B^0 topological lines[2] and the exclusive $B^0 \to D^{*-}$ decays with $D^{*-} \to D^0\pi^-$ and $D^0 \to K^+\pi^-$

[2] which allows to select 2–4 body decays of the B^0 meson, to select both signal and normalization candidates

Trigger Requirements	
L0	B0_L0Global_TIS Dst_L0HadronDecision_TOS
HLT1	B0_Hlt1TrackMVADecision_TOS B0_Hlt1TwoTrackMVADecision_TOS
B^0 topology	
HLT2	B0_Hlt2Topo2BodyDecision_TOS B0_Hlt2Topo3BodyDecision_TOS B0_Hlt2Topo4BodyDecision_TOS
$B^0 \to D^{*-}$ exclusive	
HLT2	D0_Hlt2CharmHadDstp2D0PipDecision_Dec D0_Hlt2CharmHadDstp2D0Pip_D02KmPipTurboDecision_Dec

Table 5.2.: Trigger requirements used in the analysis. The requirement between B^0 topology and $B^0 \to D^{*-}$ exclusive is a logical 'OR' (*cf.* Sec. 3.3.3).

decays. The logical "'OR" is implied between the lines of a given stage (*i.e.* L0, HLT1 or HLT2) and the logical 'AND' is implied between the three trigger steps: L0, HLT1 and HLT2 B^0 topology or L0, HLT1 and HLT2 $B^0 \to D^{*-}$ exclusive.

In this analysis, it is crucial to accurately measure the ratio of normalization to signal efficiencies. This requires knowing the yields *before* and *after* trigger cuts, which are studied using simulation samples. To achieve this, trigger cuts in the simulation are applied after the ROOT ntuples are generated (*cf.* Sec. 5.4). Although this changes the selection order compared to collision data, it does not affect the overall efficiency, as it is the product of efficiencies from all steps (*cf.* Sec. 5.7). However, due to the altered order, trigger efficiencies in the simulated samples do not accurately reflect those of the collision data. The trigger efficiencies as measured after the geometrical acceptance and preselection are reported in Sec. 5.7.

Level-0 Trigger Corrections

The efficiency of the L0Hadron trigger is obtained from the transverse momentum p_T of the $3\pi^\pm$ system. The TOS efficiency of the L0Hadron trigger as a function of p_T for $3\pi^\pm$ candidates from $B \to D^* 3\pi^\pm$ events is determined using both data and MC simulation samples, as shown in Fig. 5.1. The ratio of these efficiencies is then fitted with a third-order polynomial, as illustrated in Fig. 5.2. This fitted curve is subsequently used as a correction factor to adjust

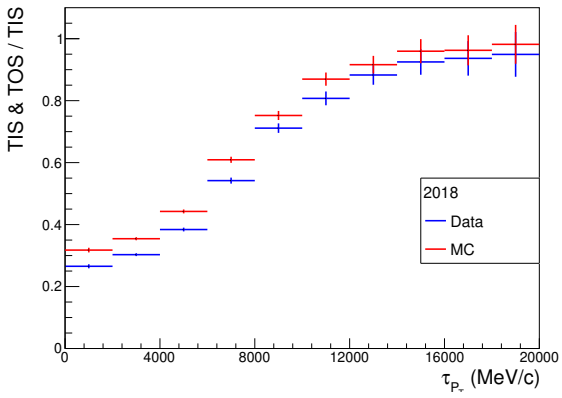

Figure 5.1.: Efficiency of the L0Hadron Trigger TOS as a function of transverse momentum p_T of $3\pi^{\pm}$ candidates in $B \longrightarrow D^*3\pi^{\pm}$ events, compared between data and MC simulations.

the trigger efficiency in the analysis (*cf.* Sec. 5.7).

The polynomial weights are applied to the p_T distributions of both signal and normalization events. This introduces correction factors to the efficiencies of signal and normalization modes as reported in App. B.1.1. The correction to the ratio of signal to normalization efficiencies is negligibly small.

Additionally, the TOS efficiency is analyzed as a function of other kinematic variables such as momentum p, transverse momentum p_T, and pseudorapidity η. The corresponding distributions in data and MC simulations are shown in Figs. 5.3 to 5.5.

The L0Hadron trigger efficiency as function of nSPDHits is studied. The L0TIS efficiencies for $B \longrightarrow D^*3\pi^{\pm}$ events, as observed in both data and MC, are illustrated in Fig. 5.6. To correct MC according to data, the `nSPDHits` distribution is rescaled as described in Sec. 4.4.3.

The ratio between *with* and *without* the corrections are reported in App. B.1.2; it is found to be negligibly small.

5.3. Preselection Criteria

After the geometrical acceptance and trigger cuts have been applied to data, the next step is *preselection*, or filtering and stripping. Filtering and stripping refers to predefined selection algorithms used to filter collision data in real-time, and simulations. These algorithms efficiently reduce the dataset size by retaining only those events that meet specific physics criteria rele-

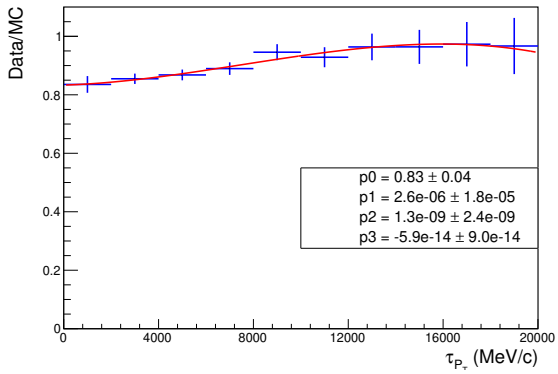

Figure 5.2.: Ratio of L0Hadron trigger TOS efficiency between data and MC for $B \longrightarrow D^*3\pi^{\pm}$ events as a function of transverse momentum p_T of $3\pi^{\pm}$ candidates, fitted with a third-order polynomial.

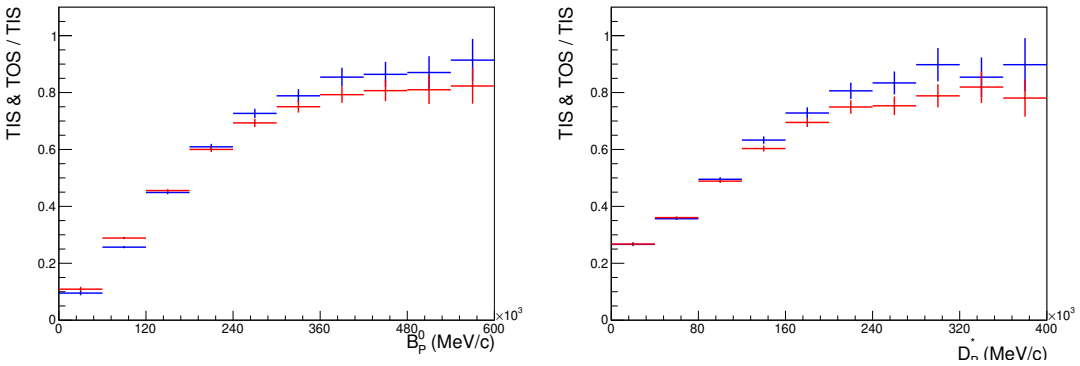

Figure 5.3.: The L0Hadron trigger TOS efficiency as a function of p of B and D^* candidates are obtained for $B \longrightarrow D^*3\pi^{\pm}$ events in data and MC

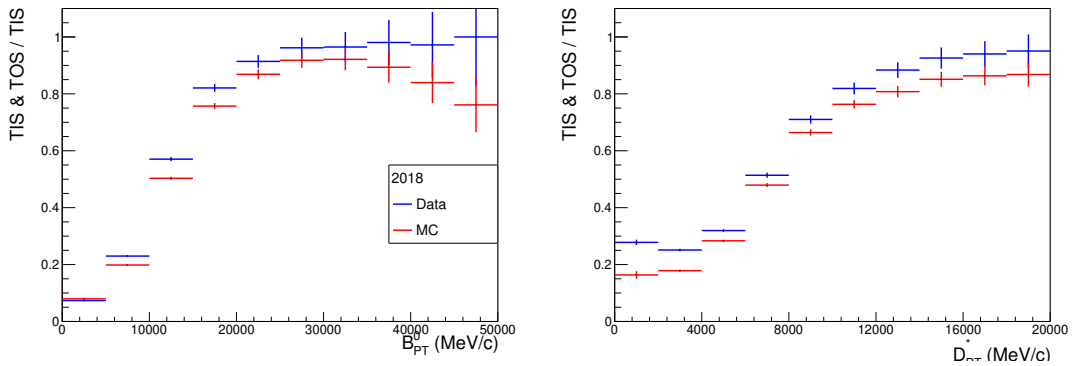

Figure 5.4.: The L0Hadron trigger TOS efficiency as a function of p_T of B and D candidates are obtained for $B \longrightarrow D^*3\pi^{\pm}$ events in data and MC

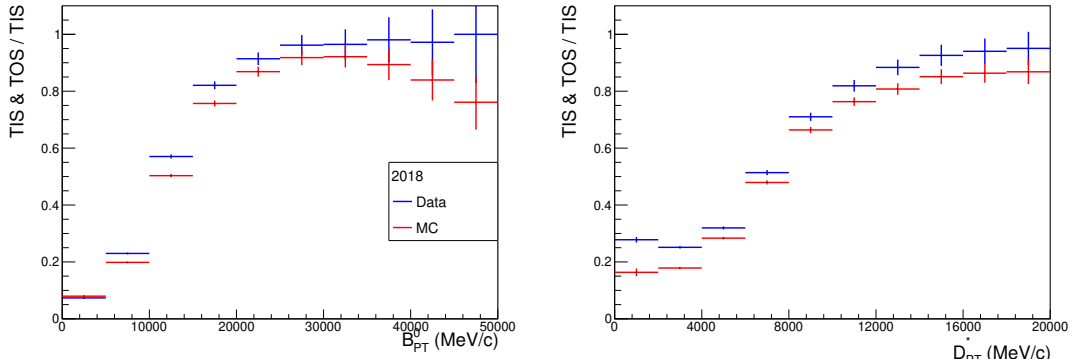

Figure 5.5.: The L0Hadron trigger TOS efficiency as a function of η of B and D candidates are obtained for $B \longrightarrow D^*3\pi^{\pm}$ events in data and MC

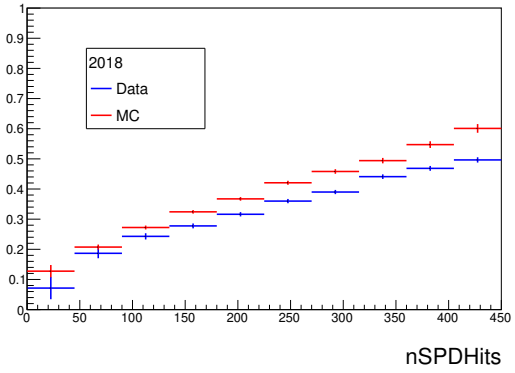

Figure 5.6.: Efficiency of the L0Hadron trigger TIS as a function of nSPDHits for $B \longrightarrow D^*3\pi^{\pm}$ events, compared between data and MC.

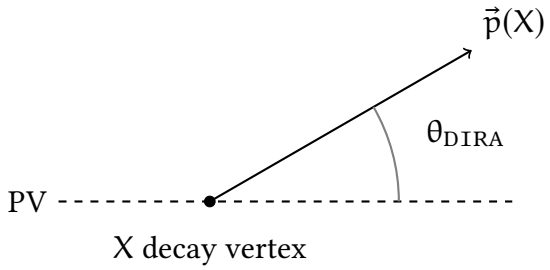

Figure 5.7.: Illustration of DIRA(X, PV) variable.

vant to a set of physics analyses.

It comprises generic selections, called *lines*, usually used by more than one analysis. The following lines `Stripping{name}ForB2XTauNuAllLines` are used, where **name** is:

- `B0d2DstarTauNu`: applied for 2015–2018 dataset, and only 2015–2016 for MC samples. The B^0 candidate is reconstructed by requiring a $D^{*\pm}$ and a $\tau^{\pm}$:
  - The D^{*-} is reconstructed from a D^0 and a π^-, and D^0 from a K^+ and a π^-, these pions coming from the D^{*-} decay, are referred to as slow pions;
  - The τ^+ from a $3\pi^{\pm}\nu_\tau$ decay.
- `B0d2DstarTauNuWS`: applied for 2015–2018 dataset. The B^0 candidate is formed from a same-sign combination of a $D^{*\pm}$ and a $\tau^{\pm}$. This is the only difference with respect to the first line. It is used to study combinatorial background, which is denoted by Wrong-Sign (WS).

These lines were specifically written for [2, 3], and are used in this analysis.

The stripping versions used are summarized in Tab. B.3.

The following variables are used:

- Distance in the Direction Angle (DIRA): the cosine of the angle between the X momentum and the line of flight from the best PV to the X particle decay vertex DIRA(X, PV) as illustrated in Fig. 5.7.
- The DOCA between the flight directions of the X_i and X_j particles DOCA(X_i, X_j).

The selection criteria, for the D^{*-} candidate, are as follows:

- The $K^-\pi^+$ system is constructed based on: track momenta (p and/or p_T), vertex quality (χ^2/ndf), low track ghost probability[3], sufficient separation from the PV indicated by variables χ^2 and χ^2_{IP}, and particle identification PID requirements.
- A D^0 candidate is then established by ensuring the absolute mass difference from the known D^0 mass is within a predefined limit. Furthermore, the decay products K^- and π^+ of the D^0 must exhibit a DOCA of less than $0.5\,\mathrm{mm}$, and form a vertex with a χ^2 quality better than 15.
- Similar track quality requirements are enforced for the π^- originating from the D^{*-}, ensuring consistency in selection standards across different decay products.
- Finally, the D^{*-} candidate is formed from the $\pi^- D^0$ system. This involves confirming a χ^2/ndf of less than 25 for the $D^0\pi^-$ vertex, constraining the mass difference between D^{*-} and D^0 to be between 135 and 160 MeV/c^2, requiring a p_T greater than 1250 MeV/c^2, and verifying that the D^{*-} mass is within 50 MeV/c^2 of the known D^{*-} mass.

For the τ^+ candidate, the selection criteria are as follows:

- The mass of the three-pion system, $m(3\pi^\pm)$, is required to fall within the range of $[400, 3500]\,\mathrm{MeV}/c^2$.
- Track quality and kinematic requirements:
  - Each track in the system must have a quality ratio $\chi^2/\mathrm{ndf} < 25$.
  - DIRA between the $3\pi^\pm$ and the PV must be greater than 0.99.
  - DIRA between any two $\pi^\pm$ candidates must be under $0.15\,\mathrm{mm}$.
  - The minimum mass of any $\pi^+\pi^-$ combination within the $3\pi^\pm$ system should be below 1670 MeV/c^2.
  - At least one daughter must have an IP chi-squared χ^2_{IP} with respect to any PV greater than 5, and no more than one daughter can have a transverse momentum (p_T) below 300 MeV/c.
- $\pi^\pm$ individual requirements:
  - Each $\pi^\pm$ must have a p_T greater than 250 MeV/c.
  - The minimum χ^2_{IP} with respect to any PV should be greater than 4.
  - The track quality ratio for each $\pi^\pm$ must be smaller than 4.

[3] the likelihood that a track does not correspond to a real particle passage.

– The PID Kaon (K PID) value for each $\pi^{\pm}$ should be less than 8.

The B^0 candidate is reconstructed by combining the previously selected D^{*-} and the $3\pi^{\pm}$ system. The selection criteria for the B^0 candidate are as follows:

- The mass difference between the combined $D^{*-}\tau^+$ system and the known B^0 mass must fall within the range $[2579, 300]\,\mathrm{MeV/c^2}$.
- DIRA between the B^0 momentum vector and the PV is required to be greater than 0.995.
- DOCA between the D^{*-} and τ^+ candidates must be smaller than 15 mm.

The stripping cuts are summarized in Tabs. 5.3 and 5.4. In addition, custom filtering cuts are applied. These cuts are similar for the 2015–2018 data collision, and 2015–2016 MC samples, but are different for the 2017 and 2018 MC samples, as shown in Tab. 5.5. D2DVVDCHI2SIGN evaluates the signed χ^2 of the vertex-to-vertex distance for different daughter particles in a decay chain.

The impact of these tighter cuts on the 2017 and 2018 MC samples is shown in Fig. 5.8. At first glance, the application of these tight cuts predominantly eliminates the prompt background, which appears beneficial. However, the analysis required to estimate the prompt background for the decay $B \longrightarrow D^{*-}3\pi^{\pm}X$ necessitates looser cut on the $\Delta z(B^0, \tau^+)$ variable. As outlined in Sec. 7.1.1.1, the estimation process cannot proceed in the same manner as before due to these modifications in the online selection criteria.

These stripping cuts are implemented within the DaVinci framework. To optimize the computing workflow, and save disk space, additional preselection cuts are applied at this stage. The cuts are summarized in Tab. 5.6., and include:

- The slow-pion p_T from the D^{*-} candidate must exceed $110\,\mathrm{MeV/c}$.
- A good τ^+ vertex quality, $\mathtt{vtx}\,(\chi^2/\mathrm{ndf})$, must be less than 10.
- The radial distance of τ^+ from the PV $r(\tau^+, \mathrm{PV})$, must be within $[0.2, 5.0]\,\mathrm{mm}$.
- The χ^2 of the impact parameter IP of the $\overline{D}^0$ candidate with respect to the PV must be greater than 10, and for the $\pi^{\pm}$ from the τ^+, it must exceed 15.
- Either the flight distance of the τ^+ from the B^0 vertex tau_FDCHI2_ORIVX must be greater than 4, to preferentially select *signal candidates*, or the mass of the B^0 must be over $5\,\mathrm{GeV/c^2}$, targeting the *normalization mode* which is fully reconstructed.

The efficiency of the online cuts is given in Sec. 5.7.

Requirement	
D^{*-} **cuts**	
vertex quality $\chi^2_{\text{track}}/\text{ndf}$	< 25
$m(D^{*-}) - m(\overline{D}^0)$	$\in [135, 160]\,\text{MeV}/c^2$
p_T	$> 1250\,\text{MeV}/c$
$\left\lvert m(D^0\pi^-) - m(D^{*-})_{\text{PDG}}\right\rvert$	$< 50\,\text{MeV}/c^2$
π^- from D^{*-} **cuts**	
p_T	$> 50\,\text{MeV}/c$
vertex quality $\chi^2_{\text{track}}/\text{ndf}$	< 30
Track ghost probability	< 0.6
D^0 **cuts**	
p_T	$> 1.2\,\text{GeV}/c$
$\left\lvert m(K^-\pi^+) - m(D^0(\text{PDG}))\right\rvert$	$< 40\,\text{MeV}/c^2$
DIRA (D^0,PV)	> 0.995
χ^2 separation from related PV,	> 36
vertex quality $\chi^2_{\text{track}}/\text{ndf}$	< 10
DOCA(K^-, π^+)	$< 0.5\,\text{mm}$
$\chi^2_{\text{DOCA}(K^-,\pi^+)}$	< 15
π^- from D^0 **cuts**	
p	$> 2\,\text{GeV}/c$
p_T	$> 250\,\text{MeV}/c$
vertex quality $\chi^2_{\text{track}}/\text{ndf}$	< 3
Track ghost probability	< 0.4
K PID	< 50
$\min[\chi^2_{\text{IP}}]$ w.r.t. any PV	> 10
K^+ from D^0 **cuts**	
p	$> 2\,\text{GeV}/c$
p_T	$> 250\,\text{MeV}/c$
vertex quality $\chi^2_{\text{track}}/\text{ndf}$	< 30
Track ghost probability	< 0.4
K PID	> -3
$\min[\chi^2_{\text{IP}}]$ w.r.t. any PV	> 10

Table 5.3.: Stripping cuts applied for 2015–2018 data and MC samples.

Requirement	
τ^+ cuts	
$m(3\pi^\pm)$	$\in [400, 3500]\,\mathrm{MeV/c^2}$
vertex quality $\chi^2_{\mathrm{track}}/\mathrm{ndf}$	< 25
DIRA (τ^+, PV)	> 0.99
$\max[\mathrm{DOCA}(\pi^\pm{}_i, \pi^\pm{}_j)]$	$< 0.15\,\mathrm{mm}$
$\min[m(\pi^+\pi^-)]$	$< 1670\,\mathrm{MeV/c^2}$
At most 1 daughter with p_T	$< 300\,\mathrm{MeV/c}$
At least 1 daughter with $\min[\chi^2_{\mathrm{IP}}]$ w.r.t. any PV	> 5
$\pi^\pm$ from τ^+ cuts	
p_T	$> 250\,\mathrm{MeV/c}$
$\min[\chi^2_{\mathrm{IP}}]$ w.r.t. any PV	> 4
vertex quality $\chi^2_{\mathrm{track}}/\mathrm{ndf}$	< 4
K PID	< 8
B^0 cuts	
$m(D^{*-}3\pi)$	$\in m(B^0)^{+300}_{-2579}\,\mathrm{MeV/c^2}$
DIRA (B^0, PV)	> 0.995
DOCA $(D^{*-}, 3\pi^\pm)$	$< 1\,\mathrm{mm}$

Table 5.4.: Stripping cuts applied for 2015–2018 data and MC samples.

Requirement	
Common filtering cuts	
$m(D^*3\pi^\pm)$	$\in m(B^0)^{+300}_{-2579}\,\mathrm{MeV}/c^2$
	OR
$m(D^*3\pi^\pm)$	$\in m(B^0)^{+1721}_{+720}\,\mathrm{MeV}/c^2$
$\mathrm{DOCA}(D^{*-}, 3\pi^\pm)$	$< 0.15\,\mathrm{mm}$

Standard cut	Tight cuts	
	$\mathtt{DIRA}(B^0, \mathrm{PV})$	> 0.995
	and	
$\mathtt{DIRA}(B^0, \mathrm{PV})$ > 0.995	$\Big(m(B^0)$	$> 4500\,\mathrm{MeV}/c^2$
	or	
	$\mathtt{D2DVVDCHI2SIGN}$	$> 4\Big)$

Table 5.5.: Filtering cuts for 2015–2018 collision data and 2015–2016 MC samples (left), and for 2017–2018 MC samples (right).

Requirement		Targeted Background
$p_T(\pi^-)$	$> 110\,\mathrm{MeV}/c$ (π^- from D^{*-})	combinatorial
$\mathtt{vtx}\,(\chi^2/\mathrm{ndf})_{\tau^+}$	< 10	combinatorial
$r(\tau^+, \mathrm{PV})$	$\in [0.2, 5.0]\,\mathrm{mm}$	spurious
$\chi^2\left[\mathrm{IP}_{\mathrm{PV}}\left(\overline{D}^0\right)\right]$	> 10	prompt
$\chi^2\left[\mathrm{IP}_{\mathrm{PV}}(\pi^\pm)\right]$	> 15 ($\pi^\pm$ from τ^+)	combinatorial
`tau_FDCHI2_ORIVX`	> 4	prompt
	or	
$m\left(B^0\right)$	$> 5\,\mathrm{GeV}/c^2$	partially reconstructed

Table 5.6.: Selection criteria applied at the DaVinci level.

Requirement		Targeted Background
$PV(\overline{D}^0)$	$= PV(\tau^+)$	combinatorial
`totCandidates`	$= 1$	track multiplicity
$\Delta z(PV, \tau^+)$	> 10	prompt
`nSPDHits`	< 450	track multiplicity
$\Delta z(B^0, \tau^+)$	> 2	remove prompt (for signal)
or		
$\Delta z(\tau^+, D^0)$	> 4	require prompt (for normalization)
AND $m(B^0)$	$> 5150\,\mathrm{MeV}/c^2$	partially reconstructed (for normalization)

Table 5.7.: Initial offline selection criteria for all modes.

5.4. Initial Offline Selection Cuts

The initial offline selection, common across all modes, is detailed in Tab. 5.7. The requirements summarize as follows:

- To eliminate combinatorial backgrounds, the $\overline{D}^0$ must share the PV with the τ^+.
- Only events with a single $B^0 \to D^{*-}\tau^+\nu_\tau$ candidate are accepted. This requirement help in reducing candidate multiplicity.
- The number of hits in the SPD detector is restricted to fewer than 450 to manage event occupancy and improve selection efficiency.
- Specific cuts:
  - For signal: Δz between the τ^+ and B^0 vertices must exceed 2, to remove efficiently prompt backgrounds.
  - For normalization: Δz between the τ^+ and D^0 vertices is required to be at least 4, ensuring that the $3\pi^\pm$ system originates directly from the B^0. In addition, the B^0 mass must exceed $5150\,\mathrm{MeV}/c^2$.

These criteria, particularly the final logical "OR" condition, are implemented primarily for efficiency computation and are documented for consistency. The final three entries in the selection criteria operate primarily as a computational strategy to retain events that satisfy either *signal* or *normalization* conditions through a logical "OR". This method ensures consistency across the dataset, particularly for the computation of efficiencies, discussed in Sec. 5.7.

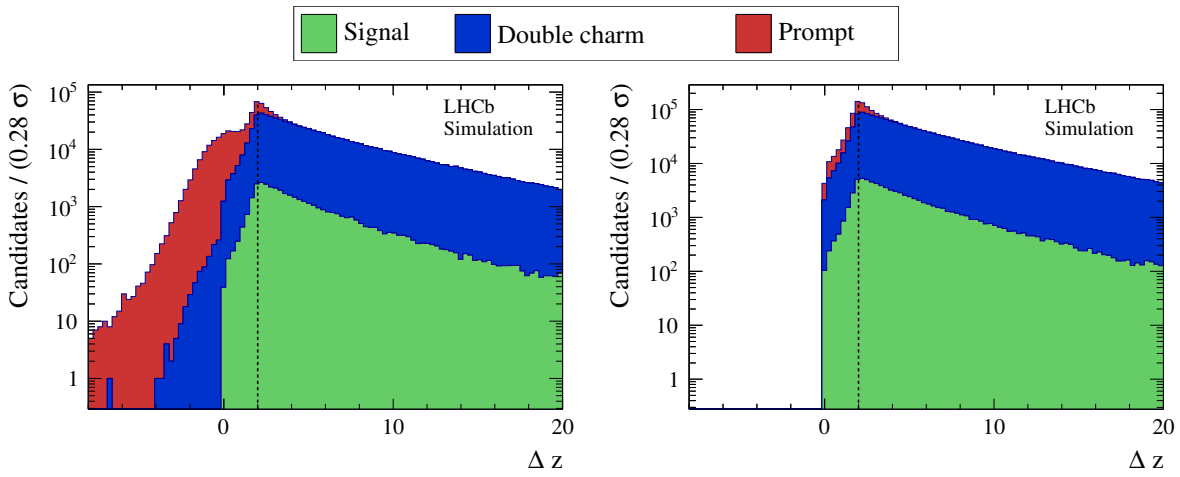

Figure 5.8.: Vertex detachment variable $\Delta z(B^0, \tau^+)$ between the simulated signal sample, double charm and prompt backgrounds, using 2015–2016 (left) and 2017–2018 (right) samples, before applying the common selection criteria.

5.5. Multivariate Analysis

MVA is a statistical technique used to classify events based on multiple input variables. The technique used in this document, follows closely [3], where the variables have been optimized.

BDT is a MVA technique [163] which enhances classification accuracy by combining the predictions of multiple decision trees.

The BDT algorithm works as follows:

1. First, the dataset is divided into two parts: a *training sample* and a *testing sample*. The training sample is used to train the *decision tree*, while the testing sample is used to evaluate the performance of the trained decision tree. A list of relevant variables (inputs) that distinguish signal from background is set. Each event is then passed through the decision tree, where it is classified as either signal or background based on the values of these variables. The tree splits the data at each node by choosing the best separation between signal and background events. This process continues recursively until a stopping criterion is met.

2. Boosting is a technique used to improve the performance of a decision tree, by combining multiple decision trees to create a strong classifier. The key idea is to train multiple decision trees sequentially, where each tree tries to correct the errors made by the previous

ones. During this process, a misclassification weight is assigned to each event: events that are misclassified receive higher weights, while correctly classified events receive lower weights. These weights are updated at each iteration, so that subsequent trees focus more on the misclassified events. This iterative process continues until a specified number of trees have been created, or the performance improvement becomes marginal.

3. Finally, a BDT score (output) is assigned to each event, which is the normalized sum of the predictions of all the trees. The BDT score is high for signal-like events and low for background-like events. By choosing a threshold on the BDT score, one can prioritize signal purity or signal efficiency.

In the following, the BDTs will be described, including the input variables, the training samples, and the performance of the BDTs. The BDTs are trained separately for different data-taking periods, specifically for 2015–2016, 2017 and 2018. As an illustrative example, plots showing the performance of the BDTs for the 2018 dataset will be presented. The resulting BDT variables will be used to obtain high signal purity (Secs. 5.6.1 and 5.6.2) or background-enriched samples for control modes (Chap. 6).

5.5.1. Anti-Combinatorial BDT

The objective of the first MVA algorithm is to remove the combinatorial backgrounds events, where the τ^+ and D^{*-} systems do not originate from the same B^0 vertex. The following variables are used for the anti-combinatorial-background BDT with the TMVA package integrated in ROOT [164]:

- D^{*-} and τ^+ transverse momentum: $p_T(D^{*-})$ and $p_T(\tau^+)$
- D^{*-} and τ^+ pseudorapidity: $\eta(D^{*-})$ and $\eta(\tau^+)$
- Quality of the impact parameter of a given particle w.r.t. the best PV of that particle: $\chi^2[\mathrm{IP}_{\mathrm{PV}}(B^0)]$ and $\chi^2[\mathrm{IP}_{\mathrm{PV}}(D^{*-})]$
- B^0 vertex quality: $\mathtt{vtx}(\chi^2/\mathrm{ndf})_{B^0}$
- Angle between the B^0 momentum and the line of flight from the PV to the B^0 decay vertex: $\mathrm{acos}\big(\mathtt{DIRA}(B^0, \mathrm{PV})\big)$
- Angle between the τ^+ momentum and the line of flight from the τ^+ origin to the decay vertex: $\mathrm{acos}(\mathtt{DIRA}(\tau^+, \mathtt{ORIVX}(\tau^+)))$
- Cylindrical distance between the τ^+ decay vertex and the PV: $\mathrm{BPVVDR}(\tau^+)$

The BDT is trained on:

Rank	Variable	Importance
1	$p_T(D^{*-})$	0.1459
2	$\log\left(\mathtt{vtx}(\chi^2/\mathrm{ndf})_{B^0}\right)$	0.1447
3	$\log\left(\mathrm{acos}\left(\mathtt{DIRA}(B^0, PV)\right)\right)$	0.1205
4	$\mathtt{BPVVDR}(\tau^+)$	0.09815
5	$p_T(\tau^+)$	0.09613
6	$\chi^2[IP_{PV}(B^0)]$	0.08272
7	$\log(\mathrm{acos}(\mathtt{DIRA}(\tau^+, \mathtt{ORIVX}(\tau^+))))$	0.08154
8	$\eta(D^{*-})$	0.07985
9	$\eta(\tau^+)$	0.077974
10	$\log\left(\chi^2[IP_{PV}(D^{*-})]\right)$	0.0725

Table 5.8.: Ranking of the combinatorial BDT input variables.

- Signal: $B^0 \longrightarrow D^{*-}\tau^+\nu_\tau$ MC
- Background: wrong-sign data, where $D^{*\pm}$ and $\tau^\pm$ have the same charge and come from different b−hadrons (*cf.* Sec. 5.3)

The training samples are selected with the initial selection (*cf.* Sec. 5.4) and a loose detachment cut $\Delta z(B^0, \tau^+) > 2$.

Figs. 5.9 and 5.10 show the discrimination power of the input variables for the signal and background as defined above.

Fig. 5.11 depicts correlations between the input variables of the combinatorial BDT. The variables exhibit relative correlations below 50-60%, except $\eta(\tau)$ vs. $\eta(D^*)$ (correlation 80% (76%) for signal (background)).

The most performant (with curve closest to the top-right corner), BDTD is chosen as the default one. Fig. 5.12 (left) shows the combinatorial BDTD distribution for the training signal and background samples. The distribution for the testing samples are also overlaid and they show good agreement with that of the training samples. A cut is applied in the middle of the anti-combinatorial BDT range, *i.e.* at 0, as a preliminary working point. This preserves approximately 77% of the signal and rejects around 75% of the combinatorial background.

The importance of each input variable is given in Tab. 5.8.

Fig. 5.13 compares the MC/data distribution of the combinatorial BDT for the fully reconstructed $B^0 \longrightarrow D^{*-}3\pi$ mode. A discrepancy is observed between the MC and data distributions,

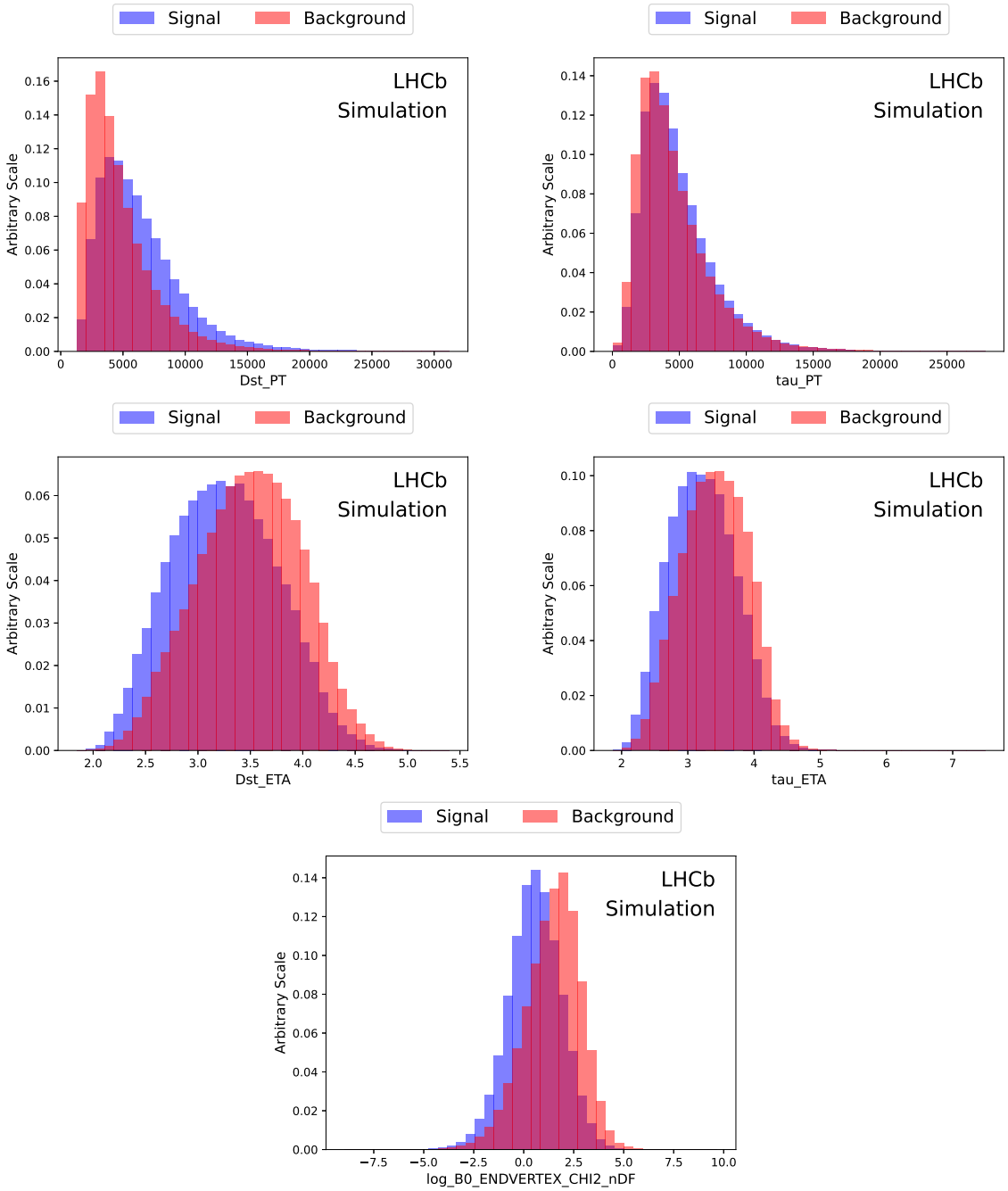

Figure 5.9.: Distributions of input variables for the combinatorial BDT for the signal (blue) and background (red).

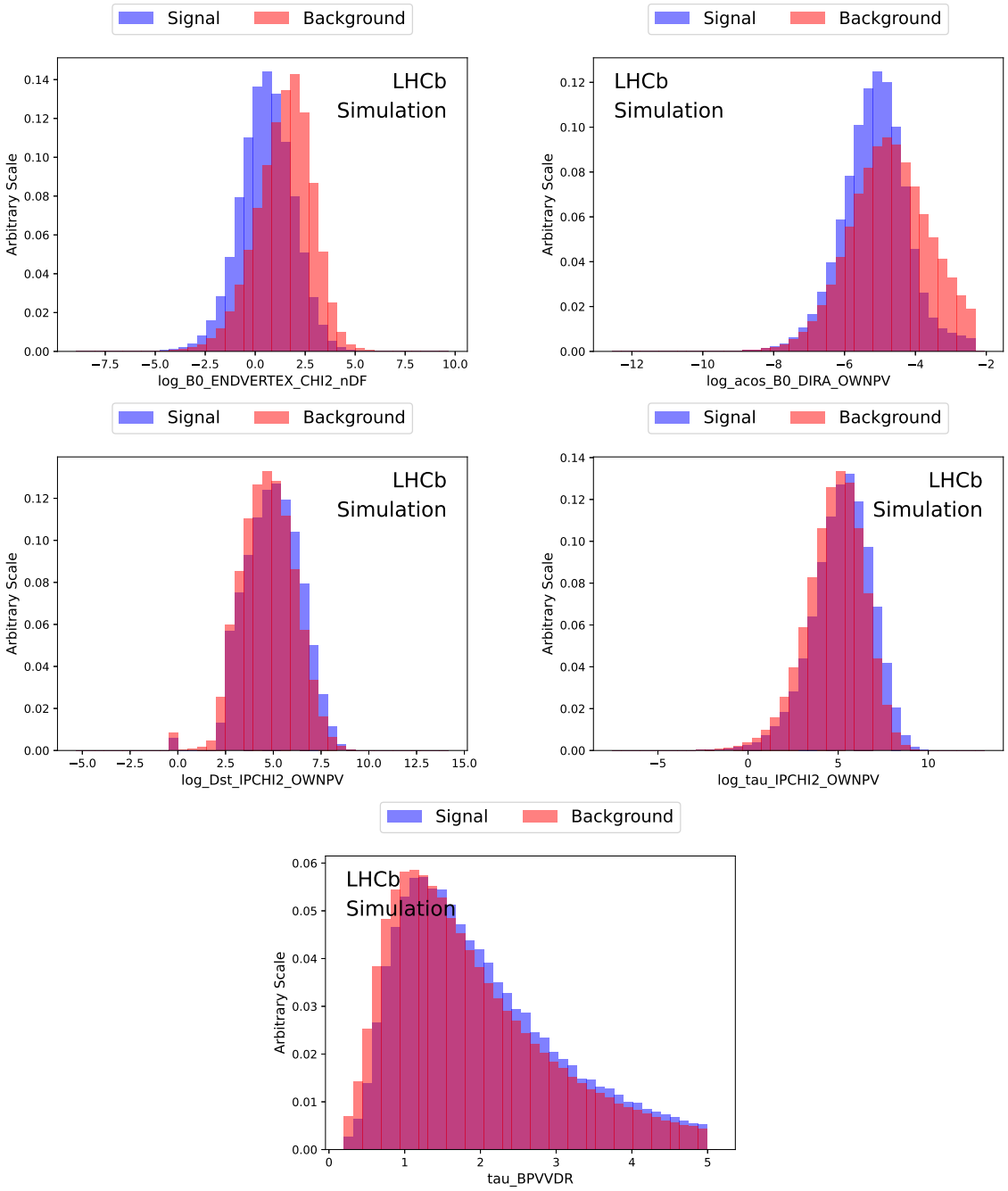

Figure 5.10.: Distributions of input variables for the combinatorial BDT for the signal (blue) and background (red).

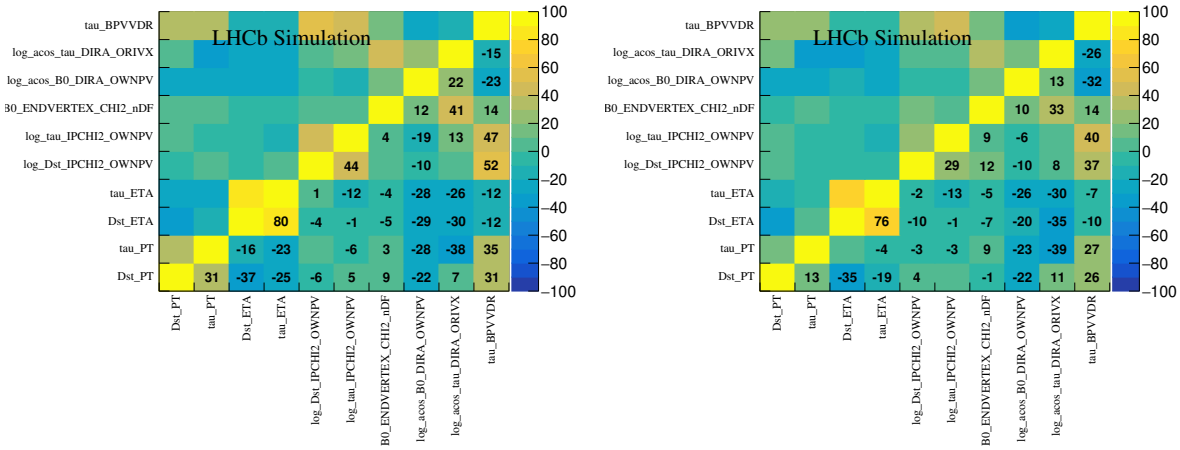

Figure 5.11.: Correlation matrix of the combinatorial BDT input variables for signal (left) and background (right) samples.

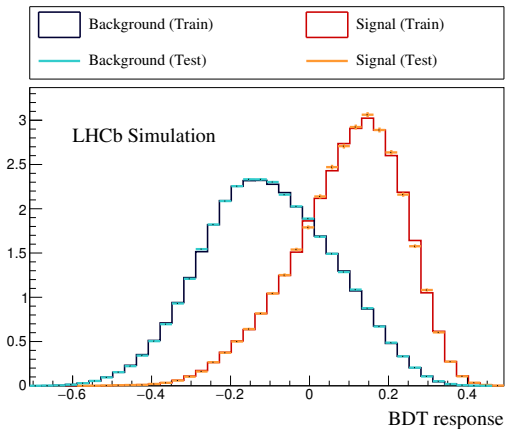

Figure 5.12.: combinatorial BDTD distribution for signal training (dark blue), signal testing (cyan), background training (dark red) and background testing (orange) samples.

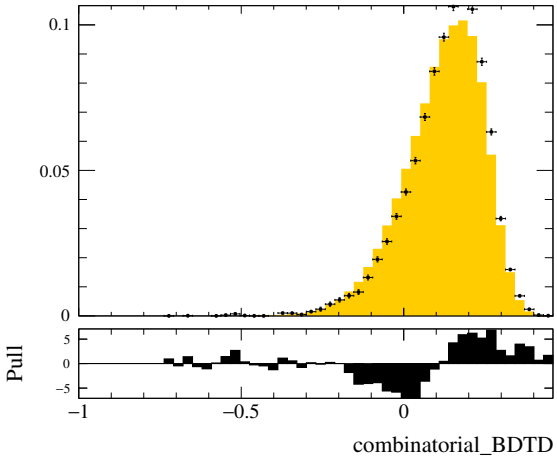

Figure 5.13.: Data (black points) / MC (coloured bins) comparison for the combinatorial BDTD distribution as for the $B^0 \to D^{*-}3\pi$ mode in the region $m(3\pi^{\pm}) < 1.6\,\mathrm{GeV}/c^2$.

indicating that the agreement is not perfect. Efforts are currently underway to investigate and understand the cause of this discrepancy.

5.5.2. Charged Isolation BDT

To reject background events that include additional charged tracks besides the signal candidates, a charged isolation technique is employed. This technique detects charged tracks that form good vertices with the signal tracks, as illustrated in Fig. 5.14, where the decay $B^0 \to D^{*-}D^0K^+$ and $D^0 \to K^-3\pi^{\pm}$ exhibits two extra charged tracks ($K^{\pm}$ in magenta) in addition to those compatible with the $B^0 \to D^{*-}\tau^+\nu_\tau$ tracks (green).

The isolation algorithms utilize both track-based and vertex-based isolation variables. The track-based variables, for a given signal-candidate track, indicate how close it is to non-signal (underlying) tracks in the event. Each of the six charged tracks in $B^0 \to D^{*-}\tau^+\nu_\tau$ has such a variable. The vertex-based variables, however, scan all the tracks usually constrained to a given cone around the flight direction of the particle whose vertex is considered.

Regardless of the decay mode considered (*i.e.* signal, normalization, or backgrounds), the isolation variables in this analysis are always computed relative to the signal candidate.

The variables considered are based on the LHCb packages, are as follows:

- Track isolation variables from a customised `TupleToolIsoGeneric`: `IsoSumBDT`(p),

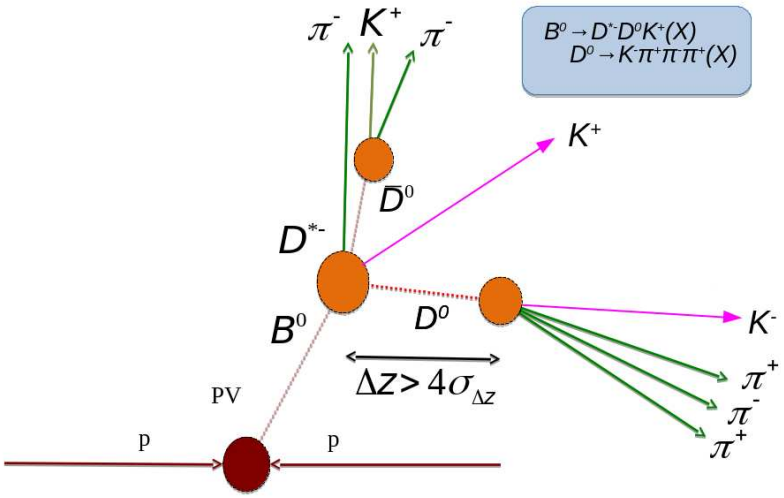

Figure 5.14.: Schematic representation of the $B^0 \to D^{*-} D^0 K^+$ decay. The green tracks are compatible with the $B^0 \to D^{*-} \tau^+ \nu_\tau$. The charged isolation detects the non-isolating (magenta) tracks.

where p is any of the 6 charged tracks in the $B^0 \to D^{*-} \tau^+ \nu_\tau$; *i.e.* $\pi^\pm$ from the D^{*-}, D^0 and τ^+ from vertices, and K^+ from the $\bar{D}^0$ vertex.

- Vertex isolation variables from (or derived from) `TupleToolVtxIsolnPlus`:
  - Number of charged tracks compatible with the τ^+ vertex after removing the tracks from D^{*-}: `nTauIso0`
  - Number of charged tracks compatible with the B^0 vertex that worsen the B^0 vertex χ^2 by not more than 25, after removing the tracks from D^{*-}: `nB0Iso25sig`

Instead of relying on rectangular cuts on these *track* and *vertex-based* variables, a custom BDT is used to incorporate them into a single *event-based* variable. Fig. 5.15 illustrates the discrimination power of these input variables for the signal and background as defined above. The correlations between the input variables for the signal and background events are shown in Fig. 5.16.

The training is performed on $b\bar{b} \to D^{*-} 3\pi X$ MC sample for both signal and background. MC samples extracted from the $b\bar{b} \to D^{*-} 3\pi X$ after the initial selections, as described in Sec. 5.4, with additional cuts listed in Tab. 5.9. The common selection for both modes includes a loose

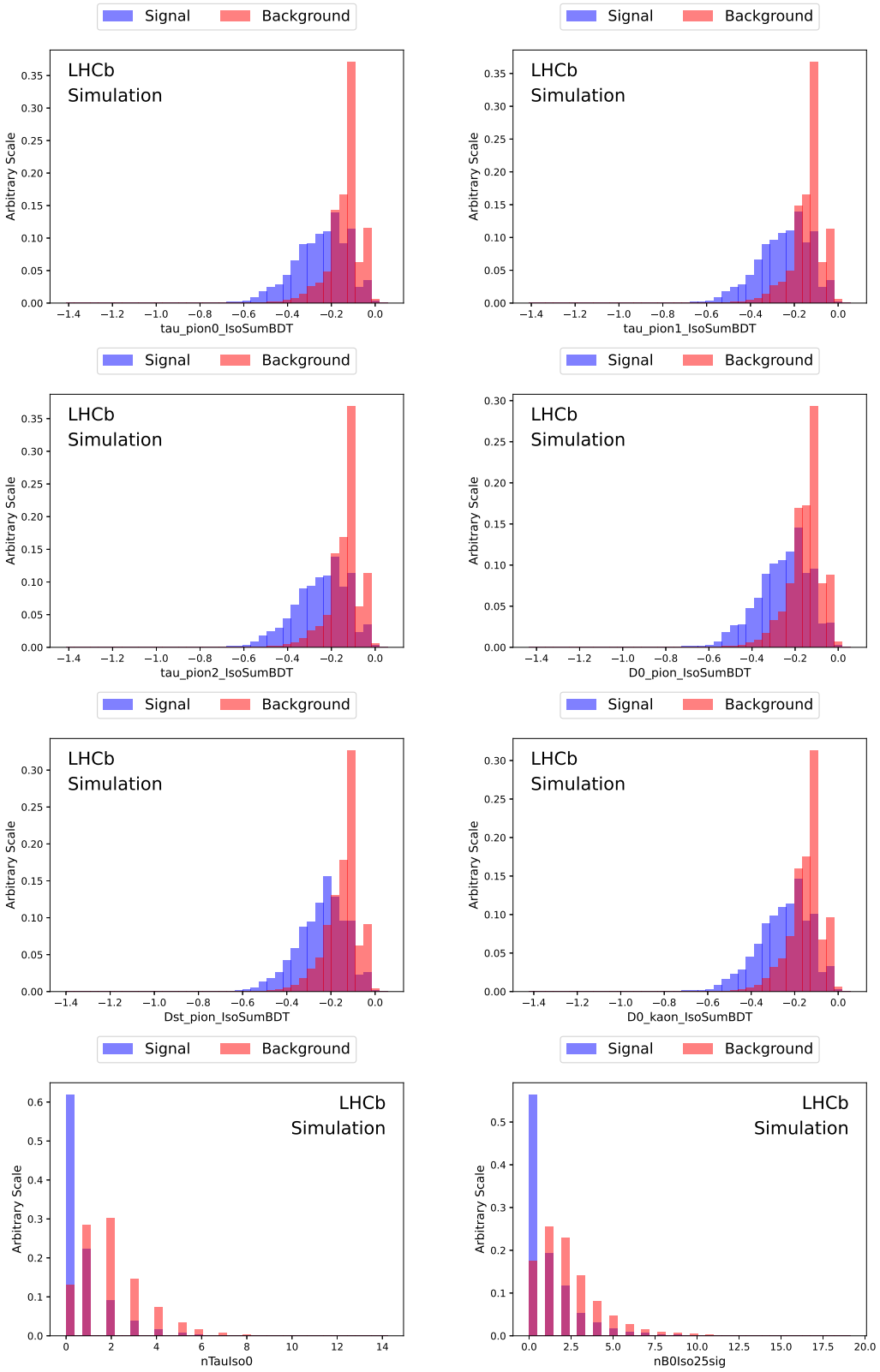

Figure 5.15.: Distributions of input variables for the isolation BDT for the signal (blue) and background (red).

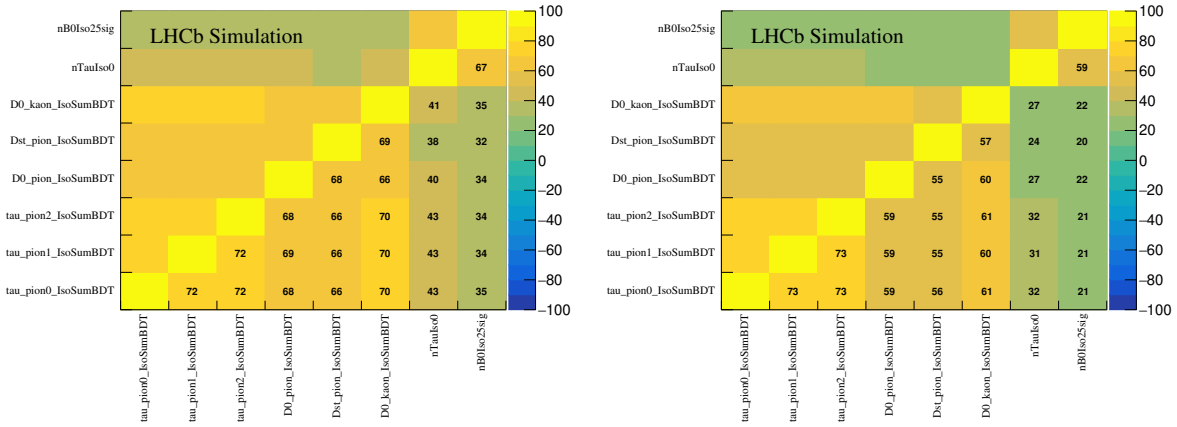

Figure 5.16.: Correlation matrix of the isolation BDT input variables for signal (left) and background (right) samples.

Requirements	
$\Delta z(B^0, \tau^+) > 2$ $m(B^0) < 5225\,\mathrm{MeV}/c^2$	
Signal	**Background**
One $K^\pm$ and $5\pi^\pm$ in the decay	Multiple $K^\pm$ or > 5 $\pi^\pm$ not from K^0_S

Table 5.9.: Selection of the training samples for the charged isolation BDT applied on top of the initial cuts discussed in Sec. 5.4.

vertex detachment requirement and a B^0 mass cut, focusing on a more signal-like phase-space region. Specifically, the signal mode will eventually need to satisfy the vertex detachment and lower B^0 reconstructed mass criteria.

The distinction between signal and background is determined using MC-truth information. The signal is required to have no extra charged tracks ($\pi^\pm$ or $K^\pm$) in the decay tree, while the background must have at least one extra track ($\pi^\pm$ or $K^\pm$). The isolation background is required to have either more than one $K^\pm$ or more than five $\pi^\pm$, excluding those from K^0_S decays. K^0_S decays typically produce a $\pi^+\pi^-$ pair 69% of the time, which decays outside the VELO and is thus 'well-isolated' from the signal candidate.

Fig. 5.17 displays the isolation BDT distribution for the signal and background in both training and testing samples, along with its background rejection as a function of signal efficiency. The AdaBoost algorithm (denoted as BDT, *cf.* App. B.3) has been identified as the most effective

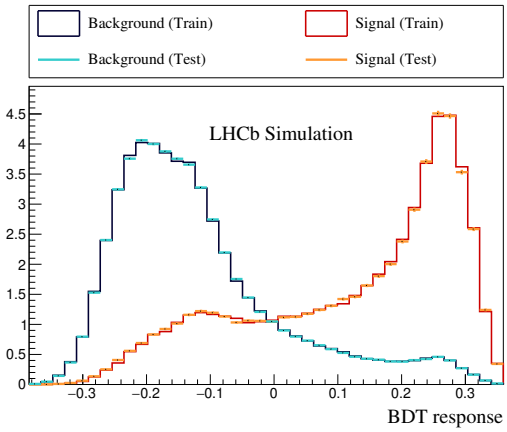

Figure 5.17.: Isolation BDT distribution for signal training (dark blue), signal testing (cyan), background training (dark red) and background testing (orange) samples.

Rank	Variable	Importance
1	nTauIso0	0.1429
2	tau_pion1_IsoSumBDT	0.1253
3	tau_pion2_IsoSumBDT	0.1226
4	tau_pion0_IsoSumBDT	0.1055
5	Dst_pion_IsoSumBDT	0.08935
6	D0_pion_IsoSumBDT	0.08629
7	nB0Iso25sig	0.08416
8	D0_kaon_IsoSumBDT	0.08116

Table 5.10.: Ranking of the isolation BDT input variables.

and has therefore been selected as the default.

5.5.3. Detachment BDT

To eliminate the background where the $3\pi^{\pm}$ system originates directly from the B^0, a vertex detachment BDT is utilized. This BDT distinguishes the $3\pi^{\pm}$ vertex from the B^0 vertex to align with the signal topology. The input variables are as follows:

- Distance between the τ^+ and B^0 vertices in the z–coordinate $\Delta z(B^0, \tau^+)$
- Distance between the τ^+ and B^0 vertices in the radial coordinate $\log\big(\Delta r(B^0, \tau^+)\big)$
- Distance between the D^0 and τ^+ vertices in the z–coordinate $\Delta z(\tau^+, D^0)$

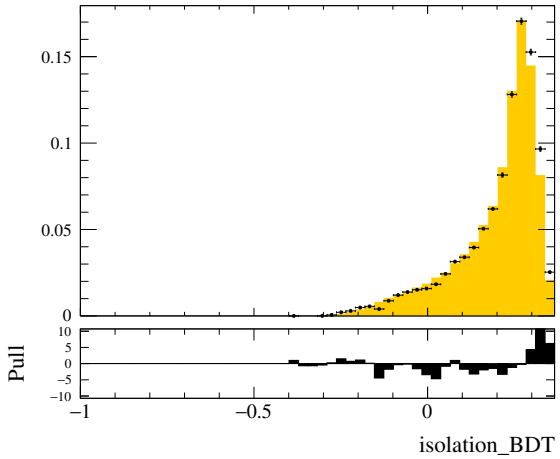

Figure 5.18.: Data (black points) / MC (coloured bins) comparison for the isolation BDT distribution as for the $B^0 \to D^{*-}3\pi$ mode.

- Angle between the τ^+ momentum and the line of flight from the τ^+ origin to the decay vertex $\mathrm{acos}(\mathtt{DIRA}(\tau, \mathtt{ORIVX}(\tau)))$
- χ^2 of the τ^+ vertex $\chi^2[\tau(\tau^+)]$
- χ^2 of the τ^+ production vertex $\chi^2[\mathtt{ORIVX}(\tau^+)]$

The training samples consist of:

- Signal: $B^0 \to D^{*-}\tau^+\nu_\tau$ MC
- Background: $b\bar{b} \to D^{*-}3\pi X$ MC

The selection criteria are specified in Tab. 5.11. Both samples must meet the loose vertex detachment requirement, $\Delta z(B^0, \tau^+) > 2$ (which will eventually be imposed for the final selection) and have the τ^+ candidates positioned further from the beampipe than the B^0 vertex, $r(\tau^+) - r(B^0) > 0$. Additionally, the signal is truth-matched with the $B^0 \to D^{*-}\tau^+\nu_\tau$ decay, while the background must not originate from the τ^+ or the charm mesons: D^0, D^+, D_s^+. This ensures that the prompt $3\pi^\pm$, coming directly from the B^0 candidate, are selected.

Fig. 5.19 shows the discrimination power of the input variables for the signal and background as defined above. The correlations between the input variables for the signal and background events are shown in Fig. 5.20.

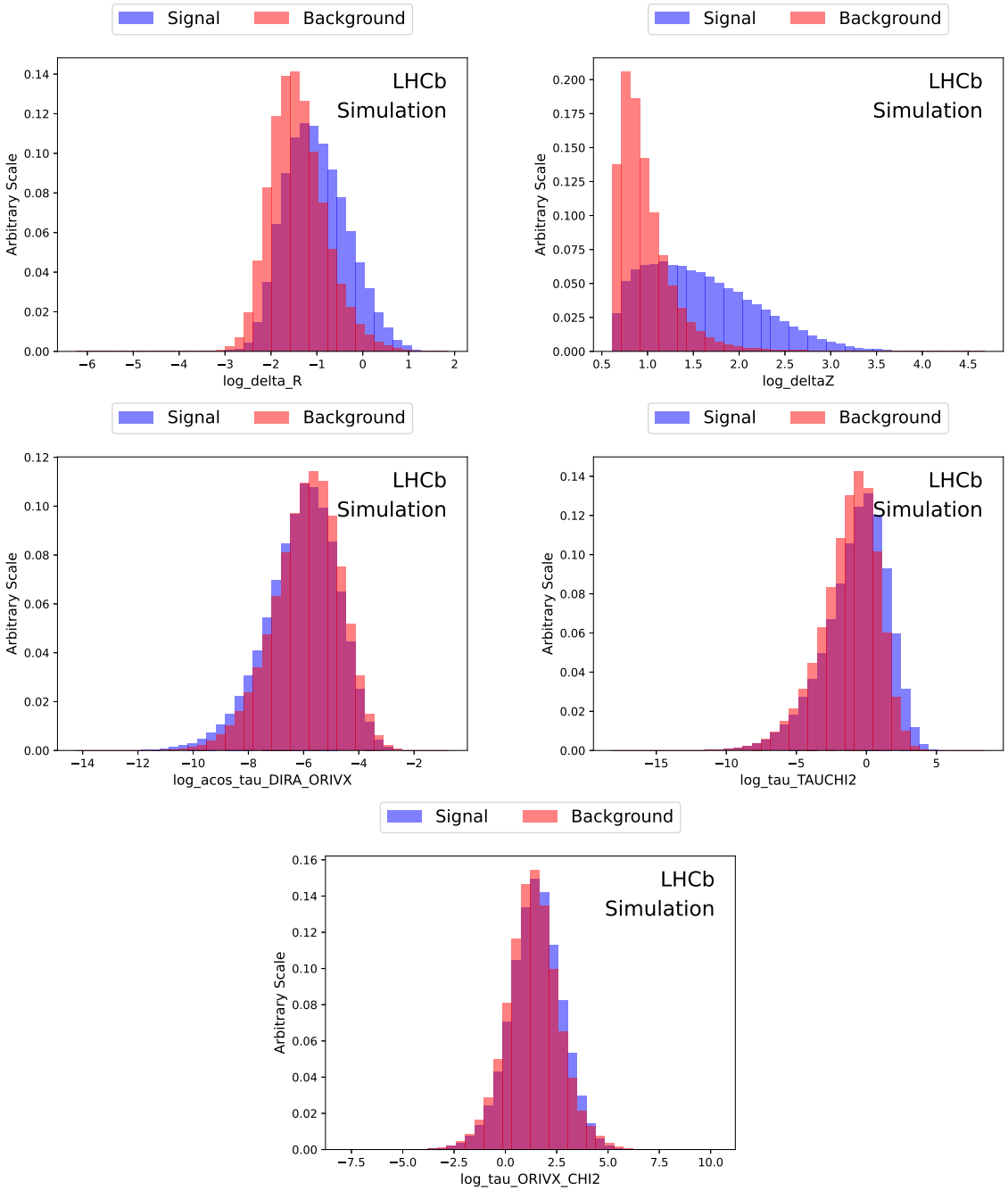

Figure 5.19.: Distributions of input variables for the detachment BDT for the signal (blue) and background (red).

Requirement	
$\Delta z(B^0, \tau^+) > 2$ $r(\tau^+) - r(B^0) > 0$	
Signal only	**Background only**
Truth-matched signal	$3\pi^{\pm}$ not from τ^+, D^0, D^+, D_s^+

Table 5.11.: Selection of the training samples for the detachment BDT applied on top of the initial cuts discussed in .

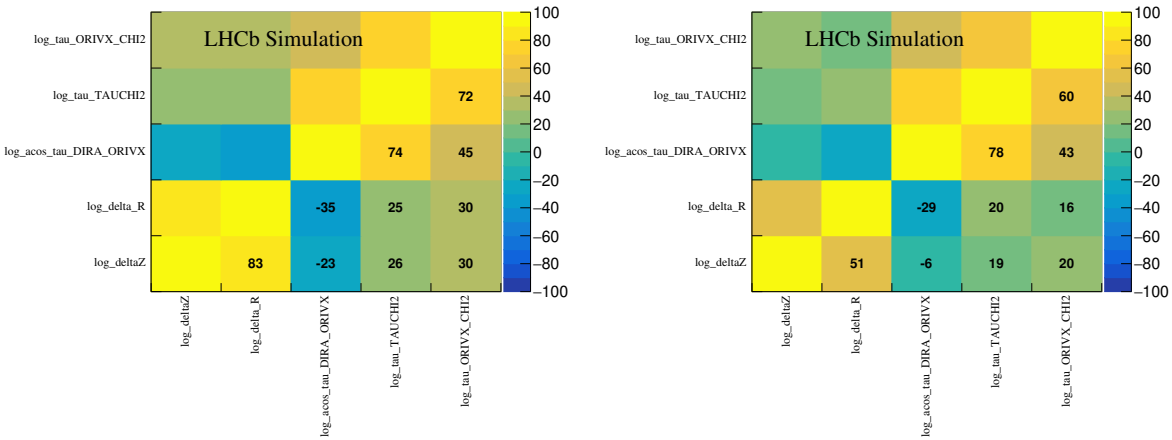

Figure 5.20.: Correlation matrix of the detachment BDT input variables for signal (left) and background (right) samples.

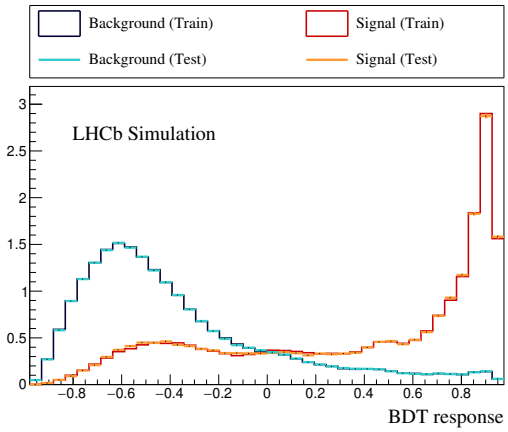

Figure 5.21.: Detachment BDT distribution for signal training (dark blue), signal testing (cyan), background training (dark red) and background testing (orange) samples.

Rank	Variable	Importance
1	$\log\big(r(\tau^+) - r(B^0)\big)$	0.2328
2	$\log\big(\Delta z(B^0, \tau^+)\big)$	0.212
3	$\log(\mathrm{acos}(\mathtt{DIRA}(\tau, \mathtt{ORIVX}(\tau))))$	0.1914
4	$\log\big(\chi^2[\tau(\tau^+)]\big)$	0.1856
5	$\log\big(\chi^2[\mathtt{ORIVX}(\tau^+)]\big)$	0.1782

Table 5.12.: Ranking of the detachment BDT input variables.

Fig. 5.21 shows the detachment BDT distribution for the signal and background in both training and testing samples, while the background rejection as a function of signal efficiency is shown in Fig. B.8. The Gradient Boost BDT (BDTG) (*cf.* App. B.3) has been identified as the most performant and is therefore chosen as the default.

A cut is applied at $\mathtt{detachment_BDTG} > 0.2$, retaining approximately 70% of the signal mode relative to the yield after the isolation cut, while rejecting around 90% of the prompt background. This cut value is considered a preliminary working point and is subject to further optimization. Nonetheless, the relatively flat distributions of both signal and background in the region $[-0.2, 0.2]$ of the detachment BDT suggest that the optimal working point should not be highly sensitive to the exact cut value.

The importance of each input variable is provided in Tab. 5.12.

Fig. 5.22 compares the MC and data distributions of the detachment BDT for the $B^0 \longrightarrow D^{*-}3\pi$ mode. The data sample has been s-weighted with respect to the B^0 mass to select an approximately pure $B^0 \longrightarrow D^{*-}3\pi$ sample. A noticeable bump in the data distribution around 1 is observed, which is likely due to the $B \longrightarrow D^{*-}D_s^+$ decay. This bump is expected to disappear if a cut on the τ mass: $m(\tau) < 1600\,\mathrm{MeV}/c^2$ is applied.

5.5.4. Anti-D_s^+ BDT

The most significant background category after rejecting the prompt background comprises events with $D^{*-}D_s^+$ X in the final state. To control the $D^{*-}D_s^+$ X contributions, a dedicated BDT, referred to as D_s^+, anti-D_s^+ or DstDs BDT, is trained using the following 17 input variables:

- Partially reconstructed variables:

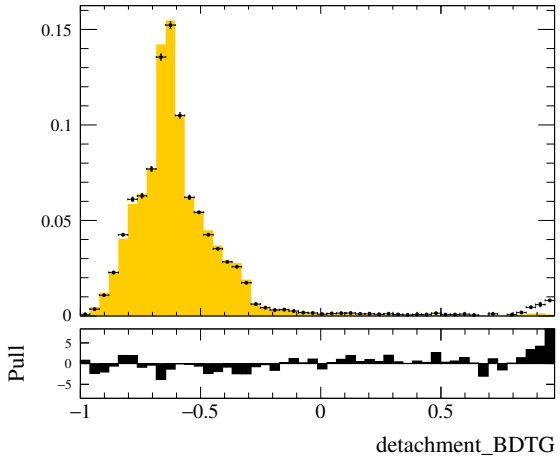

Figure 5.22.: Data (black points) / MC (colored bins) comparison for the detachment BDT distribution as for the $B^0 \longrightarrow D^{*-}3\pi$ mode.

- Signal events reconstruction variable, under the hypothesis of the signal decay (*cf.* Sec. 4.2.1):

$$p_{B^0} - p_{\tau^+} - p_{D^{*-}} \ . \tag{5.3}$$

– Background events reconstruction variables, under the background hypothesis (*cf.* Sec. 4.2.2):

- The B^0 momentum reconstructed with the scalar product method, using the corrected B^0 vertex accounting for the neutral tracks from the D_s^+ candidate $p_{B,sn}$.
- The B^0 momentum reconstructed with the vector method $p_{B,v}$:

$$\log(p_{B,v}/p_{B^0}) \ , \tag{5.4}$$

  where p_{B^0} is the momentum of the B^0 candidate, reconstructed using the charged tracks only.
- The B^0 momentum with the vector method, using the corrected B^0 vertex accounting for the neutral tracks from the D_s^+ candidate $p_{B,vn}$:

$$\log(p_{B,vn}/p_{B^0}) \tag{5.5}$$

- The normalized difference of the B^0 momenta between the scalar and vector method, using the corrected B^0 vertex for neutral tracks from the D_s^+ candidate:

$$\log(|p_{B,sn} - p_{B,vn}|/p_{B,vn}) \tag{5.6}$$

- The squared mass of the reconstructed neutral vector, N, in $D_s^+ \to 3\pi N$:

$$m(N)_\nu^2 = m(B^0)^2 + m(B^0)_{PDG}^2 + 2(p_{B,\nu} \cdot p_{D^* D_s^+} - E(B^0)_\nu E(B^0)) \quad (5.7)$$

- The reconstructed mass squared of the $D_{(s)}^{(*,**)}$ system:

$$\log\left(\sqrt{\left|m(D_s^+)_{\nu n}^2\right|}\right) \quad (5.8)$$

- Neutral and charged isolation variables

  - Background events where the $3\pi^\pm$ system is coming from D_s^+ decays are often accompanied by a large neutral energy coming from the rest of the D_s^+ decay. This neutral energy is searched in cones around the $3\pi^\pm$ system.

    The background events with $D_s^+ \to 3\pi^\pm X$ often carry significant energy in the neutral particles that is deposited in the LHCb electromagnetic calorimeter. The neutral energy around the $3\pi^\pm$ system is measured using the three variables:

    - The multiplicity of neutral objects within a cone of 0.4 opening angle[4] centered on the $3\pi^\pm$ system: `tau_0.40_nc_mult`
    - The sum of the neutral energy in a cone of 0.4 and 0.3 opening angles around the $3\pi^\pm$ system: `tau_0.40_nc_PZ` and `tau_0.30_nc_PZ`

  - Extra charged tracks isolation variables:
    - The multiplicity of charged tracks within a cone of 0.2 opening angle around the $3\pi^\pm$ system: `tau_0.20_cc_mult`
    - The sum of the P_Z of the charged tracks within a cone of 0.2 opening angle around the $3\pi^\pm$ system: `tau_0.20_cc_PZ`

- $\pi^+\pi^-$ dynamics variables: The signal decay occurs through $\tau^+ \to 3\pi^\pm\nu_\tau$ that occurs purely via the a_1 mode that decays to $\rho\pi$. Consequently the $\pi^+\pi^-$ reconstructed mass should peak around the ρ mass. On the other hand, the D_s^+ decays mostly through η and η': $\eta \to \pi^+\pi^-\pi^0$ and $\eta' \to \eta\pi^+\pi^-$. This puts the upper boundary on the $\pi^+\pi^-$ mass of around 400 MeV. These phase-space differences justify using the minimum and maximum masses of the $\pi^+\pi^-$ system in the BDT.
  - The minimum and maximum mass of the $\pi^+\pi^-$ system: $\min[m(\pi^+\pi^-)]$ and $\max[m(\pi^+\pi^-)]$

[4] Defined in the $\Delta\phi$, $\Delta\eta$ reference frame

Requirement	
$p_{B,s} > 0$	
$m(N)^2_\nu$	reject if unreconstructed
$p_{B^0} - p_\tau - p_{D^*}$	reject if unreconstructed
$\Delta z(B^0, \tau^+) > 2$	
Signal only	**Background only**
Truth-matched signal	$B^0 \to D^* DX$ MC truth (τ) candidate true ID = D_s^+

Table 5.13.: Anti-D_s^+ BDT cuts for signal and background applied on top of the initial cut-based selection (*cf.* Sec. 5.4).

- Kinematic variables:
  - The cylindrical distance between the PV and the B^0 candidate: BPVVDR(B^0)
  - The energy of the 3π system: $\log(E(3\pi))$
  - The mass of the B^0 candidate: $m(B^0)$ computed on the six-track system. This variable distinguishes fully reconstructed $D_s^+ \to 3\pi^\pm$ from the partially reconstructed signal in $\tau^+ \to 3\pi^\pm \nu_\tau$. Also, it discriminates against the $3\pi^\pm$ system where the pions do not share the same vertex.

The BDT is trained using:

- Signal: $B^0 \to D^{*-}\tau^+\nu_\tau$ MC
- Background: $b\bar{b} \to D^{*-}3\pi X$ MC

Truth–matched events to $B^0 \to D^{*-}\tau^+\nu_\tau$ decays (MC truth) are required for the signal. For the background, MC truth–matched $B^0 \to D^{*-}D_s^+ X$ events are utilized. Decays of D_s^+ via the a_1 resonance are excluded, as they closely resemble the signal decays. Tab. 5.13 details all cuts applied to the training sample, in addition to the initial cut-based selection (*cf.* Sec. 5.4).

Figs. 5.23 to 5.25 show the distribution of the input variables for the training samples.

Correlations between the variables are shown in Fig. 5.26. The variable $\log(p_{B,\nu}/p_{B^0})$ exhibits a correlation of 96% with $\log(p_{B,\nu n}/p_{B^0})$ for the signal, and 95% for the background. Although the correlation is very high, both variables are kept to maximally exploit them.

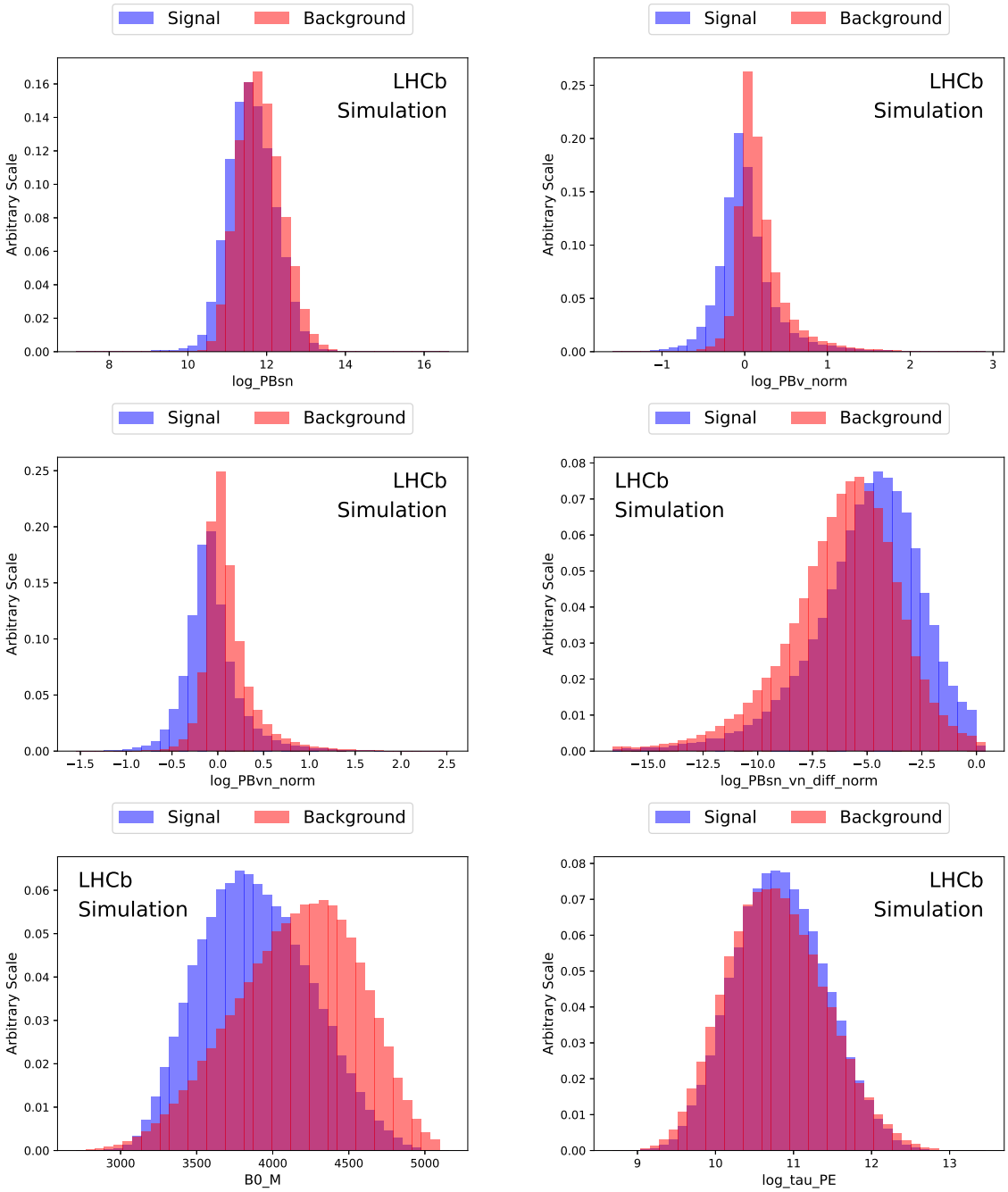

Figure 5.23.: Anti-D_s^+ BDT input variables distribution for signal (blue) and background (red) samples.

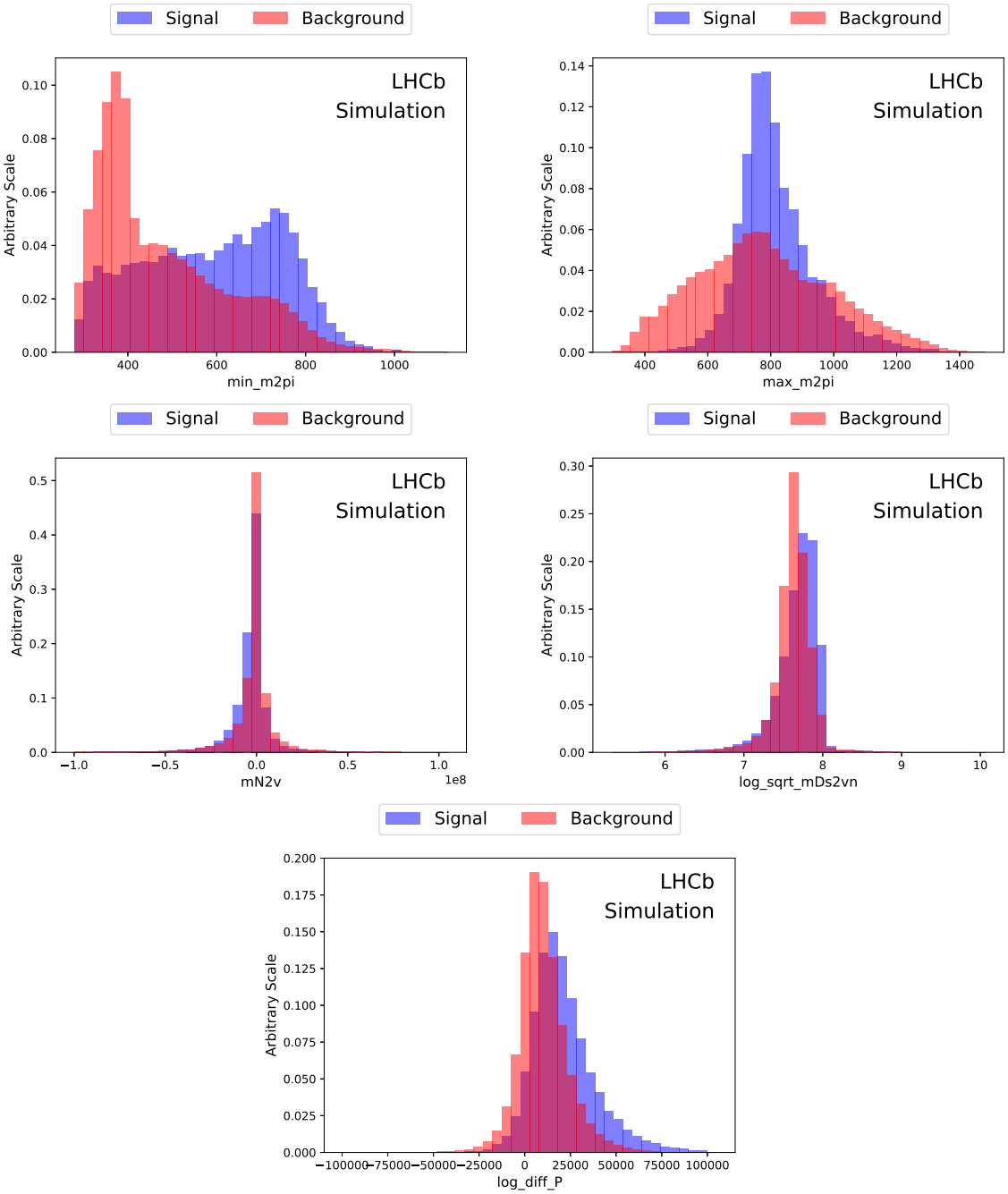

Figure 5.24.: Anti-D_s^+ BDT input variables distribution for signal (blue) and background (red) samples.

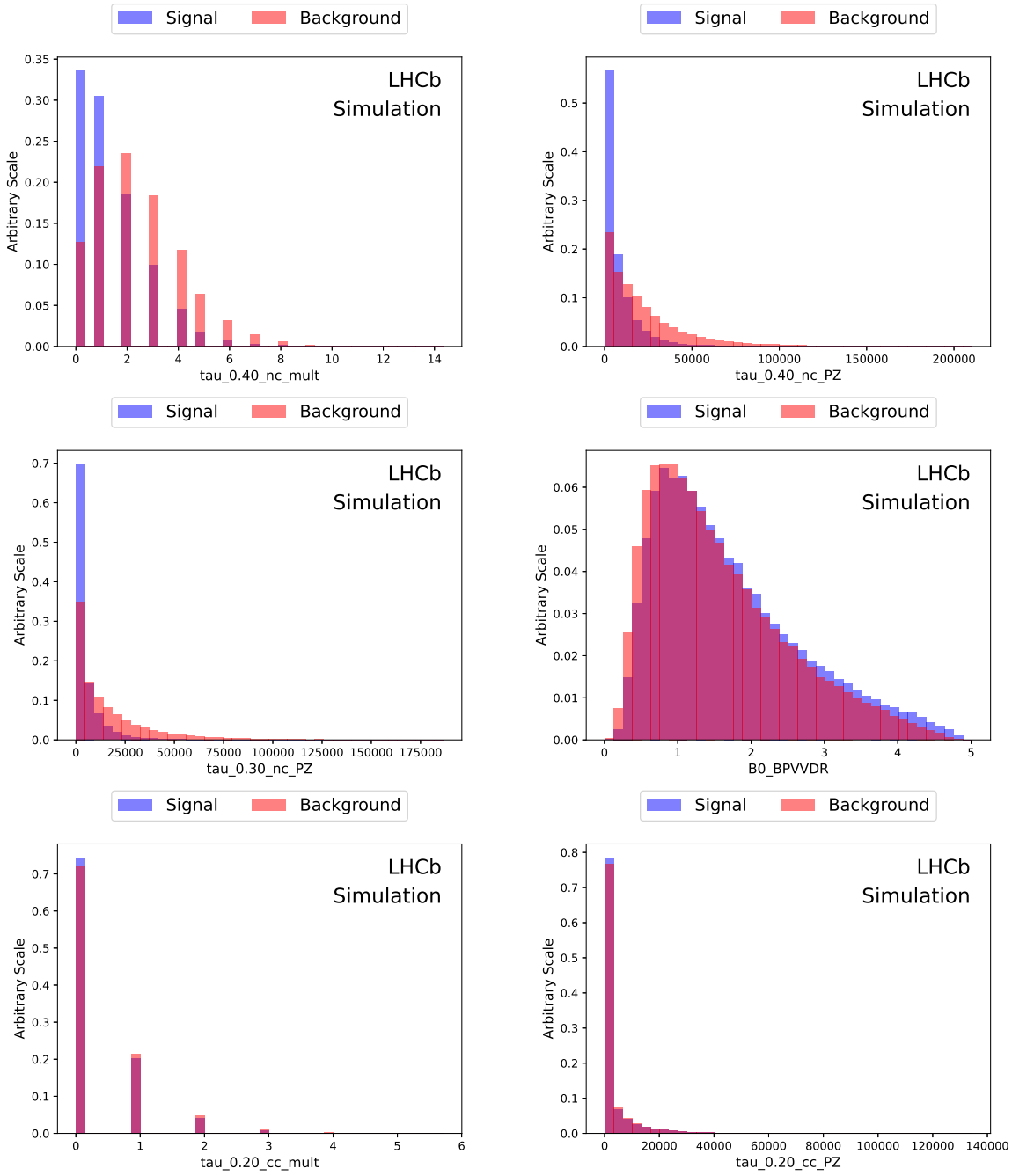

Figure 5.25.: Anti-D_s^+ BDT input variables distribution for signal (blue) and background (red) samples.

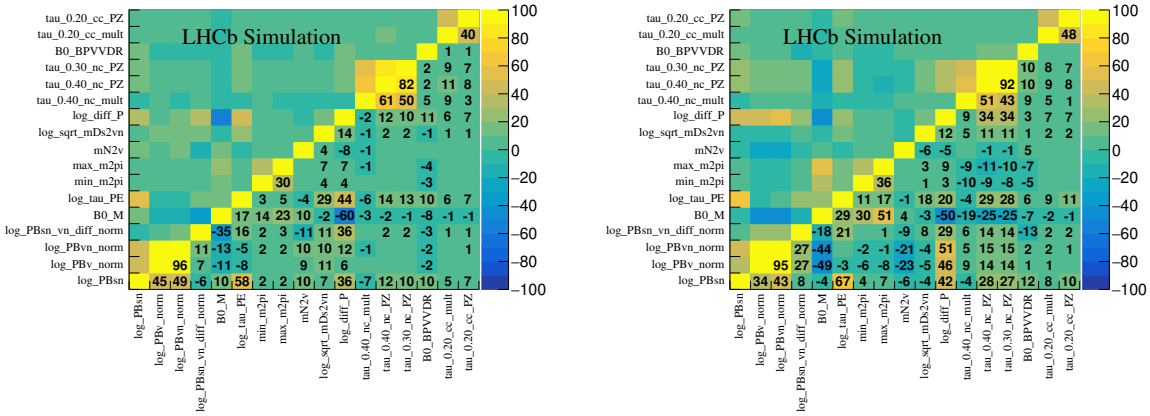

Figure 5.26.: Correlation matrix of the anti-D_s^+ BDT input variables for signal (left) and background (right) samples.

Fig. 5.27 depicts the anti-D_s^+ BDT distribution for the training and testing samples. The background rejection as a function of signal efficiency is shown in Fig. B.8. The AdaBoost BDT (*cf.* App. B.3) has been identified as the most effective and is therefore chosen as the default.

A cut is applied to the anti-D_s^+ BDT at $\texttt{DstDsX_BDT} > -0.2$, which retains nearly all the signal (signal efficiency: 97%) while rejecting approximately 40% of the background. This cut is intentionally loose, as this variable is utilized for the signal yield fit. Its primary objective is to distinguish the signal from double-charm components (mostly with D_s^+). Consequently, the cut only rejects the most obvious $B^0 \to D^{*-} D_s^+ X$ events, without sacrificing signal statistics for the final fit in Chapter 7.

The importance of the input variables is provided in Tab. 5.14. This BDT is primarily designed to discriminate the signal from double-charm backgrounds. Since it relies on the resonant structure of the $3\pi^\pm$ system, it is more meaningful to assess its data/MC agreement for the double-charm modes rather than for the prompt pions in the normalization mode. Therefore, the validation in this section does not follow the scheme used for the three preceding BDTs.

The anti-D_s^+ BDT output is compared in the normalization mode, as shown in Fig. 5.28. The agreement is good in the region containing the majority of the events.

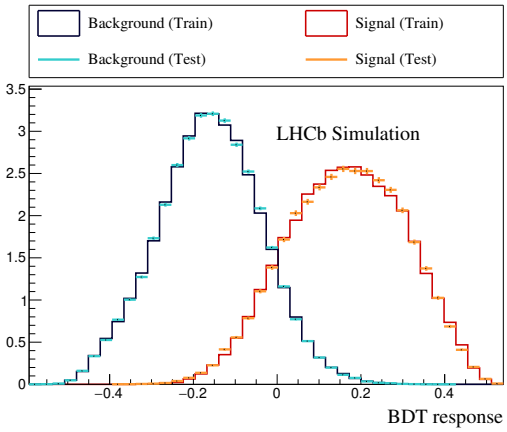

Figure 5.27.: Anti-D_s^+ BDT distribution for signal training (dark blue), signal testing (cyan), background training (dark red) and background testing (orange) samples.

Rank	Variable	Importance
1	$\log(p_{B,\nu n}/p_{B^0})$	0.1046
2	$\max[m(\pi^+\pi^-)]$	0.08875
3	$m(B^0)$	0.08186
4	$\min[m(\pi^+\pi^-)]$	0.07632
5	$\log(p_{B,\nu}/p_{B^0})$	0.0724
6	$\log(p_{B,s})$	0.06946
7	`tau_0.40_nc_PZ`	0.06421
8	$\log\left(\sqrt{\lvert m(D_s^+)^2_{\nu n}\rvert}\right)$	0.06122
9	`tau_0.30_nc_PZ`	0.0588
10	$\mathrm{BPVVDR}(B^0)$	0.05757
11	$\log(\lvert p_{B,sn} - p_{B,\nu n}\rvert/p_{B,\nu n})$	0.0529
12	$\log(E(3\pi))$	0.05289
13	$\log(p_{B,sn})$	0.04753
14	`tau_0.40_nc_mult`	0.04404
15	$m(N)^2_\nu$	0.03491
16	`tau_0.20_cc_mult`	0.02532
17	`tau_0.20_cc_PZ`	0.007238

Table 5.14.: Ranking of the anti-D_s^+ BDT input variables.

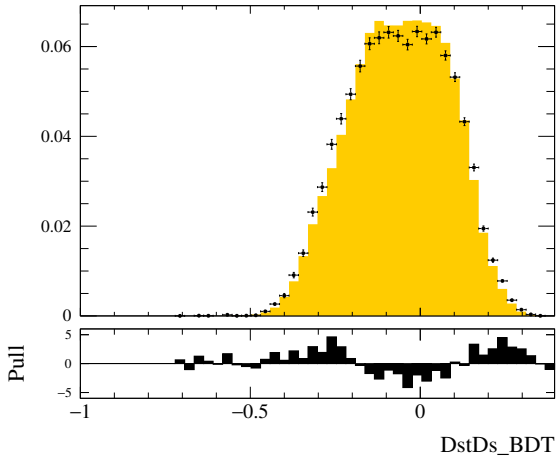

Figure 5.28.: Data (black points) / MC (colored bins) comparison for the anti-D_s^+ BDT distribution as for the $B^0 \to D^{*-}3\pi$ mode.

5.6. Mode-Specific Cuts

Due to differences in topologies and decay characteristics between the signal and normalization modes, the selection criteria vary slightly. The following sections provide detailed criteria for each mode.

5.6.1. Signal-Like Events Selection

To select the signal mode, additional cuts are applied as detailed in Tab. 5.15. The τ^+ vertex must be located 2σ downstream of the B^0 vertex to eliminate the *prompt background* arising from prompt $B^0 \to 3\pi^{\pm}X$ decays. The mass of D^{*-} is constrained to ensure the selection of the D^{*-} meson. To avoid double charm backgrounds, an upper limit is set on the τ^+ mass. Due to partial decay reconstruction, an upper boundary is also imposed on the B^0 mass. The reconstructed q^2 is required to be within $[0, 11]\,\mathrm{GeV}^2/c^4$ to reduce combinatorial backgrounds. As previously explained, four MVA cuts are applied. Lastly, the PID requirements are applied. The signal mode selection criteria are summarized in Tab. 5.15.

After the full selection, nearly all candidates originate from a b-hadron, predominantly from the B^0 meson. Crucially, the prompt background is significantly diminished, with the dominant backgrounds being the three double charm decay modes, especially the $B \to D^{*-}D_s^+X$ decays. The latter is controlled by the anti-D_s^+ BDT in the signal-yield fit, hence the application of a loose cut on this variable.

Requirement		Targeted Background
$\Delta z(B^0, \tau^+)$	> 2	prompt
$m(K^-\pi^+)$	$\in [1840, 1890]\,\mathrm{MeV}/c^2$	combinatorial D^0
$m(D^{*-}) - m(K^-\pi^+)$	$\in [143, 148]\,\mathrm{MeV}/c^2$	combinatorial D^{*-}
$m(\tau^+)$	$< 1600\,\mathrm{MeV}/c^2$	double-charm
$m(B^0)$	$< 5100\,\mathrm{MeV}/c^2$	combinatorial
q^2	$\in [0, 11]\,\mathrm{GeV}^2/c^4$	combinatorial
MVA cuts		
`DstDs_BDT`	> -0.2	$D^{*-}D_s^+ X$
`Isolation_BDT`	> 0.1	double-charm
`Combinatorial_BDTD`	> 0.0	combinatorial
`Detachment_BDTG`	> 0.2	prompt
PID cuts		
$\mathrm{ProbNN}_\pi(\pi^-)$	> 0.1 (π^- from D^{*-})	
$\mathrm{ProbNN}_\pi(\pi^\pm)$	> 0.6 ($\pi^\pm$ from τ^+)	misidentification
$\mathrm{ProbNN}_K(\pi^-)$	< 0.1 (π^- from τ^+)	

Table 5.15.: Signal mode selection criteria.

5.6.2. Normalization Mode Criteria

In order to minimize the bias on the $\mathbf{R}(D^*)$ ratio, the normalization mode selection must closely resemble the signal mode selection.

The normalization mode selection exploits the unique characteristics of this mode: the $B^0 \to D^{*-}3\pi^\pm$ decay is fully reconstructed and the $3\pi^\pm$ system originates directly from the B^0. The first requirement is achieved by constraining the B^0 mass spectrum to the range $[5150, 5400]\,\mathrm{MeV}$. The second criterion is met by enforcing a distinct $3\pi^\pm$ vertex topology. Instead of the vertex detachment criterion used for the $3\pi^\pm$ system relative to the B^0 vertex in the signal mode, the $\overline{D}^0$ vertex must lie further downstream than the $3\pi^\pm$ vertex.

Regarding the MVA selection, the detachment BDT cut is omitted, as the $B^0 \to D^{*-}3\pi$ decay has the $3\pi^\pm$ system *attached* to the B^0 decay vertex. Additionally, the anti-D_s^+ BDT, which relies on intermediate resonant states in the $3\pi^\pm$ system, is irrelevant for the normalization mode. The other two BDTs, the combinatorial and isolation BDTs, are retained with the same cuts as for the signal mode.

The PID requirements are identical to those for the signal. Although they could have been

Requirement		Targeted Background
$m(B^0)$	$\in [5150, 5400]\,\mathrm{MeV}$	combinatorial
$m(D^{*-}) - m(\overline{D}^0)$	$\in [143, 148]\,\mathrm{MeV}/c^2$	combinatorial D^{*-}
$m(K^-\pi^+)$	$\in [1840, 1890]\,\mathrm{MeV}/c^2$	combinatorial D^0
$\Delta z(\tau^+, \overline{D}^0)$	> 4	non-prompt
MVA cuts		
`Isolation_BDT`	> 0.1	double-charm
`Combinatorial_BDTD`	> 0.0	combinatorial
PID cuts		
$\mathrm{ProbNN}_\pi(\pi^-)$	> 0.1 (π^- from D^{*-})	
$\mathrm{ProbNN}_\pi(\pi^\pm)$	> 0.6 ($\pi^\pm$ from τ^+)	misidentification
$\mathrm{ProbNN}_K(\pi^-)$	< 0.1 (π^- from τ^+)	

Table 5.16.: Normalization mode selection criteria.

applied in the initial selection, they are here for consistency with the efficiency calculations.

Other cuts are maintained at the same values to reduce bias in the relative signal-to-normalization yields. The selection criteria for the normalization mode are listed in Tab. 5.16.

5.7. Efficiency Calculation

The efficiencies for both the signal and normalization modes are calculated using simulated samples. In this section, the results shown are for the combined 2015–2018 dataset, while the results for each separate dataset are reported in App. B.4. The strategy for calculating efficiencies involves computing them separately for each dataset and each polarity configuration. These efficiencies are then weighted by the luminosity of each data sample to obtain a combined result.

The efficiency of a given mode, $\varepsilon_{\mathrm{mode}}(p, d)$, is computed as the product of the online and offline efficiencies for a specific polarity p and dataset d:

$$\varepsilon_{\mathrm{mode}}(p, d) = \varepsilon_{\mathrm{online}}(p, d) \cdot \varepsilon_{\mathrm{offline}}(p, d)\ , \tag{5.9}$$

where p runs over the two polarity configurations, *up* and *down*, and d spans the datasets from 2015 to 2018. The two signal modes, $B^0 \to D^{*-}\tau^+\nu_\tau$, where the τ^+ decays either to three charged pions or to three charged pions and a neutral pion, are referred to as "`sig1`" and

"sig 2" respectively.

The online efficiency is further broken down as:

$$\varepsilon_{\text{online}}(p, d) = \varepsilon_{\text{geometry}}(p, d) \cdot \varepsilon_{\text{preselection}}(p, d) \ , \tag{5.10}$$

the first term is the geometrical acceptance (geometry), while the second term is the filtering, stripping and DaVinci (preselection) cuts efficiency. In practice, the preselection efficiency is calculated as product of the efficiencies obtained from each step:

$$\varepsilon_{\text{preselection}} = \varepsilon_{\text{Filtering}} \cdot \varepsilon_{\text{Stripping}} \cdot \varepsilon_{\text{DaVinci}} \ . \tag{5.11}$$

The offline efficiency is calculated as product of efficiencies obtained from different selection steps, which follows the selection procedure:

$$\varepsilon_{\text{offline}} = \prod_{i \in \text{steps}} \varepsilon_i = \prod_{i \in \text{steps}} \frac{N_i}{N_{i-1}} \ , \tag{5.12}$$

The p and d indices are omitted for simplicity and N_i is the number of events passing the step i. The numerator of a step i is then canceled out by the denominator of step $i + 1$. Explicitly, the offline efficiency splits into:

$$\varepsilon_{\text{offline}} = \varepsilon_{\text{CT}} \cdot \varepsilon_{\text{MS}} \cdot \varepsilon_{\text{pid}} \ , \tag{5.13}$$

where: ε_{CT} is the common and trigger cuts efficiency Tab. 5.7, ε_{MS} represents the signal or normalization cuts efficiency, listed in Tabs. 5.15 and 5.16 *except for* the PID cuts. The PID efficiency ε_{PID} is computed with a data-driven approach (`PIDCalib`) that requires all the other cuts be already applied, such that only the PID absolute efficiencies are measured.

The online and offline efficiencies are reported in Tab. 5.17.

The efficiency from different steps, are then combined with dataset and polarity configurations, to obtain the average:

$$\langle \varepsilon_{\text{mode}} \rangle = \frac{\sum \varepsilon_{\text{mode}}(i, j) \cdot L_{i,j}}{\sum L_{i,j}} \tag{5.14}$$

where the indices i and j run over the datasets and polarities, respectively. $L_{i,j}$ is the integrated luminosity of the dataset i and polarity j. The luminosity for each dataset and polarity is reported in Tab. 4.1.

Selection Step	Efficiency (%)		
	sig 1	sig 2	norm
Geometry	16.44 ± 1.98	15.76 ± 1.81	15.67 ± 1.70
Filtering & Stripping	45.55 ± 0.09	45.52 ± 0.08	45.95 ± 0.12
DaVinci	54.05 ± 0.47	54.04 ± 0.54	53.63 ± 0.51
Common & Trigger	63.26 ± 1.62	59.94 ± 1.57	41.40 ± 1.58
Mode-Specific	39.67 ± 1.83	30.91 ± 1.73	61.43 ± 1.97
PID	79.10 ± 1.37	81.59 ± 1.27	77.01 ± 1.40

Table 5.17.: Online and offline efficiency averages at different stages of the selection.

Efficiency	Value
$\varepsilon_{\mathtt{norm}} \times 10^4$	3.466 ± 0.019
$\varepsilon_{\mathtt{sig}} \times 10^4$	1.190 ± 0.005
$\varepsilon_{\mathtt{norm}}/\varepsilon_{\mathtt{sig}}$	2.952 ± 0.020

Table 5.18.: Efficiencies for the signal and normalization modes, and their ratio.

The signal efficiency is combined from the two decay modes as follows:

$$\varepsilon_{\mathtt{sig}} = \frac{\left\langle \varepsilon_{\mathtt{sig\,1}} \right\rangle \cdot \mathrm{Br}(\mathtt{sig\,1}) + \left\langle \varepsilon_{\mathtt{sig\,2}} \right\rangle \cdot \mathrm{Br}(\mathtt{sig\,2})}{\mathrm{Br}(\mathtt{sig\,1}) + \mathrm{Br}(\mathtt{sig\,2})} \,, \tag{5.15}$$

The efficiencies for the signal and normalization modes, and their ratio, are shown in Tab. B.6.

The combined efficiencies for the signal and normalization modes, and their ratio, are shown in Tab. B.6. The efficency ratio is an input to measure $\mathcal{K}(D^{*-})$ (*cf.* Eq. (4.6)).

The fraction $f_{\tau^+\to 3\pi\overline{\nu}_\tau}$ is calculated using the following formula:

$$f_{\tau^+\to 3\pi\overline{\nu}_\tau} = \frac{\left\langle \varepsilon_{\mathtt{sig\,1}} \right\rangle \cdot \mathrm{Br}(\mathtt{sig\,1})}{\left\langle \varepsilon_{\mathtt{sig\,1}} \right\rangle \cdot \mathrm{Br}(\mathtt{sig\,1}) + \left\langle \varepsilon_{\mathtt{sig\,2}} \right\rangle \cdot \mathrm{Br}(\mathtt{sig\,2})} \tag{5.16}$$

The τ^+ branching fraction inputs are given in Tab. 5.19. They are taken from the PDG [7] for data fraction $f_{\tau^+\to 3\pi\overline{\nu}_\tau}$, a simulation based fraction $f^{\mathtt{sim}}_{\tau^+\to 3\pi\overline{\nu}_\tau}$ is calculated the branching fractions used to build the MC samples. These fractions are used in the signal fit Sec. 7.1 as a fixed parameter.

	Decay	**Branching Fraction** (%)
	PDG	
`sig 1`	$\tau \longrightarrow 3\pi\nu$	9.02 ± 0.05
`sig 2`	$\tau \longrightarrow 3\pi\pi^0\nu$	4.49 ± 0.05
	Simulation	
`sig 1`	$\tau \longrightarrow 3\pi\nu$	9.32 ± 0.00
`sig 2`	$\tau \longrightarrow 3\pi\pi^0\nu$	4.61 ± 0.00

Table 5.19.: Branching fractions for the signal τ^+ decay modes.

Chapter 6

Control Samples

Before conducting the signal yield fit, it's crucial to apply data-driven corrections to the simulated samples, particularly for the most significant backgrounds. This process utilizes control samples, which are detailed in this chapter.

The chapter begins by addressing the adjustments made to the resonant structure of the D_s^+ decay, as discussed in Sec. 6.1. Following this, Sec. 6.2 discusses the fitting process for the composition of the $B \to D^{*-} D_s^+ X$ inclusive mode, which provides essential constraints for the subsequent analysis.

Lastly, Sec. 6.3 examines how the $B \to D^{*-} D^+ X$ and $B \to D^{*-} D^0 X$ samples are employed to refine the q^2 distribution within the decay modes, thereby enhancing the accuracy of the final fit templates.

Unless otherwise stated, the figures and tables from this point forward are based on the full Run 2 dataset.

6.1. D_s^+ Decay Model

The hadronic decays of the τ lepton, the signal channel, are dominated by the $a_1(1260)^+$ state, which decays to $\rho^0 \pi^+$. The situation becomes complex as the D_s^+ can also decay to the $a_1(1260)^+$, mimicking the signal decay. Moreover, the branching fraction of this decay is

Decay Mode	Br (%)
$D_s^+ \to \eta X$	29.9 ± 2.8
$D_s^+ \to \eta\pi^+$	1.68 ± 0.10
$D_s^+ \to \eta\rho^+$	8.9 ± 0.8
$D_s^+ \to \eta\pi^+\pi^0$	9.5 ± 0.5
$D_s^+ \to \eta' X$	10.3 ± 1.4
$D_s^+ \to \eta'\pi^+$	3.94 ± 0.25
$D_s^+ \to \eta'\rho^+$	5.8 ± 1.5
$D_s^+ \to \eta'\pi^+\pi^0$	5.6 ± 0.8
$\eta' \to \pi^+\pi^-\eta$	42.5 ± 0.5
$\eta' \to \rho^0\gamma$	29.5 ± 0.4
$\eta' \to \pi^0\pi^0\eta$	22.4 ± 0.5
$\eta' \to \omega\gamma$	2.52 ± 0.07
$\eta \to \pi^+\pi^-\pi^0$	23.02 ± 0.25
$\eta \to \pi^+\pi^-\gamma$	4.28 ± 0.07
$\rho^0 \to \pi^+\pi^-$	100
$\rho^+ \to \pi^+\pi^0$	100

Table 6.1.: The relevant branching fractions for D_s^+ decays to η and η' (left), and for $\eta^{(\prime)}$ and $\rho^{0,+}$ decays to various final states (right) [7].

not well-known. Additionally, there is a potential for mis-identification in the decay chain:

$$D_s^+ \to \eta' X \quad \text{with} \quad \eta' \to \rho^0\gamma\,. \tag{6.1}$$

The ρ^0, originating from the D_s^+ decay, can mistakenly be attributed to a τ^+ decay.

To ensure the simulation accurately reflects real data, the contributions from various resonances, notably the one arising from unknown branching fractions, and especially the η' resonance, must be normalized accurately. The D_s^+ branching fractions are listed in Tab. 6.1.

The sample used for the D_s^+ control sample is enriched in the $D_s^+ \to 3\pi^\pm X$ decays via reversing the D_s^+ BDT cut from the signal selection, in addition to the mass windows cuts across the variables on which the likelihood relies on, as described below. The selection criteria are summarized in Tab. 6.2. The MC samples are used to build the templates for the fit, from the D_s^+ cocktail and inclusive $b\overline{b} \to D^*3\pi X$ samples. A simultaneous maximum likelihood

Requirement
anti-D_s^+ BDT < -0.2
$\min[m(\pi^+\pi^-)] \in [240, 1600]\,\mathrm{MeV}/c^2$
$\max[m(\pi^+\pi^-)] \in [280, 1700]\,\mathrm{MeV}/c^2$
$m(\pi^+\pi^+) \in [280, 1200]\,\mathrm{MeV}/c^2$
$m(3\pi^\pm) \in [440, 1840]\,\mathrm{MeV}/c^2$

Table 6.2.: Selection of the D_s^+ decay model control sample

binned fit is performed to the four variables:

$$\min\left[m(\pi^+\pi^-)\right],\ \max\left[m(\pi^+\pi^-)\right],\ m(\pi^+\pi^-),\ m(3\pi^\pm)\ , \tag{6.2}$$

referred to as $V = \{v_1, v_2, v_3, v_4\}$ respectively. To distinguish the invariant masses of resonances that yield two pions, the masses of all two-pion combinations are reconstructed using the variables v_1–v_3. The fourth variable is exploited to separate the exclusive $D_s^+ \to 3\pi^\pm$ decay from events where an extra energy is carried by additional neutral particles, such as $D_s^+ \to \tau^+\nu_\tau$ then $\tau^+ \to 3\pi^\pm\overline{\nu}_\tau$, and $D_s^+ \to 3\pi^\pm$ X, where X is unreconstructed. The total likelihood function is the product of the likelihood functions for each of the four variables:

$$L^{tot}(V, \Theta) = \prod_{i=1}^{4} L(v_i, \Theta)\ , \tag{6.3}$$

where Θ represents the set of the following parameters:

- Free parameters: $N_{D_s^+}$, $N_{\mathrm{non}D_s^+}$, $f_{\eta X}$, $f_{\eta' X}$, $f_{\eta 3\pi}$, $f_{\eta' 3\pi}$, $f_{\omega 3\pi}$ and r_{Prm},
- Constrained parameters: $r_{\eta(\rho/\pi)}$, $r_{\eta'(\rho/\pi)}$ and $r_{Int\,\rho}$,
- Fixed parameters: $f_{a_1 X}$, $f_{\phi 3\pi}$, $f_{K^0 3\pi}$, $f_{\tau\nu}$, $f_{NR\,3\pi}$ and N_{SL}

Detailed information on the parameters is provided below. The four individual likelihood functions of Eq. (6.3) are built in a similar way:

$$L(v_k, \Theta) = \prod_{i=1}^{N} \mathcal{P}_{tot}\left(v_k^{(i)}, \Theta\right)\ ,\ \text{or}\quad L^{tot}(V, \Theta) = \prod_{i=1}^{N} \mathcal{P}_{tot}\left(V^{(i)}, \Theta\right)\ , \tag{6.4}$$

where $v_k^{(i)}$ is the k-th variable of the i-th event in the sample of size N. The total Probability

Density Function (PDF) $\mathcal{P}_{tot}$ is constructed as:

$$\mathcal{P}_{tot} = N_{D_s^+}\mathcal{P}_{D_s^+} + N_{SL}\mathcal{P}_{SL} + N_{non\ D_s^+}\mathcal{P}_{non\ D_s^+} \tag{6.5}$$

where SL stands for semileptonic D_s^+ decays: $D_s^+ \to \ell\nu X$. It corresponds to the muon misidentification as a pion, for example, in the $D_s^+ \to \rho\mu\nu$ decays, where $\rho \to \pi^+\pi^-$. the N_{SL} is fixed to 4% of the total D_s^+ yield [165].

The D_s^+ PDF is summed over all decay modes, it is by:

$$\begin{aligned}
\mathcal{P}_{D_s^+} = & \sum_{s\in\{\eta,\eta'\}} f_{sX}\left[r_{s(\rho/\pi)}\mathcal{P}_{s\rho} + \left(1 - r_{s(\rho/\pi)}\right)\mathcal{P}_{s\pi}\right] \\
& + \left(1 - f_{\eta X} - f_{\eta' X}\right)\Bigg[r_{Prm} \\
& \times \Bigg\{ \sum_{s\in\{\eta,\eta',\phi,K^0\}} f_{s3\pi}\left(f_{sa_1}\mathcal{P}_{sa_1} + (1 - f_{sa_1})\mathcal{P}_{s3\pi}\right) \\
& + f_{5\pi}\mathcal{P}_{5\pi} + f_{\tau\nu}\mathcal{P}_{\tau\nu} + f_{NR\,3\pi}\mathcal{P}_{NR\,3\pi}\Bigg\} \\
& + (1 - r_{Prm}) \times \left(r_{Int\,\rho}\mathcal{P}_{(\omega+\phi)\rho} + \left(1 - r_{Int\,,\,\rho}\right)\mathcal{P}_{(\omega+\phi)\pi}\right)\Bigg]
\end{aligned} \tag{6.6}$$

For simplicity, the fitting model ignores interference effects between the amplitudes of the PDF components. The different D_s^+ modes are classified as follows:

- *Intermediate State Decays* (Int) – *At least* one pion originates directly from an intermediate resonant state, namely:
  - π from η: through the $D_s^+ \to \eta\pi^+(\pi^0)$ decay.
  - π from η': includes the $D_s^+ \to \eta'\pi^+(\pi^0)$ decay.
  - π from ω or ϕ: covering the $D_s^+ \to \omega\pi^+(\pi^0)$ and $D_s^+ \to \phi\pi^+(\pi^0)$ decays.
- *Prompt Decays* (Prm) – All pions originate directly from the initial state, without passing through any intermediate resonance: $\eta 3\pi$, ηa_1, $\eta' 3\pi$, $\eta' a_1$, $\omega 3\pi$, ωa_1,$\phi 3\pi$, ϕa_1, $K^0 3\pi$, $K^0 a_1$, $D_s^+ \to \tau\nu$ and non-resonant 3π.

The (quasi) two-body decay modes are quantified in two ways: through the overall proportion of each decay in the dataset, and specifically through the proportion of the ρ mode relative

to others within the same category. The PDF for the D_s^+ decay model is given by Eq. (6.6), where:

- f_{sX}: The total fraction of the decay mode with state s (either η or η').
- $r_{s(\rho/\pi)}$: The relative fraction of ρ mode for state s. The ρ fraction $r_{s(\rho/\pi)}$ is Gaussian constrained around its nominal value of $2/3$ with $\sigma = 0.2$.
- r_{Prm} : The fraction of prompt pion decays (*i.e.* the pions are directly produced without passing through intermediate resonances) with respect to $N_{D_s^+} \times (1 - f_{\eta X} - f_{\eta' X})$.
- $f_{s3\pi}$ and f_{sa_1} represent the total fraction of the 3π modes and the relative fraction of the a_1 mode, respectively, with state s being either η, η', ϕ, K^0.
- The fractions for $\phi(3\pi^+ a_1)$, $D_s^+ \to \tau\nu$, and $K^0(3\pi^+ a_1)$ are fixed.
- The terms for $f_{5\pi}$, $f_{\tau\nu}$, $f_{\phi 3\pi}$, and $f_{K^0 3\pi}$ are determined by the $f_{\eta' X}$ fraction.
- The non-resonant 3π fraction is constrained by the other multi-body modes, accordingly:

$$f_{NR,\,3\pi} = 1 - \sum_{s\in\{\eta,\eta',\phi,K^0\}} f_{s3\pi} - f_{\tau\nu} \tag{6.7}$$

- $\mathcal{P}_{(\omega+\phi)\rho}$ and $\mathcal{P}_{(\omega+\phi)\pi}$ with their respective fractions $r_{Int,\ \rho}$ represents the intermediate state decays with at least one pion from ω or ϕ.
- The relative fraction of $D_s^+ \to a_1 X$ to $D_s^+ \to 3\pi X$ is fixed at 5.5% to ensure fit stability. This fraction was selected as it results in the minimum $\chi^2/ndof$ for the final signal fit Sec. 7.1.

The D_s^+ decay control sample is fitted using $N_{tot} = 22\,808$ events from the collision data.

The fit projections for the D_s^+ decay model control sample are given in Fig. 6.1 . The fit results are summarized in Tab. 6.3. The component fractions, correction weights, and yields obtained from the fit are reported in Tab. 6.4.

The correction factor is calculated as follows:

$$w_i = f_i \times \frac{N_{tot}}{N_i}\ , \tag{6.8}$$

where $N_{tot} = 22\,808$ is the total number of events in the D_s^+ cocktail MC sample, N_i is the ith template size, and N_i is the number of events in the mode i, which runs from 1 to 19, corresponding to the templates listed in Tab. 6.4.

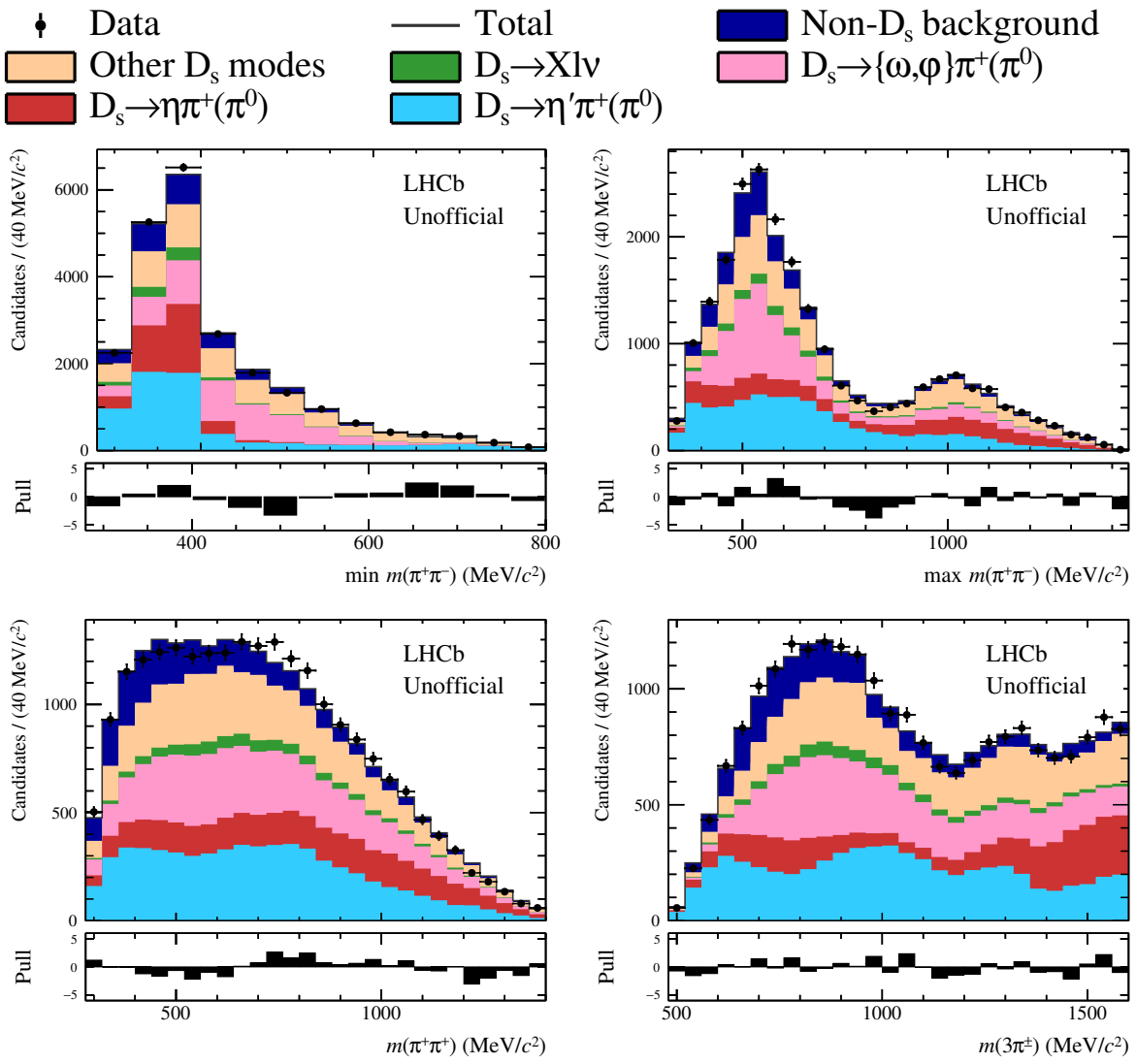

Figure 6.1.: Fit model's projections onto the four variables determined in the fit to the control data sample for the $D_s^+ \to 3\pi X$ decays.

Parameter	Value
$f_{\eta X}$	0.17 ± 0.01
$f_{\eta' X}$	0.32 ± 0.01
$r_{\eta\rho}$	0.85 ± 0.04
$r_{\eta'\rho}$	0.74 ± 0.02
$f_{\text{Int, }\rho}$	0.92 ± 0.04
$f_{\texttt{Prm}}$	0.49 ± 0.02
N_{D_s}	19446 ± 266
$N_{\text{non-}D_s^+}$	2584 ± 268

Table 6.3.: Fit results showing the fractions of the different D_s^+ decay modes in the data sample.

Index i	**Template** T_i	**Fraction** f_i	**Correction Factor** w_i
1	$\eta 3\pi^\pm$	0.007 ± 0.0	0.82 ± 0.059
2	$\eta' 3\pi^\pm$	0.007 ± 0.0	0.82 ± 0.059
3	$\omega 3\pi^\pm$	0.011 ± 0.001	0.82 ± 0.059
4	$\phi 3\pi^\pm$	0.024 ± 0.002	0.82 ± 0.059
5	$K^0 3\pi^\pm$	0.006 ± 0.0	0.82 ± 0.059
6	$D_s^+ \to \tau^+\nu_\tau$	0.013 ± 0.001	0.82 ± 0.059
7	NR $3\pi^\pm$	0.101 ± 0.014	2.24 ± 0.315
8	$a_1\eta$	0.026 ± 0.002	0.82 ± 0.059
9	$a_1\eta'$	0.004 ± 0.0	0.82 ± 0.059
10	$a_1\omega$	0.008 ± 0.001	0.82 ± 0.059
11	$a_1\phi$	0.017 ± 0.001	0.82 ± 0.059
12	$a_1 K^0$	0.003 ± 0.0	0.82 ± 0.059
13	$5\pi^\pm$	0.026 ± 0.002	0.82 ± 0.059
14	$\omega\rho^+$ or $\phi\rho^+$	0.239 ± 0.015	0.99 ± 0.061
15	$\omega\pi^+$ or $\phi\pi^+$	0.022 ± 0.01	0.65 ± 0.305
16	$\eta\rho^+$	0.145 ± 0.008	0.67 ± 0.036
17	$\eta\pi^+$	0.026 ± 0.007	1.28 ± 0.355
18	$\eta'\rho^+$	0.232 ± 0.009	1.49 ± 0.059
19	$\eta'\pi^+$	0.084 ± 0.006	0.82 ± 0.059

Table 6.4.: Relative fractions of different $D_s^+ \to 3\pi^\pm X$ templates from the fit to collision data D_s^+ control sample and the corresponding correction factors applied to the simulation.

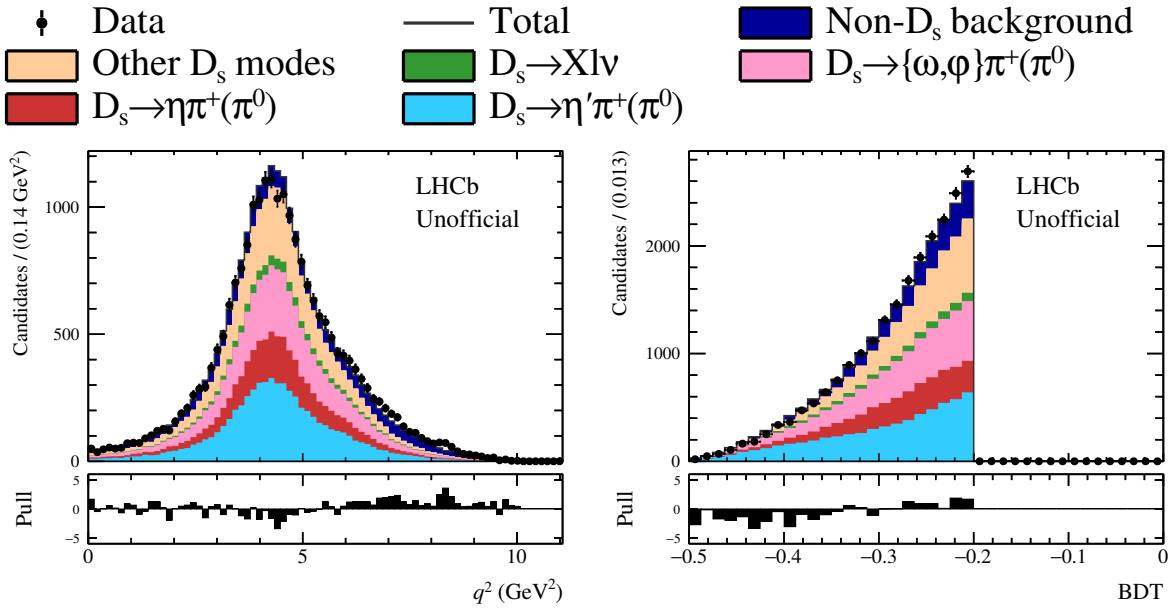

Figure 6.2.: Projections of the D_s^+ templates onto q^2 and the anti-D_s^+ BDT according to the fit results obtained from the control data sample.

The templates that have identical correction factors are defined with respect to $\eta'\pi^+$, with index 19. The statistics of each of the following modes: $\eta 3\pi^\pm$, $\eta' 3\pi^\pm$, $\omega 3\pi^\pm$, $\phi 3\pi^\pm$, $K^0 3\pi^\pm$, $a_1\eta$, $a_1\eta'$, $a_1\omega$, $a_1\phi$, $a_1 K^0$, $5\pi^\pm$ and $D_s^+ \to \tau^+\nu_\tau$, are used to adjust its fraction:

$$f_i = \frac{r_{Prm}}{f_i^{tot}} \frac{N_i}{N_{19}} , \tag{6.9}$$

where the mode with index i refers to the decay modes listed above, and $f_i^{tot} = (1 - f_{\eta X} - f_{\eta' X}) r_{Prm} \ldots$ is the total fraction defined according to the PDF model (*cf.* Eq. (6.6)). This is done to obtain a stable fit for the time being. Ongoing efforts are being conducted to improve the D_s^+ decay fits with a more physical model. Finally, the projection of the simulated D_s^+ templates onto the fitted variables, according to the results obtained from the control data sample fit are shown in Fig. 6.2.

6.2. $B \to D^* D_s^+(X)$ Control Mode

The $B \to D^* D_s^+(X)$ modes constitute an important set of backgrounds in the signal yield fit. Their relative abundances in the double-charm cocktail simulation samples are adjusted by fitting a data sample enriched with $B \to D^* D_s^+ X$ events where $D_s^+ \to 3\pi^\pm$.

Requirement	
$\Delta z(B^0, \tau^+)$	> 2
$m(K^-\pi^+)$	$\in [1840, 1890]\,\mathrm{MeV}/c^2$
$m(D^{*-}) - m(K^-\pi^+)$	$\in [143, 148]\,\mathrm{MeV}/c^2$
$m(\tau^+)$	$\in 1968.3 \pm 20\,\mathrm{MeV}/c^2$
q^2	> 0
PID cuts	
$\mathrm{ProbNN}_\pi(\pi^-)$	> 0.1 (π^- from D^{*-})
$\mathrm{ProbNN}_\pi(\pi^\pm)$	> 0.6 ($\pi^\pm$ from τ^+)
$\mathrm{ProbNN}_K(\pi^-)$	< 0.1 (π^- from τ^+)
MVA cuts	
`Isolation_BDT`	> 0.1
`Combinatorial_BDTD`	> 0.0
`Detachment_BDTG`	> 0.2

Table 6.5.: Selection of the D_s^+ production mode control sample

The $B \to D^* D_s^+ X$ control sample selection differs from the nominal selection by requiring the $3\pi^\pm$ invariant mass to be within $20\,\mathrm{MeV}/c^2$ of the D_s^+ mass, and omitting the anti-D_s^+ BDT cut, as well as the B^0 and τ^+ mass constraints. The selection criteria are summarized in Tab. 6.5.

The control sample comprises 8750 collision data events. The relative fractions of the $B \to D^{*-} D_s^+(X)$ decays remain valid for the inclusive $D_s^+ \to 3\pi^\pm X$ decays, as in the signal yield fit. Note that the $D_s^+ \to 3\pi^\pm X$ decay model corrections discussed in the previous section are not applicable here, as they pertain to the inclusive $D_s^+ \to 3\pi^\pm X$ modes, while this section focuses on exclusive $D_s^+ \to 3\pi^\pm$ events.

The fit is performed on $m(D^{*-}3\pi^\pm)$, shifted by subtracting $m(K^-\pi^+)_{D^0}$ and $m(3\pi^\pm)$ for better resolution. The probability density function used in the fit includes:

$$\mathcal{P} = f_{\mathrm{comb}}\mathcal{P}_{\mathrm{comb}} + \frac{(1 - f_{\mathrm{comb}})}{k} \sum_i f_i \mathcal{P}_i, \tag{6.10}$$

where:

- The fractions and PDF of the combinatorial background, f_{comb} and $\mathcal{P}_{\mathrm{comb}}$, modeled with WS samples, $D^{*\pm}3\pi^\pm$ system, where the $D^{*\pm}$ has the same charge as the $3\pi^\pm$.

Component	Normalization
$B^0 \to D^{*-} D_s^+$	$N_{D_s^+} \times f_{D_s^+}/k$
$B^0 \to D^{*-} D_s^{*+}$	$N_{D_s^+} \times 1/k$
$B^0 \to D^{*-} D_{s0}^{*+}$	$N_{D_s^+} \times f_{D_{s0}^{*+}}/k$
$B^0 \to D^{*-} D_{s1}^{+}$	$N_{D_s^+} \times f_{D_{s1}^{+}}/k$
$B \to D^{**-} D_s^+ X$	$N_{D_s^+} \times f_{D^{**} D_s X}/k$
$B_s^0 \to D^{*-} D_s^+ X$	$N_{D_s^+} \times f_{B_s \to D^* D_s^+ X}/k$
Background	N_{bkg}

Table 6.6.: List of components in the $D^* D_s^+$ X control fit and how they are normalized.

- The fractions of the $B \to D^{*-} D_s^+(X)$ components, f_i, are *floating* parameters in the fit, they are defined in Tab. 6.6, relatively to the most abundant $B^0 \to D^{*-} D_s^+$ decays.
- k is defined as:

$$k = 1 + f_{D_s^+} + f_{D_{s0}^{*+}} + f_{D_{s1}^+} + f_{D^{**} D_s^+ X} + f_{B_s^0 \to D^{*-} D_s^+ X} \tag{6.11}$$

  by definition $f_{D_s^{*+}} = 1$.

The shapes of each component are derived from binned templates constructed using simulated samples.

The fit projections on the fit variable, q^2, t_τ, and anti-D_s^+ BDT are shown in Fig. 6.3.

The $B \to D^{*-} D_s^+(X)$ modes are categorized into exclusive $B^0 \to D^{*-} D_s^{+(*)}$ modes and inclusive $B \to D^{*-} D_s^+(X)$ and $B_s^0 \to D^{*-} D_s^+(X)$ modes:

- The *exclusive modes* consist of the $B^0 \to D^{*-} D_s^+$ decays and those involving excited states of the D_s^+, such as D_s^{*+}, D_{s0}^{*+}, and D_{s1}^+. Their momentum distribution ($q^2 = (p_{B^0} - p_{D^{*-}})^2$) peaks at the masses of the respective D_s^+ states, as illustrated in the top–right of Fig. 6.3 for the mass squared of the D_s^+ species listed in Tab. 6.7
- The inclusive $B \to D^{*-} D_s^+(X)$ modes comprise at least one extra particle, possibly originating from feed–down processes involving excited D^{*-} and D_s^+ states. These additional particles shift the q^2 distribution to higher values, as observed in the top–right of Fig. 6.3 for the modes $B \to D^{**-} D_s^+ X$ and $B_s^0 \to D^{*-} D_s^+ X$.

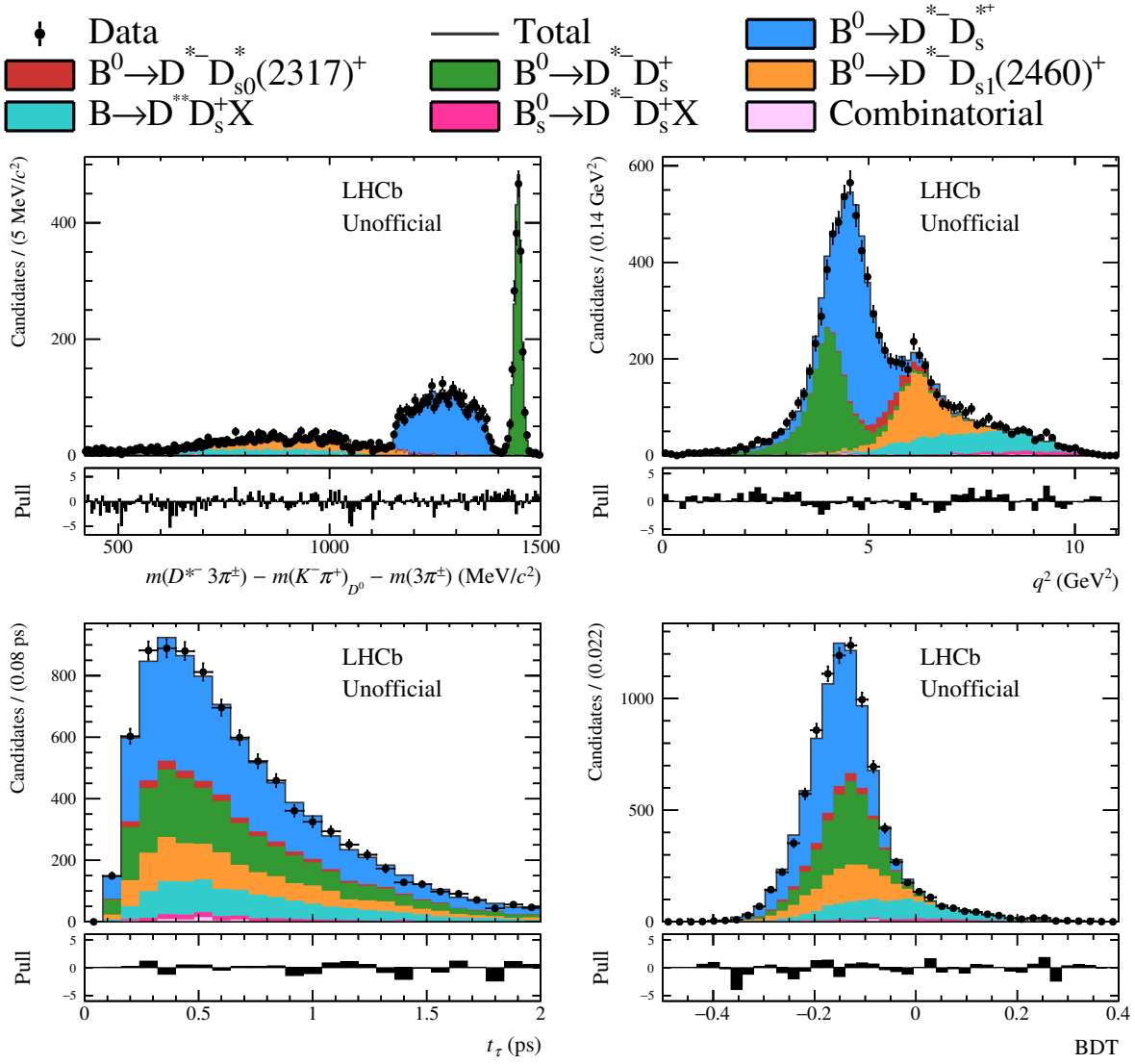

Figure 6.3.: Projections of the data-fit for the $B \to D^{*-} D_s^+ X$ components, displaying the fit variable $m(D^{*-}3\pi^{\pm})$ and signal fit variables q^2, t_τ and anti-D_s^+ BDT.

D_s^+ State	Mass^2 (GeV^2/c^4)
D_s^+	3.9
D_s^{*+}	4.5
D_{s0}^{*+}	5.4
D_{s1}^+	6.1

Table 6.7.: Invariant squared mass of the D_s^+ states of interest [7]. Uncertainties are smaller than the last digit shown.

Parameter	Value
N_{D_s}	8674 ± 96
N_{bkg}	76 ± 26
$f_{B_s \to D^* D_s X}$	0.067 ± 0.017
$f_{D^{**} D_s X}$	0.188 ± 0.034
$f_{D_{s1}'^+}$	0.438 ± 0.033
f_{D_s}	0.556 ± 0.016
$f_{D_{s0}^{*+}}$	0.050 ± 0.021

Table 6.8.: Fit results for the $B \to D^{*-}D_s^+(X)$ control sample.

The $B \to D^{*-}D_s^+(X)$ components significantly contribute to the signal fit. Therefore, the relative fractions derived in this section are used as *constraints* in the signal yield fit (*cf.* Sec. 7.1.1.1), while leaving their normalization, $N_{D_s^+}$, unconstrained. The differences between the signal and control sample selections are addressed by applying appropriate corrections to the fractions.

Tab. 6.8 reports the $B^0 \to D^{*-}D_s^+$ yield, the fractions of the other modes, and the combinatorial background yield obtained from the fit to the control sample.

6.3. $B \to D^{*-}D^0(X)$ and $B \to D^{*-}D^+(X)$ Control Modes

The other two major double-charm backgrounds present in the signal fit are $B \to D^{*-}D^0(X)$ and $B \to D^{*-}D^+(X)$. In the following, the q^2 distributions of these modes are inspected and corrected.

The selection criteria are broadly similar to those used for the signal, with the exceptions of MVA selection, and the mass requirements for B^0 and τ^+, which are relaxed to keep high

statistics.

The $D^0 \to 3\pi^{\pm}X$ final state in $B \to D^{*-}D^0(X)$ decay is dominated by the $D^0 \to K^-3\pi^{\pm}$. The branching fraction for this decay is given by:

$$\mathrm{Br}\,(D^0 \to K^-3\pi^{\pm}) = (8.23 \pm 0.14)\% \,, \tag{6.12}$$

An isolation tool assesses the $3\pi^{\pm}$ vertex for additional K. In addition, the D^0 mass is assigned to the $K^-3\pi^{\pm}$ system, with the invariant mass of the system required to be within $\pm 50\,\mathrm{MeV}/c^2$ of the D^0 mass.

To select the $B \to D^{*-}D^+X$ control sample, the decay $D^+ \to K^-2\pi^+$ with a branching fraction:

$$\mathrm{Br}(D^+ \to K^-2\pi^+) = (9.38 \pm 0.16)\% \,, \tag{6.13}$$

is used.

The opposite-sign pion in the $3\pi^{\pm}$ system, the π^-, is identified as K^- by reversing the PID requirement. The $K^-2\pi^+$ mass must be within $\pm 20\,\mathrm{MeV}/c^2$ of the mass of D^+.

Moreover, the events where tracks originate from different B mesons are excluded. This is achieved by ensuring that the reconstructed momentum of the B^0 is well-aligned with its flight direction from the primary vertex. A summary of the selection criteria for the control modes is given in Tab. 6.9.

Fig. 6.4 shows the q^2 distributions for the simulated $B \to D^{*-}D^0(X)$ (left) and $B \to D^{*-}D^+(X)$ (right) modes. The distributions are shown both before (red) and after (blue) the application of q^2 reweighting. This reweighting is performed using a third-order polynomial function that fits to the ratio of data to MC simulation.

The reweighted q^2 simulated samples are used to build templates for the signal yield fit described in Sec. 7.1.

Requirement		Comment
$\Delta z(\tau, B^0)$	> 2	
q^2	> 0	
$m(D^{*-}) - m(D^0)$	$\in [143, 148]\,\mathrm{MeV}/c^2$	
$\mathrm{acos}\,\mathtt{DIRA}(B^0)$	< 0.02	combinatorial
$\mathrm{ProbNN}_\pi(\pi^-)$	> 0.1	π^+ from D^{*-}
D^0 specific		
$\mathrm{ProbNN}_K(\pi^-)$	< 0.1	π^- from τ^+
$\min[\mathrm{ProbNN}_\pi(\pi^+), \mathrm{ProbNN}_\pi(\pi^-)]$	> 0.6	$\pi^\pm$ from τ^+
$m(K^-3\pi^\pm)$	$\in [1815, 1915]\,\mathrm{MeV}/c^2$	
`good_extra_kaon`		
D^+ specific		
$\mathrm{ProbNN}_K(\pi^-)$	> 0.1	π^- from τ^+
$m(K^-2\pi^+)$	$\in [1820, 1920]\,\mathrm{MeV}/c^2$	

Table 6.9.: Selection criteria for the D^0 and D^+ control modes.

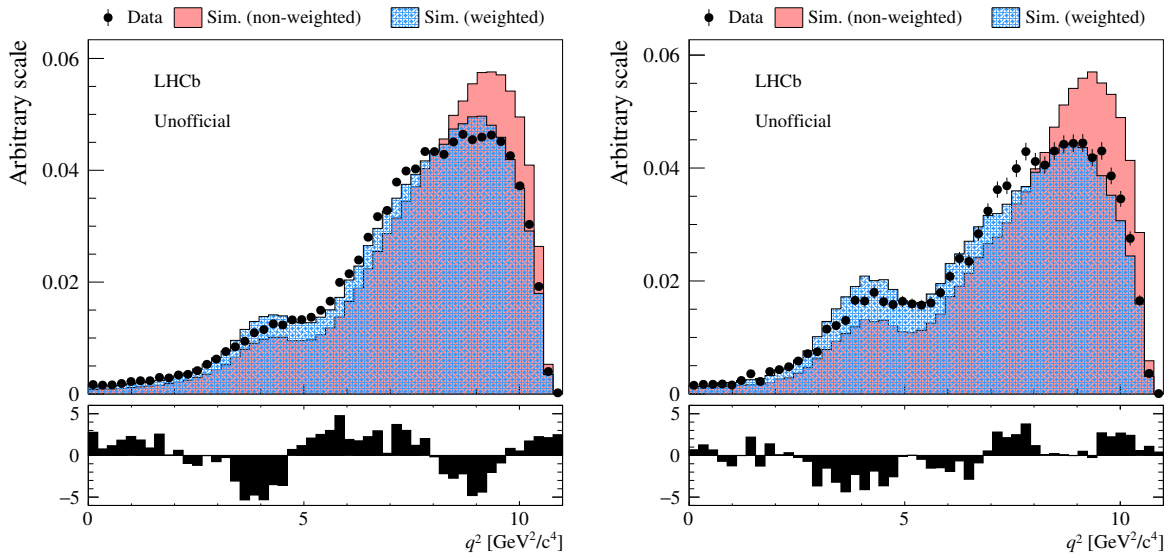

Figure 6.4.: q^2 distributions for the simulated $B \to D^{*-}D^0(X)$ (left) and $B \to D^{*-}D^+(X)$ (right) modes before (red) and after (blue) reweighting with a third order polynomial function that fits to the data/MC ratio.

Chapter 7

Signal and Normalization Fit Results

The preceding chapters provided a foundation for the analysis by detailing the methodology (*cf.* Chap. 4,) the selection process (*cf.* Chap. 5) and the fitting of control samples (*cf.* Chap. 6).

This chapter focuses on the extraction of signal and normalization yields and the calculation of the final $\mathbf{R}(D^*)$ ratio. This approach is based on methodologies established in significant prior studies (*cf.* Refs. [1–3]). Detailed descriptions of the procedures used to derive the signal and normalization yields are provided in Sec. 7.1 and Sec. 7.2, respectively. The signal yield remains blinded pending a review by the LHCb collaboration. This chapter concludes with a preliminary determination of the $\mathbf{R}(D^*)$ ratio in Sec. 7.3.

7.1. Signal Fit Results

The signal yield, N_{sig}, is determined from an extended binned maximum-likelihood fit, across three variables: the squared momentum transfer, q^2, the τ^+ decay time, t_τ, and the output from the anti-D_s^+ BDT output. The binning scheme is chosen to optimize the signal sensitivity and maintain a robust statistical significance in each bin. The binning configuration consists of eight bins for both q^2 and t_τ, alongside six bins for the BDT output.

7.1.1. Fit Model and Templates

A total of 16 q^2, τ^+ lifetime and the anti-D_s^+ BDT templates are used, 13 of which are derived from MC simulations, and 3 from data. For clarity, the templates are grouped into the following 12 categories due to their similar shapes:

- Simulation based templates:
  - The signal, including both $\tau^+ \to 3\pi^\pm\overline{\nu}_\tau$ and $\tau^+ \to 3\pi^\pm\pi^0\overline{\nu}_\tau$ modes: $B^0 \to D^{*-}\tau^+\nu_\tau$
  - The excited D^{**} states: $B^0 \to D^{**}\tau^+\nu_\tau$.
  - The double charm templates:
    - $B^0 \to D^{*-}D_s^{+(*)}$: which includes $B^0 \to D^{*-}D_s^+$, $B^0 \to D^{*-}D_s^{+*}$, $B^0 \to D^{*-}D_{s0}^{*+}$, and $B^0 \to D^{*-}D_{s1}^+$.
    - $B \to D^{**-}D_s^+X$
    - $B_s^0 \to D^{*-}D_s^+X$
    - $B \to D^{*-}D^+X$
  - The prompt B^0 template: $B \to D^{*-}3\pi^\pm X$
  - All pions of the $3\pi^\pm$ system come from the same vertex (SV): $B \to D^{*-}D^0X$ SV
  - At least one pion of the $3\pi^\pm$ comes from the D^0 vertex, while the other.s come.s from a different[1] vertex (DV): $B \to D^{*-}D^0X$ DV

  The MC-derived templates are extracted with MC-truth requirements.
- The data-derived templates represent combinatorial B, D^0, and D^* events:
  - Combinatorial B^0: build from the wrong sign data with respect to the signal, where the $D^{*\pm}$ has the same charge as the $3\pi^\pm$ system.
  - Combinatorial D^{*-} but genuine D^0
  - Combinatorial D^0

The model used to fit the data is the sum of 16 components, listed in the first column of Tab. 7.1. Each component's shape is modeled using histogram templates created from simulation samples and, in three cases, from collision data samples. The parameters controlling the relative normalization of each component are listed in the second column of Tab. 7.1, where:

[1] *e.g.* when the slow pion from D^{*-} is reconstructed as coming from D^0

- Number of $B^0 \to D^{*-}\tau^+\nu_\tau$ events, used as input for calculating $\mathcal{K}(D^{*-})$: N_{sig}
- Fraction of $\tau^+ \to 3\pi\overline{\nu}_\tau$ decays relative to the sum of $\tau^+ \to 3\pi\overline{\nu}_\tau$ and $\tau^+ \to 3\pi\pi^0\overline{\nu}_\tau$ decays: $f_{\tau^+\to 3\pi\overline{\nu}_\tau}$
- Fraction of $B \to \overline{D}^{**}\tau^+\nu_\tau$ decays relative to $B^0 \to D^{*-}\tau^+\nu_\tau$ decays: $f_{D^{**}\tau\nu}$
- Number of $B \to D^{*-}D^0X$ events where all pions in the $3\pi^\pm$ system originate from the D^0 vertex: $N^{same}_{D^0}$
- Ratio of $B \to D^{*-}D^0X$ decays where at least one pion originates from the D^0 vertex and the other pion.s from a different vertex, normalized to $N^{same}_{D^0}$: $f^{\nu_1-\nu_2}_{D^0}$
- Ratio of $B \to D^{*-}D^+X$ decays relative to those containing a D_s^+ meson: f_{D^+}
- Yield of events involving a D_s^+: $N_{D_s^+}$
- Yield of the inclusive prompt $B \to D^{*-}3\pi X$ events where the three pions come from the B vertex : $N_{B\to 3\pi^\pm X}$
- Combinatorial background events yield where the D^{*-} and the 3π system come from different B decays: $N_{B_1B_2}$
- Yield of combinatorial background events with a fake D^0: $N_{\text{fake}D^0}$
- Yield of combinatorial background events with a fake D^{*-}: $N_{\text{fake}D^*}$

The PDF used in the fit is defined as:

$$\begin{aligned}\mathcal{P}_{tot}(q^2, t_\tau, \text{BDT}) = \frac{1}{N_{tot}} \Big\{ & N_{sig}\left[f_{\tau^+\to 3\pi\overline{\nu}_\tau}\mathcal{P}_{\tau^+\to 3\pi\overline{\nu}_\tau}\right. \\ & \left. +(1 - f_{\tau^+\to 3\pi\overline{\nu}_\tau})\mathcal{P}_{\tau^+\to 3\pi\pi^0\overline{\nu}_\tau} + f_{D^{**}\tau\nu}\mathcal{P}_{B\to\overline{D}^{**}\tau^+\nu_\tau}\right] \\ & + N^{same}_{D^0}\left[\mathcal{P}_{B\to D^{*-}D^0X\,SV} + f^{\nu_1-\nu_2}_{D^0}\mathcal{P}_{B\to D^{*-}D^0X\,DV}\right] \\ & + \frac{N_{D_s^+}}{k}\left[\mathcal{P}_{B^0\to D^{*-}D_s^{*+}} + f_{D_s^+}\mathcal{P}_{B^0\to D^{*-}D_s^+} + f_{D_{s0}^{*+}}\mathcal{P}_{B^0\to D^{*-}D_{s0}^{*+}}\right. \\ & \left. + f_{D_{s1}^+}\mathcal{P}_{B^0\to D^{*-}D_{s1}^+} + f_{D^{**}D_sX}\mathcal{P}_{B\to D^{**-}D_s^+X} + f_{B_s\to D^*D_s^+X}\mathcal{P}_{B_s^0\to D^{*-}D_s^+X}\right] \\ & + N_{D_s^+}f_{D^+}\mathcal{P}_{B\to D^{*-}D^+X} + N_{B\to D^{*-}3\pi^\pm X}\mathcal{P}_{B\to D^{*-}3\pi^\pm X} \\ & + N_{B_1-B_2}\mathcal{P}_{\text{comb. B}} + N_{\text{fake }D^0}\mathcal{P}_{\text{comb. }D^0} + N_{\text{fake }D^*}\mathcal{P}_{\text{comb.}D^{*-}}\Big\} \end{aligned} \tag{7.1}$$

where the three variables (q^2, τ^+ lifetime, and anti-D_s^+ BDT) have been omitted from the template PDFs for brevity, N_{tot} is the total number of events in the sample, and $\mathcal{P}_i$ is the PDF of the i-th component. The normalization of each component is defined in Tab. 7.1.

The parameters are:

Component	**Normalization**
$B^0 \to D^{*-}\tau^+\nu_\tau$ ($\tau^+ \to 3\pi\overline{\nu}_\tau$)	$N_{\text{sig}} \times f_{\tau^+\to 3\pi\overline{\nu}_\tau}$
$B^0 \to D^{*-}\tau^+\nu_\tau$ ($\tau^+ \to 3\pi\pi^0\overline{\nu}_\tau$)	$N_{\text{sig}} \times (1 - f_{\tau^+\to 3\pi\overline{\nu}_\tau})$
$B \to \overline{D}^{**}\tau^+\nu_\tau$	$N_{\text{sig}} \times f_{D^{**}\tau\nu}$
$B \to D^{*-}3\pi^\pm X$	$N_{B\to D^{*-}3\pi^\pm X}$
$B \to D^{*-}D^0 X$ (SV)	$N^{\text{same}}_{D^0}$
$B \to D^{*-}D^0 X$ (DV)	$N^{\text{same}}_{D^0} \times f^{\nu_1-\nu_2}_{D^0}$
$B \to D^{*-}D^+ X$	$N_{D_s^+} \times f_{D^+}$
$B^0 \to D^{*-}D_s^+$	$N_{D_s^+} \times f_{D_s^+}/k$
$B^0 \to D^{*-}D_s^{*+}$	$N_{D_s^+} \times 1/k$
$B^0 \to D^{*-}D_{s0}^{*+}$	$N_{D_s^+} \times f_{D_{s0}^{*+}}/k$
$B^0 \to D^{*-}D_{s1}^{+}$	$N_{D_s^+} \times f_{D_{s1}^{+}}/k$
$B \to D^{**-}D_s^+ X$	$N_{D_s^+} \times f_{D^{**}D_s X}/k$
$B_s^0 \to D^{*-}D_s^+ X$	$N_{D_s^+} \times f_{B_s\to D^* D_s^+ X}/k$
Combinatorial B	$N_{B_1B_2}$
Combinatorial D^*	$N_{\text{fake } D^*}$
Combinatorial D^0	$N_{\text{fake } D^0}$

Table 7.1.: List of components in the signal fit and how they are normalized.

Parameter	Fit result	Efficiency correction	Corrected fraction
f_{D_s}	0.556 ± 0.016	0.981	0.546 ± 0.015
$f_{D^{*+}_{s0}}$	0.050 ± 0.021	1.039	0.052 ± 0.022
$f_{D'^{+}_{s1}}$	0.438 ± 0.033	1.116	0.489 ± 0.037
$f_{D^{**}D_sX}$	0.188 ± 0.034	1.170	0.220 ± 0.04
$f_{B_s \to D^* D_s X}$	0.067 ± 0.017	1.010	0.068 ± 0.017

Table 7.2.: Constrained parameters obtained from D_s^+ production control mode fit to data, after correcting for signal/control mode selection efficiency.

- Four free parameters: N_{sig}, $N_{D_s^+}$, f_{D^+} and $f_{D^0}^{\nu_1-\nu_2}$.
- Six Gaussian constrained parameters: $N_{B\to D^{*-}3\pi^\pm X}$,$f_{D_s^+}$, $f_{D^{*+}_{s0}}$, $f_{D^+_{s1}}$, $f_{D^{**}D_sX}$, $f_{B_s\to D^*D_s^+X}$
- Six fixed parameters: $N^{same}_{D^0}$, $f_{\tau^+\to 3\pi\bar{\nu}_\tau}$, $f_{D^{**}\tau\nu}$, $N_{B_1-B_2}$, $N_{\text{fake } D^*}$, $N_{\text{fake } D^0}$

7.1.1.1. Gaussian Constrained Parameters

Most of the parameters are constrained by Gaussian distributions with mean and uncertainty as obtained in the $B \to D^* D_s^+ X$ fit (*cf.* Sec. 6.2). The parameters $f_{D_s^+}$, $f_{D^{*+}_{s0}}$, $f_{D^+_{s1}}$, $f_{D^{**}D_s^+X}$, and $f_{B_s^0\to D^*D_s^+X}$ are used as constraints after adjusting for efficiency differences between the $B \to D^{*-} D_s^+ X$ and signal selections.

The values of the constrained parameters are reported in Tab. 7.2. To correct for the signal/control mode selection efficiency, the constrained parameters are multiplied by the efficiency correction factor $\varepsilon_{sig}/\varepsilon_{control}$, the ratio of the signal and control mode selection efficiencies. The corrected fractions are then used in the fit to data.

The central value for $N_{B\to D^{*-}3\pi^\pm X}$ is determined using the following data-driven procedure. The exclusive yield of $B \to D^* 3\pi$ is selected from the *peak region* defined by the mass range: $m(B^0) \in [5200, 5350]\,\mathrm{MeV}/c^2$.
A mass threshold of $m(B^0) < 5100\,\mathrm{MeV}/c^2$ is applied in the *prompt region* to minimize background noise from other decay channels, ensuring better separation and identification of the $B \to D^* 3\pi X$ yields.
Identifying the $B^0 \to D^{*-} 3\pi^\pm$ yield in data is challenging due to similar background types. To overcome this, a MC ratio between the inclusive and exclusive sample $b\bar{b} \to B \to D^* 3\pi X$, with *truth–matching* requirements, helps to obtain an estimation of the prompt yield:

$$N(B \to D^* 3\pi X)^{\text{data}} = N(B \to D^* 3\pi)^{\text{data}} \cdot \frac{N(B \to D^* 3\pi X)^{\text{MC}}}{N(B \to D^* 3\pi)^{\text{MC}}} \cdot f_{\text{Corr.}} \tag{7.2}$$

The correction factor $f_{\text{Corr.}}$, accounting for discrepancies between MC modeling and real data, is derived from a purely *prompt sample*:

$$f_{\text{Corr.}} = \frac{N(B \to D^* 3\pi X)^{\text{data}}_{\text{prompt}}}{N(B \to D^* 3\pi)^{\text{data}}_{\text{prompt}}} \Bigg/ \frac{N(B \to D^* 3\pi X)^{\text{MC}}_{\text{prompt}}}{N(B \to D^* 3\pi)^{\text{MC}}_{\text{prompt}}} \tag{7.3}$$

To enrich our sample with prompt events, we utilize both data and MC samples. Unlike other, the prompt sample, for data and MC, is obtained by excluding the loose 3π vertex detachment cut, which is typically applied as a preselection cut to reduce the size of the ROOT tuples. Prompt event–eliminating cuts, such as the detachment BDT cut and constraints on B^0 mass, are excluded. Furthermore, a requirement of $\Delta z < -2$ between B and τ vertices is set. The yield for prompt $B \to D^* 3\pi X$ events is then determined by setting a mass requirement of $m(B^0) < 5.1\,\text{GeV}/c^2$.

It should be noted that in the 2017 and 2018 Monte Carlo (MC) samples, a restrictive mass cut of $m(B^0) < 5.1\,\text{GeV}/c^2$ was mistakenly applied during the stripping stage, resulting in fewer prompt events (*cf.* Tab. 5.5):

$$m(B^0) > 4500\,\text{MeV}/c^2 \quad \text{or} \quad \texttt{D2DVVDCHI2SIGN} > 4\,, \tag{7.4}$$

As a consequence, these cuts are reported to data as well, to maintain consistency between the two samples.

7.1.1.2. Fixed Parameters

The yields of combinatorial events, denoted $N_{B_1 B_2}$, are fixed in the fitting procedure according to the expected values estimated for the sample. This approach is adopted to avoid potential overestimation of these components that can occur if their yields are allowed to float freely.

Combinatorial B events are analyzed using both Right-Sign (RS) and WS data samples. These events are distinguished by several characteristics: they are non-isolated, exhibit a flat distribution in $\text{acos}\big(\texttt{DIRA}(B^0, PV)\big)$, and show large values in $m(D^{*-} 3\pi^{\pm})$. The combinatorial BDT and reverses the isolation BDT cuts are excluded, to ensure that the sample is predominated by combinatorial B events.

The yield of combinatorial B events is assessed using the RS sample with standard signal selection criteria applied. In addition, the requirement:

$$\text{acos}\big(\texttt{DIRA}(B^0, PV)\big) > 0.03\,, \tag{7.5}$$

is applied to accurately identify these events. The obtained yield is $N_{B_1 B_2} = 178 \pm 13$.

The yields of the combinatoric D^0 and D^{*-} are determined through a two-dimensional unbinned maximum-likelihood fit applied to the reconstructed mass of the D^0, and the mass difference between the reconstructed D^{*-} and D^0, respectively defined as:

$$m(K^-\pi^+) \quad \text{and} \quad \Delta M \equiv m(D^{*-}) - m(K^-\pi^+) \,. \tag{7.6}$$

Combinatorial D^0 events distribution do not peak in either of the fit variables. To avoid overlap between the two categories, only those combinatorial D^{*-} events are associated with a genuine D^0, specifically where the $K^-\pi^+$ system originates from the D^0. The D^{*-} and D^0 pions are ensured not to originate from the same D^{*-}. These events show a peak in $m(K^-\pi^+)$ but not in ΔM, thereby distinguishing the two categories.

The signal, comprising genuine D^0 and D^{*-} candidates, is modeled in the distribution of $m(K^-\pi^+)$ using a combination of the Crystal Ball and Gaussian functions. For ΔM, the modeling involves a sum of two Crystal Balls, featuring both left- and right-hand tails, and a Gaussian. The combinatorial D^0 is represented by an exponential function in $m(K^-\pi^+)$ and a specialized RooFit function[2].

The combinatorial D^{*-}, yet genuine D^0, is modeled using the signal PDF in $m(K^-\pi^+)$ and, similarly to the combinatorial D^0, in ΔM. Additionally, mis-identified D^{*-} events in the fitted sample are characterized by shapes derived from simulation after MC-truth requirements, they are modeled as the signal.

Fig. 7.1 shows the fit projections on the two fitted variables along with the pull distributions, where the agreement is generally observed within 2–3σ and occasionally around 4σ. The templates constructed for this purpose are utilized in the signal fit and are normalized according to the yields of fake D^0.

The number of D^0 events decaying into three pions, denoted as $N^{\text{same}}_{D^0}$, is derived by scaling the truth-matched yield obtained from simulation. This scaling is obtained via the ratio of the yields of $D^0 \to K^-3\pi^\pm$ decays observed in data and simulation, respectively, as shown in Fig. 7.2. The yields are determined through the fitting of a Gaussian to model the signal and an exponential to account for the combinatorial backgrounds.

The fraction of $B \to D^{**}\tau\nu$ events relative to the signal ones, $f_{D^{**}\tau\nu}$, is fixed in the fit to the expected value from the simulation. Here, B denotes either B^0, B^+, or B^0_s, while D^{**} refers to any doubly excited D state, including D^{**}_s, which decays to $D^{*-}X$. The simulation

[2]The RooFit function is defined as: $1 - e^{-\alpha(m-m_0)}$, where α and m_0 are free parameters.

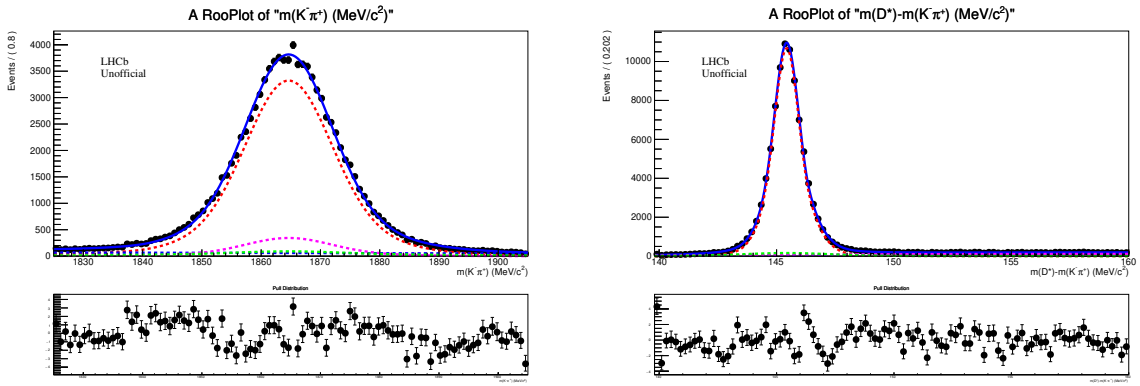

Figure 7.1.: Projections of the two-dimensional fit to the $m(K^-\pi^+)$ (left) and $\Delta M \equiv m(D^{*-}) - m(K^-\pi^+)$ (right) for the collision data sample after the full selection. Signal (red), combinatorial D^0 (blue), combinatorial D^{*-} (magenta), mis-identified D^{*-} (green).

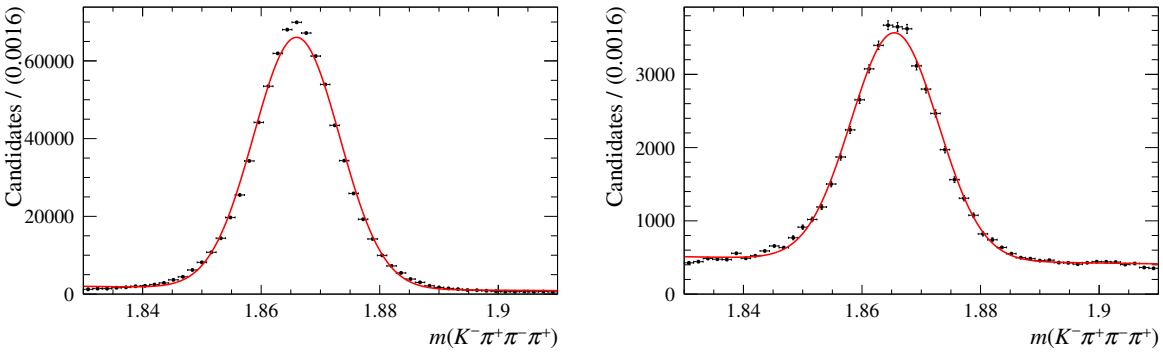

Figure 7.2.: Fit to $m(K^-3\pi^\pm)$ in MC (left) and data (right) around the D^0 mass. The D^0 yields are used to scale the MC sample in order to deduce the $N^{\text{same}}_{D^0}$ parameter.

overestimates the number of $B \to D^{**}\tau\nu$ events, as the branching fraction input might be too large.

To align the simulation with the expected values from theoretical calculations and experimental measurements, a weight $\mathcal{W}$ is introduced:

$$\mathcal{W} = \frac{R(D^{**}) \times \mathrm{Br}(B \to D^{**}\mu\nu)}{\mathrm{Br}(B^0 \to D^{**}\tau\nu)|_{\mathrm{Sim.}} \times \mathrm{Br}(D^{**} \to D^{*})|_{\mathrm{Sim.}}} \,, \tag{7.7}$$

The branching fractions are compared to the theoretical expectations for each D^{**} state. The theoretical $R(D^{**})$ predictions from [166] and the branching fractions [7] of $B \to D^{**}\mu\nu$ are combined to obtain the expected $B \to D^{**}\tau\nu$ branching fraction, in the numerator. While, the denominator is the product of the branching fraction input used to produce the simulation sample.

The different branching ratios are given in Tab. 4.3. The theoretical value of $R(D^{**})$ are taken from [166]:

$$R(D_1^{'}) = 0.05 \pm 0.02 \,, \quad R(D_1) = 0.10 \pm 0.02 \,, \quad R(D_2^{*}) = 0.07 \pm 0.01. \tag{7.8}$$

The theoretical $R(D_s^{**})$ is not available, so a weight of 0.5 is assigned, with an associated systematic uncertainty (*cf.* Chap. 8).

Tab. 7.3 reports the yields N_j of $B^0 \to D_j^{**}\tau\nu$ events for each D_j^{**} state, obtained from the $b\overline{b} \to D^{*-}3\pi X$ MC sample. A weighted yield is obtained by multiplying the observed yield by the weight $\mathcal{W}$. Finally, the feed-down fraction is obtained by summing over the D^{**} states:

$$f_{D^{**}\tau\nu} = \sum_{j=1}^{8} \mathcal{W}_j \times N_j / N_{tot} = 2.4\% \,, \tag{7.9}$$

where the total D^* yield is $N_{tot} = 114012$ and the weighted D^{**} yield is:

$$\sum_{j=1}^{8} \mathcal{W}_j \times N_j = 2777 \,. \tag{7.10}$$

The relative abundance of the $\tau^+ \to 3\pi\overline{\nu}_\tau$ to the sum of $\tau^+ \to 3\pi\overline{\nu}_\tau$ and $\tau^+ \to 3\pi\pi^0\overline{\nu}_\tau$, $f_{\tau^+ \to 3\pi\overline{\nu}_\tau}$

Index j	State	$\mathcal{W}_j$	N_j	$\mathcal{W}_j \times N_j$
1	$D_1(2420)^0$	0.3497	1618	566
2	$D_2^*(2460)^0$	0.1667	736	123
3	$D_1(2430)^0$	0.1023	2366	242
4	$D_1(2420)^+$	0.3263	2321	757
5	$D_2^*(2460)^+$	0.1225	1164	143
6	$D_1(H)^+$	0.1174	3438	404
7	$D_{s1}(2536)^+$	0.1700	2525	429
8	$D_{s2}^*(2573)^+$	0.5	227	113
	Total			2777

Table 7.3.: $B \to D^{**}\tau\nu$ events in $b\bar{b} \to D^*3\pi X$ inclusive MC sample and the corresponding weighted yields for different D^{**} states ($B \in \{B^0, B^+, B_s^0\}$).

is extracted from the efficiency calculation (*cf.* Sec. 5.7, Eq. (5.16)):

$$f_{\tau^+\to 3\pi\overline{\nu}_\tau} = \frac{\left\langle \varepsilon_{\mathtt{sig\,1}} \right\rangle \cdot \mathrm{Br}(\mathtt{sig\,1})}{\left\langle \varepsilon_{\mathtt{sig\,1}} \right\rangle \cdot \mathrm{Br}(\mathtt{sig\,1}) + \left\langle \varepsilon_{\mathtt{sig\,2}} \right\rangle \cdot \mathrm{Br}(\mathtt{sig\,2})} = 0.782 \pm 0.003 \ . \tag{7.11}$$

with the efficiencies of the two signal modes: $\left\langle \varepsilon_{\mathtt{sig\,1}} \right\rangle$ and $\left\langle \varepsilon_{\mathtt{sig\,2}} \right\rangle$ for the $\tau^+ \to 3\pi\overline{\nu}_\tau$ and $\tau^+ \to 3\pi\pi^0\overline{\nu}_\tau$ decay modes, respectively. The corresponding values are reported in Tab. 5.19 and the branching fractions are taken from Ref. [38].

7.1.2. Fit Validation with Toy MC

The fit is validated through simulated pseudo-experiments, referred to as toys. Following the nominal fit conducted on a data sample containing $N_{\mathtt{tot}}$ events, a series of $N = 1000$ pseudo-experiments is performed. In each experiment, events are generated according to a Poisson distribution with mean $N_{\mathtt{tot}}$, based on the nominal fit model. These generated events are then refitted, resulting in estimates of $N_{\mathtt{sig\ toy}}$ and other parameters from each toy experiment. The initial values for the fit parameters in each pseudo-experiment are set to the best-fit values obtained from the blinded signal fit in the data.

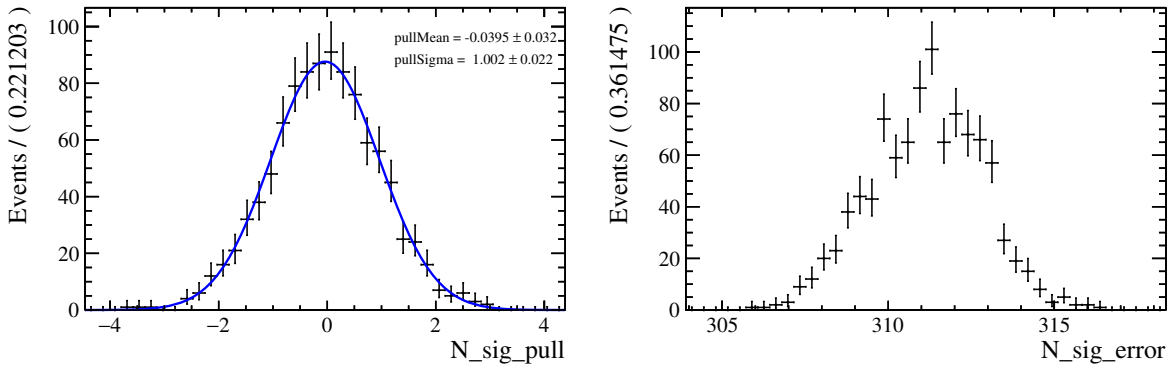

Figure 7.3.: Pull distribution (left) and the error distribution (right) for the signal yield N_{sig} in the toy MC.

Fig. 7.3 shows the pull distribution, defined as:

$$\text{pull}(N_{sig}) = \frac{N_{sig}^{toy} - N_{sig}}{\sigma_{N_{sig}}}\,, \tag{7.12}$$

The pull mean and standard deviation are found to be compatible with zero and unity, respectively, indicating no observable bias in the signal yield or its uncertainty as derived from the fit.

Distributions of the other fit parameters, along with their correlation coefficients, are presented in App. C.1.1. Most of the parameters show pull distributions compatible with unity, respectively, except for $f_{B_s^0 \to D^* D_s^+ X}$. Further studies are needed to understand the origin of the discrepancy.

7.1.3. Blinding Scheme

In this stage of the analysis, the signal yield, denoted as N_{sig}, is intentionally blinded to prevent any biasing of analysts by preliminary results. To ensure the blinding of N_{sig}, it is multiplied by a random factor, χ, drawn from a Gaussian distribution with a mean of $\mu = 1.0$ and a standard deviation of $\sigma = 0.3$, constrained to the range $[0.1, 1.9]$. The parameter actually passed to the fitting procedure is N_{sig}/χ, which represents the true signal yield,

while the fitting program reports the modified value of N_{sig} [3]. Consequently, both N_{sig} and its uncertainty are scaled by the same factor x, ensuring that the relative uncertainty, $\sigma_{N_{sig}}/N_{sig}$, is accurately reported and remains unaffected by the blinding.

While N_{sig} is blinded, it is conceivable to infer its value from the known size of the dataset after accounting for all background yields. Therefore, the difference between the blinded and actual yields of the three N_{sig}-dependent components, $N_{sig}(1 - 1/x)(1 + f_{D^{**}\tau\nu})$, is evenly distributed among the background components, excluding those with yields that are preset prior to the fit.

7.1.4. Blinded Fit to Data

The fit is performed with the signal yield blinded, as described in Sec. 7.1.3. The number of collision data events used in the fit is 88053. The total PDF is unblinded but the components will not drawn to prevent unblinding.

The value of the parameters of the blinded fit using the Run 2 collision data are documented in Tab. 7.4, the projection on the fit variables are shown in Fig. 7.4.

The fit quality, expressed as χ^2 per degree of freedom, is evaluated as $\chi^2/374 = 1.46$. This fit model's with the data is further verified through a flattened distribution presented in Fig. 7.5, where each 3-dimensional bin's content is compared against the fitted model. The pull distribution of the fit across the $8 \times 8 \times 6$ bins is shown in Fig. 7.6.
The correlation matrix among the fitted parameters is shown in Fig. 7.7 , with the N_{D_s} parameters showing correlations between ±50 to ±60% with $f_{B_s \to D^* D_s X}$, $f_{D^{**} D_s X}$, f_{D^+}, and $f_{D^0}^{\nu_1 - \nu_2}$. This indicates potential challenges in distinctly separating these categories in the fit.
The projections of the control variables used in Secs. 6.1 and 6.2 from the signal fit are shown in Figs. 7.8 and 7.9.
A significant disagreement between data and total PDF is observed for $\min(\pi^+\pi^-)$ and $m(3\pi)$. The latter is planned to be studied further in Sec. 8.5.6, as a potential source of systematic uncertainty.
The relative statistical uncertainty of the signal yield is:

$$\sigma_{N_{sig}} / N_{sig} = 4.1\% \tag{7.13}$$

[3] In the fitting process, only the blinded value of N_{sig} is adjusted, since x is a fixed constant. As the fitting program only reports floating parameters during the fit, x remains undisclosed, thus ensuring the actual yield N_{sig}/x remains blinded.

Parameter	Values	
Free Parameters		
N_{sig}	7815 ± 323	
N_{D_s}	53148 ± 752	
f_{D^+}	0.11 ± 0.01	
$f_{D^0}^{\nu_1-\nu_2}$	2.43 ± 0.20	
Constrained Parameters		
	Constrained Value	Fit Value
$N_{B\to D^{*-}3\pi^\pm X}$	6133 ± 400	6940 ± 347
f_{D_s}	0.546 ± 0.015	0.55 ± 0.01
$f_{D_{s0}^{*+}}$	0.052 ± 0.022	0.04 ± 0.02
$f_{D_{s1}^{\prime+}}$	0.489 ± 0.037	0.43 ± 0.02
$f_{D^{**}D_sX}$	0.220 ± 0.040	0.35 ± 0.03
$f_{B_s\to D^*D_sX}$	0.068 ± 0.017	0.08 ± 0.01
Fixed Parameters		
$N_{B_1B_2}$	178 ± 13	
$N_{D^0}^{same}$	3233 ± 57	
N_{fakeD^0}	802 ± 25	
N_{fakeD^*}	1862 ± 49	
$f_{D^{**}\tau\nu}$	0.024 ± 0.000	
$f_{\tau^+\to 3\pi^\pm\overline{\nu}_\tau}$	0.768 ± 0.002	

Table 7.4.: Values of the parameters obtained from/used for fits to the Run 2 collision data, with $f_{D^0}^{\nu_1-\nu_2}$ and $f_{D_s^+}$ floated. The signal yield remains blinded.

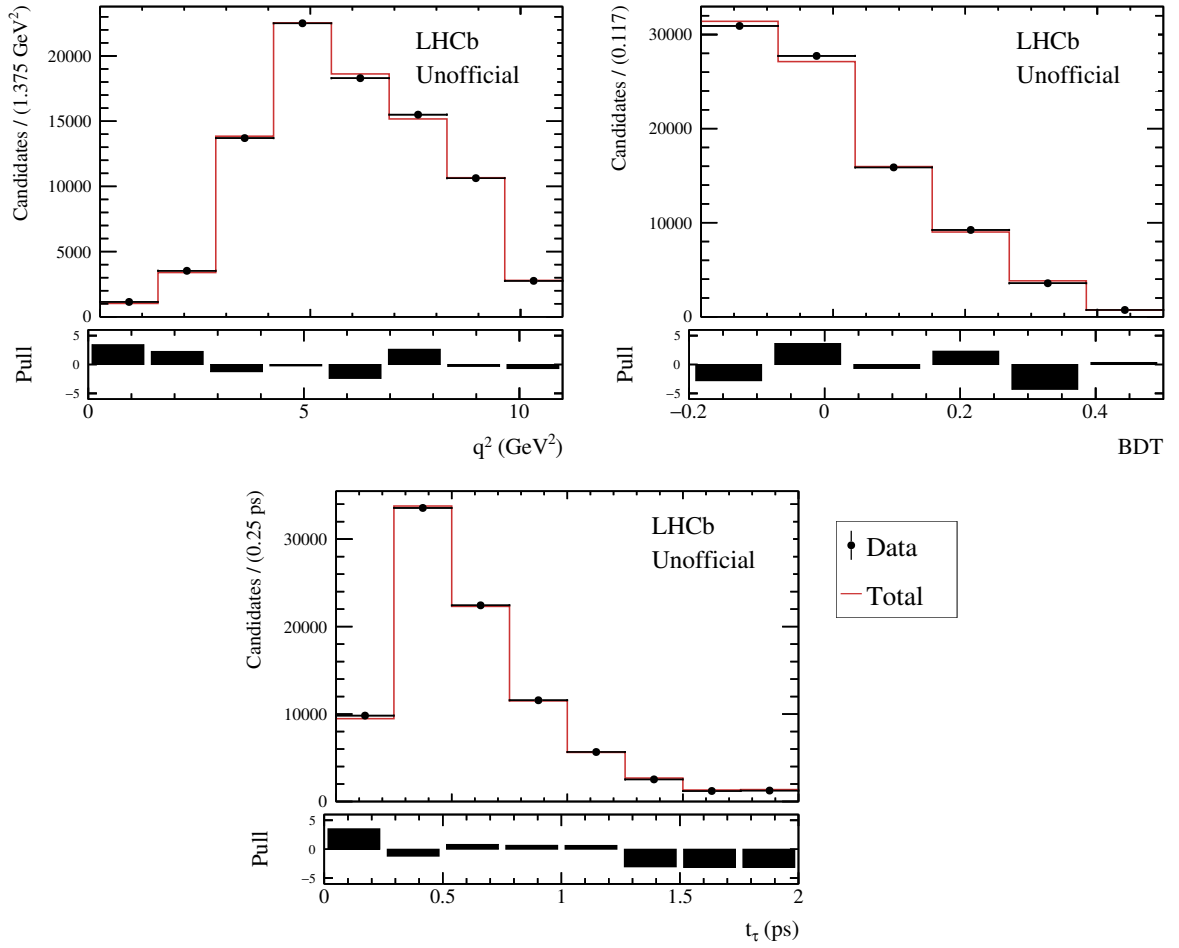

Figure 7.4.: The signal fit projections on the fit variables to the Run 2 data sample, with $f_{D^0}^{\nu_1-\nu_2}$ and $f_{D_s^+}$ floated.

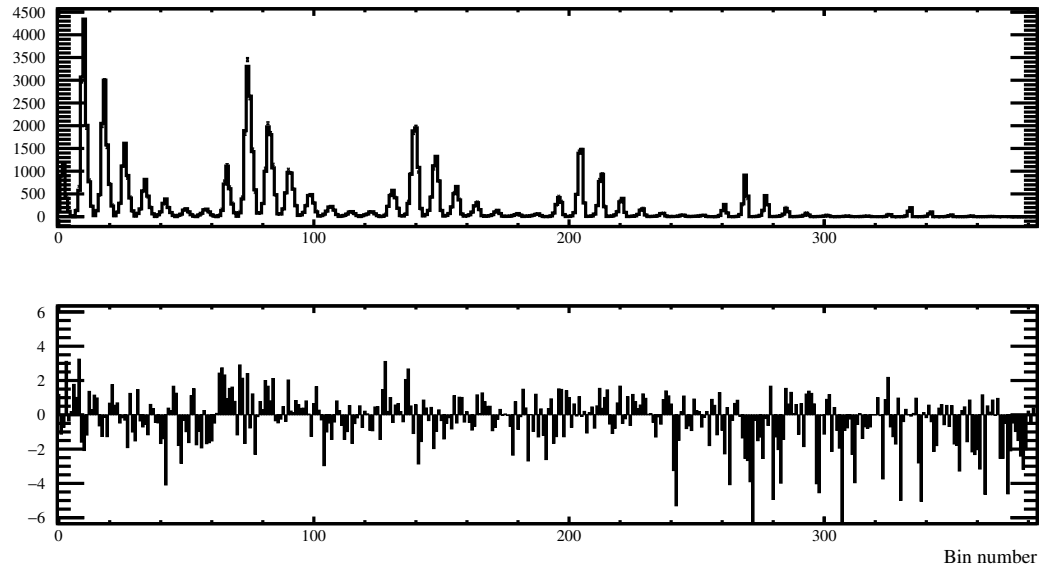

Figure 7.5.: The signal fit flattened projection across its $8\times8\times6$ bins for the Run 2 data sample (top) and its pull distribution (bottom). The x−axis represents an arbitrary bin index. $f_{D^0}^{\nu_1-\nu_2}$ and $f_{D_s^+}$ are floated

.

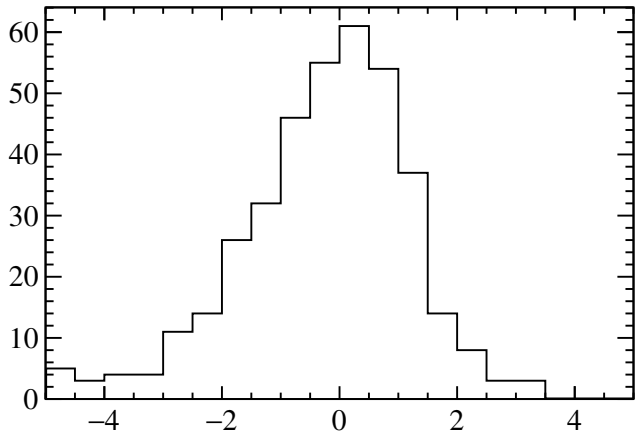

Figure 7.6.: The pull values of $8 \times 8 \times 6$ bins for the fit to data sample.

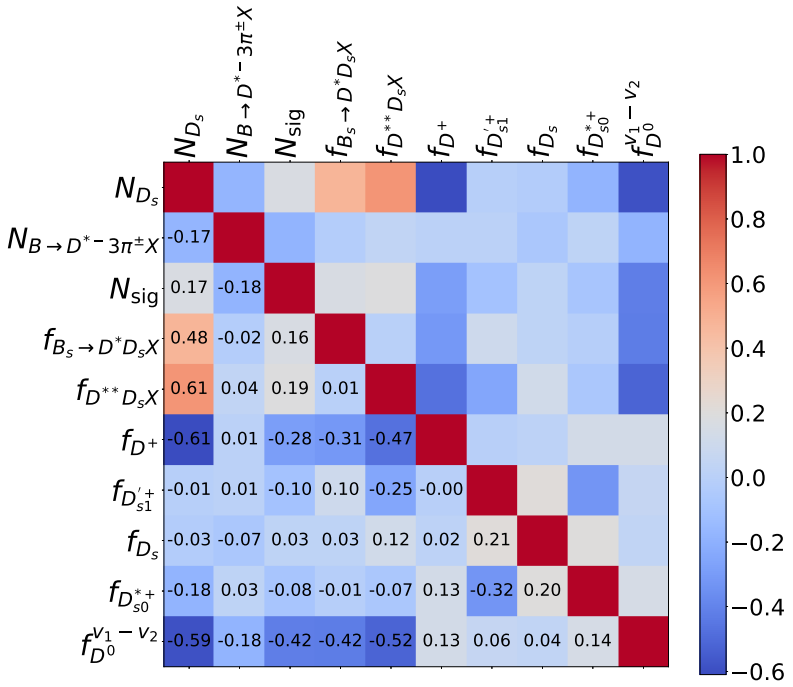

Figure 7.7.: Correlation coefficients of the signal fit variables in the Run 2 collision data fit, with $f_{D^0}^{\nu_1-\nu_2}$ and $f_{D_s^+}$ floated.

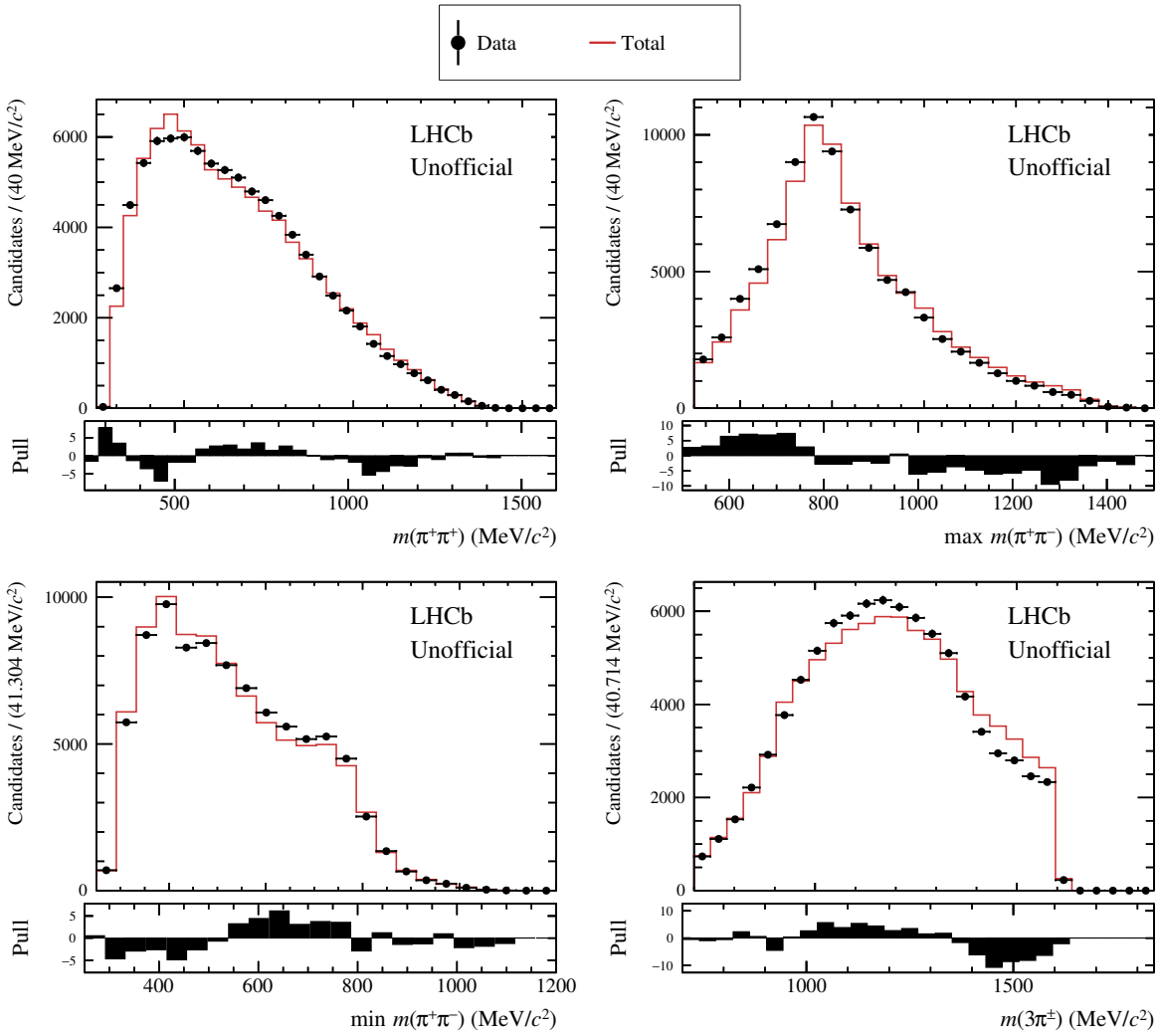

Figure 7.8.: The signal fit projections on the D_s^+ control variables to the Run 2 data sample, with $f_{D^0}^{\nu_1-\nu_2}$ and $f_{D_s^+}$ floated.

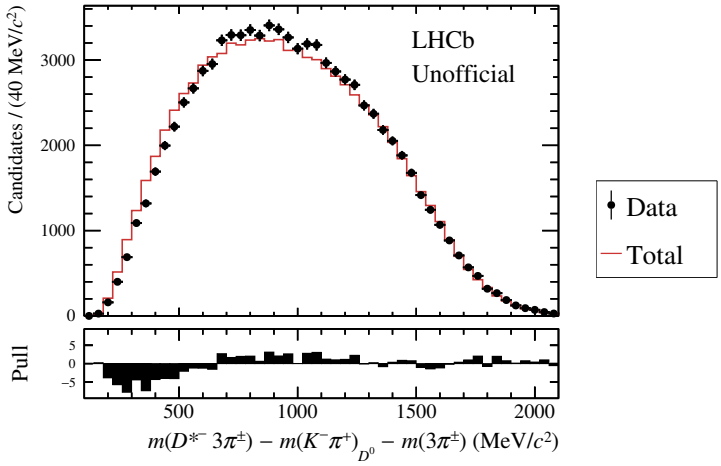

Figure 7.9.: The signal fit projections on $m(D^*3\pi)$ to the Run 2 data sample.

The relative statistical uncertainty on the signal yield in Run 1 was 6.64%, this was obtained after fixing the D^0 and D_s^+ fractions. Similar strategy is applied to the Run 2 data (*cf.* Sec. 7.1.7.)

7.1.5. Fit Results for Different Datasets

The signal fit, performed as in Sec. 7.1.4, with floating $f_{D^0}^{\nu 1-\nu 2}$ and $f_{D_s^+}$, for different datasets is given in Tab. 7.5 for the Run 2, 2018, 2017, and 2015–2016 datasets.The relative statistical uncertainty, the fit quality as χ^2 per degree of freedom, and the integrated luminosity are also provided in Tab. 7.6.

Before fixing the D^0 and D_s^+ fractions, the relative statistical uncertainty of the signal yield is estimated to be approximately 4.1% for the full Run 2 dataset. For the individual datasets, the uncertainties are estimated to be 7.8% for 2015–2016, 6.9% for 2017, and 6.1% for 2018. This trend reflects a reduction in uncertainty, consistent with the anticipated improvement from increased integrated luminosity.

These results show that the 2015–2016 dataset exhibits lower statistics compared to previous analyses [3], leading to a higher uncertainty in the signal yield.
However, in the published analysis [3] using the 2015–2016 dataset, the relative statistical uncertainty on the signal yield was reported to be 6.2%, with *floating* D^0 and D_s^+ fractions and 5.9% with *fixed* D^0 and D_s^+ fractions. An investigation is ongoing to understand the reason for this discrepancy. This could result from the unoptimized control fit (*cf.* Sec. 6.1) and the signal fit described in this section.
Additionally, the behavior of the no-Charm yield, $N_{B\to D^{*-}3\pi X}$, is noteworthy; the *constrained*

Parameters	Datasets: Run 2	2018	2017	2015–2016
Free Parameters				
N_{sig}	7815 ± 323	3177 ± 193	2557 ± 176	2201 ± 171
N_{D_s}	53148 ± 752	18622 ± 393	15790 ± 334	17902 ± 373
f_{D^+}	0.11 ± 0.01	0.1 ± 0.01	0.09 ± 0.01	0.16 ± 0.01
$f_{D^0}^{\nu_1-\nu_2}$	2.43 ± 0.2	3.09 ± 0.29	3.22 ± 0.31	1.5 ± 0.31
Constrained Parameters				
	Constrained Value			
$N_{B\to D^{*-}3\pi^{\pm}X}$	6133 ± 400	2020 ± 191	1800 ± 192	2329 ± 303
f_{D_s}	0.546 ± 0.015	0.532 ± 0.025	0.554 ± 0.028	0.564 ± 0.028
$f_{D_{s0}^{*+}}$	0.052 ± 0.022	0.064 ± 0.032	0.063 ± 0.034	0.127 ± 0.037
$f_{D_{s1}^{\prime+}}$	0.489 ± 0.037	0.481 ± 0.049	0.416 ± 0.053	0.440 ± 0.055
$f_{D^{**}D_sX}$	0.220 ± 0.040	0.200 ± 0.052	0.242 ± 0.051	0.281 ± 0.059
$f_{B_s\to D^*D_sX}$	0.068 ± 0.017	0.078 ± 0.023	0.065 ± 0.024	0.080 ± 0.025
	Fit Value			
$N_{B\to D^{*-}3\pi^{\pm}X}$	6940 ± 347	2467 ± 174	2184 ± 171	1616 ± 217
f_{D_s}	0.55 ± 0.01	0.52 ± 0.02	0.55 ± 0.02	0.59 ± 0.02
$f_{D_{s0}^{*+}}$	0.04 ± 0.02	0.07 ± 0.03	0.07 ± 0.03	0.09 ± 0.03
$f_{D_{s1}^{\prime+}}$	0.43 ± 0.02	0.44 ± 0.03	0.42 ± 0.03	0.38 ± 0.03
$f_{D^{**}D_sX}$	0.35 ± 0.03	0.28 ± 0.04	0.31 ± 0.04	0.38 ± 0.04
$f_{B_s\to D^*D_sX}$	0.08 ± 0.01	0.09 ± 0.02	0.05 ± 0.02	0.09 ± 0.02
Fixed Parameters				
$N_{B_1B_2}$	178 ± 13	80 ± 9	64 ± 8	34 ± 6
$N_{D^0}^{same}$	3233 ± 57	1231 ± 35	1016 ± 32	985 ± 31
N_{fakeD^0}	802 ± 25	384 ± 13	301 ± 12	304 ± 12
N_{fakeD^*}	1862 ± 49	762 ± 27	674 ± 25	627 ± 25
$f_{D^{**}\tau\nu}$	0.024 ± 0.00	0.024 ± 0.00	0.023 ± 0.00	0.025 ± 0.00
$f_{\tau^+\to 3\pi^{\pm}\overline{\nu}_\tau}$	0.768 ± 0.002	0.770 ± 0.003	0.768 ± 0.002	0.767 ± 0.004

Table 7.5.: Values of the parameters obtained from/used for fits to the Run 2, 2018, 2017, and 2015–2016 collision data, with $f_{D^0}^{\nu_1-\nu_2}$ and $f_{D_s^+}$ floated. The signal yield remains blinded.

	Datasets			
	Run 2	2018	2017	2015–2016
$\sigma_{N_{sig}}/N_{sig}$	4.1%	6.1%	6.9%	7.8%
$\chi^2/374$	1.46	1.08	1.43	1.05
Integrated Luminosity (fb^{-1})	5.8	2.9	1.7	1.9

Table 7.6.: The relative statistical uncertainty of the signal yield, the χ^2 per degree of freedom, and the integrated luminosity for the Run 2, 2018, 2017, and 2015–2016 datasets. $f_{D^0}^{\nu_1-\nu_2}$ and $f_{D_s^+}$ are floated.

value generally falls below the *fit value*, with the exception of the 2015–2016 dataset where it exceeds it. This behavior warrants further investigation to elucidate these differences.
The unblinded signal fit to the inclusive MC samples is in progress to evaluate its reliability.

7.1.6. Qualitative Uncertainty Estimation

The statistical uncertainty of the signal yield is estimated with the D^0 and D_s^+ fractions fixed to their best-fit values (*cf.* Sec. 7.1.7). This approach is the same as the one used in the Run 1 analysis. Considering the entire Run 2 period, which roughly doubles the $b\bar{b}$ cross-section compared to Run 1, accounting for relative luminosities of Run 1 and Run 2,

$$\int \mathcal{L}(\text{Run 2}) \Big/ \int \mathcal{L}(\text{Run 1}) = 5.8\,\text{fb}^{-1}/3.2\,\text{fb}^{-1} \tag{7.14}$$

and an approximate 15% improvement in trigger efficiency, one would anticipate around $2 \times 1.81 \times 1.15 \approx 4.2$ more signal events with respect to the Run 1 dataset. Thus, the naive expected relative statistical uncertainty would be $6.64/\sqrt{4.2} \approx 3.2\%$.

7.1.7. Fixing D^0 and D_s^+ Fractions

The statistical uncertainty on the signal yield is estimated by fixing the $f_{D^0}^{\nu_1-\nu_2}$ and f_{D_s} fractions to their best-fit values, following the same approach as the Run 1 and 2015–2016 analyses [1–3], to facilitate direct comparison. The fit is then reiterated using these fixed fractions.
The fit results are shown in Tab. 7.7 .
The uncertainty on the signal yield is reduced to 3.5% when the D^0 and D_s^+ fractions are fixed. This is consistent with the expected relative statistical uncertainty of 3.2% (*cf.* Sec. 7.1.6).

Parameter	Value
Free Parameters	
N_{sig}	7909 ± 280
N_{D_s}	50446 ± 530
f_{D^+}	0.12 ± 0.01
Constrained Parameters	
$N_{B\to D^{*-}3\pi^{\pm}X}$	6778 ± 340
$f_{B_s\to D^* D_s X}$	0.07 ± 0.01
$f_{D^{**}D_s X}$	0.35 ± 0.02
$f_{D'^{+}_{s1}}$	0.44 ± 0.02
$f_{D^{*+}_{s0}}$	0.05 ± 0.02
Fixed Parameters	
$N_{B_1-B_2}$	178 ± 13
$N^{same}_{D^0}$	3233 ± 57
$N_{fake D^0}$	802 ± 25
$N_{fake D^*}$	1862 ± 49
$f_{D^{**}\tau\nu}$	0.024 ± 0.00
$f_{\tau^+\to 3\pi^{\pm}\overline{\nu}_\tau}$	0.768 ± 0.002
$f^{\nu_1-\nu_2}_{D^0}$	2.43 ± 0.20
f_{D_s}	0.55 ± 0.01

Table 7.7.: Values of the parameters obtained from/used for fits to the Run 2 collision data, with D^0 and D_s^+ fractions fixed. The signal yield remains blinded.

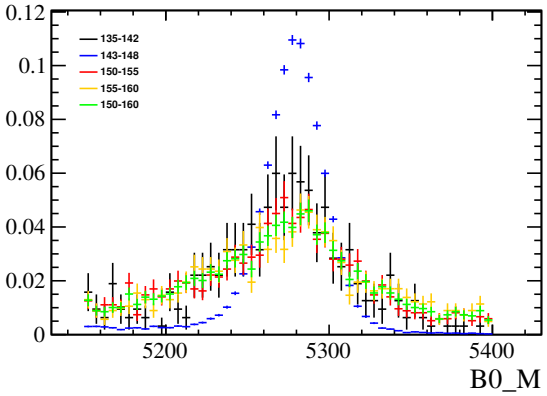

Figure 7.10.: The B^0 mass distributions in different Δm regions (specified in the legend).

7.2. Normalization Fit Results

In the previous publication [3], the normalization yield was determined using the sPlot method. This method is now discarded since narrow cuts on variables are used after applying sWeight. Instead, an extrapolation method is used to determine the normalization yield.
The normalization data sample is selected as described in Sec. 5.6.2. Its yield is obtained from an unbinned maximum likelihood fit to the mass of the $D^{*-}3\pi^{\pm}$ system. The signal shape is modeled on the $B^0 \to D^{*-}3\pi$ MC sample, consisting of a Crystal Ball and two Gaussian functions sharing a common mean. The $B^0 \to D^{*-}3\pi^{\pm}$ decays result in the B^0 peak in the reconstructed B^0 mass, as shown in Fig. 7.11.

Other sources, such as $B^+ \to \overline{D}^{*0/-}3\pi^{\pm}$ decays, with the π^0/π^- in the $\overline{D}^{*0/-}$ decay replaced by a slow charged pion, can also contribute to the B^0 peak, with a wider width compared to that from true $B^0 \to D^{*-}3\pi^{\pm}$ decays, as illustrated in Fig. 7.10. These contributions are denoted as the B^0 peak from the *fake* D^{*-} contribution hereafter, and the true $B^0 \to D^{*-}3\pi^{\pm}$ decay is denoted as the *true* D^{*-} contribution.
Performing a B^0 mass fit with only a peaking signal component and a combinatorial background component is insufficient to obtain the yield of the true $B^0 \to D^{*-}3\pi$ decays, because the peak includes contributions from both the true and fake D^{*-}. The fake D^{*-} contribution needs to be properly subtracted.
The following cuts on the D^0 mass and Δm variables are applied :

$$\begin{aligned} m(D^0) &\in [1840, 1890]\,\mathrm{MeV}/c^2, \\ \Delta m &\in [143, 148]\,\mathrm{MeV}/c^2. \end{aligned} \tag{7.15}$$

The normalization yield is determined using the extrapolation method, as follows:

(i) Perform a B^0 mass fit in the mass windows in Eq. (7.15) using a Crystal Ball function and two Gaussians for the signal, and an exponential function for the background. This provides the total B^0 yield N_{tot}. The fit result is shown in Fig. 7.11.

(ii) Perform a B^0 mass fit in several regions at the Δm sideband and obtain the B^0 yield in each region. The regions are in $2\,\mathrm{MeV}/c^2$ bin widths, from 138 to $160\,\mathrm{MeV}/c^2$. The yields are shown in Fig. 7.12.

(iii) Fit the B^0 yield as a function of Δm using a third-order polynomial function[4]. Integrating the fitted function in the Δm mass ranges provides the fake D^{*-} yield N_{fake}. The fit result is shown in Fig. 7.13.

(iv) Subtract the fake D^{*-} yield from the total B^0 yield to obtain the true B^0 yield N_B.

(v) Obtain the total D_s^+ yield from the fit to the $3\pi^\pm$ mass in the range of $[1900, 2050]\,\mathrm{MeV}/c^2$. The model uses a Crystal Ball function and two Gaussians for the signal, while the background is modeled using an exponential function. The fit result is shown in Fig. 7.14. Assuming the same fraction of the fake D^{*-} contribution in the total D_s^+ yield as in the total B^0 yield, the true D_s^+ yield, $N_{D_s^+}$ is obtained.

(vi) Subtract the true D_s^+ yield from the true B^0 yield to obtain the normalization yield N_{norm}.

7.2.1. Extrapolation Method in $m(D^0)$ and Δm Mass Windows

7.2.2. MC Constraints on the Resolution Parameters

In practice, some B^0 mass fits to the data in the Δm sideband give resolution parameters of several hundred MeV, which are unreasonable. Therefore, the MC sample is used to constrain the resolution parameters. The B^0 mass peak in the Δm sideband primarily arises from $B^+ \to D^0 3\pi^\pm$ decays, and $B^0 \to D^{*-} 3\pi^\pm$ decays, where the D^0 candidate is combined with a fake slow pion to form the D^{*-} candidate.

In principle, the B^0 mass peak in the data includes contributions from both B^+ and B^0 decays. Thus, the resolution parameters should be constrained using a combined B^+ and B^0 sample. However, aligning the numbers of MC events requires knowledge of the relative production rates of the two decays, necessitating additional work. For convenience, the resolution parameters are constrained according to those in B^0 MC for the default result, the B^+ MC used as an alternative to introduce a systematic uncertainty.

[4] A systematic uncertainty is introduced by using a second-order polynomial function for the fit.

Δm MeV/c^2	B^0 MC Constrain MeV/c^2
(138, 140)	24 ± 3
(140, 142)	27 ± 1
(150, 152)	34 ± 1
(152, 154)	40 ± 1
(154, 156)	42 ± 2
(156, 158)	47 ± 2
(158, 160)	47 ± 2

Table 7.8.: Resolution parameters from the B^0 mass fits in data. The parameter is obtained from constrained fit with the resolution parameter constrained according the B^0 MC.

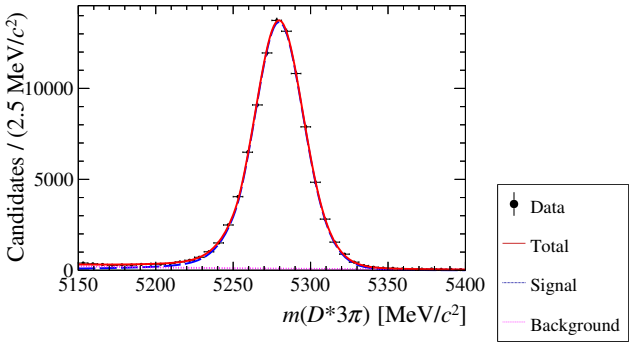

Figure 7.11.: Fit of the B^0 mass within the nominal $m(D^0)$ mass window and Δm regions, ranging from 143 to 148 MeV/c^2, applied to data. The corresponding fit models are superimposed.

The constraints obtained from the B^0 MC sample are summarized in Tab. 7.8.

7.2.3. Fit Results

The results from the extrapolation method in m_{D^0} and Δm mass windows are summarized in Tab. 7.9. The total B^0 yield is 103590 ± 353, with 9057 ± 315 fake D^{*-} decays. The true B^0 yield is 94533 ± 473. The total D_s^+ yield is 1490 ± 66, with 1360 ± 60 true D_s^+ decays. The normalization yield is 93173 ± 478.

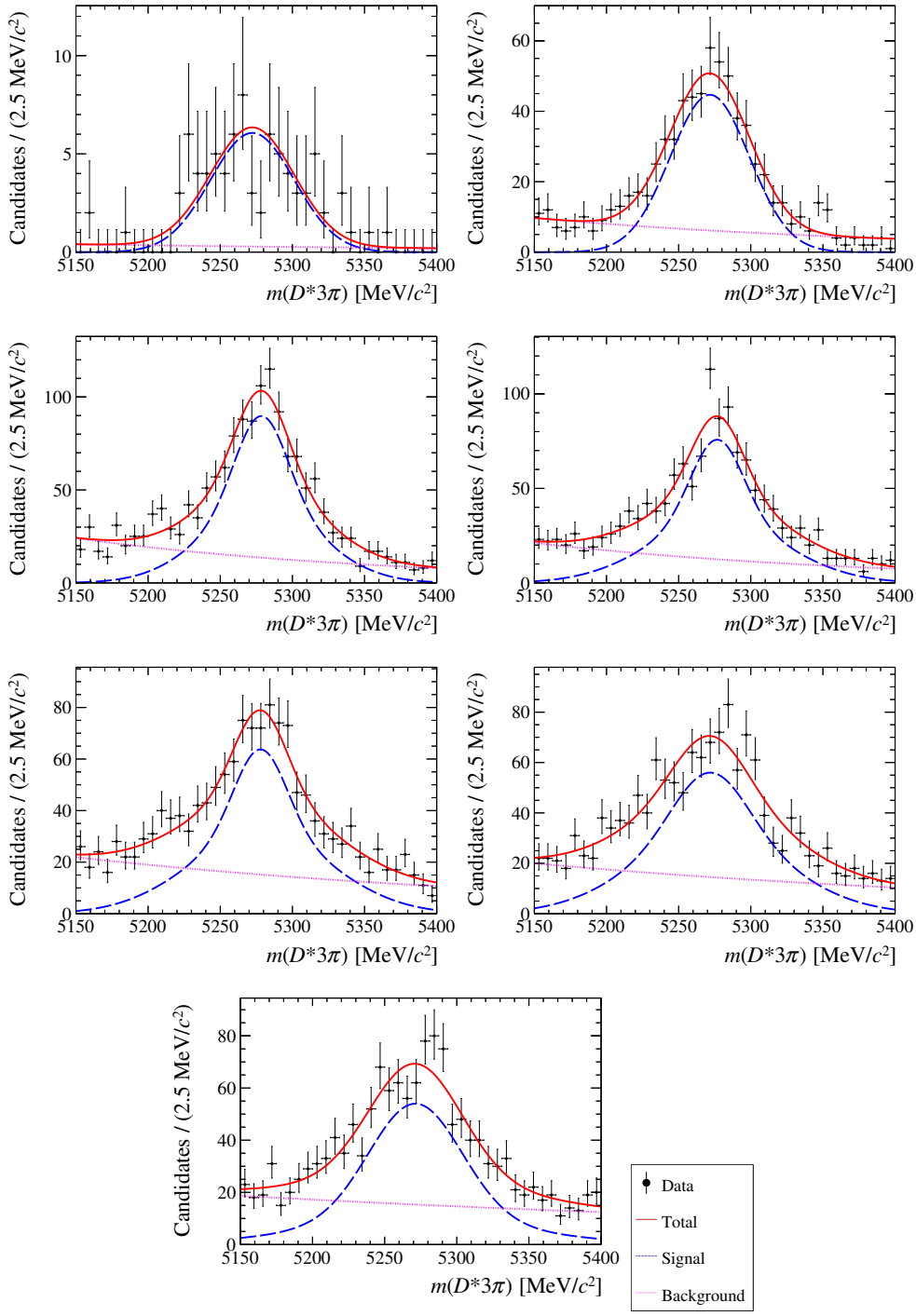

Figure 7.12.: B^0 mass fits in the the different Δm mass regions to the data in the $m(D^0)$ windows. The resolution parameters are constrained using the MC sample from B^0. From top left to bottom right, the Δm mass regions are: [138, 140], [140, 142], [150, 152], [152, 154], [154, 156], and [156, 158] $\mathrm{MeV/c^2}$.

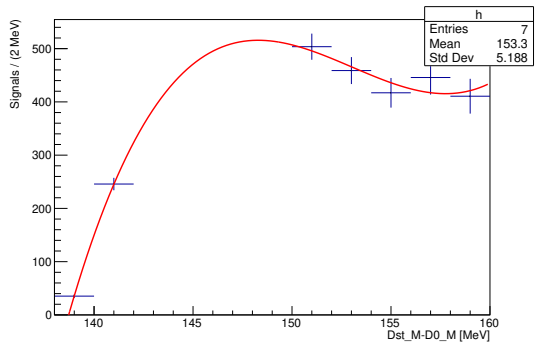

Figure 7.13.: Extrapolation of the B^0 yield in data, using a third-polynomial fitting function. The x axis represent the Δm and the y axis the B^0 yield.

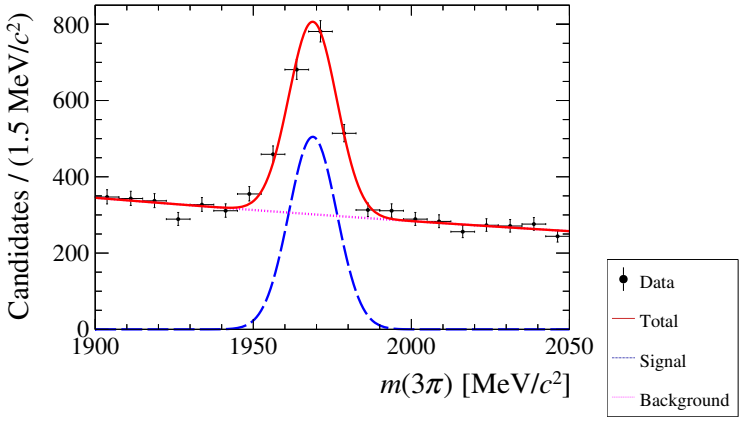

Figure 7.14.: D_s^+ mass fits to the data. The corresponding fit models are superposed and the signal respresent the $D_s^+ \to 3\pi^\pm$ decays.

Parameter	Value
N_{tot}	103590 ± 353
N_{fake}	9057 ± 315
N_B	94533 ± 473
$N_{D_s^+}$	1360 ± 60
N_{norm}	93173 ± 441

Table 7.9.: Normalization yield from the extrapolation method, errors are estimated using the bootstrapping method.

7.2.3.1. Uncertainty Propagation in Subtractions

In extrapolation methods, subtraction operations, such as subtracting the true D_s^+ yield from the true B^0 yield, involve correlated quantities. To account for this correlation and correct the naive error, the uncertainty propagation is handled using the bootstrapping method. Approximately 5000 toy samples are randomly generated with replacement from the original sample to determine the central values of the yields, as presented in Tab. 7.9. The number of entries in each toy sample fluctuates according to a Poisson distribution, with the mean equal to the number of entries in the original sample. For each toy sample, the yields are determined using the same extrapolation method. The standard deviation of a given quantity across these samples is taken as its statistical uncertainty, which is found to be ±441 events.

7.3. Preliminary Results

At this stage, all the necessary components are in place to measure $\mathbf{R}(D^*)$. The external branching fractions used for $\mathcal{K}(D^{*-})$ and $\mathbf{R}(D^*)$ are reported in Tab. 7.10. They depend on the $\mathbf{R}(D^*)$ central value and introduce 0.10 absolute uncertainty to it.

Using the obtained signal and normalization yields, the $\mathcal{K}(D^{*-})$ (*cf.* Eq. (4.6)) is:

$$\mathcal{K}(D^{*-}) = 1.829 \pm 0.067 \ . \tag{7.16}$$

The uncertainty includes that from the yields, efficiencies and branching fractions involved.Finally, $\mathbf{R}(D^*)$ is obtained as:

$$\mathbf{R}(D^*)|_{\texttt{Run 2}} = 0.265 \pm 0.010\,(\texttt{stat.}) \pm X\,(\texttt{syst.}) \pm 0.012\,(\texttt{ext.}) \ . \tag{7.17}$$

where the central value is blinded. The first uncertainty is statistical, the second is systematic[5] and the third one is the uncertainty from the external branching fractions. The relative statistical uncertainty on $\mathbf{R}(D^*)$ is 3.8%. A sketch of systematic uncertainty estimation is given in Chap. 8.

The partial Run 2 result using data collected during 2015–2016, as published in Ref. [3] is:

$$\mathbf{R}(D^*)|_{2015\text{–}2016} = 0.260 \pm 0.015\,(\texttt{stat.}) \pm 0.016\,(\texttt{syst.}) \pm 0.012\,(\texttt{ext.}) \ . \tag{7.18}$$

The relative statistical uncertainty on The $\mathbf{R}(D^*)$ ratio was measure with a relative statistical uncertainty of 6.7% in Run 1 and 5.8% using the 2015–2016 data sample only. With the Run 2

[5] To be estimated.

Decay	**Branching Ratio**	**Refs.**
$\tau^+ \to 3\pi^\pm\nu_\tau$ (excluding $K^0_S \to \pi^+\pi^-$)	$(9.02 \pm 0.05)\%$	PDG[38]
$\tau^+ \to 3\pi^+\pi^0\nu_\tau$ (excluding $K^0_S \to \pi^+\pi^-$)	$(4.49 \pm 0.05)\%$	PDG [38]
$B^0 \to D^{*-}\ell\nu_\tau$ (where $\ell = e, \mu$)	$(4.97 \pm 0.01\,(\texttt{stat.}) \pm 0.12)\,(\texttt{syst.})\%$	HFLAV [8]
$B^0 \to D^{*-}3\pi^\pm$	$(7.21 \pm 0.29) \times 10^{-3}$	PDG [38]

Table 7.10.: The external branching fractions used for the $\mathcal{K}(D^{*-})$ and $\mathbf{R}(D^*)$ computation.

dataset, this uncertainty decreased to 3.8%. Further improvements on the control and the signal fits are expected to improve the precision of the measurement.
In addition, the statistical uncertainty is expected to decrease to the 2.9% level when combining the results from the Run 1 and Run 2 datasets.

Chapter 8

Systematic Uncertainties

The systematic uncertainties affecting the $\mathbf{R}(D^*)$ measurement are discussed in this chapter. The evaluation of these uncertainties for the full Run 2 analysis is still in the early stages. Currently, only the systematic uncertainties from the 2015–2016 dataset have been assessed. A plan for evaluating the remaining uncertainties is outlined. Some individual systematic uncertainties may differ from those in previous analyses due to refinements in the selection and fitting procedures. However, most methods will remain applicable.

8.1. Signal Model Uncertainties

The fraction of tau decays to three pions, $f_{\tau\to 3\pi}$, is derived in Sec. 7.1.1.2, Eq. (5.16). In the signal fitting procedure, this parameter is fixed at the central value. An alternative fit tests the parameter set to the central value ±1 standard deviation.

Uncertainties also arise from the understanding of the FFs in $B^0 \to D^{*-}\tau^+\nu_\tau$. The BGL parametrization for the FFs is used in the nominal analysis, as detailed in Sec. 4.4.3.1. Systematic variations are assessed by implementing the CLN parametrization on the MC samples. The relative difference in the signal yield is taken as the systematic uncertainty.

Contributions to the signal from other τ^+ decays, such as those resulting in three or five charged tracks (*e.g.*, $K^+\pi^-\pi^+$, $K^+K^-\pi^+$, $\pi^+\pi^-\pi^+\pi^0\pi^0$), are possible. These decays have much lower branching fractions compared to the signal modes. The systematic uncertainty from these decays, $\sigma_{\text{other }\tau\text{ dec.}} = 1\%$, established in the Run 1 analysis, is applicable to the Run 2

analysis as well.

The feed-down from $B \to D^{**}\tau\nu_\tau$ is estimated using MC contributions and theoretical assumptions [166]. The feed-down fraction $f_{D^{**}\tau\nu}$ is adjusted by ±50% to assess the systematic uncertainty.

8.2. Uncertainties in Selection Processes

The PID variables ProbNN_π and ProbNN_K are utilized to differentiate pions from D^* and τ^+ and to exclude K^- misidentified as π^- in the $\tau^+ \to 3\pi^\pm$ system. The efficiencies of these variables at specified cut values influence both signal and normalization efficiencies. Ultimately, their ratio affects the $\mathcal{K}(D^{*-})$ outcome.

The PID efficiencies are derived using the data-driven `PIDCalib` package [148]. This method involves using a calibration sample of pions to measure their PID efficiencies at specified cut values, with efficiency parameterized by the phase-space region of each pion track. Calibration histograms for efficiency are thus generated. Subsequently, MC samples for signal or normalization are processed, with all selections applied except for the PID criterion. Each simulated pion's efficiency is then determined based on the phase-space bin it occupies, to the corresponding calibration histogram value.
The total efficiency for an event is determined by multiplying the efficiencies of the considered tracks. This method's systematic impact was examined in the Run 1 analysis [1, 2]; the impact of the finite size of the calibration samples was found negligible. However, a systematic uncertainty arises from the binning scheme used in the efficiency calibration histograms. The default binning scheme is:

- 7 bins between 1.5 and 5 in η,
- 3 bins between 0 and 600 in nSPDHits,
- 3 bins between 1 000 and 5 150, 5 150 and 9 300, and 9 300 and 15 600 $\mathrm{MeV/c}$,
- 30 bins between 19 000 and 1 000 000 $\mathrm{MeV/c}$ in track momentum.

This scheme is identical with that used in the Run 1 analysis. To assess the effect of the binning scheme on track momentum, two alternative schemes are used:

- Coarse scheme: 15 bins between 1 900 and 100 000 $\mathrm{MeV/c}$;
- Fine scheme: 30 bins between 1 900 and 100 000 $\mathrm{MeV/c}$.

PID efficiencies are recalculated using the new efficiency calibration histograms. The $\mathcal{K}(D^{*-})$ result's deviation from the default value under each new scheme is measured. The larger of the two deviations is considered as the systematic uncertainty.
The impact of MC reweighting in the nominal case was examined by evaluating changes in the efficiency ratio of the signal and normalization modes when reweighting is removed. Additionally, a $3\pi^{\pm}$ correction is applied to the normalization mode. The limited size of the simulation samples used to estimate efficiencies in $B^0 \to D^{*-}\tau^+\nu_\tau$ and $B^0 \to D^{*-}3\pi$ decays leads to systematic uncertainties as well.

The main difference in selection between the signal and normalization modes is the anti-D_s^+ BDT cut. The signal sample is selected with anti-D_s^+ BDT output > -0.2. This is varied to see the resultant variation on the signal yield and efficiency. The chosen alternate point is -0.18 which corresponds to a 5% reduction in the D_s^+ background yield. At this alternate point of selection, the resultant change on $\mathcal{K}(D^{*-})$ is less than 0.1% in 2015–2016 analysis.

The primary distinction in selection criteria between the signal and normalization modes is the anti-D_s^+ BDT cut. For the signal, the anti-D_s^+ BDT output threshold is set above -0.2. This threshold is adjusted to -0.18 to evaluate the impact on signal yield and efficiency.

Systematic uncertainties in the stripping (online) selection efficiency estimations may arise from discrepancies between data and simulation, particularly concerning the $3\pi^{\pm}$ vertex and its associated error. A 2% uncertainty is attributed to this source in the Run 1 analysis, and the same value is adopted here.

8.3. Template Samples Size

In the Run 1 analysis, the dominant systematic uncertainty originates from the limited size of the templates used in the signal fit. As discussed in Sec. 7.1.1, these templates are primarily constructed from MC samples. The size of these templates, after applying the complete selection criteria, affects the signal yield, $N_{\mathtt{sig}}$, in the final fit. Therefore, the relative uncertainty in N_{sig} directly influences the uncertainty in $\mathbf{R}(D^*)$.

A common method to estimate this uncertainty involves *bootstrapping* the templates and then perform the signal fit for each resulting set of templates. Typically, bootstrapping in many analyses involves resampling with replacement at the individual event level. However, for this project, as discussed in App. A.2, it would be ideal to resample entire ReDecay blocks. Despite this, due to the negligible bin-to-bin correlations in ReDecay, event-based bootstrapping is considered an effective approximation for estimating the systematic uncertainty related to template size and is adopted in subsequent analyses.

The bootstrapping procedure for generating templates can be outlined as follows:

1. Construct nominal templates from Monte Carlo simulations (MC) or from data for combinatorial backgrounds.
2. Resample the templates by replacing events, resulting in new templates of size Poisson(n), where n denotes the size of the original template. Utilize block bootstrapping for MC and event bootstrapping for data.
3. Estimate the signal yield, denoted by N_{sig}.
4. Repeat steps 2 and 3 for N iterations to compute the mean signal yield $\overline{N_{sig}}$ and the standard deviation $\sigma_{bootstrap}$.
5. Calculate the relative uncertainty due to template size as $\sigma_{\text{templ. stat.}} = \frac{\sigma_{bootstrap}}{\overline{N_{sig}}}$.

The multiplicative blinding scheme ensures that both the signal yield N_{sig} and its statistical uncertainty σ are scaled by the same factor. This scaling cancels out in the ratio of relative uncertainty σ/N_{sig}.

8.4. Empty Bins in Templates

The three-dimensional templates used in the fit contain *empty bins*. The systematic deviation associated with these empty bins is estimated by constructing a three-dimensional density function using Kernel Density Estimations (KDEs). These functions are developed for each component and subsequently transformed into histogram templates. The fit is then executed using these new templates.

8.5. Uncertainties in Background Models

Uncertainties in the background model arise from the modeling of the D_s^+ decay, double-charm backgrounds, and combinatorial backgrounds.

8.5.1. Impact of D_s^+ Decay Correction Weights

The uncertainties associated with the D_s^+ decay model are estimated by adjusting the weights of the D_s^+ contributions based on a Gaussian distribution that reflects their uncertainties. Initially, only the central values are employed in the template weights prior to the signal fit.

8.5.2. $B \to D^{*-}(D^0, D_s^+)X$ Background Model

The statistical uncertainty on the $B^0 \to D^{*-}\tau^+\nu_\tau$ yield is determined with the D^0 and D_s^+ background fractions fixed at their optimal fit values. The systematic contribution from this procedure is quantified by the quadratic difference between the uncertainties on $\mathcal{K}(D^{*-})$ before and after these parameters are fixed.

8.5.3. $B \to D^{*-}(D^+, D^0, D_s^+)X$ Background Template Shapes

The fit variables in the signal fit, q^2, t_τ, and BDT, exhibit non-negligible correlations with certain kinematic variables, potentially affecting template shapes and fit outcomes. The primary variables likely to impact results are $m(D^*3\pi)$, $m(3\pi\pm)$, $\min[m(\pi^+\pi^-)]$, and $\max[m(\pi^+\pi^-)]$, all of which were also analyzed in the Run 1 analysis. The influence of these four variables on the shapes of D^+ and D^0 background templates is investigated. For D_s^+ background templates, only the effect of $m(D^*3\pi)$ is examined, as the impacts of the other three variables are accounted for in the D_s^+ weight variations described previously.

The alteration in template shapes is examined by creating alternative templates through the application of linear weights, which are functions of the four specified kinematic variables:

$$\omega_{m(D^*3\pi)} = 1 + 2\alpha_{m(D^*3\pi)}\left(\frac{m(D^*3\pi) - 2700}{5100 - 2700} - \frac{1}{2}\right), \tag{8.1a}$$

$$\omega_{m(3\pi)} = 1 + 2\alpha_{m(3\pi)}\left(\frac{m(3\pi) - 3m_\pi}{1600 - 3m_\pi} - \frac{1}{2}\right), \tag{8.1b}$$

$$\omega_{\min[m(\pi^+\pi^-)]} = 1 + 2\alpha_{\min[m(\pi^+\pi^-)]}\left(\frac{\min[m(\pi^+\pi^-)] - 2m_\pi}{880 - 2m_\pi} - \frac{1}{2}\right), \tag{8.1c}$$

$$\omega_{\max[m(\pi^+\pi^-)]} = 1 + 2\alpha_{\max[m(\pi^+\pi^-)]}\left(\frac{\max[m(\pi^+\pi^-)] - 2m_\pi}{1440 - 2m_\pi} - \frac{1}{2}\right). \tag{8.1d}$$

where m_π denotes the pion mass. Two extreme templates are constructed using α values set at $+1$ ($\mathrm{temp_{pos}}$) and -1 ($\mathrm{temp_{neg}}$). A set of intermediate templates is then generated through linear interpolation between these extremes, using various weights defined by the range of α values:

$$1 + a_i\left(\frac{\mathrm{temp_{pos}} - \mathrm{temp_{nom}}}{\mathrm{temp_{nom}}}\right) \quad \text{when} \quad a_i \geqslant 0, \tag{8.2a}$$

$$1 + a_i\left(\frac{\mathrm{temp_{nom}} - \mathrm{temp_{neg}}}{\mathrm{temp_{nom}}}\right) \quad \text{when} \quad a_i < 0. \tag{8.2b}$$

Here $a_i = a_1, a_2, a_3$ and a_4 stands for $m(D^*3\pi)$, $m(3\pi\pm)$, $\min[m(\pi^+\pi^-)]$ and $\max[m(\pi^+\pi^-)]$, respectively.

8.5.4. $B \to D^{*-}3\pi^{\pm}X$ Background Template Shapes

The $B \to D^{*-}3\pi^{\pm}X$ background templates are varied with weights to the four kinematic variables, as mentioned in the previous section.

8.5.5. Combinatorial Templates

The combinatorial templates for B_1B_2 and fake D^*, D^0 events are derived from data. The systematic uncertainty associated with fixing their normalization in the nominal signal fit is estimated by adjusting them to $\pm1\sigma$ of their nominal values.

8.5.6. $m(3\pi)$ Variation

Significant discrepancies are observed between the data and the total PDF for the $m(3\pi)$ variable projection in the data fit, across various bins of the fit variables. This discrepancy is primarily attributed to contributions from D_s^+ backgrounds. Accordingly, the D_s^+ templates are adjusted using weights derived from the $m(3\pi)$ distributions, following the approach described in previous sections. The deviations in the total PDF are then superimposed on the nominal projection to verify that these discrepancies are effectively addressed.

8.6. Normalization Model Uncertainties

During the estimation of normalization yield, the signal shape parameters: Crystal Ball shape parameters, σ of the wider Gaussian and fraction between the two Gaussians are fixed to the values obtained from simulation. These fixed values are varied by $\pm1\sigma$ and the resultant deviation on N_{norm} is taken as a systematic uncertainty from this source.

8.7. Summary

A summary of the systematic uncertainties for the 2015–2016 dataset is provided in App. D. The total systematic uncertainty is evaluated to be $+6.2\%$ and -5.9%. Most of the systematic uncertainties are expected to reduce with the larger dataset, when including the 2017–2018 data.

Conclusions & Prospects

This work presents the measurement of the $\mathbf{R}(D^*)$ ratio using proton-proton collision data collected by the LHCb detector from 2015 to 2018, corresponding to an integrated luminosity of 5.8 fb^{-1}. The τ^+ lepton is reconstructed through its hadronic decay modes $\tau^+ \longrightarrow 3\pi^\pm(\pi^0)\nu_\tau$. The partial Run 2 analysis, using 2015–2016 datasets, has been published [3], the result reads:

$$\mathbf{R}(D^*)|_{2015\text{–}2016} = 0.260 \pm 0.015\,(\texttt{stat.}) \pm 0.016\,(\texttt{syst.}) \pm 0.012\,(\texttt{ext.})\,,$$

Significant enhancements have been made to this published analysis. Key aspects addressed can be summarized as follows: changes in online selection and trigger configurations have been explored, and a vertex correction scheme has been developed to reconcile differences between new data algorithms and existing MC simulations. Efficiency calculations have been refined by treating multiple event candidates and aligning data with MC through additional corrections. A new method for calculating the normalization fit has been introduced. Analysis code enhancements have facilitated the generation of separate results per dataset for cross-checks, providing greater flexibility. New D_s^+ MC samples have been incorporated into the training of BDTs, as well as in the D_s^+ decay control mode and signal fits.

A preliminary signal fit has been implemented, and the $\mathbf{R}(D^*)$ ratio has been measured. The final result, however, remains blinded by a multiplicative factor pending further improvements in the signal fit and estimation of systematic uncertainties:

$$\mathbf{R}(D^*)|_{\text{Run 2}} = 0.265 \pm 0.010\,(\texttt{stat.}) \pm X\,(\texttt{syst.}) \pm 0.012\,(\texttt{ext.})\,,$$

The statistical uncertainty on $\mathbf{R}(D^*)$ is measured to be 3.8%. In addition, when combining the results from the Run 1 and Run 2 datasets, the statistical uncertainty is expected to decrease further, to be at 2.9% level.
A significant portion of the systematic uncertainty is statistical in nature; therefore, increasing the sample size is expected to reduce this uncertainty as well.
Once fully validated and published, the results shown in this analysis will update the current

world average for $\mathbf{R}(D^*)$ and contribute to the ongoing efforts to understand potential NP phenomena related to LFU in semileptonic $b \to c\ell^-\bar{\nu}_\ell$ decays.

In the near future, the number of free parameters in the signal fit will be reduced from *four* to *two*. This reduction will be achieved by incorporating new decay modes measured by BESIII [9, 10], which will add constraints to the D_s^+ yield and D^+ fraction.

This document has presented a nearly complete documentation of the analysis. Current efforts are directed towards the signal fit refinements and systematic uncertainty estimation. Moreover, a reanalysis of Run 1 data is in progress to improve the precision of the combined results.

Future investigations will test LFU in semileptonic decays within a broader context such as: a variety of decay channels, accessibily to new observables, and larger collision data. Notably, Upcoming measurements will involve ratios of other mesons, including $\mathbf{R}(D^{**})$, $\mathbf{R}(D^{0(*)})$, $\mathbf{R}(D^+)$, $\mathbf{R}(D_s^{+(*)})$, and $\mathbf{R}(J/\Psi)$. Additionally, baryon measurements like $\mathbf{R}(\Lambda_c^*)$ will also be considered. Other observables, where different leptons are present in the final states, will be explored, such as $\mathbf{R}(D^{(*)})^{\tau/e}$ and $\mathbf{R}(D^{(*)})^{\mu/e}$.

Moreover, the q^2 distribution, angular observables, τ^+ and D^* polarizations will not only refine our understanding of the SM picture but will also provide insight into the spin structures of potential NP models. The upcoming data collection phases will enhance the precision of LFU observables, particularly in $b \to c\ell^-\bar{\nu}_\ell$ and $b \to u\ell^-\bar{\nu}_\ell$ transitions. By the end of Run 3, LHCb aims to improve the precision of these measurements by a factor of three to four. Post-2030, following the Phase-II Upgrade, further precision gains are anticipated with the addition of $300\,\text{fb}^{-1}$ collected data, which will significantly reduce systematic uncertainties.

Bibliography

[1] LHCb collaboration et al. "Measurement of the ratio of branching fractions $\mathcal{B}(\overline{B}^0 \to D^{*+}\tau^-\overline{\nu}_\tau)/\mathcal{B}(\overline{B}^0 \to D^{*+}\mu^-\overline{\nu}_\mu)$". In: *Physical Review Letters* 115.11 (Sept. 9, 2015), p. 111803. ISSN: 0031-9007, 1079-7114. DOI: 10.1103/PhysRevLett.115.111803. arXiv: 1506.08614 [hep-ex]. URL: http://arxiv.org/abs/1506.08614.

[2] LHCb Collaboration et al. "Measurement of the Ratio of the $B^0 \to D^{*-}\tau^+\nu_\tau$ and $B^0 \to D^{*-}\mu^+\nu_\mu$ Branching Fractions Using Three-Prong τ-Lepton Decays". In: *Physical Review Letters* 120.17 (Apr. 25, 2018), p. 171802. DOI: 10.1103/PhysRevLett.120.171802. URL: https://link.aps.org/doi/10.1103/PhysRevLett.120.171802.

[3] LHCb Collaboration et al. "Test of lepton flavour universality using $B^0 \to D^{*-}\tau^+\nu_\tau$ decays with hadronic τ channels". In: *Physical Review D* 109.11 (June 12, 2024), p. 119902. DOI: 10.1103/PhysRevD.109.119902. URL: https://link.aps.org/doi/10.1103/PhysRevD.109.119902.

[4] LHCb Collaboration et al. "Study of $B^0 \to D^{*-}\pi^+\pi^-\pi^+$ and $B^0 \to D^{*-}K^+\pi^-\pi^+$ decays". In: *Physical Review D* 87.9 (May 3, 2013), p. 092001. DOI: 10.1103/PhysRevD.87.092001. URL: https://link.aps.org/doi/10.1103/PhysRevD.87.092001.

[5] BABAR Collaboration et al. "Measurement of the $B^0 \to D^{*-}\pi^+\pi^-\pi^+$ branching fraction". In: *Physical Review D* 94.9 (Nov. 15, 2016), p. 091101. DOI: 10.1103/PhysRevD.94.091101. URL: https://link.aps.org/doi/10.1103/PhysRevD.94.091101.

[6] Belle Collaboration et al. "Observation of $B^0 \to D^{*-}(5\pi)^+$, $B^+ \to D^{*-}(4\pi)^{++}$ and $B^+ \to \overline{D}^{*0}(5\pi)^+$". In: *Physical Review D* 70.11 (Dec. 22, 2004), p. 111103. DOI: 10.1103/PhysRevD.70.111103. URL: https://link.aps.org/doi/10.1103/PhysRevD.70.111103.

[7] S. Navas et al. "Particle Data Group, to be published in 2024". In: *PRD* (2024). DOI: 110, 03000.

[8] Y. Amhis et al. "Averages of b -hadron, c -hadron, and τ -lepton properties as of 2021". In: *Physical Review D* 107.5 (Mar. 23, 2023), p. 052008. ISSN: 2470-0010, 2470-0029. DOI: 10.1103/PhysRevD.107.052008. URL: https://link.aps.org/doi/10.1103/PhysRevD.107.052008.

[9] BESIII Collaboration et al. "Measurement of the absolute branching fraction of the inclusive decay $D_s^+ \to \pi^+\pi^+\pi^-X$". In: *Physical Review D* 108.3 (Aug. 1, 2023), p. 032001. ISSN: 2470-0010, 2470-0029. DOI: 10.1103/PhysRevD.108.032001. arXiv: 2212.13072 [hep-ex]. URL: http://arxiv.org/abs/2212.13072.

[10] BESIII Collaboration et al. "Measurements of the branching fractions of the inclusive decays $D^0(D^+) \to \pi^+\pi^+\pi^-X$". In: *Physical Review D* 107.3 (Feb. 13, 2023), p. 032002. DOI: 10.1103/PhysRevD.107.032002. URL: https://link.aps.org/doi/10.1103/PhysRevD.107.032002.

[11] BABAR Collaboration et al. "Evidence for an Excess of $\overline{B} \to D^{(*)}\tau^-\overline{\nu}_\tau$ Decays". In: *Physical Review Letters* 109.10 (Sept. 6, 2012), p. 101802. DOI: 10.1103/PhysRevLett.109.101802. URL: https://link.aps.org/doi/10.1103/PhysRevLett.109.101802.

[12] The BABAR Collaboration et al. "Measurement of an excess of $\overline{B} \to D^{(*)}\tau^-\overline{\nu}_\tau$ decays and implications for charged Higgs bosons". In: *Physical Review D* 88.7 (Oct. 31, 2013), p. 072012. DOI: 10.1103/PhysRevD.88.072012. URL: https://link.aps.org/doi/10.1103/PhysRevD.88.072012.

[13] Belle Collaboration et al. "Measurement of the branching ratio of $\overline{B} \to D^{(*)}\tau^-\overline{\nu}_\tau$ relative to $\overline{B} \to D^{(*)}\ell^-\overline{\nu}_\ell$ decays with hadronic tagging at Belle". In: *Physical Review D* 92.7 (Oct. 26, 2015), p. 072014. DOI: 10.1103/PhysRevD.92.072014. URL: https://link.aps.org/doi/10.1103/PhysRevD.92.072014.

[14] Belle Collaboration et al. "Measurement of the branching ratio of $\overline{B}^0 \to D^{*+}\tau^-\overline{\nu}_\tau$ relative to $\overline{B}^0 \to D^{*+}\ell^-\overline{\nu}_\ell$ decays with a semileptonic tagging method". In: *Physical Review D* 94.7 (Oct. 27, 2016), p. 072007. DOI: 10.1103/PhysRevD.94.072007. URL: https://link.aps.org/doi/10.1103/PhysRevD.94.072007.

[15] S. Hirose et al. *Measurement of the τ lepton polarization and* $R(D^*)$ *in the decay* $\bar{B} \to D^*\tau^-\bar{\nu}_\tau$. arXiv.org. Dec. 2, 2016. DOI: 10.1103/PhysRevLett.118.211801. URL: https://arxiv.org/abs/1612.00529v2.

[16] S. Hirose et al. "Measurement of the τ lepton polarization and $R(D^*)$ in the decay $\bar{B} \to D^*\tau^-\bar{\nu}_\tau$". In: *Physical Review Letters* 118.21 (May 26, 2017), p. 211801. ISSN: 0031-9007, 1079-7114. DOI: 10.1103/PhysRevLett.118.211801. arXiv: 1612.00529 [hep-ex]. URL: http://arxiv.org/abs/1612.00529.

[17] The Belle Collaboration et al. "Measurement of $\mathcal{R}(D)$ and $\mathcal{R}(D^*)$ with a semileptonic tagging method". In: *Physical Review Letters* 124.16 (Apr. 24, 2020), p. 161803. ISSN: 0031-9007, 1079-7114. DOI: 10.1103/PhysRevLett.124.161803. arXiv: 1910.05864 [hep-ex]. URL: http://arxiv.org/abs/1910.05864.

[18] Belle II Collaboration et al. *A test of lepton flavor universality with a measurement of* $R(D^*)$ *using hadronic* B *tagging at the Belle II experiment*. Jan. 5, 2024. DOI: 10.48550/arXiv.2401.02840. arXiv: 2401.02840 [hep-ex]. URL: http://arxiv.org/abs/2401.02840. Pre-published.

[19] LHCb Collaboration et al. "Measurement of the Ratio of Branching Fractions $\mathcal{B}(\overline{B}^0 \to D^{*+}\tau^-\overline{\nu}_\tau)/\mathcal{B}(\overline{B}^0 \to D^{*+}\mu^-\overline{\nu}_\mu)$". In: *Physical Review Letters* 115.11 (Sept. 9, 2015), p. 111803. DOI: 10.1103/PhysRevLett.115.111803. URL: https://link.aps.org/doi/10.1103/PhysRevLett.115.111803.

[20] The Belle Collaboration et al. "Measurement of the τ lepton polarization and $R(D^*)$ in the decay $\overline{B} \to D^*\tau^-\overline{\nu}_\tau$ with one-prong hadronic τ decays at Belle". In: *Physical Review D* 97.1 (Jan. 10, 2018), p. 012004. DOI: 10.1103/PhysRevD.97.012004. URL: https://link.aps.org/doi/10.1103/PhysRevD.97.012004.

[21] LHCb collaboration et al. *Measurement of lepton universality parameters in* $B^+ \to K^+\ell^+\ell^-$ *and* $B^0 \to K^{*0}\ell^+\ell^-$ *decays*. Nov. 7, 2023. DOI: 10.1103/PhysRevD.108.032002. arXiv: 2212.09153 [hep-ex]. URL: http://arxiv.org/abs/2212.09153. Pre-published.

[22] W. N. Cottingham and D. A. Greenwood. *An introduction to the standard model of particle physics*. [Reprinted ed.] Beijing, 2010. ISBN: 978-7-5100-0554-1.

[23] Christopher G. Tully. *Elementary particle physics in a nutshell / monograph*. Beijing: World Publishing Corporation, 2013. ISBN: 978-7-5100-5823-3.

[24] André. Rougé. *Introduction à la physique subatomique*. Palaiseau (Essone): Éditions de l'École polytechnique, 2005. ISBN: 978-2-7302-1231-1.

[25] Christoph Kopper. *Champs relativistes et leur quantifications*. 2018-2019. École Polytechnique.

[26] Pascal Paganini. *An introduction to the Standard Model of Particle Physics*. 2019th ed. École Polytechnique.

[27] François Gelis. *Quantum field theory: from basics to modern topics*. Cambridge, United Kingdom ; New York, NY: Cambridge University Press, 2019. ISBN: 978-1-108-48090-1.

[28] W Pauli. "Exclusion Principle, Lorentz Group and Reflection of Space-Time and Charge". In: *W. Pauli, L. Rosenfeld and V. Weisskopf, Eds., Niels Bohr and the Development of Physics, McGraw-Hill* (1955), pp. 30–51.

[29] Gerhart Lüders. "Proof of the TCP theorem". In: *Annals of Physics* 2.1 (July 1, 1957), pp. 1–15. ISSN: 0003-4916. DOI: 10.1016/0003-4916(57)90032-5. URL: https://www.sciencedirect.com/science/article/pii/0003491657900325.

[30] Sheldon L. Glashow. "Partial-symmetries of weak interactions". In: *Nuclear Physics* 22.4 (Feb. 1, 1961), pp. 579–588. ISSN: 0029-5582. DOI: 10.1016/0029-5582(61)90469-2. URL: https://www.sciencedirect.com/science/article/pii/0029558261904692.

[31] Steven Weinberg. "A Model of Leptons". In: *Physical Review Letters* 19.21 (Nov. 20, 1967), pp. 1264–1266. DOI: 10.1103/PhysRevLett.19.1264. URL: https://link.aps.org/doi/10.1103/PhysRevLett.19.1264.

[32] Abdus Salam. "Weak and electromagnetic interactions". In: *Selected Papers of Abdus Salam*. Vol. Volume 5. World Scientific Series in 20th Century Physics Volume 5. WORLD SCIENTIFIC, May 1994, pp. 244–254. ISBN: 978-981-02-1662-7. DOI: 10.1142/9789812795915_0034. URL: https://www.worldscientific.com/doi/abs/10.1142/9789812795915_0034.

[33] Stephen L. Adler. "Axial-Vector Vertex in Spinor Electrodynamics". In: *Physical Review* 177.5 (Jan. 25, 1969), pp. 2426–2438. DOI: 10.1103/PhysRev.177.2426. URL: https://link.aps.org/doi/10.1103/PhysRev.177.2426.

[34] J. S. Bell and R. Jackiw. "A PCAC puzzle: $\pi^0 \to \gamma\gamma$ in the σ-model". In: *Il Nuovo Cimento A (1965-1970)* 60.1 (Mar. 1, 1969), pp. 47–61. ISSN: 1826-9869. DOI: 10.1007/BF02823296. URL: https://doi.org/10.1007/BF02823296.

[35] G. D'Ambrosio et al. "Minimal Flavour Violation: an effective field theory approach". In: *Nuclear Physics B* 645.1-2 (Nov. 2002), pp. 155–187. ISSN: 05503213. DOI: 10.1016/S0550-3213(02)00836-2. arXiv: hep-ph/0207036. URL: http://arxiv.org/abs/hep-ph/0207036.

[36] Lincoln Wolfenstein. "Parametrization of the Kobayashi-Maskawa Matrix". In: *Physical Review Letters* 51.21 (Nov. 21, 1983), pp. 1945–1947. DOI: 10.1103/PhysRevLett.51.1945. URL: https://link.aps.org/doi/10.1103/PhysRevLett.51.1945.

[37] M. Gell-Mann. "A schematic model of baryons and mesons". In: *Physics Letters* 8.3 (Feb. 1, 1964), pp. 214–215. ISSN: 0031-9163. DOI: 10.1016/S0031-9163(64)92001-3. URL: https://www.sciencedirect.com/science/article/pii/S0031916364920013.

[38] Particle Data Group et al. "Review of Particle Physics". In: *Progress of Theoretical and Experimental Physics* 2022.8 (Aug. 8, 2022), p. 083C01. ISSN: 2050-3911. DOI: 10.1093/ptep/ptac097. URL: https://doi.org/10.1093/ptep/ptac097.

[39] Hua-Xing Chen et al. "The hidden-charm pentaquark and tetraquark states". In: *Physics Reports*. The hidden-charm pentaquark and tetraquark states 639 (June 10, 2016), pp. 1–121. ISSN: 0370-1573. DOI: 10.1016/j.physrep.2016.05.004. URL: https://www.sciencedirect.com/science/article/pii/S037015731630103X.

[40] Daniel Johnson et al. *Exotic Hadrons at LHCb*. Mar. 6, 2024. DOI: 10.1146/annurev-nucl-102422-040628. arXiv: 2403.04051 [hep-ex, physics:hep-ph]. URL: http://arxiv.org/abs/2403.04051. Pre-published.

[41] Nora Brambilla et al. "The XYZ states: Experimental and theoretical status and perspectives". In: *Physics Reports*. The XYZ states: experimental and theoretical status and perspectives 873 (Aug. 20, 2020), pp. 1–154. ISSN: 0370-1573. DOI: 10.1016/j.physrep.2020.05.001. URL: https://www.sciencedirect.com/science/article/pii/S0370157320301915.

[42] LHCb Collaboration et al. "Observation of $J/\psi p$ Resonances Consistent with Pentaquark States in $\Lambda_b^0 \to J/\psi K^- p$ Decays". In: *Physical Review Letters* 115.7 (Aug. 12, 2015), p. 072001. DOI: 10.1103/PhysRevLett.115.072001. URL: https://link.aps.org/doi/10.1103/PhysRevLett.115.072001.

[43] Nima Arkani–Hamed et al. "The hierarchy problem and new dimensions at a millimeter". In: *Physics Letters B* 429.3 (June 18, 1998), pp. 263–272. ISSN: 0370-2693. DOI: 10.1016/S0370-2693(98)00466-3. URL: https://www.sciencedirect.com/science/article/pii/S0370269398004663.

[44] R. D. Peccei and Helen R. Quinn. "CP Conservation in the Presence of Pseudoparticles". In: *Physical Review Letters* 38.25 (June 20, 1977), pp. 1440–1443. DOI: 10.1103/PhysRevLett.38.1440. URL: https://link.aps.org/doi/10.1103/PhysRevLett.38.1440.

[45] Michael Dine et al. "A simple solution to the strong CP problem with a harmless axion". In: *Physics Letters B* 104.3 (Aug. 27, 1981), pp. 199–202. ISSN: 0370-2693. DOI: 10.1016/0370-2693(81)90590-6. URL: https://www.sciencedirect.com/science/article/pii/0370269381905906.

[46] Michael Dine et al. "A simple solution to the strong CP problem with a harmless axion". In: *Physics Letters B* 104.3 (Aug. 27, 1981), pp. 199–202. ISSN: 0370-2693. DOI: 10.1016/0370-2693(81)90590-6. URL: https://www.sciencedirect.com/science/article/pii/0370269381905906.

[47] David J. E. Marsh. "Axion cosmology". In: *Physics Reports*. Axion cosmology 643 (July 1, 2016), pp. 1–79. ISSN: 0370-1573. DOI: 10.1016/j.physrep.2016.06.005. URL: https://www.sciencedirect.com/science/article/pii/S0370157316301557.

[48] C. D. Froggatt and H. B. Nielsen. "Hierarchy of quark masses, cabibbo angles and CPviolation". In: *Nuclear Physics B* 147.3 (Jan. 22, 1979), pp. 277–298. ISSN: 0550-3213. DOI: 10.1016/0550-3213(79)90316-X. URL: https://www.sciencedirect.com/science/article/pii/055032137990316X.

[49] David E. Morrissey and Michael J. Ramsey-Musolf. "Electroweak baryogenesis". In: *New Journal of Physics* 14.12 (Dec. 2012), p. 125003. ISSN: 1367-2630. DOI: 10.1088/1367-2630/14/12/125003. URL: https://dx.doi.org/10.1088/1367-2630/14/12/125003.

[50] Gianfranco Bertone et al. "Particle dark matter: evidence, candidates and constraints". In: *Physics Reports* 405.5 (Jan. 1, 2005), pp. 279–390. ISSN: 0370-1573. DOI: 10.1016/j.physrep.2004.08.031. URL: https://www.sciencedirect.com/science/article/pii/S0370157304003515.

[51] Steven Weinberg. "The cosmological constant problem". In: *Reviews of Modern Physics* 61.1 (Jan. 1, 1989), pp. 1–23. DOI: 10.1103/RevModPhys.61.1. URL: https://link.aps.org/doi/10.1103/RevModPhys.61.1.

[52] Edmund J. Copeland et al. "Dynamics of dark energy". In: *International Journal of Modern Physics D* 15.11 (Nov. 2006), pp. 1753–1935. ISSN: 0218-2718. DOI: 10.1142/S021827180600942X. URL: https://www.worldscientific.com/doi/abs/10.1142/S021827180600942X.

[53] Super-Kamiokande Collaboration et al. "Evidence for Oscillation of Atmospheric Neutrinos". In: *Physical Review Letters* 81.8 (Aug. 24, 1998), pp. 1562–1567. DOI: 10.1103/PhysRevLett.81.1562. URL: https://link.aps.org/doi/10.1103/PhysRevLett.81.1562.

[54] LSND Collaboration et al. "Evidence for neutrino oscillations from the observation of $\overline{\nu}_e$ appearance in a $\overline{\nu}_\mu$ beam". In: *Physical Review D* 64.11 (Nov. 13, 2001), p. 112007. DOI: 10.1103/PhysRevD.64.112007. URL: https://link.aps.org/doi/10.1103/PhysRevD.64.112007.

[55] Muon g−2 Collaboration et al. "Measurement of the Positive Muon Anomalous Magnetic Moment to 0.46 ppm". In: *Physical Review Letters* 126.14 (Apr. 7, 2021), p. 141801. DOI: 10.1103/PhysRevLett.126.141801. URL: https://link.aps.org/doi/10.1103/PhysRevLett.126.141801.

[56] S. L. Glashow et al. "Weak Interactions with Lepton-Hadron Symmetry". In: *Physical Review D* 2.7 (Oct. 1, 1970), pp. 1285–1292. DOI: 10.1103/PhysRevD.2.1285. URL: https://link.aps.org/doi/10.1103/PhysRevD.2.1285.

[57] ATLAS Collaboration. *Precise test of lepton flavour universality in W-boson decays into muons and electrons in* pp *collisions at* $\sqrt{s} = 13$ *TeV with the ATLAS detector*. Mar. 4, 2024. DOI: 10.48550/arXiv.2403.02133. arXiv: 2403.02133 [hep-ex]. URL: http://arxiv.org/abs/2403.02133. Pre-published.

[58] BABAR Collaboration et al. "Measurement of branching fractions and rate asymmetries in the rare decays $B \to K^{(*)}\ell^+\ell^-$". In: *Physical Review D* 86.3 (Aug. 24, 2012), p. 032012. DOI: 10.1103/PhysRevD.86.032012. URL: https://link.aps.org/doi/10.1103/PhysRevD.86.032012.

[59] Belle Collaboration et al. "Measurement of the Differential Branching Fraction and Forward-Backward Asymmetry for $B \to K^{(*)}l^+l^-$". In: *Physical Review Letters* 103.17 (Oct. 20, 2009), p. 171801. DOI: 10.1103/PhysRevLett.103.171801. URL: https://link.aps.org/doi/10.1103/PhysRevLett.103.171801.

[60] LHCb collaboration et al. "Test of lepton universality using $B^+ \to K^+\ell^+\ell^-$ decays". In: *Physical Review Letters* 113.15 (Oct. 6, 2014), p. 151601. ISSN: 0031-9007, 1079-7114. DOI: 10.1103/PhysRevLett.113.151601. arXiv: 1406.6482 [hep-ex]. URL: http://arxiv.org/abs/1406.6482.

[61] R. Aaij et al. "Test of lepton universality with $\Lambda_b^0 \to pK^-\ell^+\ell^-$ decays". In: *Journal of High Energy Physics* 2020.5 (May 11, 2020), p. 40. ISSN: 1029-8479. DOI: 10.1007/JHEP05(2020)040. URL: https://doi.org/10.1007/JHEP05(2020)040.

[62] R. Aaij et al. "Test of lepton universality with $B^0 \to K^{*0}\ell^+\ell^-$ decays". In: *Journal of High Energy Physics* 2017.8 (Aug. 16, 2017), p. 55. ISSN: 1029-8479. DOI: 10.1007/JHEP08(2017)055. URL: https://doi.org/10.1007/JHEP08(2017)055.

[63] Andreas Crivellin and Stefan Pokorski. "Can the Differences in the Determinations of V_{ub} and V_{cb} Be Explained by New Physics?" In: *Physical Review Letters* 114.1 (Jan. 7, 2015), p. 011802. DOI: 10.1103/PhysRevLett.114.011802. URL: https://link.aps.org/doi/10.1103/PhysRevLett.114.011802.

[64] LHCb Collaboration. *Measurement of the ratios of branching fractions $\mathcal{R}(D^*)$ and $\mathcal{R}(D^0)$*. Sept. 19, 2023. DOI: 10.1103/PhysRevLett.131.111802. arXiv: 2302.02886 [hep-ex]. URL: http://arxiv.org/abs/2302.02886. Pre-published.

[65] LHCb Collaboration et al. "Test of lepton flavor universality by the measurement of the $B^0 \to D^{*-}\tau^+\nu_\tau$ branching fraction using three-prong τ decays". In: *Physical Review D* 97.7 (Apr. 25, 2018), p. 072013. DOI: 10.1103/PhysRevD.97.072013. URL: https://link.aps.org/doi/10.1103/PhysRevD.97.072013.

[66] LHCb collaboration et al. *Measurement of the branching fraction ratios $R(D^+)$ and $R(D^{*+})$ using muonic τ decays*. 2024. arXiv: 2406.03387 [hep-ex]. URL: https://arxiv.org/abs/2406.03387.

[67] Belle II Collaboration Kojima Kazuki. "Recent Belle II results on semileptonic decays and tests of lepton-flavor universality". 31st International Symposium on Lepton Photon Interactions at High Energies (Melbourne, Australia). July 18, 2023. URL: https://indico.cern.ch/event/1114856/contributions/5423684/attachments/2685890/4660084/2023-07-04_LP2023_KojimaFinalVer_main.pdf.

[68] LHCb Collaboration et al. "Observation of the Decay $\Lambda_b^0 \to \Lambda_c^+ \tau^- \overline{\nu}_\tau$". In: *Physical Review Letters* 128.19 (May 13, 2022), p. 191803. DOI: 10.1103/PhysRevLett.128.191803. URL: https://link.aps.org/doi/10.1103/PhysRevLett.128.191803.

[69] LHCb collaboration et al. *Measurement of the* D^* *longitudinal polarization in* $B^0 \to D^{*-}\tau^+\nu_\tau$ *decays*. Nov. 9, 2023. DOI: 10.48550/arXiv.2311.05224. arXiv: 2311.05224 [hep-ex]. URL: http://arxiv.org/abs/2311.05224. Pre-published.

[70] Marat Freytsis et al. "Flavor models for $\bar{B} \to D^{(*)}\tau\bar{\nu}$". In: *Physical Review D* 92.5 (Sept. 14, 2015), p. 054018. ISSN: 1550-7998, 1550-2368. DOI: 10.1103/PhysRevD.92.054018. arXiv: 1506.08896 [hep-ph]. URL: http://arxiv.org/abs/1506.08896.

[71] I. Doršner et al. "Physics of leptoquarks in precision experiments and at particle colliders". In: *Physics Reports* 641 (June 2016), pp. 1–68. ISSN: 03701573. DOI: 10.1016/j.physrep.2016.06.001. arXiv: 1603.04993 [hep-ex, physics:hep-ph]. URL: http://arxiv.org/abs/1603.04993.

[72] Estia Eichten and Brian Hill. "Static effective field theory: $1/m$ corrections". In: *Physics Letters B* 243.4 (July 5, 1990), pp. 427–431. ISSN: 0370-2693. DOI: 10.1016/0370-2693(90)91408-4. URL: https://www.sciencedirect.com/science/article/pii/0370269390914084.

[73] Benjamin Grinstein. "The static quark effective theory". In: *Nuclear Physics B* 339.2 (July 30, 1990), pp. 253–268. ISSN: 0550-3213. DOI: 10.1016/0550-3213(90)90349-I. URL: https://www.sciencedirect.com/science/article/pii/055032139090349I.

[74] Howard Georgi. "An Effective Field Theory for Heavy Quarks at Low-energies". In: *Phys. Lett. B* 240 (1990), pp. 447–450. DOI: 10.1016/0370-2693(90)91128-X.

[75] R. D. Kenway. "The Isgur-Wise Function". In: *Nuclear Physics B - Proceedings Supplements* 34 (Apr. 1994), pp. 153–158. ISSN: 09205632. DOI: 10.1016/0920-5632(94)90332-8. arXiv: hep-lat/9312021. URL: http://arxiv.org/abs/hep-lat/9312021.

[76] Nathan Isgur and Mark B. Wise. "Weak decays of heavy mesons in the static quark approximation". In: *Physics Letters B* 232.1 (Nov. 23, 1989), pp. 113–117. ISSN: 0370-2693. DOI: 10.1016/0370-2693(89)90566-2. URL: https://www.sciencedirect.com/science/article/pii/0370269389905662.

[77] Nathan Isgur and Mark B. Wise. "Weak transition form factors between heavy mesons". In: *Physics Letters B* 237.3 (Mar. 22, 1990), pp. 527–530. ISSN: 0370-2693. DOI: 10.1016/0370-2693(90)91219-2. URL: https://www.sciencedirect.com/science/article/pii/0370269390912192.

[78] A. Bazavov et al. "Semileptonic form factors for $B \to D^* \ell \nu$ at nonzero recoil from 2 + 1-flavor lattice QCD". In: *The European Physical Journal C* 82.12 (Dec. 16, 2022), p. 1141. ISSN: 1434-6052. DOI: 10.1140/epjc/s10052-022-10984-9. arXiv: 2105.14019 [hep-ex, physics:hep-lat]. URL: http://arxiv.org/abs/2105.14019.

[79] Matthias Neubert. "Heavy-quark symmetry". In: *Physics Reports* 245.5 (Sept. 1, 1994), pp. 259–395. ISSN: 0370-1573. DOI: 10.1016/0370-1573(94)90091-4. URL: https://www.sciencedirect.com/science/article/pii/0370157394900914.

[80] J. G. Körner and G. A. Schuler. "Exclusive semileptonic heavy meson decays including lepton mass effects". In: *Zeitschrift für Physik C Particles and Fields* 46.1 (Mar. 1, 1990), pp. 93–109. ISSN: 1431-5858. DOI: 10.1007/BF02440838. URL: https://doi.org/10.1007/BF02440838.

[81] I. Caprini et al. "Dispersive Bounds on the Shape of $B \to D^{(*)} \ell \nu$ Form Factors". In: *Nuclear Physics B* 530.1-2 (Oct. 1998), pp. 153–181. ISSN: 05503213. DOI: 10.1016/S0550-3213(98)00350-2. arXiv: hep-ph/9712417. URL: http://arxiv.org/abs/hep-ph/9712417.

[82] C. Glenn Boyd et al. "Constraints on Form Factors for Exclusive Semileptonic Heavy to Light Meson Decays". In: *Physical Review Letters* 74.23 (June 5, 1995), pp. 4603–4606. DOI: 10.1103/PhysRevLett.74.4603. URL: https://link.aps.org/doi/10.1103/PhysRevLett.74.4603.

[83] C. Glenn Boyd et al. *Model-Independent Determinations of* $B \to D \ell \nu$, $D^* \ell \nu$ *Form Factors*. Aug. 1, 1995. DOI: 10.48550/arXiv.hep-ph/9508211. arXiv: hep-ph/9508211. URL: http://arxiv.org/abs/hep-ph/9508211. Preprinted.

[84] C. Glenn Boyd et al. "Precision Corrections to Dispersive Bounds on Form Factors". In: *Physical Review D* 56.11 (Dec. 1, 1997), pp. 6895–6911. ISSN: 0556-2821, 1089-4918. DOI: 10.1103/PhysRevD.56.6895. arXiv: hep-ph/9705252. URL: http://arxiv.org/abs/hep-ph/9705252.

[85] Paolo Gambino et al. "The V_{cb} puzzle: an update". In: *Physics Letters B* 795 (Aug. 2019), pp. 386–390. ISSN: 03702693. DOI: 10.1016/j.physletb.2019.06.039. arXiv: 1905.08209 [hep-ex, physics:hep-ph]. URL: http://arxiv.org/abs/1905.08209.

[86] Judd Harrison and Christine T. H. Davies. $B \to D^*$ *vector, axial-vector and tensor form factors for the full* q^2 *range from lattice QCD*. Jan. 26, 2024. DOI: 10.48550/arXiv.2304.03137. arXiv: 2304.03137 [hep-lat, physics:hep-ph]. URL: http://arxiv.org/abs/2304.03137. Pre-published.

[87] Y. Aoki et al. $B \to D^* \ell \nu_\ell$ *semileptonic form factors from lattice QCD with Möbius domain-wall quarks*. June 8, 2023. DOI: 10.48550/arXiv.2306.05657. arXiv: 2306.05657 [hep-ex, physics:hep-lat, physics:hep-ph]. URL: http://arxiv.org/abs/2306.05657. Pre-published.

[88] B. Dey. "Extraction of form Factors from a Four-Dimensional Angular Analysis of $\overline{B} \to D^* \ell^- \overline{\nu}_\ell$". In: *Physical Review Letters* 123.9 (Aug. 29, 2019), p. 091801. ISSN: 0031-9007, 1079-7114. DOI: 10.1103/PhysRevLett.123.091801. arXiv: 1903.10002 [hep-ex]. URL: http://arxiv.org/abs/1903.10002.

[89] Ipsita Ray and Soumitra Nandi. *Test of new physics effects in* $\bar{B} \to (D^{(*)}, \pi) \ell^- \bar{\nu}_\ell$ *decays with heavy and light leptons*. Dec. 21, 2023. DOI: 10.48550/arXiv.2305.11855. arXiv: 2305.11855 [hep-ex, physics:hep-lat, physics:hep-ph]. URL: http://arxiv.org/abs/2305.11855. Pre-published.

[90] Florian U. Bernlochner et al. "Combined analysis of semileptonic B decays to D and D^*: $R(D^{(*)})$, $|V_{cb}|$, and new physics". In: *Physical Review D* 95.11 (June 8, 2017), p. 115008. ISSN: 2470-0010, 2470-0029. DOI: 10.1103/PhysRevD.95.115008. arXiv: 1703.05330 [hep-ph]. URL: http://arxiv.org/abs/1703.05330.

[91] Sneha Jaiswal et al. *Extraction of* $|V_{cb}|$ *from* $B \to D^{(*)} \ell \nu_\ell$ *and the Standard Model predictions of* $R(D^{(*)})$. arXiv.org. July 31, 2017. DOI: 10.1007/JHEP12(2017)060. URL: https://arxiv.org/abs/1707.09977v2.

[92] Marzia Bordone et al. "Theory determination of $\bar{B} \to D^{(*)} \ell^- \bar{\nu}$ form factors at $O(1/m_c^2)$". In: *The European Physical Journal C* 80.2 (Feb. 2020), p. 74. ISSN: 1434-6044, 1434-6052. DOI: 10.1140/epjc/s10052-020-7616-4. arXiv: 1908.09398 [hep-ex, physics:hep-ph]. URL: http://arxiv.org/abs/1908.09398.

[93] Dante Bigi et al. "$R(D^*)$, $|V_{cb}|$, and the Heavy Quark Symmetry relations between form factors". In: *Journal of High Energy Physics* 2017.11 (Nov. 2017), p. 61. ISSN: 1029-8479. DOI: 10.1007/JHEP11(2017)061. arXiv: 1707.09509 [hep-ph]. URL: http://arxiv.org/abs/1707.09509.

[94] Dante Bigi and Paolo Gambino. "Revisiting B $\to$ D$\ell\nu$". In: *Physical Review D* 94.9 (Nov. 11, 2016), p. 094008. ISSN: 2470-0010, 2470-0029. DOI: 10.1103/PhysRevD.94.094008. arXiv: 1606.08030 [hep-ex, physics:hep-ph]. URL: http://arxiv.org/abs/1606.08030.

[95] G. Martinelli et al. "Exclusive determinations of $|V_{cb}|$ and R(D*) through unitarity". In: *The European Physical Journal C* 82.12 (Dec. 1, 2022), p. 1083. ISSN: 1434-6052. DOI: 10.1140/epjc/s10052-022-11050-0. arXiv: 2109.15248 [hep-ex, physics:hep-lat, physics:hep-ph]. URL: http://arxiv.org/abs/2109.15248.

[96] G. Martinelli et al. "$|V_{cb}|$ and R($D^{(*)}$) using lattice QCD and unitarity". In: *Physical Review D* 105.3 (Feb. 7, 2022), p. 034503. ISSN: 2470-0010, 2470-0029. DOI: 10.1103/PhysRevD.105.034503. arXiv: 2105.08674 [hep-ex, physics:hep-lat, physics:hep-ph]. URL: http://arxiv.org/abs/2105.08674.

[97] H. P. Nilles. "Supersymmetry, supergravity and particle physics". In: *Physics Reports* 110.1 (Aug. 1, 1984), pp. 1–162. ISSN: 0370-1573. DOI: 10.1016/0370-1573(84)90008-5. URL: https://www.sciencedirect.com/science/article/pii/0370157384900085.

[98] Jogesh C. Pati and Abdus Salam. "Lepton Number as the Fourth Color". In: *Phys. Rev. D* 10 (1974), pp. 275–289. DOI: 10.1103/PhysRevD.10.275.

[99] Edward Farhi and Leonard Susskind. "Technicolour". In: *Physics Reports* 74.3 (Aug. 1, 1981), pp. 277–321. ISSN: 0370-1573. DOI: 10.1016/0370-1573(81)90173-3. URL: https://www.sciencedirect.com/science/article/pii/0370157381901733.

[100] Kaustubh Agashe et al. "The Minimal composite Higgs model". In: *Nucl. Phys. B* 719 (2005), pp. 165–187. DOI: 10.1016/j.nuclphysb.2005.04.035.

[101] Damir Bečirević et al. "Leptoquark model to explain the B-physics anomalies, R_K and R_D". In: *Physical Review D* 94.11 (Dec. 20, 2016), p. 115021. ISSN: 2470-0010, 2470-0029. DOI: 10.1103/PhysRevD.94.115021. arXiv: 1608.08501 [hep-ex, physics:hep-ph]. URL: http://arxiv.org/abs/1608.08501.

[102] Martin Bauer and Matthias Neubert. "One Leptoquark to Rule Them All: A Minimal Explanation for $R_{D^{(*)}}$, R_K and $(g-2)_\mu$". In: *Physical Review Letters* 116.14 (Apr. 8, 2016), p. 141802. ISSN: 0031-9007, 1079-7114. DOI: 10.1103/PhysRevLett.116.141802. arXiv: 1511.01900 [hep-ph]. URL: http://arxiv.org/abs/1511.01900.

[103] Svjetlana Fajfer and Nejc Košnik. "Vector leptoquark resolution of R_K and $R_{D^{(*)}}$ puzzles". In: *Physics Letters B* 755 (Apr. 2016), pp. 270–274. ISSN: 03702693. DOI: 10.1016/j.physletb.2016.02.018. arXiv: 1511.06024 [hep-ex, physics:hep-ph]. URL: http://arxiv.org/abs/1511.06024.

[104] Alejandro Celis et al. "Sensitivity to charged scalars in $B \to D^{(*)}\tau\nu_\tau$ and $B \to \tau\nu_\tau$ decays". In: *Journal of High Energy Physics* 2013.1 (Jan. 2013), p. 54. ISSN: 1029-8479. DOI: 10.1007/JHEP01(2013)054. arXiv: 1210.8443 [hep-ex, physics:hep-ph]. URL: http://arxiv.org/abs/1210.8443.

[105] Minoru Tanaka and Ryoutaro Watanabe. "New physics in the weak interaction of $\bar{B} \to D^{(*)}\tau\bar{\nu}$". In: *Physical Review D* 87.3 (Feb. 19, 2013), p. 034028. ISSN: 1550-7998, 1550-2368. DOI: 10.1103/PhysRevD.87.034028. arXiv: 1212.1878 [hep-ph]. URL: http://arxiv.org/abs/1212.1878.

[106] Admir Greljo et al. *On the breaking of Lepton Flavor Universality in B decays*. July 2, 2015. DOI: 10.48550/arXiv.1506.01705. arXiv: 1506.01705 [hep-ph]. URL: http://arxiv.org/abs/1506.01705. Pre-published.

[107] Lorenzo Calibbi et al. "Effective field theory approach to $b \to s\ell\ell^{(\prime)}$, $B \to K^{(*)}\nu\bar{\nu}$ and $B \to D^{(*)}\tau\nu$ with third generation couplings". In: *Physical Review Letters* 115.18 (Oct. 27, 2015), p. 181801. ISSN: 0031-9007, 1079-7114. DOI: 10.1103/PhysRevLett.115.181801. arXiv: 1506.02661 [hep-ex, physics:hep-ph]. URL: http://arxiv.org/abs/1506.02661.

[108] Yuval Grossman and Zoltan Ligeti. "The Inclusive $\bar{B} \to \tau\bar{\nu}X$ Decay in Two Higgs Doublet Models". In: *Physics Letters B* 332.3-4 (July 1994), pp. 373–380. ISSN: 03702693. DOI: 10.1016/0370-2693(94)91267-X. arXiv: hep-ph/9403376. URL: http://arxiv.org/abs/hep-ph/9403376.

[109] Sacha Davidson et al. "Model independent constraints on leptoquarks from rare processes". In: *Zeitschrift für Physik C Particles and Fields* 61.4 (Dec. 1994), pp. 613–643. ISSN: 0170-9739, 1434-6052. DOI: 10.1007/BF01552629. arXiv: hep-ph/9309310. URL: http://arxiv.org/abs/hep-ph/9309310.

[110] Yasuhito Sakaki et al. "Testing leptoquark models in $\bar{B} \to D^{(*)}\tau\bar{\nu}$". In: *Physical Review D* 88.9 (Nov. 14, 2013), p. 094012. ISSN: 1550-7998, 1550-2368. DOI: 10.1103/PhysRevD.88.094012. arXiv: 1309.0301 [hep-ph]. URL: http://arxiv.org/abs/1309.0301.

[111] W. Buchmüller et al. "Leptoquarks in lepton-quark collisions". In: *Physics Letters B* 191.4 (June 1987), pp. 442–448. ISSN: 03702693. DOI: 10.1016/0370-2693(87)90637-X. URL: https://linkinghub.elsevier.com/retrieve/pii/037026938790637X.

[112] Andreas Crivellin et al. "Explaining $B \to D\tau\nu$, $B \to D^*\tau\nu$ and $B \to \tau\nu$ in a 2HDM of type III". In: *Physical Review D* 86.5 (Sept. 13, 2012), p. 054014. ISSN: 1550-7998, 1550-2368. DOI: 10.1103/PhysRevD.86.054014. arXiv: 1206.2634 [hep-ex, physics:hep-ph]. URL: http://arxiv.org/abs/1206.2634.

[113] Andrzej J. Buras et al. "Higgs-mediated FCNCs: Natural Flavour Conservation vs. Minimal Flavour Violation". In: *Journal of High Energy Physics* 2010.10 (Oct. 2010), p. 9. ISSN: 1029-8479. DOI: 10.1007/JHEP10(2010)009. arXiv: 1005.5310 [hep-ph]. URL: http://arxiv.org/abs/1005.5310.

[114] Gianluca Blankenburg and G. Isidori. "B->tau nu in multi-Higgs models with MFV". In: (July 6, 2011).

[115] ATLAS Collaboration. *Search for leptoquark pair production decaying into* $te^-\bar{t}e^+$ *or* $t\mu^-\bar{t}\mu^+$ *in multi-lepton final states in* pp *collisions at 13 TeV with the ATLAS detector*. June 30, 2023. DOI: 10.48550/arXiv.2306.17642. arXiv: 2306.17642 [hep-ex]. URL: http://arxiv.org/abs/2306.17642. Pre-published.

[116] CMS Collaboration. "Search for a singly produced third-generation scalar leptoquark decaying to a τ lepton and a bottom quark in proton-proton collisions at $\sqrt{s} = 13$ TeV". In: *Journal of High Energy Physics* 2018.7 (July 2018), p. 115. ISSN: 1029-8479. DOI: 10.1007/JHEP07(2018)115. arXiv: 1806.03472 [hep-ex]. URL: http://arxiv.org/abs/1806.03472.

[117] CMS Collaboration. "Constraints on models of scalar and vector leptoquarks decaying to a quark and a neutrino at $\sqrt{s} = 13$ TeV". In: *Physical Review D* 98.3 (Aug. 10, 2018), p. 032005. ISSN: 2470-0010, 2470-0029. DOI: 10.1103/PhysRevD.98.032005. arXiv: 1805.10228 [hep-ex]. URL: http://arxiv.org/abs/1805.10228.

[118] ATLAS Collaboration. "Searches for third-generation scalar leptoquarks in $\sqrt{s} = 13$ TeV pp collisions with the ATLAS detector". In: *Journal of High Energy Physics* 2019.6 (June 2019), p. 144. ISSN: 1029-8479. DOI: 10.1007/JHEP06(2019)144. arXiv: 1902.08103 [hep-ex]. URL: http://arxiv.org/abs/1902.08103.

[119] Jason Aebischer et al. "Confronting the vector leptoquark hypothesis with new low- and high-energy data". In: *The European Physical Journal C* 83.2 (Feb. 16, 2023), p. 153. ISSN: 1434-6052. DOI: 10.1140/epjc/s10052-023-11304-5. arXiv: 2210.13422 [hep-ex, physics:hep-ph]. URL: http://arxiv.org/abs/2210.13422.

[120] The BABAR Collaboration. "The BABAR Detector". In: *Nuclear Instruments and Methods in Physics Research Section A: Accelerators, Spectrometers, Detectors and Associated Equipment* 479.1 (Feb. 2002), pp. 1–116. ISSN: 01689002. DOI: 10.1016/S0168-9002(01)02012-5. arXiv: hep-ex/0105044. URL: http://arxiv.org/abs/hep-ex/0105044.

[121] W Kozanecki. "The PEP-II B-factory: status and prospects". In: *Nuclear Instruments and Methods in Physics Research Section A: Accelerators, Spectrometers, Detectors and Associated Equipment* 446.1 (May 11, 2000), pp. 59–64. ISSN: 0168-9002. DOI: 10.1016/

S0168-9002(00)00022-X. URL: https://www.sciencedirect.com/science/article/pii/S016890020000022X.

[122] H. Tajima. "Instrumentation for the BELLE detector". In: *Nuclear Physics B - Proceedings Supplements*. Advanced Technology and Particle Physics 78.1 (Aug. 1, 1999), pp. 14–19. ISSN: 0920-5632. DOI: 10.1016/S0920-5632(99)00516-2. URL: https://www.sciencedirect.com/science/article/pii/S0920563299005162.

[123] B. Aubert. "Measurement of the CP-Violating Asymmetry Amplitude sin2beta". In: *Physical Review Letters* 89.20 (Oct. 29, 2002), p. 201802. ISSN: 0031-9007, 1079-7114. DOI: 10.1103/PhysRevLett.89.201802. arXiv: hep-ex/0207042. URL: http://arxiv.org/abs/hep-ex/0207042.

[124] Belle Collaboration et al. "Observation of Large CP Violation in the Neutral B Meson System". In: *Physical Review Letters* 87.9 (Aug. 14, 2001), p. 091802. DOI: 10.1103/PhysRevLett.87.091802. URL: https://link.aps.org/doi/10.1103/PhysRevLett.87.091802.

[125] T. Abe et al. *Belle II Technical Design Report*. Nov. 1, 2010. DOI: 10.48550/arXiv.1011.0352. arXiv: 1011.0352 [hep-ex, physics:physics]. URL: http://arxiv.org/abs/1011.0352. Pre-published.

[126] Lyndon Evans and Philip Bryant. "LHC Machine". In: *Journal of Instrumentation* 3.08 (Aug. 2008), S08001. ISSN: 1748-0221. DOI: 10.1088/1748-0221/3/08/S08001. URL: https://dx.doi.org/10.1088/1748-0221/3/08/S08001.

[127] The ATLAS Collaboration et al. "The ATLAS Experiment at the CERN Large Hadron Collider". In: *Journal of Instrumentation* 3.08 (Aug. 2008), S08003. ISSN: 1748-0221. DOI: 10.1088/1748-0221/3/08/S08003. URL: https://dx.doi.org/10.1088/1748-0221/3/08/S08003.

[128] The CMS Collaboration et al. "The CMS experiment at the CERN LHC". In: *Journal of Instrumentation* 3.08 (Aug. 2008), S08004. ISSN: 1748-0221. DOI: 10.1088/1748-0221/3/08/S08004. URL: https://dx.doi.org/10.1088/1748-0221/3/08/S08004.

[129] The LHCb Collaboration et al. "The LHCb Detector at the LHC". In: *Journal of Instrumentation* 3.08 (Aug. 2008), S08005. ISSN: 1748-0221. DOI: 10.1088/1748-0221/3/08/S08005. URL: https://dx.doi.org/10.1088/1748-0221/3/08/S08005.

[130] The ALICE Collaboration et al. "The ALICE experiment at the CERN LHC". In: *Journal of Instrumentation* 3.08 (Aug. 2008), S08002. ISSN: 1748-0221. DOI: 10.1088/1748-0221/3/08/S08002. URL: https://dx.doi.org/10.1088/1748-0221/3/08/S08002.

[131] G Apollinari et al. "High-Luminosity Large Hadron Collider (HL-LHC) Preliminary Design Report". In: (2015). DOI: 10.5170/CERN-2015-005. URL: http://cds.cern.ch/record/2116337.

[132] Christian Elsasser. *LHCb bb production angle plots*. bb production angle plots. URL: https://lhcb.web.cern.ch/speakersbureau/html/bb_ProductionAngles.html.

[133] *LHCb Operations Plots WebPage*. URL: https://lbgroups.cern.ch/online/OperationsPlots/index.htm.

[134] P R Barbosa-Marinho et al. *LHCb VELO (VErtex LOcator): Technical Design Report*. Geneva: CERN, 2001. URL: https://cds.cern.ch/record/504321.

[135] J Gassner et al. *Layout and Expected Performance of the LHCb TT Station*. Geneva: CERN, 2004. URL: https://cds.cern.ch/record/728548.

[136] R. Calabrese et al. "Performance of the LHCb RICH detectors during LHC Run 2". In: *Journal of Instrumentation* 17.07 (July 2022), P07013. ISSN: 1748-0221. DOI: 10.1088/1748-0221/17/07/P07013. URL: https://dx.doi.org/10.1088/1748-0221/17/07/P07013.

[137] P R Barbosa-Marinho et al. *LHCb inner tracker: Technical Design Report*. Geneva: CERN, 2002. URL: https://cds.cern.ch/record/582793.

[138] P R Barbosa-Marinho et al. *LHCb outer tracker: Technical Design Report*. Geneva: CERN, 2001. URL: http://cds.cern.ch/record/519146.

[139] R. E. Kalman. "A New Approach to Linear Filtering and Prediction Problems". In: *Journal of Basic Engineering* 82.1 (Mar. 1960), pp. 35–45. ISSN: 0021-9223. DOI: 10.1115/1.3662552. eprint: https://asmedigitalcollection.asme.org/fluidsengineering/article-pdf/82/1/35/5518977/35_1.pdf. URL: https://doi.org/10.1115/1.3662552.

[140] R. Frühwirth. "Application of Kalman filtering to track and vertex fitting". In: *Nuclear Instruments and Methods in Physics Research Section A: Accelerators, Spectrometers, Detectors and Associated Equipment* 262.2 (Dec. 15, 1987), pp. 444–450. ISSN: 0168-9002. DOI: 10.1016/0168-9002(87)90887-4. URL: https://www.sciencedirect.com/science/article/pii/0168900287908874.

[141] R. Aaij et al. "Design and performance of the LHCb trigger and full real-time reconstruction in Run 2 of the LHC". In: *Journal of Instrumentation* 14.04 (Apr. 2019), P04013. ISSN: 1748-0221. DOI: 10.1088/1748-0221/14/04/P04013. URL: https://dx.doi.org/10.1088/1748-0221/14/04/P04013.

[142] Roger Forty. "Ring-imaging Cherenkov detectors for LHC-B". In: *Nuclear Instruments and Methods in Physics Research Section A: Accelerators, Spectrometers, Detectors and Associated Equipment*. BEAUTY '96 384.1 (Dec. 21, 1996), pp. 167–174. ISSN: 0168-9002. DOI: 10.1016/S0168-9002(96)00951-5. URL: https://www.sciencedirect.com/science/article/pii/S0168900296009515.

[143] N Brook et al. *LHCb RICH1 Engineering Design Review Report*. Geneva: CERN, 2005. URL: https://cds.cern.ch/record/897981.

[144] "LHCb detector performance". In: *International Journal of Modern Physics A* 30.07 (Mar. 10, 2015), p. 1530022. ISSN: 0217-751X. DOI: 10.1142/S0217751X15300227. URL: https://www.worldscientific.com/doi/10.1142/S0217751X15300227.

[145] S Amato et al. *LHCb calorimeters: Technical Design Report*. Geneva: CERN, 2000. URL: https://cds.cern.ch/record/494264.

[146] Yu Guz. "The LHCb Calorimeter system: design, performance and upgrade". In: *Journal of Instrumentation* 12.07 (July 2017), p. C07024. ISSN: 1748-0221. DOI: 10.1088/1748-0221/12/07/C07024. URL: https://dx.doi.org/10.1088/1748-0221/12/07/C07024.

[147] A. A. Alves Jr et al. "Performance of the LHCb muon system". In: *Journal of Instrumentation* 8.02 (Feb. 2013), P02022. ISSN: 1748-0221. DOI: 10.1088/1748-0221/8/02/P02022. URL: https://dx.doi.org/10.1088/1748-0221/8/02/P02022.

[148] Lucio Anderlini et al. *The PIDCalib package*. Geneva: CERN, 2016. URL: https://cds.cern.ch/record/2202412.

[149] R. Aaij et al. *The LHCb Trigger and its Performance in 2011*. Apr. 3, 2013. DOI: 10.1088/1748-0221/8/04/P04022. arXiv: 1211.3055 [hep-ex]. URL: http://arxiv.org/abs/1211.3055. Pre-published.

[150] M. Clemencic et al. "The LHCb Simulation Application, Gauss: Design, Evolution and Experience". In: *Journal of Physics: Conference Series* 331.3 (Dec. 2011), p. 032023. ISSN: 1742-6596. DOI: 10.1088/1742-6596/331/3/032023. URL: https://dx.doi.org/10.1088/1742-6596/331/3/032023.

[151] Torbjörn Sjöstrand et al. "A brief introduction to PYTHIA 8.1". In: *Computer Physics Communications* 178.11 (June 1, 2008), pp. 852–867. ISSN: 0010-4655. DOI: 10.1016/j.cpc.2008.01.036. URL: https://www.sciencedirect.com/science/article/pii/S0010465508000441.

[152] S. Agostinelli et al. "Geant4—a simulation toolkit". In: *Nuclear Instruments and Methods in Physics Research Section A: Accelerators, Spectrometers, Detectors and Associated Equipment* 506.3 (July 1, 2003), pp. 250–303. ISSN: 0168-9002. DOI: 10.1016/S0168-9002(03)01368-8. URL: https://www.sciencedirect.com/science/article/pii/S0168900203013688.

[153] *Letter of Intent for the LHCb Upgrade*. CERN-LHCC-2011-001, LHCC-I-018. Geneva: CERN, 2011. URL: http://cds.cern.ch/record/1333091.

[154] Roel Aaij et al. *The LHCb upgrade I*. 2023. URL: https://cds.cern.ch/record/2859353. Pre-published.

[155] *RTA and DPA dataflow diagrams for Run 1, Run 2, and the upgraded LHCb detector*. 2020. URL: https://cds.cern.ch/record/2730181.

[156] G. Corti et al. "Software for the LHCb experiment". In: *IEEE Trans. Nucl. Sci.* 53 (2006), pp. 1323–1328. DOI: 10.1109/TNS.2006.872627.

[157] Dawid Gerstel. "Test of Lepton Flavour Universality using the B0 to D* tau nu decays at LHCb". PhD thesis. AMU - Aix Marseille Université, Nov. 30, 2020. URL: https://hal.science/tel-03100295.

[158] D. Müller et al. "ReDecay: a novel approach to speed up the simulation at LHCb". In: *The European Physical Journal C* 78.12 (Dec. 12, 2018), p. 1009. ISSN: 1434-6052. DOI: 10.1140/epjc/s10052-018-6469-6. URL: https://doi.org/10.1140/epjc/s10052-018-6469-6.

[159] Florian U. Bernlochner et al. "Model independent analysis of semileptonic B decays to D^{**} for arbitrary new physics". In: *Physical Review D* 97.7 (Apr. 12, 2018), p. 075011. ISSN: 2470-0010, 2470-0029. DOI: 10.1103/PhysRevD.97.075011. arXiv: 1711.03110 [hep-ph]. URL: http://arxiv.org/abs/1711.03110.

[160] Florian U. Bernlochner et al. *Das ist der HAMMER: Consistent new physics interpretations of semileptonic decays*. Oct. 13, 2020. DOI: 10.1140/epjc/s10052-020-8304-0. arXiv: 2002.00020 [hep-ex, physics:hep-ph]. URL: http://arxiv.org/abs/2002.00020. Pre-published.

[161] Alex Rogozhnikov. "Reweighting with Boosted Decision Trees". In: *Journal of Physics: Conference Series* 762.1 (Oct. 2016), p. 012036. ISSN: 1742-6596. DOI: 10.1088/1742-6596/762/1/012036. URL: https://dx.doi.org/10.1088/1742-6596/762/1/012036.

[162] R. Aaij et al. "Angular analysis of $B^0 \to D^{*-}D_s^{*+}$ with $D_s^{*+} \to D_s^+\gamma$ decays". In: *Journal of High Energy Physics* 2021.6 (June 29, 2021), p. 177. ISSN: 1029-8479. DOI: 10.1007/JHEP06(2021)177. URL: https://doi.org/10.1007/JHEP06(2021)177.

[163] Byron P. Roe et al. "Boosted decision trees as an alternative to artificial neural networks for particle identification". In: *Nuclear Instruments and Methods in Physics Research Section A: Accelerators, Spectrometers, Detectors and Associated Equipment* 543.2 (May 11, 2005), pp. 577–584. ISSN: 0168-9002. DOI: 10.1016/j.nima.2004.12.018. URL: https://www.sciencedirect.com/science/article/pii/S0168900205000355.

[164] Jan Therhaag. "TMVA - Toolkit for Multivariate Data Analysis in ROOT". In: *Proceedings of 35th International Conference of High Energy Physics — PoS(ICHEP 2010)*. Vol. 120. SISSA Medialab, Mar. 23, 2011, p. 510. DOI: 10.22323/1.120.0510. URL: https://pos.sissa.it/120/510.

[165] Bo Fang. "Study of the $D_s^+ \to \eta' \pi^+ \pi^- \pi^+$ decays at BESIII and precise measurement of the branching fraction of the $B^0 \to D^{*-} \tau^+ \nu$ decay at LHCb". Theses. Université Paris-Saclay; Université de Wuhan (Chine), Jan. 2024. URL: https://theses.hal.science/tel-04530585.

[166] Florian U. Bernlochner et al. "Semitauonic b-hadron decays: A lepton flavor universality laboratory". In: *Reviews of Modern Physics* 94.1 (Feb. 4, 2022), p. 015003. DOI: 10.1103/RevModPhys.94.015003. URL: https://link.aps.org/doi/10.1103/RevModPhys.94.015003.

Appendix

Appendix A

Methodology

In this part, additional material is provided to complete the methodology of the analysis. The q^2 and τ^+ lifetime resolutions are given in App. A.1. The principle of ReDecay method is explained in App. A.2. The PDG values used in the analysis are listed in App. A.3. The reweighting of the $B^0 \to D^{*-}\mu^+\nu_\mu$ sample is detailed in App. A.4.

A.1. Reconstruction of the Decay Kinematics

Left plot of Fig. A.1 shows the normalized resolution of q^2 and the right plot shows the resolution of t_τ; both for the simulated signal $B^0 \to D^{*-}\tau^+\nu_\tau$ sample after initial selection(*cf.* Sec. 5.4).

A.2. Fast Simulation with ReDecay

To make the measurement competitive, a key requirement was to increase the precision by reducing systematic errors from previous $\mathbf{R}(D^*)$ measurements with hadronic τ reconstruction. The main source of systematic uncertainty was the limited size of simulated event samples. To achieve parity between systematic and statistical uncertainties, it was necessary to expand the sample size by 4-6 times for most event types, as shown in Tab. 4.2.

To reduce these systematic uncertainties, particularly those stemming from limited simulated event samples, various fast simulation strategies available at LHCb, have been explored. The

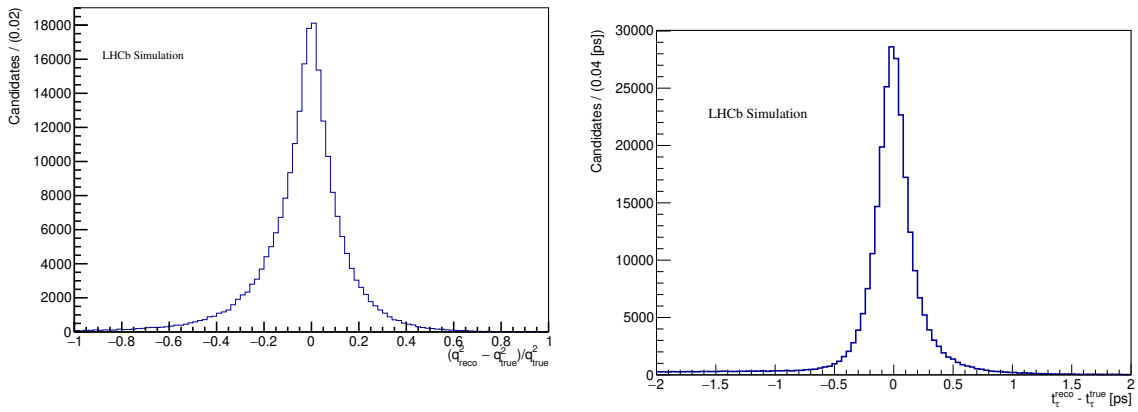

Figure A.1.: Comparison of reconstructed and true values for the simulated signal $B^0 \to D^{*-}\tau^+\nu_\tau$ sample after initial selection (Section 5.4). Left: q^2, with an RMS of 0.19. Right: t_τ, with an RMS of 0.36 ps.

retained method was the ReDecay algorithm [158], a technique that simulates the decay of the mother hadron multiple times (usually 100 times) while reusing the stable parts of the event, such as tracks not originating from the mother hadron. This approach ensures that only the original event is fully simulated, while generating additional events at minimal computational cost. A succinct breakdown of the method is as follows:

- **Initial Simulation:** An event is fully simulated, capturing the B^0 at its origin with its momentum and the underlying non-signal tracks (Fig. A.2, left).
- **Event Recreation:** For subsequent events, the B^0 is allowed to decay anew, combined with the preserved tracks from the original event's background. An example is shown on the right side of Fig. A.2.
- **Block Formation:** This procedure is repeated for $N-1$ events, forming a ReDecay block. The entire simulation consists of several such blocks, each based on a single original event.

The primary concern with ReDecay was the potential for correlations within blocks due to recycling elements of events, which could compromise the statistical diversity of the dataset. To address this, critical variable distributions were examined in validation samples to assess any significant reduction in variation. The applicability of this method was demonstrated in a previous study [157].

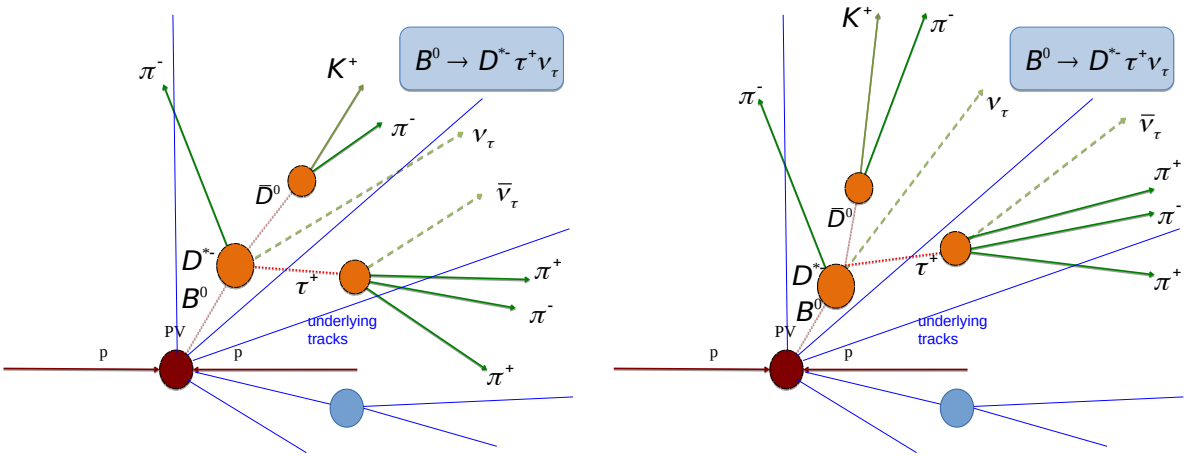

Figure A.2.: Illustration of two signal mode events ($\tau^+ \longrightarrow 3\pi\overline{\nu}_\tau$) within a single ReDecay block, highlighting the simulation process. While the vertices and tracks associated with the signal mode vary between the events, the underlying event's components are consistently reused.

A.3. PDG Review

This is a summary of essential branching fractions, lifetimes, and masses, used in this analysis. All the values come from the Particle Data Group Review [7].

Particle	Decay	Br[%]
$D^*(2010)^-$	$\mathbf{D^*(2010)^- \to \overline{D}^0\pi^-}$	67.7 ± 0.5
	$D^*(2010)^- \to D^-\pi^0$	30.7 ± 0.5
	$D^*(2010)^- \to D^-\gamma$	1.6 ± 0.4
$\overline{D}^0$	$\mathbf{\overline{D}^0 \to K^+\pi^-}$	3.950 ± 0.031
τ^-	$\tau^- \to \mu^-\overline{\nu}_\mu\nu_\tau$	17.39 ± 0.04
	$\tau^- \to e^-\overline{\nu}_e\nu_\tau$	17.82 ± 0.04
	$\tau^- \to \pi^-\pi^0\nu_\tau$	25.49 ± 0.09
	$\tau^- \to \pi^-\nu_\tau$	10.82 ± 0.05
	$\boldsymbol{\tau^- \to \pi^+\pi^-\pi^+\nu_\tau}$ (excluding $\mathbf{K^0_S \to \pi^+\pi^-}$)	9.02 ± 0.05
	$\boldsymbol{\tau^- \to \pi^+\pi^-\pi^+\pi^0\nu_\tau}$ (excluding $\mathbf{K^0_S \to \pi^+\pi^-}$)	4.49 ± 0.05

Table A.1.: Selected branching fractions of the particles in the $B^0 \to D^{*-}\tau^+\nu_\tau$ signal decay chain. Highlighted are the modes chosen in this analysis allowing for good vertices reconstruction.

Particle	Mean lifetime $[10^{-12}\,\mathrm{s}]$
B^0	(1.519 ± 0.004)
D_s^+	$(5.05 \pm 0.04) \times 10^{-1}$
D^+	(1.040 ± 0.007)
D^0	$(4.101 \pm 0.015) \times 10^{-1}$
τ^+	$(2.903 \pm 0.005) \times 10^{-1}$

Table A.2.: Mean lifetimes of the selected particles relevant to the study.

Particle	Invariant Mass $[\,\mathrm{MeV/c^2}]$
B^0	5279.65 ± 0.12
D^{*-}	2010.26 ± 0.05
D_s^+	1968.34 ± 0.07
D^+	1869.65 ± 0.05
D^0	1864.83 ± 0.05
τ^+	1776.86 ± 0.12

Table A.3.: Invariant masses of the selected particles relevant to the study.

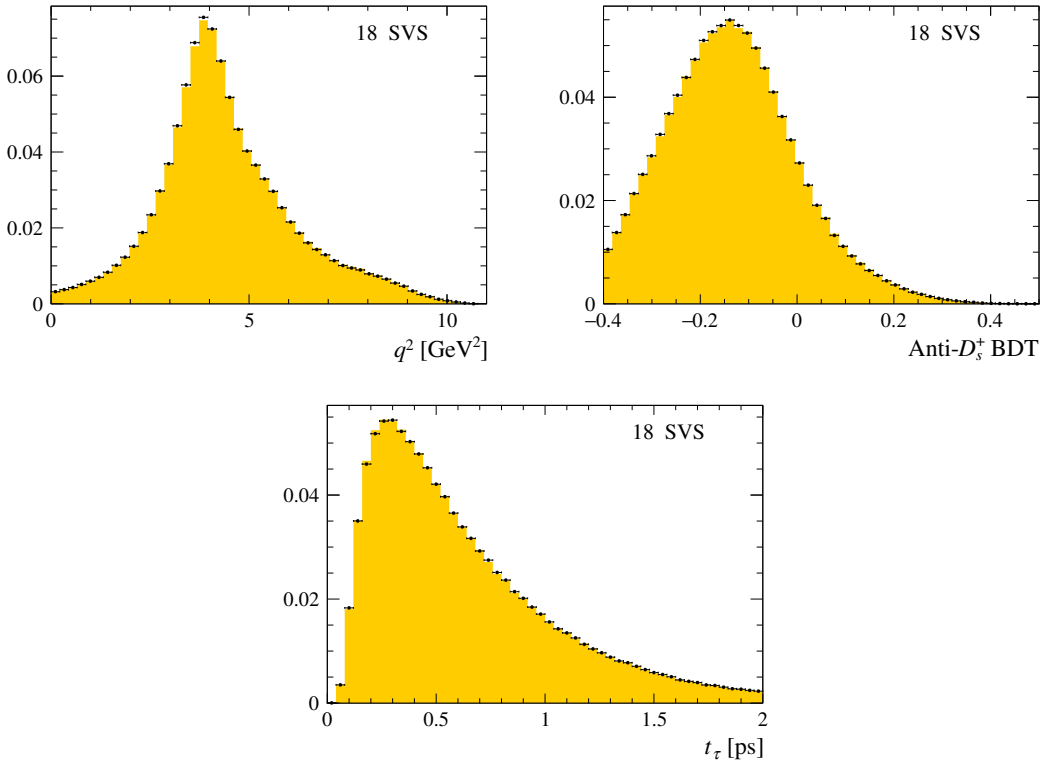

Figure A.3.: Distributions of q^2 (top left), anti-D_s^+ BDT output (top right), and τ^+ lifetime (bottom) for the inclusive $b\bar{b} \to D^{*-}3\pi X$ MC sample, before (yellow histogram) and after (black data points) correction for D^* polarization.

A.4. Monte-Carlo Correction

A.4.1. Polarization of D^* in Two-Body Decays

Fig. A.3 shows the distributions of the signal fit variables distributions before and after the correction. While no significant deviations are observed in the distributions due to the correction, the adjustment is nonetheless implemented across the sample to ensure accuracy.

A.4.2. Polarization of D_s^* in Two-Body Decays

Fig. A.4 shows the distributions of the q^2, anti-D_s^+ BDT output, and τ^+ lifetime variables before and after the correction. The correction factor is applied to the sample to ensure consistency.

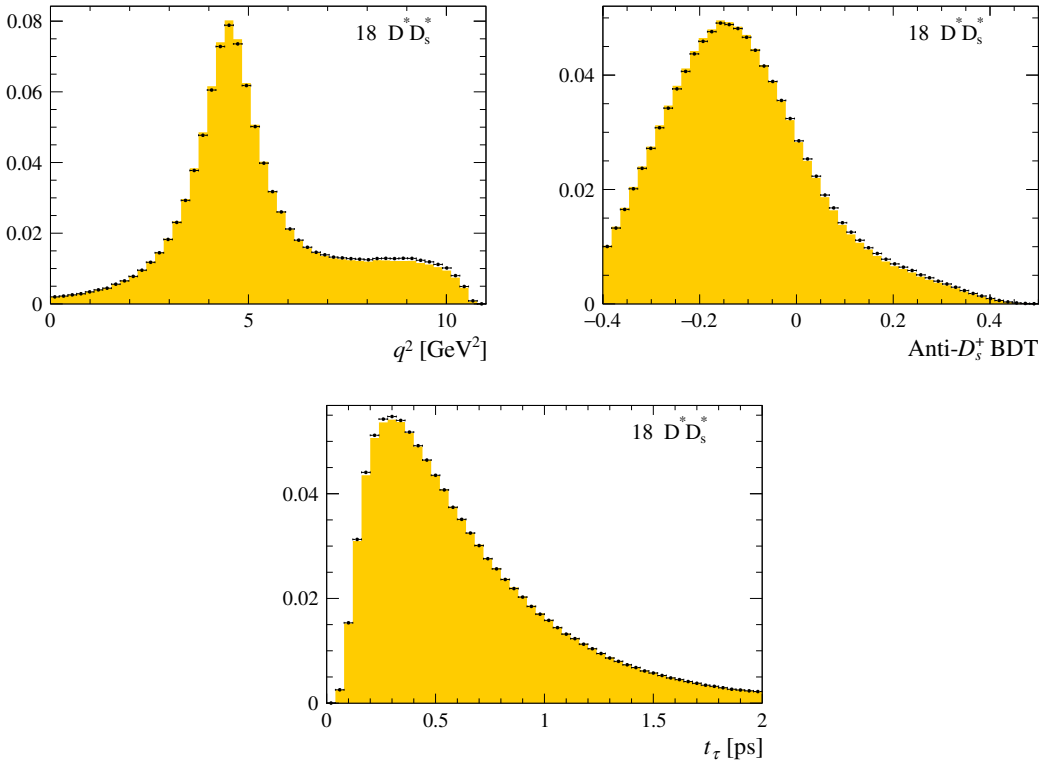

Figure A.4.: Distributions of q^2 (top left), anti-D_s^+ BDT output (top right), and τ^+ lifetime (bottom) for the inclusive $b\bar{b} \to D^{*-}3\pi X$ MC sample, before (yellow histogram) and after (black data points) correction for the D_s^* polarization.

A.4.3. Vertex Error Correction

Fig. A.5 shows the σ^* distributions for different $\max(1/p_T)$ bins from MC samples. The bottom-right panel shows σ^* as a function of $\max(1/p_T)$ along with the corresponding fitted function.

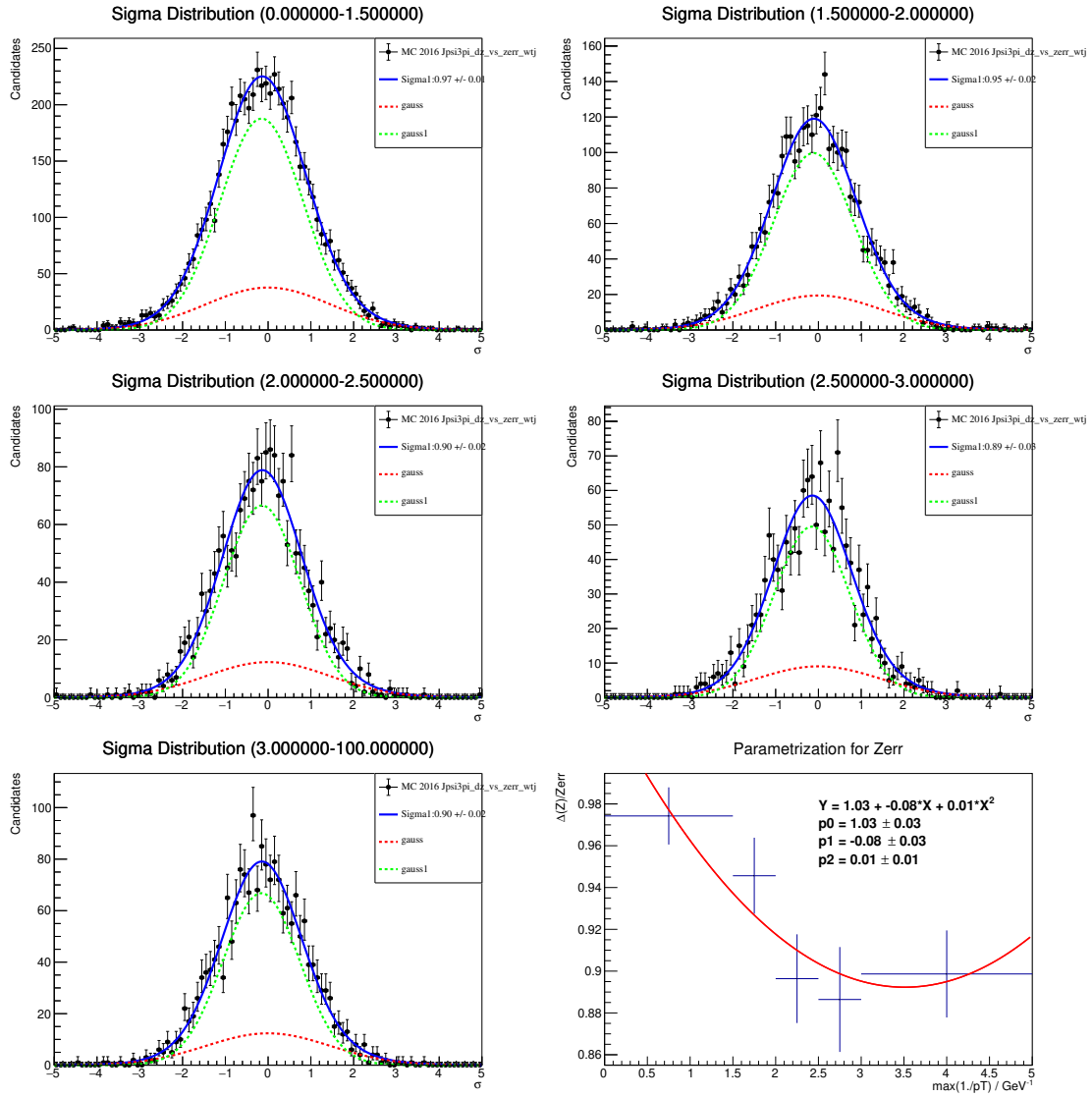

Figure A.5.: σ* distributions for different $\max(1/p_T)$ bins from MC samples. The bottom-right panel shows σ* as a function of $\max(1/p_T)$ along with the corresponding fitted function.

Appendix B

Selection and Efficiency

In this part, additional material about the selection procedure and efficiency calculations is given. .

B.1. L0 Trigger Corrections

B.1.1. TOS Efficiency

2018/2017 efficiency ratio for data $\sim 94\%$

2018/2017 efficiency for MC (raw) $\sim 89\%$ and $\sim 95\%$ for MC (corr)

For 2015/2016, the correction factor for the TOS efficiency is ~ 0.998.

B.1.2. TIS Efficiency

2018/2017 efficiency ratio for data $\sim 91\%$

2018/2017 efficiency for MC (raw) $\sim 85\%$ and $\sim 93\%$ for MC (corr)

For 2015/2016, the correction factor for the TOS efficiency is ~ 1.004.

	Sample	TIS&TOS/TIS 2017	TIS&TOS/TIS 2018
Norm.	data	0.482 ± 0.004	0.455 ± 0.004
	MC (raw)	0.535 ± 0.002	0.477 ± 0.002
	MC (corr)	0.491 ± 0.002	0.468 ± 0.002
Sig.	MC (raw)	0.446 ± 0.003	0.391 ± 0.002
	MC (corr)	0.407 ± 0.003	0.385 ± 0.002
ratio	sig/norm (raw)	0.833	0.821
	sig/norm corr	0.831	0.824
	Ratio correction factor	0.997	1.004

Table B.1.: TOS efficiency for 2017 and 2018 data and MC samples.

	Sample	TIS&TOS/TOS 2017	TIS&TOS/TOS 2018
Norm.	data	0.372 ± 0.004	0.339 ± 0.003
	MC (raw)	0.340 ± 0.002	0.291 ± 0.002
	MC (corr)	0.365 ± 0.002	0.339 ± 0.002
Sig.	MC (raw)	0.379 ± 0.003	0.324 ± 0.003
	MC (corr)	0.406 ± 0.003	0.379 ± 0.003
ratio	sig/norm (raw)	1.114	1.116
	sig/norm corr	1.114	1.116
	Ratio correction factor	1.000	1.000

Table B.2.: TIS efficiency for 2017 and 2018 data and MC samples.

Year	2015	2016	2017	2018
Stripping version	24r1	28r1	29r2	34

Table B.3.: Stripping versions used for the 2015–2018 dataset.

B.2. Preselection

The stripping versions used are summarized in Tab. B.3.

B.3. Multivariate Analysis

B.3.1. BDT Methods

The BDT methods : BDT, BDTD and BDTG are used. These methods come within the TMVA package [164]. They are chosen to optimize the performance of each selection. The following configurations have been used:

- BDT: BDT method refers to AdaBoost method, which adjusts the weights of misclassified events. It uses 850 trees, with 2.5% min percentage of training events in a leaf node, and a maximum depth of 3. The learning rate is set to 0.5, and the bagging[1] fraction is set to 0.5, It also uses a Gini index for measuring the quality of a split. Finally, the number of grid points for the cut optimization is set to 20.
- BDTD: uses the AdaBoost method with 400 trees, a 5% minimum percentage of training events in a leaf node, and a maximum depth of 3. The learning rate is set according to the AdaBoost method, and the Gini index is used to measure the quality of a split. Additionally, it applies a decorrelation transformation to the input variables, with the number of grid points for cut optimization set to 20.
- BDTG: uses gradient boosting, which builds tree sequentially, where each tree tries to correct the errors of the previous one. It uses 1000 trees, with 2.5% min percentage of training events in a leaf node, and a maximum depth of 2. The learning rate is set to 0.1, and the bagging fraction is set to 0.5. Finally, the number of grid points for the cut optimization is set to 20.

[1]Bagging is used to reduce variance

BDT	ROC Integral
Combinatorial	0.819
Isolation	0.857
Detachment	0.845
DstDs	0.957

Table B.4.: ROC integral for the four BDTs.

B.3.1.1. Input Data/MC Comparison

The comparison of the input variables between data and MC, used in the BDT training, is shown in this section.

B.3.1.2. Combinatorial BDT

The comparison of the combinatorial BDT input variables between data and MC is shown in Fig. B.1.

B.3.1.3. Isolation BDT

The comparison of the isolation BDT input variables between data and MC is shown in Figs. B.2 and B.3.

B.3.1.4. Detachment BDT

The comparison of the detachment BDT input variables between data and MC is shown in Fig. B.4.

B.3.1.5. Anti-D_s^+ BDT

The comparison of the anti-D_s^+ BDT input variables between data and MC is shown in Figs. B.5 to B.7.

B.3.1.6. BDT ROC Curves

The ROC curves for the four BDTs are shown in Fig. B.8. The ROC integral is reported in Tab. B.4.

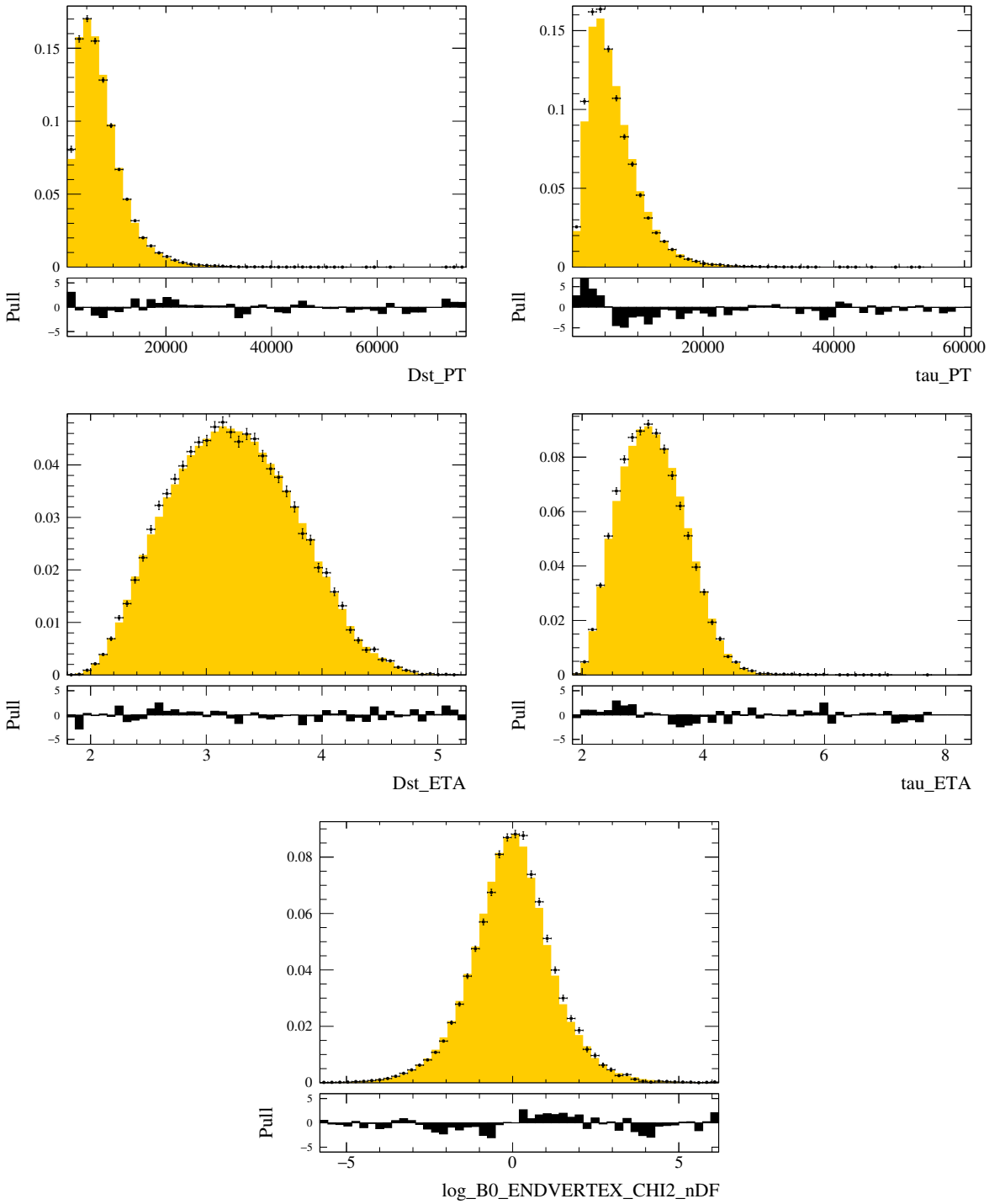

Figure B.1.: Comparison of Data (black points) and MC (colored bins) for the combinatorial BDT input variables.

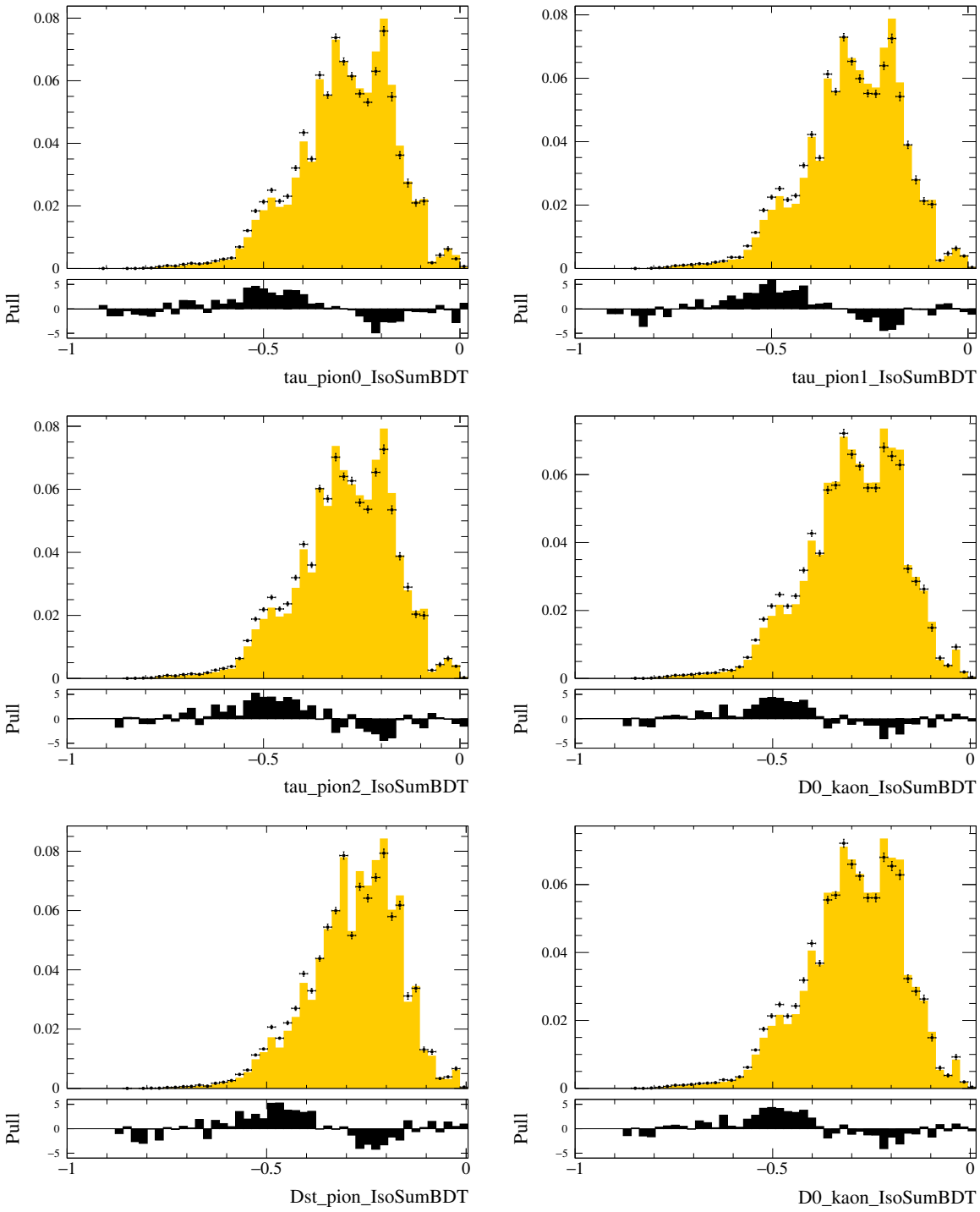

Figure B.2.: Comparison of Data (black points) and MC (colored bins) for the isolation BDT input variables.

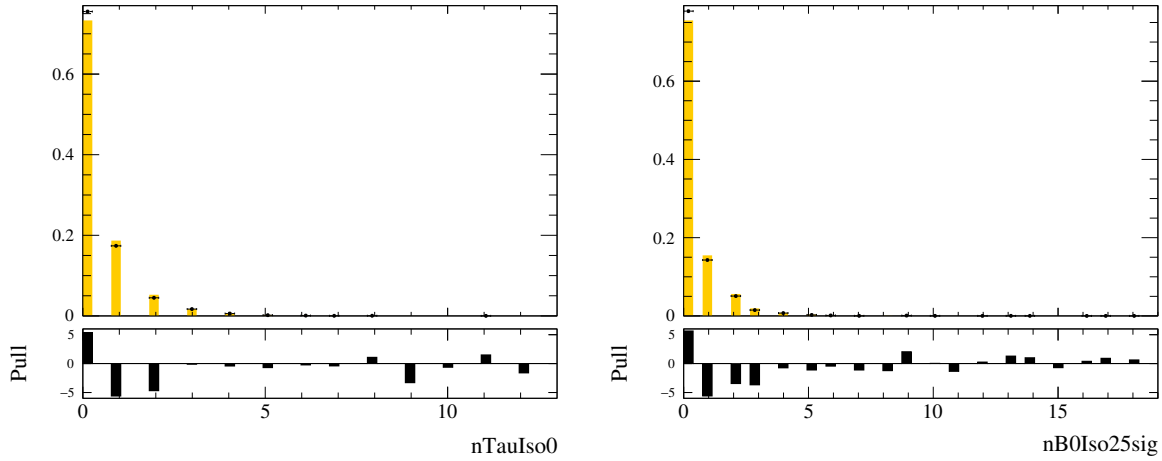

Figure B.3.: Comparison of Data (black points) and MC (colored bins) for the isolation BDT input variables.

	sig 1	sig 2	norm
Geometry	16.44 ± 3.44	15.86 ± 3.0	15.56 ± 2.91
Preselection	100.0 ± 0.0	100.0 ± 0.0	100.0 ± 0.0
Da Vinci	0.45 ± 0.28	0.37 ± 0.42	1.18 ± 0.45
Common and Trigger	60.93 ± 2.90	57.71 ± 2.66	39.88 ± 3.0
Mode-Specific	39.30 ± 3.28	30.90 ± 2.93	60.94 ± 3.75
PID	76.43 ± 2.49	78.99 ± 2.20	74.13 ± 2.70
Total	0.01 ± 0.75	0.01 ± 1.11	0.03 ± 0.73

Table B.5.: Efficiency averages at different stages of the selection for 2015–2016 dataset.

B.4. Efficiency Calculation

B.4.1. Selection Step Efficiency

The signal, normalization efficiencies and their ratio are shown in Tab. B.6. The average efficiencies at different stages of the selection for the 2015–2016 dataset are shown in Tab. B.5.

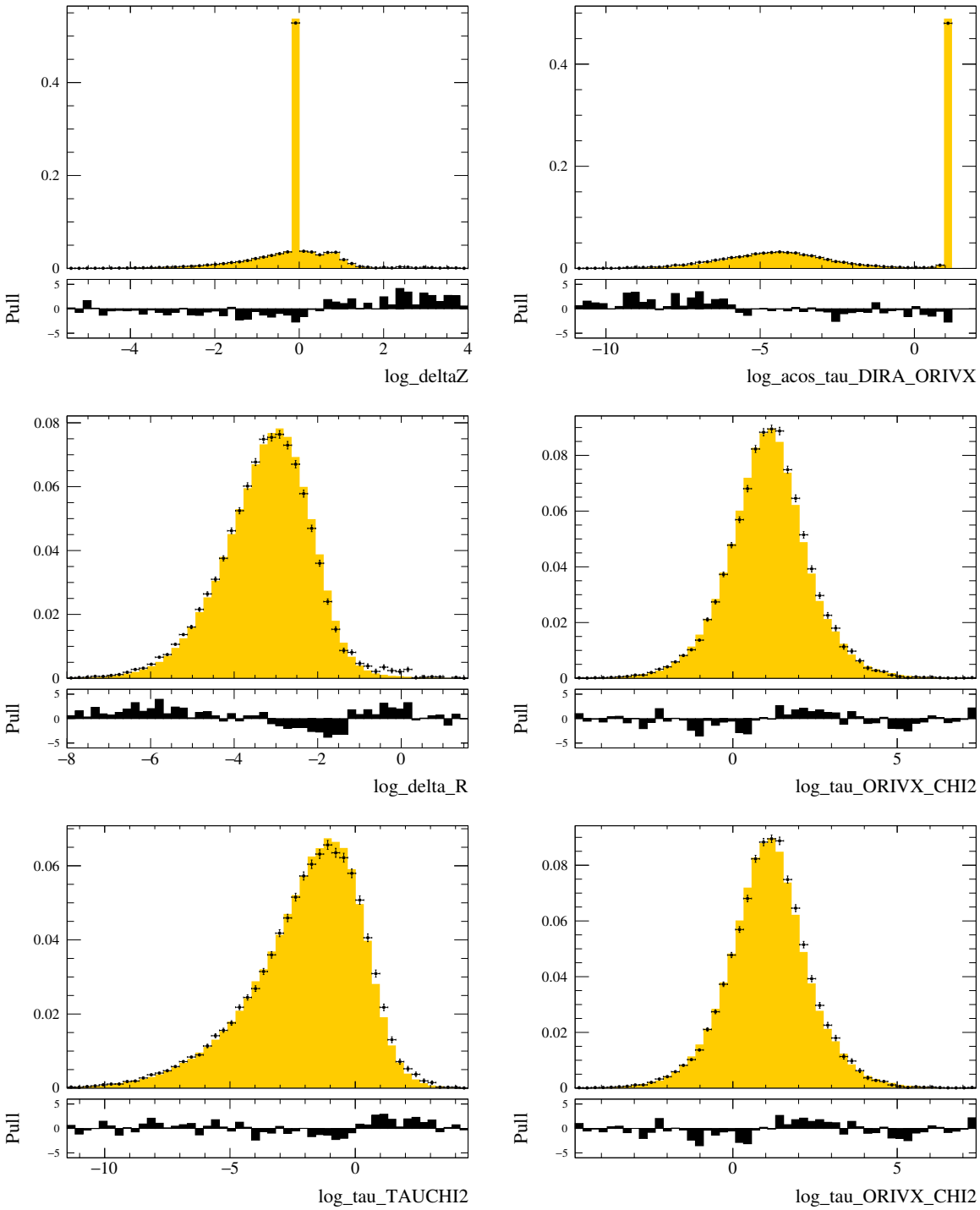

Figure B.4.: Comparison of Data (black points) and MC (colored bins) for the detachment BDT input variables.

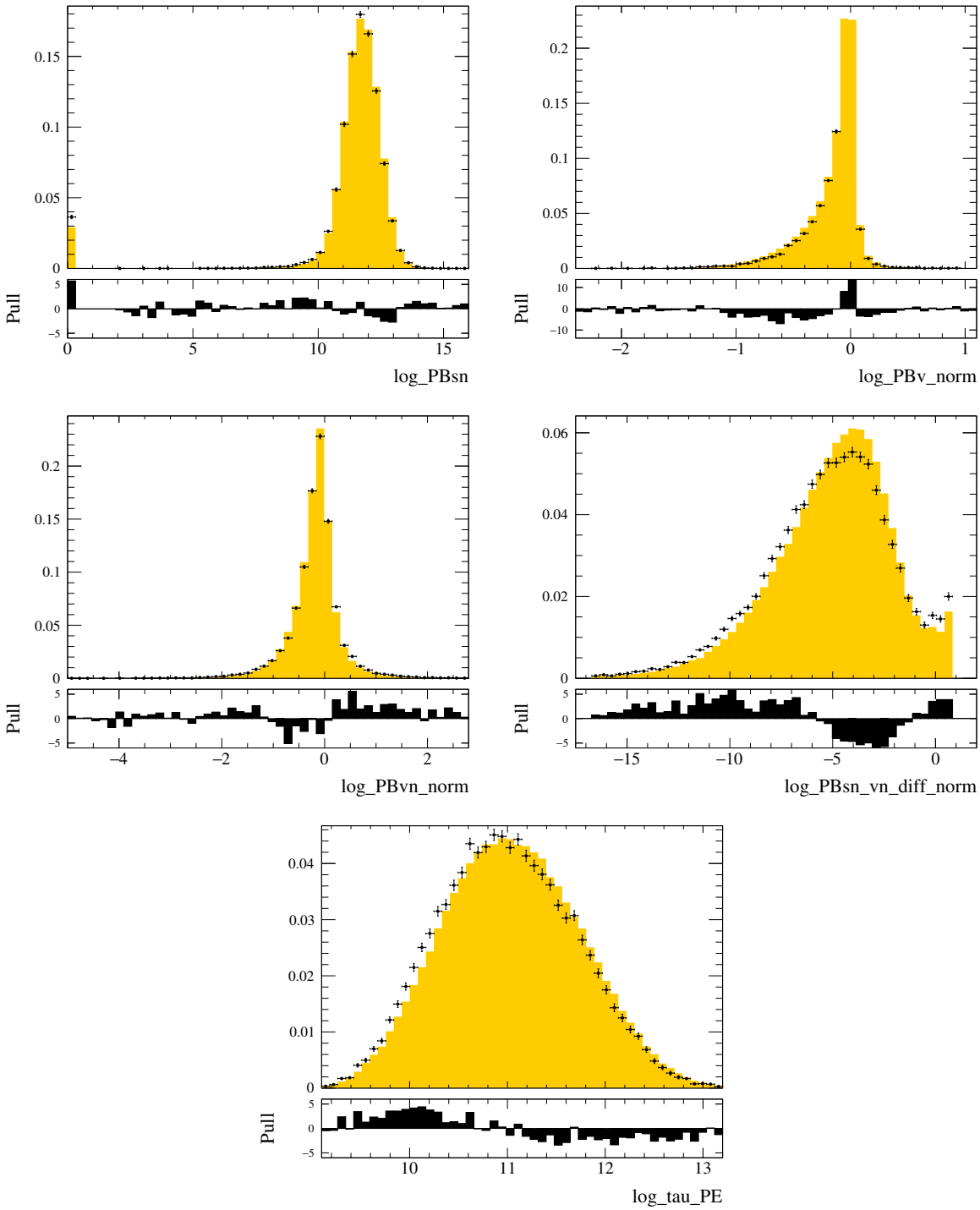

Figure B.5.: Comparison of Data (black points) and MC (colored bins) for the anti-D_s^+ BDT input variables.

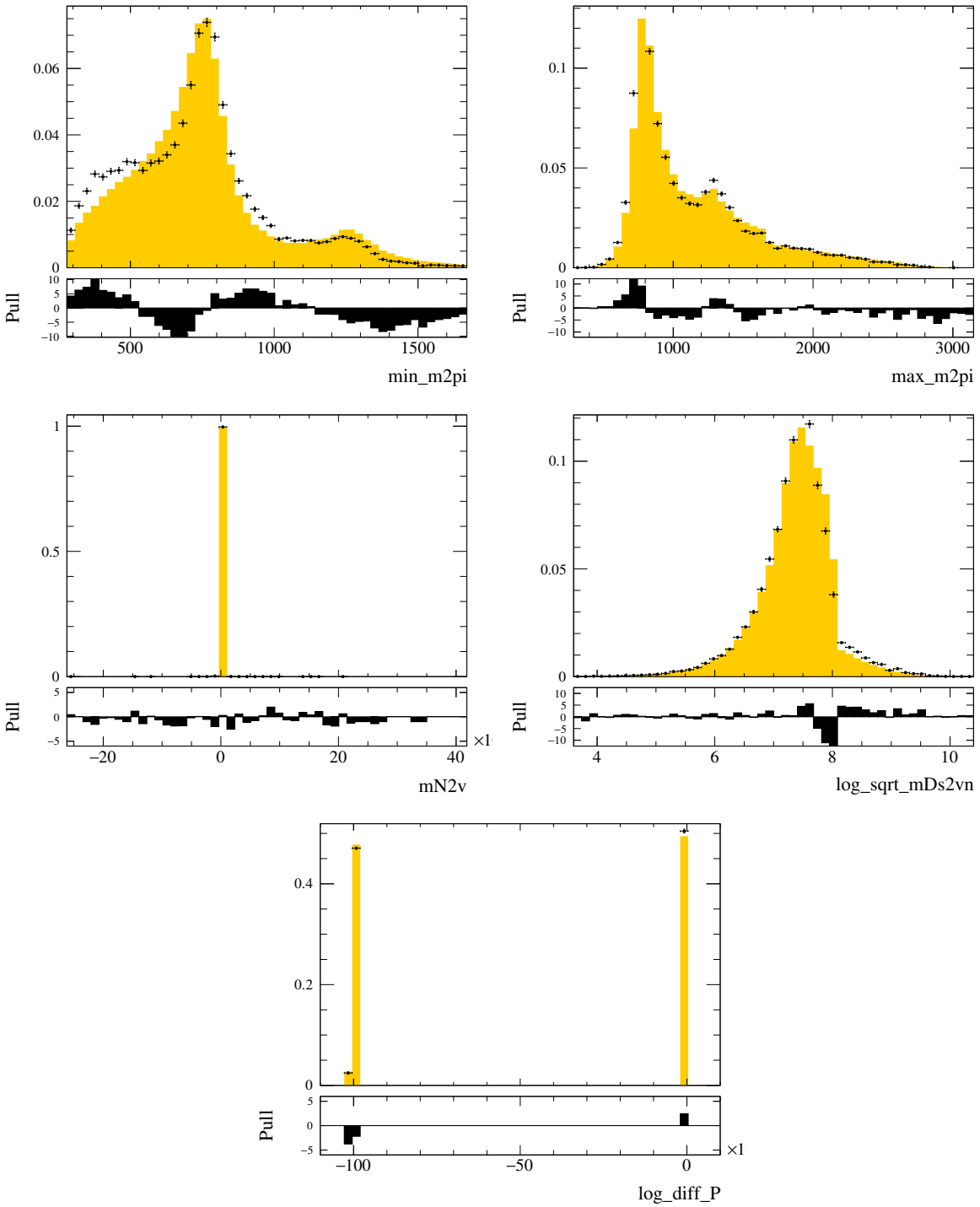

Figure B.6.: Comparison of Data (black points) and MC (colored bins) for the anti-D_s^+ BDT input variables.

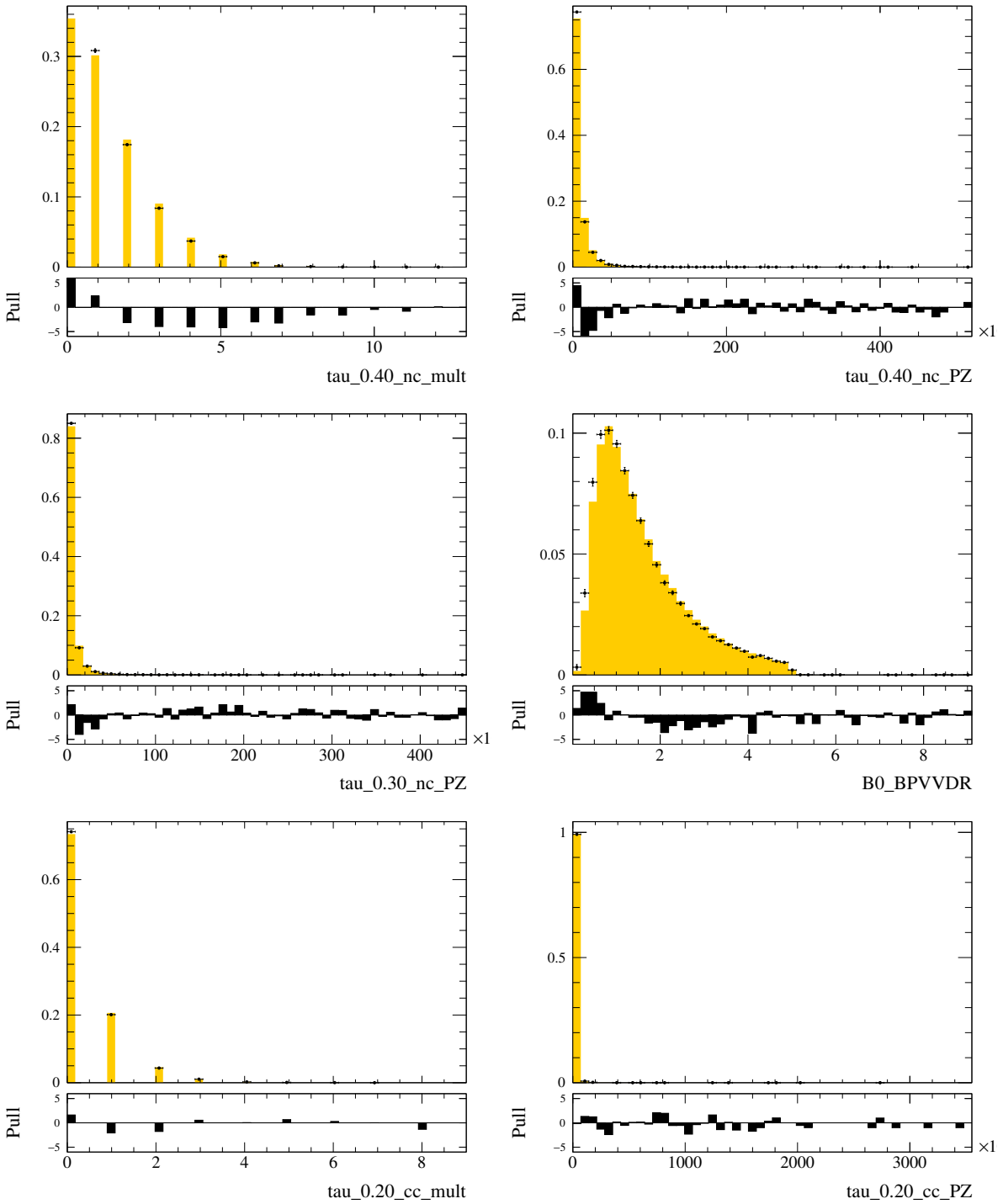

Figure B.7.: Comparison of Data (black points) and MC (colored bins) for the anti-D_s^+ BDT input variables.

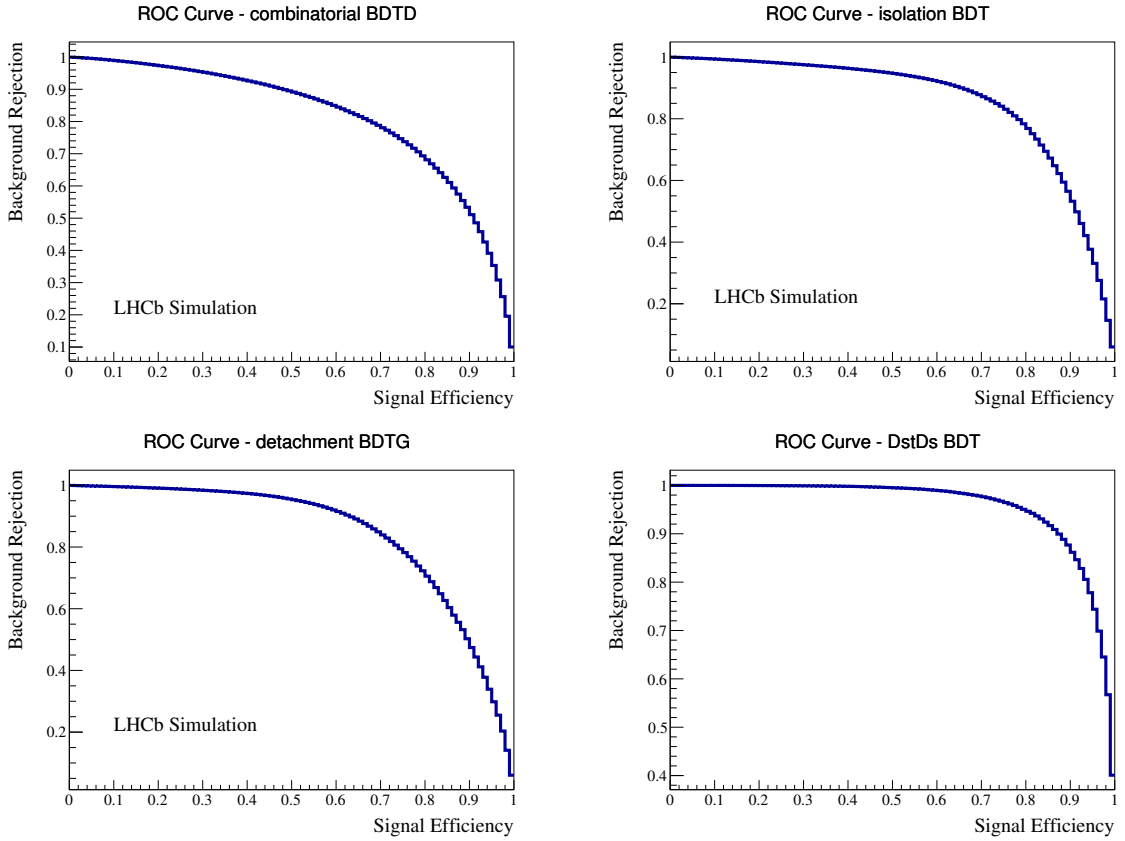

Figure B.8.: Background rejection vs signal efficiency for the combinatorial (top left), isolation (top right), detachment (bottom left) and anti-D_s^+ (bottom right) BDTs.

	Datasets				
	2015–2016	**2017**	**2018**	**2017–2018**	**Run 2**
$\varepsilon_{\mathrm{norm}} \times 10^4$	3.244 ± 0.036	4.028 ± 0.029	3.349 ± 0.025	3.650 ± 0.019	3.466 ± 0.019
$\varepsilon_{\mathrm{sig}} \times 10^4$	1.141 ± 0.009	1.354 ± 0.006	1.134 ± 0.006	1.231 ± 0.004	1.190 ± 0.005
$\varepsilon_{\mathrm{norm}}/\varepsilon_{\mathrm{sig}}$	2.883 ± 0.039	3.018 ± 0.025	2.994 ± 0.027	3.005 ± 0.019	2.952 ± 0.020

Table B.6.: Efficiencies for the signal and normalization modes, and their ratio, for various datasets.

	Datasets				
	2015–2016	**2017**	**2018**	**2017–2018**	**Run 2**
$f_{\tau^+\to 3\pi\overline{\nu}_\tau}$	0.767 ± 0.004	0.768 ± 0.002	0.770 ± 0.003	0.769 ± 0.002	0.768 ± 0.002
$f^{\text{Sim.}}_{\tau^+\to 3\pi\overline{\nu}_\tau}$	0.768 ± 0.004	0.769 ± 0.002	0.771 ± 0.003	0.770 ± 0.002	0.769 ± 0.002

Table B.7.: Fraction $f_{\tau^+\to 3\pi\overline{\nu}_\tau}$ for various datasets.

B.5. Trigger Configuration Key Table

The list of TCK configurations used for 2017 and 2018 is given in Fig. B.9. The TCK highlighted in color are the most common.

Year	Type	Polarity	TCK	L0 Trigger									
				L0Hadron		L0Photon		L0Electron		L0Muon		L0DiMuon	
				E_T (MeV/c^2)	nSPD hits	E_T (MeV/c^2)	nSPD hits	E_T (MeV/c^2)	nSPD hits	p_T ($\mathrm{GeV}/c \times 20$)	nSPD hits	p_T ($\mathrm{GeV}/c \times 20$)	nSPD hits	p_T ($\mathrm{GeV}/c \times 20$)^2
2016	MC	both	0x6138160F	3744	450	2784	450	2400	450	36	450	900	900	120
2017	MC	both	0x62661709	3456	450	2472	450	2112	450	28	450	676	900	120
	data	up	0x21511703	3216	450	2304	450	2112	450	22	450	400	900	120
			0x21601708	3216	450	2304	450	2112	450	22	450	400	900	120
			0x21561707	3720	450	2712	450	2304	450	34	450	1296	900	120
			0x21511705	3696	450	2976	450	2592	450	30	450	676	900	120
			0x21511706	3888	450	3072	450	2688	450	38	450	1296	900	120
			0x21611709	3456	450	2472	450	2112	450	28	450	676	900	120
			0x21511704	3552	450	2784	450	2256	450	26	450	576	900	120
			0x21511702	2976	450	2112	450	1872	450	14	450	324	900	120
		down	**0x21551707**	3720	450	2712	450	2304	450	34	450	1296	900	120
			0x21611709	3456	450	2472	450	2112	450	28	450	676	900	120
			0x21611708	3216	450	2304	450	2112	450	22	450	400	900	120
			0x21551707	3720	450	2712	450	2304	450	34	450	1296	900	120
2018	MC	both	0x617d18a4	3792	450	2952	450	2376	450	35	450	1296	900	120
	data	up	0x21771801	3792	450	2952	450	2376	450	35	450	1296	900	120
			0x21771802	3792	450	2952	450	2376	450	35	450	1296	900	120
			0x217d18a4	3792	450	2952	450	2376	450	35	450	1296	900	120
			0x21771801	3792	450	2952	450	2376	450	35	450	1296	900	120
		down	0x217b18a2	3792	450	2952	450	2376	450	35	450	1296	900	120
			0x21751801	3792	450	2952	450	2376	450	35	450	1296	900	120
			0x217d18a4	3792	450	2952	450	2376	450	35	450	1296	900	120

Figure B.9.: TCK table for the 2017 and 2018 data taking periods.

Appendix C

Fit results

C.1. Signal Fit

C.1.1. Fit Validation

C.2. Normalization Fit

The normalization fit for different datasets is given in Tab. C.2. The errors for 2018, 2017 and 2015–2016 datasets are overestimated due to correlations during the subtraction.

	N_{D_s}	$N_{B\to D^{*-}3\pi^{\pm}X}$	N_{sig}	$f_{B_s\to D^{*}D_sX}$	$f_{D^{**}D_sX}$	$f_{D^{+}}$	$f_{D'^{+}_{s1}}$	f_{D_s}	$f_{D^{*+}_{s0}}$	$f^{\nu_1-\nu_2}_{D^0}$
N_{D_s}	1.00	−0.12	0.29	0.52	0.69	−0.72	−0.07	0.06	−0.17	−0.74
$N_{B\to D^{*-}3\pi^{\pm}X}$	−0.12	1.00	−0.17	−0.03	0.05	−0.01	−0.00	−0.06	0.03	−0.16
N_{sig}	0.29	−0.17	1.00	0.21	0.28	−0.37	−0.13	0.06	−0.07	−0.48
$f_{B_s\to D^{*}D_sX}$	0.52	−0.03	0.21	1.00	−0.03	−0.36	0.19	0.06	−0.04	−0.49
$f_{D^{**}D_sX}$	0.69	0.05	0.28	−0.03	1.00	−0.58	−0.39	0.15	−0.04	−0.62
$f_{D^{+}}$	−0.72	−0.01	−0.37	−0.36	−0.58	1.00	0.06	−0.05	0.14	0.39
$f_{D'^{+}_{s1}}$	−0.07	−0.00	−0.13	0.19	−0.39	0.06	1.00	0.20	−0.40	0.12
f_{D_s}	0.06	−0.06	0.06	0.06	0.15	−0.05	0.20	1.00	0.22	−0.04
$f_{D^{*+}_{s0}}$	−0.17	0.03	−0.07	−0.04	−0.04	0.14	−0.40	0.22	1.00	0.14
$f^{\nu_1-\nu_2}_{D^0}$	−0.74	−0.16	−0.48	−0.49	−0.62	0.39	0.12	−0.04	0.14	1.00

Table C.1.: Correlation matrix for the signal fit parameters in the pseudo-experiment fits.

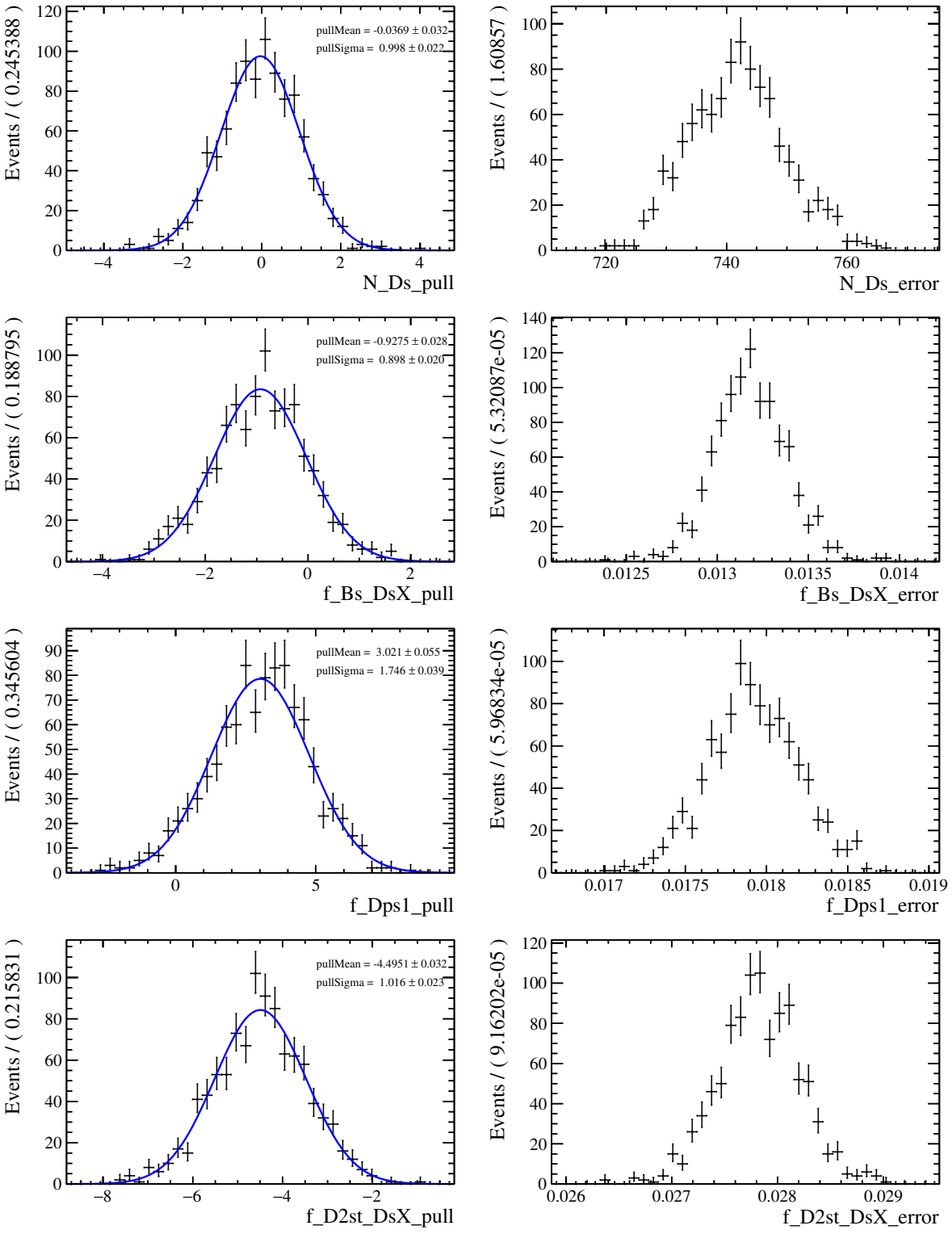

Figure C.1.: Pull distributions for the signal fit parameters.

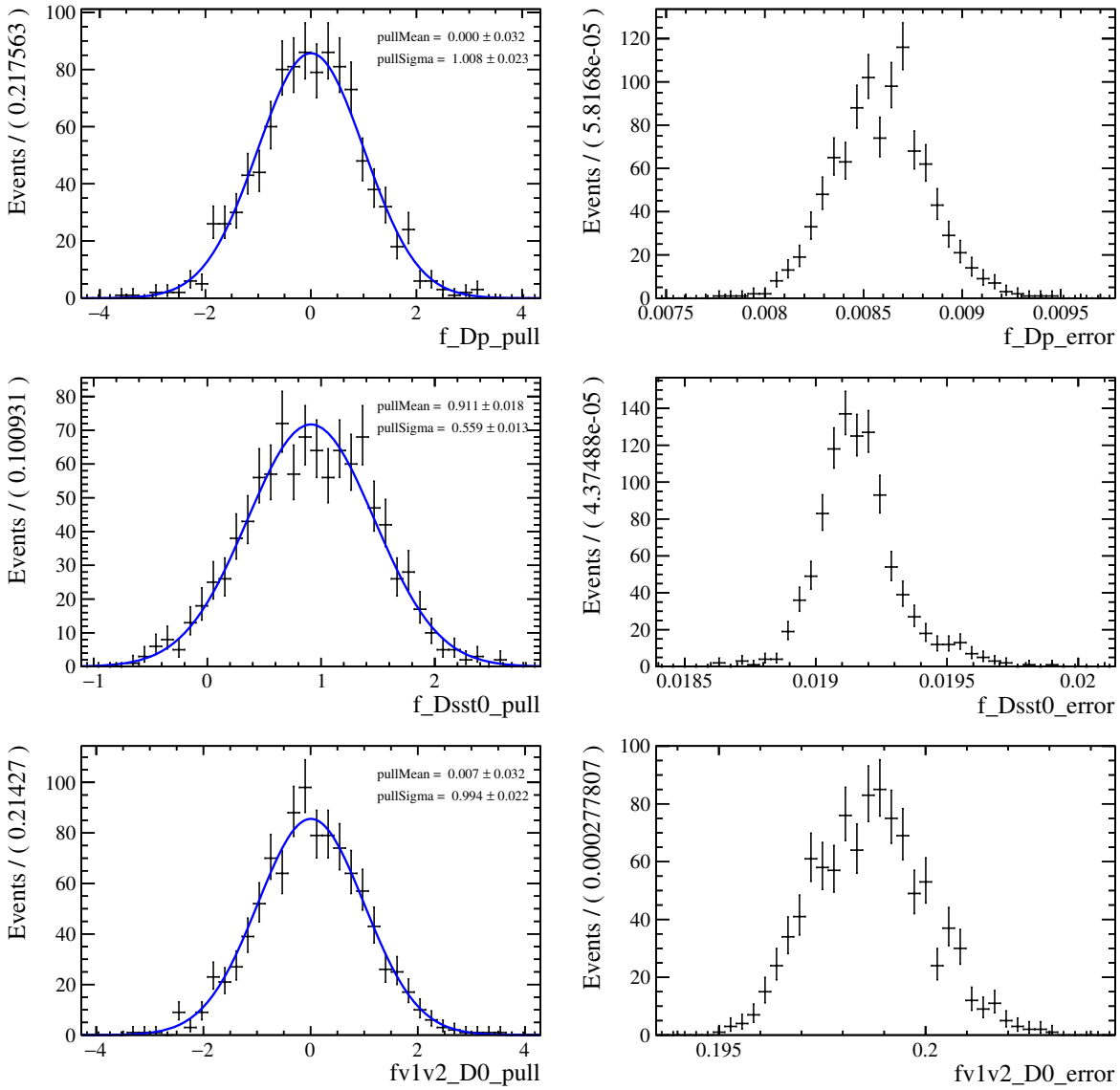

Figure C.2.: Pull distributions for the signal fit parameters.

Parameter	Run 2	2018	2017	2015–2016
N_{tot}	103590 ± 353	34929 ± 196	29507 ± 180	30098 ± 182
N_{fake}	9057 ± 315	930 ± 78	760 ± 78	645 ± 74
N_{B}	94533 ± 473	34000 ± 211	28747 ± 196	29453 ± 197
$N_{D_s^+}$	1360 ± 60	432 ± 36	377 ± 33	427 ± 33
N_{norm}	93173 ± 441	33567 ± 214	28370 ± 199	29026 ± 200

Table C.2.: Normalization yield from the extrapolation method, for Run 2, 2018, 2017, and 2015–2016 datasets.

Appendix D

Systematic Uncertainties

The systematics for 2015–2016 analysis [3] are given in App. D

Source	**Systematic Uncertainties** [%]
Signal decay template shape	1.8
Signal decay efficiency	0.9
Fractions of signal τ^+ decays	0.3
Possible contributions from other τ^+ decays	1.0
Fixing the $\overline{D}^{**}\tau^+\nu_\tau$ and $D_s^{**+}\tau^+\nu_\tau$ fractions	$^{+1.8}_{-1.9}$
Normalization mode PDF choice	1.0
Knowledge of the $D_s^+ \to 3\pi X$ decay model	1.0
Specifically the $D_s^+ \to a_1 X$ fraction	1.5
$B \to D^{*-}D_s^+(X)$ template shapes	0.3
$B \to D^{*-}D^0(X)$ template shapes	1.2
$B \to D^{*-}D^+(X)$ template shapes	$^{+2.2}_{-0.8}$
Fixing $B \to D^{*-}D_s^+(X)$ bkg model parameters	1.1
Fixing $B \to D^{*-}D^0(X)$ bkg model parameters	1.5
$B \to D^{*-}3\pi X$ template shapes	1.2
Combinatorial background normalization	$^{+0.5}_{-0.6}$
PID efficiency	0.5
Kinematic reweighting	0.7
Vertex error correction	0.9
Normalization mode efficiency (modeling of $m(3\pi)$)	1.0
Preselection efficiency	2.0
Signal efficiency (size of simulation sample)	1.1
Normalization efficiency (size of simulation sample)	1.1
Empty bins in templates	1.3
PDF shapes uncertainty (size of simulation sample)	2.0
Total systematic uncertainty	$^{+6.2}_{-5.9}$
Total statistical uncertainty	5.9

Table D.1.: Summary of relative systematic uncertainties on the ratio $\mathcal{K}(D^{*-})$ [3].

List of Acronyms

2HDM	Two Higgs Doublet Model
BDT	Boosted Decision Tree
BGL	Boyd-Grinstein-Lebed
BSM	Beyond the Standard Model
CKM	Cabibbo-Kobayashi-Maskawa
CLN	Caprini-Lellouch-Neubert
DIRA	Distance in the Direction Angle
DOCA	Distance of Closest Approach
ECAL	Electromagnetic Calorimeter
EFF	Event Filter Farm
EFT	Effective Field Theory
EW	Electroweak
FCCC	Flavor Changing Charged Current
FCNC	Flavor Changing Neutral Current
FEB	Front-End Board
FF	Form Factor
GIM	Glashow, Iliopoulos and Maiani
GUTs	Grand Unified Theories
HCAL	Hadronic Calorimeter
HL-LHC	High-Luminosity Large Hadron Collider
HPDs	Hybrid Photon Detectors
HQET	Heavy Quark Effective Theory

IP	Impact Parameter
IR	Infrared
IT	Inner Tracker
KDE	Kernel Density Estimation
LEP	Large Electron-Positron Collider
LFU	Lepton Flavor Universality
LFV	Lepton Flavor Violation
LHC	Large Hadron Collider
MC	Monte-Carlo
MFV	Minimal Flavor Violation
MSSM	Minimal Supersymmetric Standard Model
MVA	MultiVariate Analysis
NC	Neutral Current
NP	New Physics
OT	Outer Tracker
PDF	Probability Density Function
PID	Particle Identification
PMNS	Pontecorvo-Maki-Nakagawa-Sakata
PS	Preshower
PV	Primary Vertex
QCD	Quantum Chromodynamics
QFT	Quantum Field Theory
RGE	Renormalization Group Equation
RICH	Ring Imaging Cherenkov
RS	Right-Sign
RTA	Real-Time Analysis
SLAC	Stanford Linear Accelerator Center
SM	Standard Model of Particle Physics
SPD	Scintillating Pad Detector
SUSY	Supersymmetry

SV	Secondary Vertex
SVS	Scalar to Vector Scalar
TCK	Trigger Configuration Key
TIS	Trigger Independent of Signal
TOS	Trigger On Signal
TT	Tracker Turicensis
UV	Ultraviolet
VELO	Vertex Locator
WS	Wrong-Sign